ROTORCRAFT IN-PLANE NOISE REDUCTION USING ACTIVE/PASSIVE APPROACHES WITH INDUCED VIBRATION TRACKING

by

Miang Hwee Chia

A dissertation submitted in partial fulfillment
of the requirements for the degree of
Doctor of Philosophy
(Aerospace Engineering)
in The University of Michigan
2017

Doctoral Committee:

Professor Peretz P. Friedmann, Chair
Professor Carlos E. Cesnik
Professor David R. Dowling
Assistant Professor Karthik Duraisamy

Miang Hwee Chia

cmianghw@umich.edu

ORCID iD: 0000-0002-1364-7802

To Lead, To Excel, To Overcome

ACKNOWLEDGEMENTS

First and foremost, I would like to thank my advisor, Professor Peretz P. Friedmann. I am forever grateful for the faith he has given me, especially in the initial year when I was struggling to get back to a firm academic footing, after a hiatus of twelve years from school. He is like the father I never felt I had, extremely firm and tough in his expectations and yet gentle at those crucial moments to just keep me going. I would like to thank Professor Karthik Duraisamy, who is my co-advisor for all intents and purposes. Your AE729 class could not have come at a more opportune time. I would also like to thank Dr. Ashwani Padthe, the co-author for all my publications. Many thanks for showing me the ropes of research and the finer points of technical writing. I would also like to thank Drs Thomas Millot, Tim Myrtle, Marino de Terlizzi, Dan Patt, Li Liu, and Bryan Glaz, the giants on whose shoulders I gently tread on for this work.

This endeavor would also not have been possible without the financial support from my company, Defence Science and Technology Agency, Singapore. Special thanks goes to Chief Executive, Mr Tan Peng Yam, and Director, Mr Pek Beng Tit for giving me this opportunity. I would also like to thank former Director (Air Force Research Laboratory), Mr Joe Sciabica, Deputy Secretary(Ministry of Na-

tional Development), BG(NS) Tan Meng Dui and Vice President (Singapore Institute of Technology), Mr Tsoi Mun Heng for recommending me for graduate school then.

I would like to thank the friends I met at the University of Michigan, Clara Ang, Daniel Biggs, Adam Duran, Sriram Ganesan, Daning Huang, Nicolas Lamorte, Eric Muir, Ziyang Pang, Ryan Patterson, Abhinav Sharma, Puneet Singh, Chia-Yu Tang and Huai-Te Yu.

Last but not least, I would like to dedicate this work to my family, my wife, Ee Wan Khoo, and three kids, Mei Xi Chia, Mei Han Chia and Mei Si Chia, for bearing with my idiosyncrasies at home after a long day at work. I love you.

TABLE OF CONTENTS

DEDICATION ii

ACKNOWLEDGEMENTS iii

LIST OF FIGURES x

LIST OF TABLES xvii

LIST OF APPENDICES xviii

LIST OF SYMBOLS xix

ABSTRACT xxvii

CHAPTER

I. INTRODUCTION, LITERATURE REVIEW, AND OBJECTIVES . 1

1.1 Review of Approaches to Helicopter Noise and Vibration Reduction 3

1.1.1 Active Control Approaches 3

1.1.2 Passive Control Approaches 12

1.2 Literature on OBC Configuration Design 17

1.3 Literature on In-Plane Noise Reduction 19

1.3.1 Active Control of In-Plane Noise 20

1.3.2 Passive Control of In-Plane Noise 24
1.4 Objectives and Novel Contributions of this Dissertation . . . 25

II. DESCRIPTION OF THE ROTORCRAFT AEROELASTIC ANALYSIS CODE 28

2.1 Structural Dynamics Model 28
2.1.1 Global Galerkin Model 29
2.1.2 Galerkin Type Finite Element Model 29
2.2 Aerodynamic Model 30
2.3 Coupled aeroelastic response/trim solution 32
2.4 Control Approach 33
2.4.1 Implementation of the HHC Algorithm 37
2.4.2 Actuator Saturation 41

III. ACOUSTIC MODEL 44

3.1 Rotor Noise Sources 45
3.2 Governing Equations 48
3.2.1 Ffowcs William-Hawkings (FW-H) Equation 48
3.2.2 Farrasat's Formulation 1 and 1A 50
3.3 Modified WOPWOP 54
3.4 HELIcopter NOise Reduction (HELINOIR) 57

IV. THE AEROELASTIC-AEROACOUSTIC FRAMEWORK 63

4.1 Data Flow 63
4.2 Computational Implementation 65
4.2.1 Coordinate System 65
4.2.1.1 Transformation Matrices 67

4.2.1.2 Coordinate Transformation for Deformed Blade Position . . . 68
4.2.1.3 Coordinate Transformation for Blade Loading . . . 70
4.2.2 Time Steps . . . 71
4.2.3 Inboard Shed Wake Core Radius . . . 71
4.2.4 Dimensional Parameters . . . 72

V. RESULTS . . . 73

5.1 Parametric Study of OBC Configuration . . . 74
5.1.1 Validation of Microflap CFD Setup . . . 74
5.1.2 OBC Configuration for Parametric Study . . . 78
5.1.3 Vibration Reduction . . . 83
5.1.4 Influence of Microflap Chordwise Position on Vibration Reduction . . . 88
5.1.5 Noise Reduction . . . 90
5.2 Validation Studies . . . 94
5.2.1 HART Wind Tunnel Test . . . 95
5.2.1.1 Background . . . 95
5.2.1.2 HART Validation Test Case . . . 96
5.2.1.3 Blade Aerodynamic Loads . . . 97
5.2.1.4 BVISPL on Carpet Plane . . . 98
5.2.1.5 Acoustic Pressure History . . . 99
5.2.2 Boeing SMART Rotor Wind Tunnel Test . . . 100
5.2.2.1 Background . . . 100
5.2.2.2 Boeing SMART Rotor Validation Test Case . . . 101
5.2.2.3 In-Plane Acoustic Pressure Histories . . . 102
5.3 Verification Studies . . . 105

5.3.1 Global Galerkin Model 106
5.3.1.1 Baseline Flight Condition 106
5.3.1.2 Active Noise Reduction 107
5.3.1.3 Active Vibration Reduction and Noise Penalty 109
5.3.2 Galerkin Type FEM 110
5.3.2.1 Baseline Noise and Vibration 112
5.4 Results - In-Plane Noise Control 113
5.4.1 Baseline Flight Condition 114
5.4.2 Active Control of In-Plane Noise 115
5.4.2.1 Baseline Noise 115
5.4.2.2 Noise Reduction Using Far-Field Feedback 115
5.4.2.3 Noise Reduction Using Near-Field Feedback 121
5.4.2.4 Effects of Advance Ratio 127
5.4.2.5 Noise Reduction Using a Dual Plain Flap Configuration 129
5.4.3 Passive Control of In-Plane Noise 132
5.4.3.1 Baseline Noise 134
5.4.3.2 Impact of Tip Geometry Modification on Noise 134
5.4.3.3 Impact of Tip Geometry Modification on Vibration 138
5.4.4 Comparison Between Active and Passive Control . 140
5.4.4.1 Noise Reduction Performance 140
5.4.4.2 Impact on Vibration 140
5.4.4.3 Noise Control Mechanism 141

VI. SUMMARY AND CONCLUSIONS 144

6.1 Conclusions 145
6.2 Future Work 149

APPENDICES 150

BIBLIOGRAPHY 248

LIST OF FIGURES

Figure

1.1 Various elements of the complex aerodynamic environment of a helicopter [79]. 2
1.2 Hierarchy of active control approaches (Adapted from Ref. 34). . . 5
1.3 Examples of passive blade tip modifications [84]. 13
1.4 A 20%c conventional plain flap configuration. 17
1.5 Sliding microflap configuration. 18
1.6 Rotor noise components and directivity characteristics. (Adapted from Ref. 105) 20
1.7 Effects of active flap motion on blade aerodynamic forces and generation of positive peak pressure [105]. 21
2.1 Higher harmonic control architecture 34
3.1 External noise spectrum of UH-1A [98]. 45
3.2 Control surface. 50
3.3 Schematic of the WOPWOP algorithm (Adapted from Ref. 10). . . . 55
3.4 Schematic of the HELINOIR algorithm. 59
3.5 Source/sink representation for thickness noise generation. 61
3.6 Verification of the compact model acoustic pressure predictions for a UH-60 rotor at μ=0.30, M_{tip}=0.63, at an observer located 3R in front of the rotor plane. 62
4.1 Data flowchart between AVINOR and HELINOIR for active control. 64
4.2 The transformation from the “4B", “4A", to the “4" system. 67

4.3 "1A" System. 67
4.4 Orientation of tangential and perpendicular air velocities and aerodynamic loads 70
4.5 Vortex classification in the rotor flow field [84]. 72
5.1 Grids used for CFD simulations. 75
5.2 Steady state aerodynamic loads of baseline and microflap airfoils at $M_\infty = 0.1$ 76
5.3 Steady state aerodynamic loads of baseline and microflap airfoils at $M_\infty = 0.6$ 77
5.4 Comparison of unsteady lift and moment generated by the 6%c and 10%c microflaps at M=0..6, $\alpha = 0°$, and reduced frequency of microflap oscillation $k = 0.02$. 78
5.5 Microflap placement on airfoil section. 80
5.6 Spanwise configurations of the plain flap on the rotor blade. 81
5.7 Spanwise configurations of the microflap on the rotor blade. 81
5.8 Skid microphone location and carpet plane used for noise simulation. 83
5.9 Baseline rotor hub loads for various torsional frequencies. 84
5.10 Load reduction for single flap/microflap configurations. 85
5.11 Load reduction of dual flap/microflap Configurations. 86
5.12 Single flap deflection history. 86
5.13 Percentage reduction in the vibration cost function using a single flap and a single microflap. 87
5.14 Percentage reduction in the vibration cost function using a dual flap and a dual microflap. 88
5.15 Load reduction for single microflap at 10%c. 89
5.16 Percentage reduction in the vibration cost function using a single microflap at different chordwise positions. 90
5.17 Carpet plots for dual microflap noise reduction at various blade torsional frequencies. 91

5.18 Maximum BVI reduction for single flap/microflap configurations. . 92
5.19 Maximum BVI reduction for dual flap/microflap configurations. . 93
5.20 Average BVI reduction for single flap/microflap configurations. . . 94
5.21 Average BVI reduction for dual flap/microflap configurations. . . . 94
5.22 HART test setup. 96
5.23 Baseline HART blade loading using AVINOR/HELNOIR compared against experimental results [107] at x=0.87R 98
5.24 Validation of the acoustic computations against the HART experimental data. 99
5.25 Validation of AVINOIR/HELNOIR by comparing acoustic pressure histories at two locations, one on the advancing side and the other on the retreating side. 100
5.26 In-plane microphone layout for the Boeing-SMART rotor wind tunnel test. (Data from Ref. 105) 103
5.27 Validation of the acoustic computations against the Boeing SMART experimental data. (Experimental data from Ref. 105) 104
5.28 Predicted acoustic pressure components at Microphone M15. 105
5.29 Comparison of the baseline noise levels on the carpet plane using different aeroelastic-aeroacoustic code combination 107
5.30 Comparison of the noise levels computed on the carpet plane using HELINOIR during active noise control employing a single microflap (b) and a single plain flap (c), at $\mu = 0.15$, $C_T = 0.005$ and $\alpha_D = 6.5°$. 108
5.31 Comparison of the vibration levels computed using the AVINOR/HELINOIR during active noise control using a single microflap and a single plain flap for a heavy BVI descending flight condition. 109
5.32 Flap deflection histories over a rotor revolution during active noise reduction. 110

5.33 Comparison of the vibration levels computed during active vibration control using a single microflap and a single plain flap at $\mu = 0.15$, $C_T = 0.005$ and $\alpha_D = 6.5°$. 111
5.34 Comparison of the noise levels computed on the carpet plane using HELINOIR during active vibration control using a single microflap (b) and a single plain flap (c) at $\mu = 0.15$, $C_T = 0.005$ and $\alpha_D = 6.5°$. 111
5.35 Comparison of the noise levels from a straight blade computed on the carpet plane employing a global Galerkin model (a) and Galerkin type FEM (b) and (c) at $\mu = 0.15, C_T = 0.005$ and $\alpha_D = 6.5°$ 112
5.36 Comparison of the vibration levels from a baseline blade employing a global Galerkin model and Galerkin type FEM at $\mu = 0.15, C_T = 0.005$ and $\alpha_D = 6.5°$ 113
5.37 In plane observer surface located at 10R in front of the helicopter. Azimuthal variation is shown in (b) and elevational variation is shown in (c). 114
5.38 Baseline and the reduced in-plane noise levels obtained using a single plain flap and a single feedback microphone located on the observer surface at 10R. 116
5.39 Acoustic pressure histories at observer location, $(\frac{x}{R}, \frac{y}{R}, \frac{z}{R}) = (-9.70, -0.27, -2.41)$, before and after active control. 118
5.40 Reduction in the in-plane noise levels obtained at 10R using various far-field feedback configurations. 119
5.41 Vibration penalty during closed-loop in-plane noise reduction using various feedback microphone configurations for single plain flap. 120
5.42 Flap deflection history for active in-plane noise reduction using a single feedback location. 121
5.43 Near-field onboard microphone feedback location on left boom and tip of the right skid. 122

5.44 Reduction in LFSPL at 10R using skid feedback. 123
5.45 Reduction in LFSPL at 10R using various boom feedback locations. 124
5.46 Sound Pressure Levels before and after active control. 125
5.47 Insertion Loss due to active control. 125
5.48 Vibration penalty during in-plane noise reduction using a single plain flap with a left boom feedback. 126
5.49 Flap deflection history for active in-plane noise reduction with a left boom feedback. 126
5.50 Adaptive controller performance during in-plane noise reduction with feedback at left boom position at level cruise, $\mu = 0.3$. 127
5.51 Baseline and the reduced in-plane noise levels obtained using a single plain flap and near-field feedback microphone at the left boom for level cruise, $\mu = 0.2$. 128
5.52 Baseline and the reduced in-plane noise levels obtained using a single plain flap and near-field feedback microphone at the left boom for level cruise, $\mu = 0.3$. 129
5.53 Baseline and the reduced in-plane noise levels obtained using a single plain flap and near-field feedback microphone at the left boom for level cruise, $\mu = 0.2$. 130
5.54 Comparison of the noise levels computed on the 10R observer surface using a dual plain flap configuration with different feedback locations. 131
5.55 Vibration penalty for the dual plain flap configuration with near and far-field feedback locations. 132
5.56 Flap deflection history for dual flap configuration during active in-plane noise reduction using near-field Left Boom feedback. . . . 133
5.57 Rotor blade with passive control. 133
5.58 In-plane LFSPL noise levels obtained using a baseline blade and blade with tip sweep, $\Lambda_s = 6°$, on the observer surface at 10R, $\mu = 0.3$. 135

5.59 Change in the LFSPL obtained at 10R for different tip geometries at $\mu = 0.3$. 135
5.60 Acoustic pressure histories at observer location $(\frac{x}{R}, \frac{y}{R}, \frac{z}{R}) = (-9.70, -0.27, -2.41)$ with baseline blade (a), swept tip (b), dihedral tip (c) and anhedral tip (d). 137
5.61 Insertion loss due to passive control. 138
5.62 Vibration levels for different tip geometries at $\mu = 0.3$ 139
5.63 Loading noise source density of baseline blade and blade with tip sweep, $\Lambda_s = 6°$. 142
5.64 Change in loading noise source density due to implementation of passive /active control. 142
A.1 Transformation from the "0" system to the "1" system 154
A.2 The transformation from the "2" system to the "4" system 155
A.3 The transformation from the "3" system to the "5" system 156
B.1 Undeformed element coordinate system. 183
B.2 Undeformed curvilinear coordinate system. 183
B.3 Finite element nodal degrees of freedom 200
C.1 A schematic description of the new CFD based RFA model 206
C.2 Normal velocity distribution corresponding to generalized airfoil and flap motions 209
C.3 Vortex-lattice approximation for rotor wake model 218
C.4 Single peak circulation distribution model and the resulting far wake approximation 219
C.5 CAMRAD/JA dual peak model and the resulting far wake approximation 219
C.6 Improved dual peak model, leading to dual concentrated vortex lines 222
C.7 Reverse flow region 223
C.8 Orientation of tangential and perpendicular air velocities and aerodynamic loads. 225

D.1 A schematic of the helicopter in descending flight 238

LIST OF TABLES

Table

5.1 Baseline rotor parameters. 79

5.2 First two torsional frequencies (/rev) and the corresponding nondimensional torsional stiffness. 82

5.3 Baseline HART rotor parameters [59]. 97

5.4 Baseline SMART rotor parameters. 102

5.5 Far-field feedback microphone locations. 116

5.6 Near-field feedback microphone locations. 122

LIST OF APPENDICES

Appendix

A. Global Galerkin Model 151

B. Galerkin Type Finite Element Model 179

C. Aerodynamic Model 204

D. Solution Procedure 230

LIST OF SYMBOLS

a_0	Speed of sound
a_l, a_m, a_d, a_{l0}, a_{l2}, a_{m0}, a_{m2}, a_{d0}, a_{d2}	Coefficients used in the ONERA dynamic stall model
A	Blade cross sectional area
A_{cs}	Control surface cross sectional area
b	Blade semi-chord
c_b	Blade chord
c_{cs}	Control surface chord
c_p	Sectional pressure coefficient
$\mathbf{c}$	Vector containing RFA coefficients
C_{df}	Parasitic drag coefficient of the fuselage
C_l, C_m, C_{hm}	Sectional lift, moment and hinge moment coefficients
C_Q	Torque coefficient
C_T	Thrust coefficient
C_W	Helicopter weight coefficient
$\mathbf{C_0}, \mathbf{C_1}, \mathbf{C}_n, \mathbf{D}, \mathbf{E}, \mathbf{R}$	Coefficient matrices from the RFA aerodynamic model
$\mathbf{C}_{Oj}$, $\mathbf{C}_{Ij}$, $\mathbf{C}_{NWij}$	Influence coefficients used in the free wake calculation
$\Delta C_L, \Delta C_M, \Delta C_D$	Contributions to the sectional lift, moment, and drag from the dynamic stall model
D	Drag force
D_0, D_1	Generalized normal velocity distributions corresponding to flap deflection
D_f	Parasitic drag of the fuselage
$\mathbf{D}(\psi, \phi)$	Wake distortion
e	Blade root offset from center of rotation
$\hat{e}_{xi}, \hat{e}_{yi}, \hat{e}_{zi}$	Unit vectors associated with the i^{th} coordinate system

E_l, E_m, E_d, E_{l0}, E_{l2}, E_{m0}, E_{m2}, E_{d0}, E_{d2}	Coefficients used in the ONERA dynamic stall model
$EI_{\eta\eta}$, $EI_{\zeta\zeta}$	Principal bending stiffness of the blade cross-section
f	Function that describes the moving surface generating sound
$\mathbf{f}$	Generalized load vector
$\mathbf{f_b}(.)$	Blade motion equations
$\mathbf{f_t}(.)$	Trim equations
F_T	Vertical force
$F_{HX4}, F_{HY4}, F_{HZ4}$	4/rev components of hub shear
$\mathbf{F_H}$	Instantaneous hub shear
$\mathbf{F_{Rk}}$	Resultant blade root forces for the k^{th} blade
g	Acceleration due to gravity
$g_{S_L}, g_{S_F}, g_{S_T}$	Distributed structural damping factors in lag, flap and torsion
$\mathbf{g_a}(.)$	Aerodynamic (RFA) state equations
$\mathbf{g_{aR}}(.)$	Reduced form of the aerodynamic (RFA) state equations
GJ_b	Torsional stiffness of the blade cross-section
GJ_c	Torsional stiffness of the control surface
$\mathbf{G}$	Laplace transform of $\mathbf{f}$
h	Plunge displacement at 1/4-chord
$\mathbf{h}$	Generalized motion vector
H	Horizontal force
$H(f)$	Heaviside function, $H(f) = 0$ for $f < 0$ and $H(f) = 1$ for $f > 0$
H_m	Sectional hinge moment
$\mathbf{H}$	Laplace transform of the generalized motion vector
$\imath$	$= \sqrt{-1}$
I_{MB2}, I_{MB3}	Principal mass moments of inertia of the blade cross-section
I_{MC2}, I_{MC3}	Principal mass moments of inertia of the control surface cross-section
$\mathbf{I}$	Identity matrix
$J(\mathbf{z}_k, \mathbf{u}_k)$	Quadratic-form objective function
k	Reduced frequency = $\omega b/U$
K_{NW}	Number of azimuthal steps for near wake retained

l_i	Components of local force intensity that acts on the fluid, $l_i = P_{ij} n_j$
l_r	Local force intensity on fluid in radiation direction $l_r = l_i r_i$
$\mathbf{l}$	Left rectangular matrix used in RFA coefficient evalution
L_b	Blade length
L_{cs}	Control surface length
m_{cs}	Mass of control surface per unit length
M	Local mach number
M_{AT}	Advancing tip Mach number, $M_{AT} = (U + \Omega R)/a_0$
M_b	Mass of one blade
M_c	Mass of one control surface
M_r	Mach number in the radiation direction
M^{pt}	Rotor pitching moment about the hub center
M^{rl}	Rotor rolling moment about the hub center
M^{yw}	Rotor yawing moment about the hub center
$M_{HX4}, M_{HY4}, M_{HZ4}$	4/rev components of hub moment
$\mathbf{M_H}$	Instantaneous hub moment
$\mathbf{M_{Rk}}$	Resultant blade root moments for the k^{th} blade
n_d	Number of reduced frequency data points at which aerodynamic load responses are generated
n_L	Number of aerodynamic lag terms in the RFA approach
N_b	Number of rotor blades
N_δ	Number of control surfaces on the blade
$N_{H06}, \ldots, N_{H17}$	Noise levels of the 6^{th} - 17^{th} harmonics of blade passage frequency
p	Air pressure
p'	Acoustic pressure
$\bar{p}$	Nondimensional air pressure
$\mathbf{p_A}$	Distributed aerodynamic load per unit length of the blade
$\mathbf{p_D}$	Distributed structural damping load per unit length of the blade
$\mathbf{p_{Gb}}$	Distributed gravitational load per unit length of the blade
$\mathbf{p_{Ib}}$	Distributed inertial load per unit length of the blade

$q_{wi}, q_{vi}, q_{\phi i}$	Coefficients of the flap/lead-lag/torsional mode shapes
q_∞	Dynamic Pressure
$\mathbf{q}$	Induced velocity
$\mathbf{q_b}$	Vector of blade degrees of freedom
$\mathbf{q_t}$	Vector of trim variables
$\mathbf{q_A}$	Distributed aerodynamic moment per unit length of the blade
$\mathbf{q_D}$	Distributed structural damping moment per unit length of the blade
$\mathbf{q_{Gb}}$	Distributed gravitational moment per unit length of the blade
$\mathbf{q_{Ib}}$	Distributed inertial moment per unit length of the blade
Q_t	Tail rotor torque
$\mathbf{Q}$	Aerodynamic transfer matrix
$\tilde{\mathbf{Q}}$	RFA approximation of the aerodynamic transfer matrix
$\mathbf{Q_z}$	Weighting matrix for plant output
r_l, r_m, r_d, , r_{l0}, r_{l2}, r_{m0}, r_{m2}, r_{d0}, r_{d2}	Coefficients used in the ONERA dynamic stall model
r	Distance between observer and source $\lvert\mathbf{x}-\mathbf{y}\rvert$
r_i	Components of vector $\hat{r}$
$\hat{r}$	Unit vector in radiation direction $(\mathbf{x}-\mathbf{y})/r$
$\mathbf{r}$	Right column vector used in RFA coefficient evalution
$\mathbf{r_b}$	Position of the blade when it generates the wake element
$\mathbf{r_p}$	Position vector of a point on the deformed blade
$\mathbf{r_w}$	Position of a wake element
$\mathbf{r_{EA}}$	Position vector for a point on the elastic axis
R	Blade radius
R_{LM}, R_D	Reverse flow factors for lift(moment) and drag, respectively
$\mathbf{R}$	Weighting matrix for control input
$\mathbf{R}_0$	Position vector of deformed elastic axis
$\mathbf{R_p}$	Position vector of a point on the blade before deformation
$\mathbf{R_t}$	Vector of trim residuals
$\bar{s}$	Nondimensional Laplace variable $\bar{s}=\frac{sb}{U}$

$\mathbf{S}$	Cross-weighting term in objective function J
t	Time
$\bar{t}$	Nondimensional time, reduced time
t_k	Time of controller update
T	Axial tension
T_t	Tail rotor thrust
T_{ij}	Lighthill stress tensor $T_{ij} = \rho v_i v_j + P_{ij} - a_\infty \rho' \delta_{ij}$
$\mathbf{T}$	Sensitivity matrix relating control input to plant output
$\hat{\mathbf{T}}$	Estimate of the sensitivity matrix $\mathbf{T}$
$\hat{\mathbf{T}}_{LS}$	Least-squares estimate of the sensitivity matrix $\mathbf{T}$
u, v, w	Displacements of a point on the blade's elastic axis due to blade deformation
u_n	Normal velocity of the fluid
U	Air velocity relative to the blade section
U_P,U_T	Perpendicular and tangential components of freestream velocity experienced by the blade
$\mathbf{u}(\mathbf{x}, t)$	Disturbance in flow velocity
$\mathbf{u}_k$	Control input at time t_k
$\mathbf{u}_{k,\text{opt}}$	Optimal control input
$\Delta\mathbf{u}_k$	$= \mathbf{u}_k - \mathbf{u}_{k-1}$
$\Delta\mathbf{U}_k$	Matrix composed of $\Delta\mathbf{u}_k$
v_n	Normal velocity of noise generating surface
v_i, v_j	Components of fluid velocity in directions x_i and x_j
$\mathbf{v}$	Velocity vector
$\mathbf{V_A}$	Total air velocity vector
$\mathbf{V_{A1}}$	Airflow velocity due to forward flight, blade rotation and induced inflow
$\mathbf{V_{A2}}$	Airflow velocity due to blade dynamics
$\mathbf{V_{EA}}$	Velocity of a point on the elastic axis of the blade due to blade dynamics
$\bar{w}$	Normal velocity
$\mathbf{w}$	Disturbance to plant
W	Helicopter weight
$W(x, t)$	Normal velocity distribution
W_0, W_1	Generalized normal velocity distributions on the airfoil
$\mathbf{W}$	Matrix relating plant response to disturbance
x	Streamwise coordinate

x_{cs}	Distance from the hub to the center of the control surface
x_{rev}	Reverse flow boundary
$\vec{x}$	Observer position vector, with components x_i
$\mathbf{x}$	Aerodynamic state vector
X_t	Horizontal offset of tail rotor center from hub
X_A	Offset between the aerodynamic center and the elastic axis
X_H	Offset between the hinge point and the elastic axis
X_{Ib}	Offset of the blade cross-sectional center of mass from the elastic axis
X_{Ic}	Offset of the control surface cross-sectional center of mass from the hinge point
X_{IIb}	Offset of the blade cross-sectional center of area from the elastic axis
X_{IIc}	Offset of the control surface cross-sectional center of area from the hinge point
X_{FA}	Longitudinal offset between rotor hub and helicopter aerodynamic center
X_{FC}	Longitudinal offset between rotor hub and helicopter center of gravity
$\mathbf{X}$	Laplace transform of the aerodynamic state vector
$\bar{y}_{ob}, \bar{z}_{ob}$	Coordinates of a point on a blade cross-section relative to the elastic axis, measured in the "5" System.
$\vec{y}$	Source position vector, with components y_i
Y	Lateral force
$\mathbf{z}_0$	Initial output condition of plant output
$\mathbf{z}_k$	Plant output at time t_k
$\mathbf{z}_{\text{NR}}$	Output vector for noise reduction
$\mathbf{z}_{\text{PWR}}$	Output vector for power reduction
$\mathbf{z}_{\text{VR}}$	Output vector for vibration reduction
Z_t	Vertical offset of tail rotor center from hub
Z_{FA}	Vertical offset between rotor hub and helicopter aerodynamic center
Z_{FC}	Vertical offset of fuselage center of gravity from hub
$\Delta\mathbf{z}_k$	$= \mathbf{z}_k - \mathbf{z}_{k-1}$
$\Delta\mathbf{Z}_k$	Matrix composed of $\Delta\mathbf{z}_k$
α	Angle of attack of the airfoil

α_{cr}	Critical angle of attack of the airfoil used for the separation criterion in the ONERA model
α_{re}	Relaxation factor
α_{tpp}	Tip-path plane angle
α_A	Blade local angle of attack
α_D	Descent angle
α_R	Rotor shaft angle of attack
β	Prandtl-Glauert compressibility correction, $\sqrt{1-M^2}$
β_p	Blade precone angle
δ	Dirac delta function
δ_f	Flap deflection
δ_{ij}	Kronecker delta
δ_{limit}	Saturation limit on flap deflection
$\delta_{\max}$	Maximum flap deflection
δ_{Nc}, δ_{Ns}	N/rev cosine and sine amplitude of the flap deflection
ϵ	Small dimensionless magnitude of the order of the blade slopes
$\lambda_x, \lambda_y, \lambda_z$	Main rotor inflow ratio components
λ_t	Tail rotor uniform inflow ratio
Π_l, Π_m, Π_d	States of the ONERA dynamic stall model
ϕ	Elastic twist about the elastic axis
ϕ_w	Wake age
ϕ_R	Lateral roll angle
ν	Airfoil or microflap oscillation frequency
ρ	Air density
ρ_b	Density of blade structure
ρ_c	Density of control surface structure
ρ_I	Radial position of interior circulation peak
γ	Lock number
γ_b	Intersection angle between vortex and blade
γ_n	Poles for RFA
γ_s	Strength of shed vorticity
γ_t	Strength of trailed vorticity
$\Gamma(r)$	Circulation distribution
Γ_I, Γ_O	Inboard and outboard circulation peaks, in dual wake model
η_b, ζ_b	Principal coordinates of a point in the blade cross-section

η_c, ζ_c	Coordinates in the flap attached coordinate system
$\vec{\eta}$	Coordinates in the blade fixed frame.
μ	Advance ratio $= V_\infty \cos\alpha/\Omega R$
θ_0, θ_{1s},θ_{1c}	Collective and cyclic pitch components
θ_{0t}	Tail rotor collective pitch
θ_{pc}	Pilot pitch input $\theta_0 + \theta_{1c}\cos\psi + \theta_{1s}\sin\psi$
θ_{tw}	Blade pretwist angle
θ_G	Geometric pitch angle, $\theta_{pc} + \theta_{tw}$
ψ	Azimuth angle
σ	Rotor solidity
σ_t	Tail rotor solidity
τ	Source time
ω	Airfoil or microflap angular frequency of oscillation
ω_{Fi}	ith flapping frequency of the rotating blade
ω_{Li}	ith lead-lag frequency of the rotating blade
ω_{Ti}	ith torsional frequency of the rotating blade
Ω	Rotor angular velocity
ξ	Nondimensional quantity $\xi = x/b$

ABSTRACT

ROTORCRAFT IN-PLANE NOISE REDUCTION USING ACTIVE/PASSIVE APPROACHES WITH INDUCED VIBRATION TRACKING

by

Miang Hwee Chia

Chair: Professor Peretz P. Friedmann

A comprehensive study of the use of active and passive approaches for in-plane noise reduction, including the vibrations induced during noise reduction, was conducted on a hingeless rotor configuration resembling the MBB BO-105 rotor. First, a parametric study was performed to examine the effects of rotor blade stiffness on the vibration and noise reduction performance of a 20%c plain trailing edge flap and a 1.5%c sliding microflap. This was accomplished using a comprehensive code AVINOR (for Active VIbration and NOise Reduction). A two-dimensional unsteady reduced order aerodynamic model (ROM), using the Rational Function Approximation approach and CFD-based oscillatory aerodynamic load data, was used in the comprehensive code. The study identified a hingeless blade configuration with torsional frequency of 3.17/rev as an optimum configuration for studying vibration and noise reduction using on-blade control devices such as flaps or

microflaps.

Subsequently, a new suite of computational tools capable of predicting in-plane low frequency sound pressure level (LFSPL) rotorcraft noise and its control was developed, replacing the acoustic module WOPWOP in AVINOR with a new acoustic module HELINOIR (for HELIcopter NOIse Reduction), which overcomes certain limitations associated with WOPWOP. The new suite, consisting of the AVINOR/HELINOIR combination, was used to study active flaps, as well as microflaps operating in closed-loop mode for in-plane noise reduction. An alternative passive in-plane noise reduction approach using modification to the blade tip in the 10%R outboard region was also studied. The new suite consisting of the AVINOR/HELINOIR combination based on a compact aeroacoustic model was validated by comparing with wind tunnel test results, and subsequently verified by comparing with computational results.

For active control, the in-plane noise reduction obtained with a single 20%c plain trailing edge flap during level flight at a moderate advance ratio was examined. Different configurations of far-field and near-field feedback microphone locations were examined to develop a fundamental understanding of the feedback microphone locations on the noise reduction process A near-field microphone located on the tip of a nose boom was found to produce a LFSPL reduction of up to 6dB. However, this noise reduction was accompanied by an out-of-plane noise increase of 18dB and 60% increase in vertical hub shear. For passive control, three tip geometries having sweep, dihedral, and anhedral, were considered. The tip dihedral reduced LFSPL by up to 2dB without a vibratory load penalty. However,

this was accompanied by an increase in the mid frequency sound pressure levels (MFSPL). The tip sweep and tip anhedral produced an increase in in-plane LFSPL below the horizon. A comparison of the active and passive approaches indicated that active approaches implemented by a plain flap with a feedback microphone located on the nose boom is superior to the passive control approaches. However, there is a general trade-off between LFSPL reduction, MFSPL generation and vibratory hub loads induced by noise control.

CHAPTER I

INTRODUCTION, LITERATURE REVIEW, AND OBJECTIVES

The helicopter is a versatile flight vehicle designed for a diverse range of flying conditions and missions, from hover to heavy lift, and at different weight configurations. These demands require the helicopter to operate in a complex aerodynamic environment as shown in Fig. 1.1. In forward flight, rotor blades are subjected to asymmetric and unsteady flow with the advancing blade experiencing a higher dynamic pressure than the retreating blade. The uneven distribution of Mach number over the azimuth and span of the rotor results in a host of flow regimes. These flow regimes include transonic flow, typically on the advancing blade, reverse flow, and dynamic stall, typically on the retreating blade. The shed wake and trailed vortices remain close to the blade, to produce a strongly three dimensional induced velocity field. These time varying airloads, originating from the different flow regimes and wake induced inflow, interacting with the long, flexible blades, are a major source of vibration and noise.

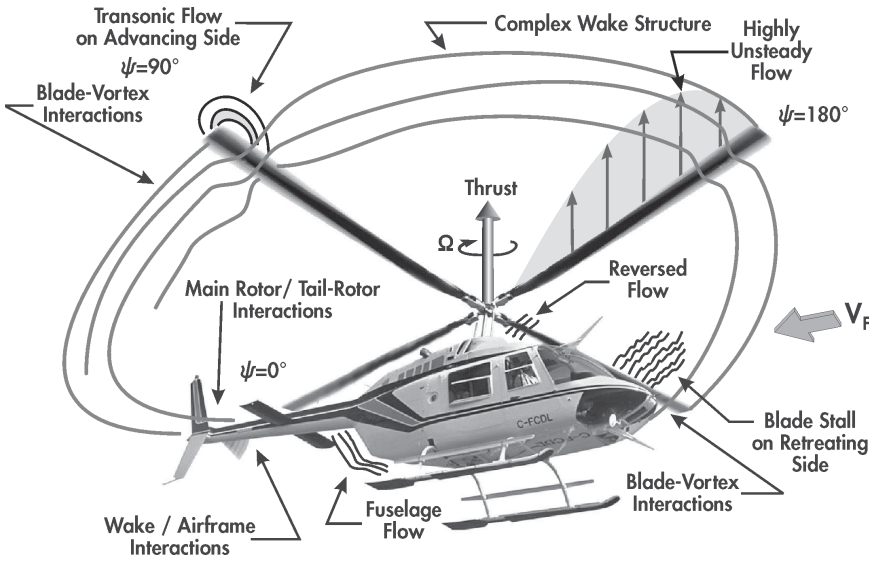

Fig. 1.1. Various elements of the complex aerodynamic environment of a helicopter [79].

Vibratory loads transmitted to the fuselage from the rotor shaft contribute to the crew and passenger discomfort. This vibration also reduces the operating life of the airframe and components, adding to operational and maintenance costs. Noise has undesirable impact on both crew comfort and flight operations. At low speed descending flight corresponding to approach condition, a characteristic ”slapping" noise is heard on the ground, limiting community acceptance and helicopter usage in urban areas. This “slapping" noise is attributed to the blade vortex interaction (BVI) phenomenon, which occurs when the rotating blades encounter strong, concentrated tip vortices shed by the preceding blade, creating large high frequency oscillations in the aerodynamic pressure on the blades. At level cruise, low frequency in-plane noise, typically less than 200 Hz, is transmitted over long distances without significant attenuation, increasing the aural detection range and compromising the element of surprise in military operations.

The wide range of mission objectives and the complex aerodynamic environment where rotorcrafts are expected to operate in, imply that rotor design has to account for multiple design points.

1.1 Review of Approaches to Helicopter Noise and Vibration Reduction

Vibration and noise in helicopters are coupled phenomena, which have been a source of concern in helicopters design for a long time [62]. Two broad approaches, namely active and passive, have evolved to control noise and/or vibration. Active approaches involve the use of a sensor, a control law and an actuator to reduce the unwanted phenomena. On the other hand, passive approaches use dampers or structural design to reduce the unwanted phenomena. No power is required for passive approaches. The passive approach to vibration and noise reduction that has been in use for the last five decades has gained wide acceptance. In the last three decades, active approaches have emerged as effective for controlling both noise and vibration over a range of flight conditions. However, they have not been implemented on a production helicopter yet [34].

1.1.1 Active Control Approaches

Active control approaches influence vibrations at its source by modifying the aerodynamic environment around the rotor, or by canceling vibrations in the fuselage. A key advantage of active control approaches is that they can be used effec-

tively over a range of flight conditions.

A wide variety of active control approaches have evolved for controlling helicopter noise and vibration. These can be divided into two broad categories. The first category involves noise and vibration reduction at the rotor source before they propagate to the fuselage or external environment. The second category involves controlling them in the fuselage or the cabin and is known as active control of structural response (ACSR). In the first category of active control, where the primary objective is to reduce noise and vibration at the source, two approaches have evolved namely Higher Harmonic Control (HHC) and Individual Blade Control (IBC). In the HHC approach, actuation is introduced in the non-rotating swashplate by superimposing appropriate time dependent pitch commands. In the IBC approach, the rotor blades are controlled independently in the rotating frame. The IBC approach can be subdivided into pitch link actuation and On Blade Control (OBC). On-Blade Control is a form of IBC, where the control surfaces are located on the rotating blade and each blade has its own controller. The hierarchy of active control approaches described above is shown in Fig. 1.2. A comprehensive review of these active approaches can be found in Ref. 34.

The OBC approach has several advantages over the other active control approaches like HHC or pitch link IBC. The OBC requires significantly less actuation power owing to its small size and placement in the blade outboard region, which facilitates effective control authority. It is a relatively fail safe design as an OBC can malfunction without affecting the primary flight control system, and therefore does not have an adverse impact on airworthiness. Another advantage of OBC

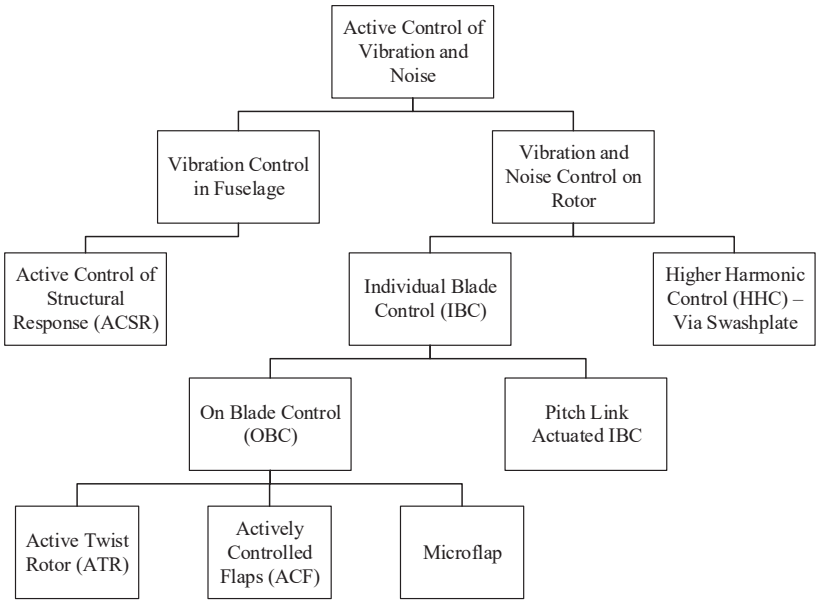

Fig. 1.2. Hierarchy of active control approaches (Adapted from Ref. 34).

is that there is flexibility in the bandwidth of the activation schedule, configuration and placement of the device on the rotor, thus expanding the design space and potential application over a wider flight conditions. Implementations of OBC include the Active Twist Rotor (ATR) [117], Actively Controlled Flaps (ACF), and microflaps. The focus of this dissertation will be on the ACF and microflaps. A more detailed discussion of these OBC devices is provided in Section 1.2.

The active flaps and microflaps induce a time dependent elastic twist on the blade that results in a redistribution of the unsteady aerodynamic loading on the rotor. This changes the tip vortex strength and the induced velocity field interacting with the rotor. The aerodynamic loading is also a noise source that can cancel out other out-of-phase noise sources. Furthermore, the active blade control inputs can modify blade flapping and torsional deflections, which increase the

blade-vortex miss distances during interactions. Therefore, rotor noise and vibration can be reduced by the combined effect of blade airloads and blade deflection with proper control inputs.

Millot and Friedmann [70] performed the first comprehensive computational study to demonstrate the effectiveness of ACF, implemented through servo-flaps, for vibration reduction. A coupled flap-lag-torsional isotropic blade model, including geometric nonlinearities due to moderate deflections was used. A modified quasi-steady Theodorsen aerodynamic model was used to determine the air loads for the blade/ servo flap combination. This parametric study showed that a 12% span, $25\%c$ servo flap placed at the 75% span location on a torsionally soft blade was capable of vibration reduction of between $80 - 90\%$ at an advance ratio of $\mu = 0.3$. This pioneering result has since served as a benchmark and catalyst for future active control studies.

Subsequently, Milgram and Chopra performed a parametric study on a plain trailing edge flap [69] for vibration reduction. The analytical model used was based on the UMARC comprehensive analysis code developed by the University of Maryland. Finite elements were used to model the structural dynamic properties of the rotor blade. An unsteady, compressible flow aerodynamic model developed by Leishmann and Hariharan combined with a free wake model was used to model the airloads. Significant reduction in 4/rev hub loads was achieved. They also showed that the plain flap used for vibration reduction performance was relatively insensitive to flap length, spanwise location, and flap chord ratio as the controller was able to compensate for the changes by varying the control deflec-

tions. However, the effects of actuator saturation were not considered.

To improve the aerodynamic model used in Ref. 70, Myrtle and Friedmann [73] replaced the quasisteady aerodynamic model with a two-dimensional, compressible, time-domain, unsteady aerodynamic model based on the rational function (RFA) approach. They also showed for the first time the superiority of a dual ACF configuration over a single ACF configuration [74] for vibration reduction. To capture the influence of the shed wake and tip vortices on the induced velocity in BVI, de Terlizzi and Friedmann [22] introduced a free-wake model into the aerodynamic model. The wake model improved the vibration prediction for low speed descending flight under heavy BVI conditions. To improve the vibration predictions at high speeds, a dynamic stall model based on the ONERA dynamic stall model [89] was incorporated into the analysis by Depailler and Friedmann [25] and demonstrated the efficacy of ACF for vibration reduction at advance ratio as high as $\mu = 0.55$. The capability of this aerolastic analysis model was further augmented with the introduction of a modified version of the acoustic prediction tool, WOPWOP [12]. This unified aeroelastic/aeroacoustic analysis program was validated against experimental and acoustic data and used to study vibration reduction and accompanying out-of-plane BVI noise penalty during a low speed descending flight condition [86]. In a subsequent study, the code was used to investigate the effectiveness of ACF for simultaneous BVI noise and vibration reduction [87].

More recently, Liu, Padthe, and Friedmann developed a CFD-based Reduced Order Model (ROM) in order to study the microflap as an alternative to the ACF

[61]. They demonstrated the effectiveness and control authority of the microflap for simultaneous BVI noise and vibration reduction in rotorcraft [80]. A key finding is that the microflap was more effective than the ACF for BVI noise reduction but is less effective for vibration reduction. In the same study, the effects of actuator saturation were also considered. The methodology described earlier has been implemented at the University of Michigan in a comprehensive code for Active VIbration and NOise Reduction, denoted as AVINOR [41]. A modified version of AVINOR was used in the rotorcraft vibration and noise control studies conducted in this dissertation.

The active control approaches have also been experimentally demonstrated in both wind tunnel and flight tests. One the most significant demonstration of the HHC approach was performed during the Higher-harmonic-control Aeroacoustic Rotor Test (HART) at the open-jet anechoic test section of the German-Dutch Wind Tunnel (DNW). It consisted of two wind tunnel tests, known as HART I [107, 108] conducted in 1994 and HART II [58, 100, 112, 124] in 2001. The overarching objective of the HART tests was to improve the physical understanding and mathematical modelling of the effects of the higher harmonic blade pitch control technique on BVI noise and vibration reduction. The HART rotor is a 40% dynamically and Mach scaled model of a four-bladed hingeless MBB BO-105 main rotor. In HART I, a BVI noise reduction of 6dB was obtained using a minimum noise (MN) setting and 30% vibration reduction was achieved using minimum vibration (MV) setting. Both MN and MV settings were conducted using open loop 3/rev open-loop control, but with different phase and amplitudes. Another key observation made was

that there is a trade off between noise reduction and vibration reduction, except in a small subset of HHC settings where both noise and vibrations were noticeably reduced. It was also determined that the primary mechanism by which HHC increases or decreases the BVI noise is through the modification of the rotor wake and blade tip vortices. The blade tip deformations, aerodyanmic loads and acoustic signature data from HART I were used by Patt, Liu, and Friedmann to validate the AVINOR code [87]. In HART II, more extensive instrumentation was used to further improve the physical understanding governing BVI noise generation and reduction.

The NASA/Army/MIT ATR was successfully tested in the NASA Langley Transonic Dynamics Tunnel in open loop [117] and subsequently in closed-loop modes [103], primarily for vibration reduction. The ATR is a four-bladed, articulated rotor with active blades, consisting of embedded piezoelectric active fiber composite (AFC) actuators that allow direct control of blade twist. Using a 1/rev collective twist actuation and a combination of longitudinal and lateral cyclic actuation at 4/rev, significant reductions in the 1/rev and 4/rev vibrations of up to 90% was achieved. A 5/rev input was found to be most effective for BVI noise reduction. A noise reduction of up to 2.8dB was achieved, however there was an adverse impact on both the low frequency noise and vibration levels. It was also acknowledged that ATR was not as effective for BVI noise reduction when compared to other active control approaches available at that time, e.g. HHC, and was more suitable for vibration reduction [7, 8].

The pitch link IBC system was tested at the NASA Ames 40×80 wind tunnel

on a full scale four-bladed BO-105 rotor [44]. The test showed that with a specific combination of 2/rev and 5/rev control inputs, it was capable of simultaneous reduction of BVI noise, as well as vibratory hub shear in the open loop mode. More significant were the subsequent flight tests conducted on the IBC equipped BO-105 test bed [5], also known as BO105 S1 helicopter. During the open loop phase of the flight tests, it was found that there was a good correlation between noise reduction measured by onboard microphone located on the skid and that measured on the ground. This paved the way for the subsequent closed loop flight test when signficant BVI noise reduction on ground up to 5dB were demonstrated. The flight test demonstrated closed loop BVI noise reduction for the first time. The BVI noise reduction achieved is attributed to the IBC controlling the miss distance between the blade tip vortices and rotor blade through variation of local lift distribution over the rotor disk [26].

The smart material actuated rotor technology (SMART) active flap rotor demonstration conducted in 2008 was the most successful wind tunnel test of the ACF [109]. The SMART rotor is a full scale, five-bladed bearingless MD900 rotor modified with a piezoelectric actuated trailing edge flap. The results showed reductions of up to 6dB in BVI noise and in-plane noise, though not simultaneously, and reductions in vibratory hub loads of up to 80%. In these tests, the noise reduction was achieved by open-loop control inputs with $\pm 3^{\circ}$ flap deflection limits. The SMART rotor wind tunnel test conclusively demonstrated the effectiveness of the active flap for both control of noise and vibration. The impact of the active flap on control power and reliability of the flap actuation system was also demonstrated.

The Sikorsky active flap demonstration rotor wind tunnel test was another successful demonstration of the ACF. Closed loop vibration reduction test corresponding to cruise at 120 knots resulted in a 95% reduction in the 4/rev vertical acceleration [119]. BVI noise reduction at a forward flight speed of 80 knots was also reported [64]. The SMART rotor and Sikorsky active flap wind tunnel tests will be discussed further in Section 1.3.1, since these wind tunnel tests addressed both in-plane noise in addition to BVI noise.

The ACF technology moved beyond the wind tunnel test development stage when it was flight tested by Eurocopter on a BK-117 incorporating the 'Adaptive Dynamicsche Systeme' (ADASYS) hingeless rotor system. The four-bladed ADASYS system was equipped with three piezoelectrically actuated active flaps [26]. A significant reduction in the 4/rev vibratory loads of up to 90% was demonstrated using open loop control [51]. Most recently in 2009, Eurocopter demonstrated a new active flap demonstrator based on the EC145 airframe, known as the Blue Pulse active control system [91]. The Blue Pulse improves upon the ADASYS system with new hardware, and achieved both blade tracking and stability enhancement. The vibration reduction capability was also significantly enhanced and BVI noise reduction was considered, but not emphasized.

From the many successful wind tunnel and flight tests, particularly with the improved technology development for the ADASYS to Blue Pulse rotor by Eurocopter in the last decade, it is evident that the transition of ACF technology from prototype testing to production implementation is a possibility within a relatively short term.

1.1.2 Passive Control Approaches

A widely implemented and technically mature approach for vibration and noise reduction employs passive and semi-passive devices like cabin suppressors, isolators, absorbers, and attenuators [62, 93, 113]. However, these devices add significant weight penalties and are designed for a fixed operating condition and payload. They also do not reduce vibration at the rotor source. A detailed discussion of these approaches is beyond the scope of the current review. The focus of this review is on passive approaches involving rotor tip geometry modifications and structural design optimization.

Helicopter rotors with advanced tip geometry, other than the standard rectangular plan form, have been widely used to improve overall rotor performance, vibration and acoustics of the helicopter. The blade tip is located in a region of high dynamic pressure, as well as high blade displacements, and therefore this region influences blade loading and deformation. Various blade tip planforms have been developed, including swept, anhedral, Ogee, tapered tips and combination of these, as shown in Fig. 1.3. A comprehensive review of the development of rotor blade tip shapes is provided in Ref. 13.

A tip sweep tends to lower the effective tip Mach number in the tip region [98]. This reduces compressibility effects on the advancing blade of rotor and improves the performance of the rotor, particularly in high speed forward flight. It also reduces high speed impulsive noise by delaying shock formation. Examples of a swept tip can be found on the UH-60 and AH-64. However, it should be noted

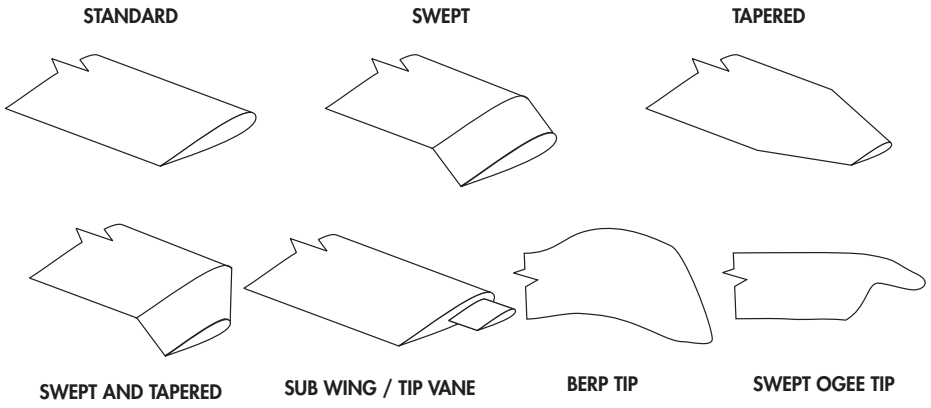

Fig. 1.3. Examples of passive blade tip modifications [84].

that while a swept tip alleviates shock wave development on the advancing blade, it also introduces strong aeroelastic couplings [16], which can result in instability. A tapered tip also has a similar effect of delaying the onset of compressibility. For example, a AH-1S blade with a tapered tip not only reduces the high speed impulsive (HSI) peak noise levels by 6dB and also allows the helicopter to fly 10 knots faster at the same power compared with the standard untapered blade (Ref. 9).

Landgrebe and Bellinger proposed an Ogee tip [54] to diffuse and reduce the intensity of the tip vortex, so as to alleviate BVI effects. A subsequent whirl tower test performed on the UH-1H rotor modified with an Ogee tip showed a significant reduction in BVI noise and vibrations, without compromising hover and forward flight performance [67].

Tip anhedral was first considered for rotor blade design by Mantay and Yaeger [68]. The results from the wind tunnel tests showed that the rotor performance was enhanced by the addition of anhedral to a rectangular planform. Further tests conducted by Brocklehurst [14] confirmed the beneficial effect of anhedral on a British Experimental Rotor Program (BERP) rotor, especially the improvement in the Fig-

ure of Merit for hover. In a computational study [21], de Terlizzi showed that anhedral tips could alleviate BVI by displacing the location of trailed wake, thereby increasing the blade vortex separation distance. Furthermore, tip anhedral could also reduce the strength of tip vortices by creating secondary vortices inboard, thus reducing the vertical vibratory hub shears. In the same study, he showed that dihedral had the opposite effect of increasing the vibratory hub shears.

The Advanced Technology Institute of Commuter-Helicopter (ATIC) program, was initiated in Japan to investigate passive control approaches for rotor noise reduction [75, 76]. The focus was on the effect of tip shapes on blade vortex miss distances, interaction angles between blade and tip vortex trajectory and tip vortex strength on BVI noise. The tip shapes tested included anhedral, dihedral, swept-forward and swept back blade shapes. Based on the wind tunnel tests conducted at the DNW, it was concluded that all the tip shapes tested were capable of alleviating BVI noise, although the mechanisms were somewhat different. Both the anhedral and dihedral reduce BVI by increasing the blade vortex miss distance. On the other hand, the swept back or swept forward tip shapes could be used to avoid parallel interactions.

Another form of passive control approach is the use of structural optimization techniques in the design process. In this approach, an objective function, typically vibration, is minimized through modification of the mass, stiffness and geometrical properties of the rotor blade, subject to appropriate constraints like blade stability margins, blade geometry, and blade stresses. Comprehensive surveys on this approach can be found in Refs. 15, 33, 36

Celi and Friedmann [17] used an implicit aerodynamic formulation to develop an aeroelastic analysis for a homogeneous isotropic blade with straight and swept tips. They carried out an optimization study, using the cross sectional geometry as a design variable , to minimize the vibratory vertical hub shear for a hingeless rotor blade with both straight and swept tips. Constraints were imposed on frequency placement and blade stability in hover. For the straight blade, a reduction of 20-50% in the 4/rev vertical hub force was achieved. For the blade with swept tip, an additional vibration reduction of about 10% was achieved.

Yuan and Friedmann [125] carried out a structural optimization study of a composite rotor blade with a swept tip for vibration reduction. The objective function was the vibratory hub loads in forward flight subject to frequency and aeroelastic stability constraints. The design variables were the ply orientations in the horizontal and vertical walls of the composite blade section, tip sweep and anhedral. It was found that significant vibration reduction of up to 50% could be achieved and that tip sweep played a significant role. However, it should be noted that the aerodynamic model used was based on quasi-steady Theodorsen theory and uniform inflow wake model.

Ganguli and Chopra [37] performed an optimization study for an isotropic four-bladed, soft-in-plane hingeless rotor to minimize the oscillatory hub loads. The design variables were nonstructural mass and its placement, blade bending stiffness in flap, lag and torsion and blade tip geometry. The constraints were frequency placement, autorotational inertia and aeroelastic stability of the blade in forward flight. In a subsequent study [38], a composite blade was considered, with

the ply angles of the laminated wall as additional design variables. In both studies, a reduction in the 4/rev loads of up to 60% was achieved. The optimum design for vibration reduction was swept back, drooped down, and tapered along the blade span. However, a relatively simple aerodynamic model, employing quasi-steady aerodynamics and linear inflow model, was used.

Recently, Wilke [118] performed a multi-objective optimization to develop a blade planform and twist design to improve aerodynamic performance and HSI noise overflight condition required for certification. Both hover and forward flight conditions were investigated. It was found that a blade designed specifically for forward flight performed worse in hover and vice versa. The resulting trade-off blade design was a double swept tip with dihedral and twist. There was a power requirement reduction of up to 2.4% in hover and forward flight and a overflight HSI noise reduction of up to 1.1dB. The impact on vibration was not considered.

It is evident from this review that the major emphasis in rotor blade design has been on aerodynamic performance enhancement and vibration reduction, with efforts focused on noise reduction having a somewhat secondary role. Even in those studies that dealt with noise, the emphasis has been on the low speed approach case with BVI noise, which is normally the loudest flight condition and a certification requirement. Most studies on active noise control have been experimental and the control was almost exclusively open-loop. Finally, there is no clear consensus on the best tip shape design for helicopter, as each tip design is probably well suited for certain narrowly defined operating conditions but not for others.

1.2 Literature on OBC Configuration Design

As discussed in Section 1.1.1, several active control approaches, such as the HHC and the IBC, have been developed for rotorcraft vibration and noise reduction. The IBC approach, implemented through on-blade devices such as the actively controlled trailing-edge flaps (ACF) [88,110], Fig. 1.4, and microflaps [61,82], Fig. 1.5, have been studied and shown to be effective for both vibration and noise reduction. During its deflection, an ACF or microflap generates a pitching moment which causes a redistribution of the aerodynamic loads. The on-blade control devices also directly influence the blade aerodynamics through an additional lift force. Thus, the performance of on-blade control devices is directly related to the blade stiffness in flap and torsion. Therefore, active rotor blade design requires the optimization of blade stiffness properties so as to maximize the on-blade control device effectiveness without compromising the rotor baseline performance.

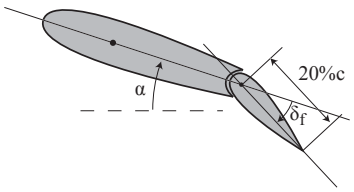

Fig. 1.4. A 20%c conventional plain flap configuration.

The effect of design parameters such as torsional stiffness, flap length, and flap location on the vibration reduction performance of an ACF was first examined in Ref. 70, and subsequently in Ref. 69. It was found that by increasing torsional stiffness, the control input and actuation power required to achieve the same degree of vibration reduction increased. Therefore, ACF effectiveness was best on torsion-

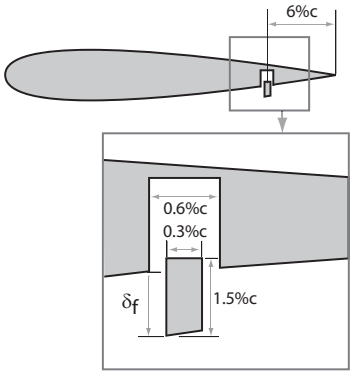

Fig. 1.5. Sliding microflap configuration.

ally soft blades. The other design parameters that were identified as influential for vibration reduction were spanwise length and location of the ACF. The ACF was found to be effective when moved outboard towards the blade tip due to the increased dynamic pressure. However, this improved effectiveness was accompanied by an increase in the flap actuation power and a drag penalty which affected the performance of the vehicle. Fulton [35] performed a parametric study on a 27% Mach Scaled Apache blade and determined that the ACF was most effective for vibration reduction at an optimal natural frequency of 3.3/rev in torsion. The studies in Ref. 35, 69, 70 were conducted using elementary aerodynamic models based on the potential flow theory and using open-loop control methods. Recently, Jain and Yeo [45] studied the effect of blade torsional frequencies on rotor performance (L/D ratio) in the presence of an ACF, deflected at a 1/rev frequency. The baseline rotor performance was found to degrade with a reduction in the torsional frequency. However, the ACF was most effective in the case of a torsionally soft blade, thus compensating for the degradation in the baseline performance.

A stationary microflap or Gurney flap having a height of 1.5 - 2% of blade chord

was found to produce the best lift-to-drag ratio [57, 77]. It was also found Refs. 4 and 56 that a Gurney flap close to the trailing edge is the most effective in increasing sectional lift. Therefore, the optimal location is likely to be as far aft as the volume constraints on the trailing edge allows. The use of an oscillating microflap for active control is a recent innovation and there are limited studies on the impact of the microflap configuration for active control [83].

Furthermore, newer helicopters are experimenting with stiffer blade configurations [6] and therefore, it is necessary to examine the performance of different on-blade control devices and configurations over a wider range of blade stiffnesses than considered previously.

1.3 Literature on In-Plane Noise Reduction

In-plane, low-frequency rotorcraft noise is of particular concern from a military operation standpoint as it tends to propagate for long distances without significant attenuation. Furthermore, HSI noise caused by transonic conditions near the blade tip at high advance ratio can raise the in-plane noise to unacceptable levels. Both affect the aural detection range of a rotorcraft, and hence its operational characteristics. Figure 1.6 shows the different noise components and directivity characteristics of rotor noise. Despite these operational considerations, in-plane noise prediction and control has not been studied as extensively as out-of-plane Blade Vortex Interaction (BVI) noise [34, 44, 123]. Until recently, in-plane noise suppression techniques were limited to passive means, such as thinning, sweeping or

tapering the blade, to reduce the thickness and HSI noise [20,98]. The use of active control for in-plane noise reduction is a recent development that will be discussed next.

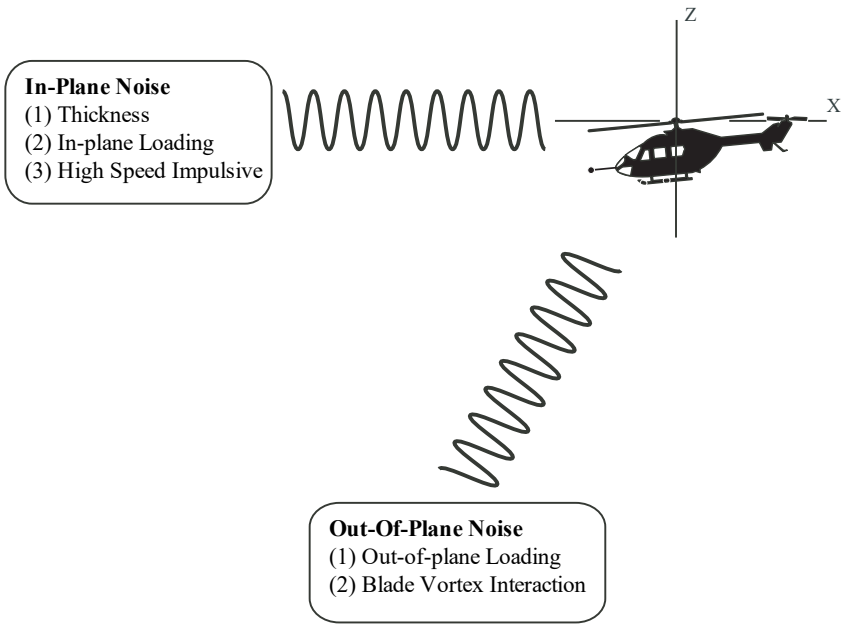

Fig. 1.6. Rotor noise components and directivity characteristics. (Adapted from Ref. 105)

1.3.1 Active Control of In-Plane Noise

During the past 25 years, OBC implemented by actively controlled partial span plain flaps, and more recently microflaps, has been shown to be effective for rotorcraft vibration and BVI noise reduction, and rotor performance enhancement [34]. For active noise control, the focus has been on out-of-plane BVI noise in low speed descending flight. Only a few recent studies have examined active control of in-plane noise [42,96,105,121].

For in-plane, low frequency noise reduction at moderate forward airspeed, an

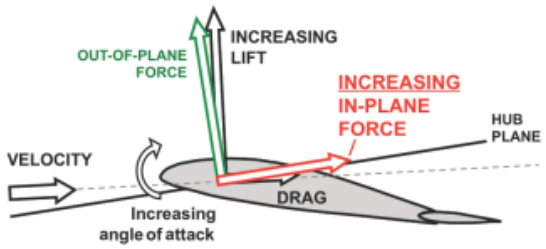

Fig. 1.7. Effects of active flap motion on blade aerodynamic forces and generation of positive peak pressure [105].

“anti-noise" approach was first proposed by Sim [104] and Gopalan and Schmitz [42]. The approach is based on the assumptions that: (1) thickness and in-plane loading noise components are uncoupled to first order and (2) the HSI noise is not considered for $M_{AT} < 0.9$. Therefore, the negative peak pressure of the thickness noise component, which predominantly radiates forward in the plane of the rotor, can be suppressed by positive peak pressure of the “anti-noise" pulses generated using actively controlled flaps with correct phasing. The flaps are used to increase the angle of attack of the rotor blade, which leads to higher lift and in-plane component of the loading force. This in-plane loading force generates the positive peak pressure to cancel the negative thickness peak pressure, reducing the overall acoustic pressure, as illustrated in Fig. 1.7.

The “anti-noise" strategy using a single harmonic control schedule was first experimentally demonstrated in early 2008 as part of the Boeing Smart Materials Actuated Rotor Technology (SMART) rotor project in the 40’x80’ National Full Scale Aerodynamics Complex (NFAC) Wind Tunnel at NASA Ames Research Center [105]. The SMART rotor is a 34’ diameter full-scale, bearingless, five-bladed rotor modified from an existing MD900 Explorer rotor system. The single trailing

edge flap has a spanwise length of 18.4%R, is centered at 83%R and a flap chord of 25%c. A noise reduction of up to 6dB was achieved in this demonstration using a 4/rev harmonic control schedule. However, this was accompanied by an increase in 5/rev vibratory hub loads of up to 300%. The performance penalty on the rotor due to the increase in the in-plane force to generate the “antinoise" was not quantified.

In 2009, a UH-60A rotor system with an IBC system was tested at the NFAC with the objective of demonstrating the capability of IBC for improving rotor performance and reducing vibrations, pitch link loads and in-plane noise [78]. Power reductions of up to 5% and L/D improvement was found using a 2/rev IBC input. For the in-plane noise investigation, an open loop single frequency and phase sweep was conducted from 2/rev - 5 /rev at three different flight conditions. The frequency and phase which showed the greatest acoustic reduction was then subjected to an amplitude sweep. It was found that for an IBC input at 3/rev, phase of 230° and amplitude of 1°, the negative acoustic peak pressure that dominated the low frequency harmonic content was reduced by nearly 50% at one of the in-plane microphone. The impact on vibration and performance was not investigated. The wind tunnel test suggests that IBC is also capable of localized reduction of in-plane noise.

In 2010, a non-harmonic control schedule, also known as the AFDD Model 01 waveform, was demonstrated in a joint Sikorsky/UTRC/U.S. Army wind tunnel test program in NFAC in the framework of the active flap demonstration program [106]. The rotor is a 29.2’ diameter, full-scale, four-bladed main rotor modi-

fied from a S-434TM helicopter. The single trailing edge flap has a spanwise length of 11.4%R, is centered at 72%R and a flap chord of 22.2%c. In the same test, closed loop control for forward in-plane noise reduction was also demonstrated for the first time. A linear frequency domain T-matrix controller with three near-field, in-plane feedback microphones were used. A noise reduction of 3.2dB was achieved at the in-plane microphone (M06). This was accompanied by an increase in vibratory hub loads of up to 220% and rotor performance penalty of up to 2% [106].

At the University of Maryland, Sargent and Schmitz [96] explored the feasibility of using an active tip air jet to generate the in-plane loading required for noise control. The Active Jet Acoustic Control Test Rotor (AJAX ETR) is a single blade, untwisted rotor with an air duct which runs along the blade to provide the control. The air duct allows the transfer of modulated air from the blade root to the tip, to generate the appropriate level of in-plane loading and harmonics. The 2/rev harmonic control reduced the peak negative amplitude of the test rotor's radiated noise by 5 Pa (from a peak of -14 Pa) at the target microphone. There was no study done on the vibration and performance penalties.

As part of the VLRCOE project, the Pennsylvania State University has been studying alternative ways to model the thickness and loading noise, so that in-plane noise can be predicted accurately and efficiently. The aim of the project is to reduce in-plane noise using active control, without incurring performance penalty. An alternative computational model, referred to as the dual compact model, has been proposed for improved noise prediction and an open-loop active flap schedule for in-plane noise control [120].

1.3.2 Passive Control of In-Plane Noise

As discussed in Section 1.1.2, typical passive control methods consist of blade tip planform modifications such as sweep, anhedral, dihedral, etc. For BVI noise, blade tip shapes that produce vortex diffusion, e.g. Ogee tip, have been shown to be effective (Ref. 54). Blade sweep is also effective in reducing BVI noise by avoiding or delaying parallel interactions between the blade and the vortices (Ref. 122). For in-plane noise, thinning and tapering the tip of the rotor blade reduces the thickness noise contribution (Ref. 20). At high rotor tip speed, sweeping the blade reduces the effects of compressibility, effectively delaying delocalization and the onset of HSI noise (Ref. 3). However, the contribution of blade sweep at moderate tip speed has not been clearly studied. A BERP like rotor, Fig. 1.3, with sweep was tested in the DNW and the measured in-plane noise spectra showed only marginal difference from the baseline unswept blade [71]. It was also shown in Ref. 66 that the sweep angle is not an important parameter, when compared to the taper ratio since the sweep angle affects the quadrupole noise, which is not dominant at moderate tip speed. On the other hand, it was shown in Ref. 90 that the sweep angle introduces a phase shift effect between spanwise distributed source and sink couples, resulting in in-plane noise reduction.

Tip anhedral which improves the hover figure of merit [13], and tip dihedral which is used for improved forward flight performance have been studied for noise reduction application. Based on wind tunnel tests performed at the DNW, both the tip anhedral and dihedral were capable of BVI noise reduction. This

was attributed to the tip anhedral and tip dihedral increasing the BVI miss distance [75, 76, 122]. However, there is very limited literature on the effect of tip anhedral / dihedral on in-plane noise.

Despite the valuable insights gained, these studies had limitations, because some were purely CFD-based aerodynamic studies, while the rest used simplistic structural dynamic models [13]. Such blade models have limited value since blade structural dynamics have been identified in Ref. 122 to be important in predicting blade airloads for noise prediction, particularly for swept and anhedral tips where it introduces strong bending torsion coupling, that influence both blade vibrations and aeroelastic stability. Furthermore, these studies have not explored the adverse effects of noise reduction on the hub vibratory loads. It has been shown in Ref. 33 that for accurate prediction of helicopter noise and the effects of its suppression on the vibratory loads, it is essential to account for blade deflections and rotor trim using a high fidelity rotor aeroelastic model coupled with an aeroacoustic model.

1.4 Objectives and Novel Contributions of this Dissertation

The principal new contributions of this dissertation are concisely summarized below:

1. Conducted a parametric study examining both single and dual flap and microflap configurations operating in closed-loop mode to determine the best blade torsional stiffness, as well as variations in the spanwise and chordwise placement of microflaps for implementing OBC for vibration and BVI

noise reduction on a rotor blade resembling a MBB BO-105 rotor blade. This optimal configuration was subsequently used in the studies for control of in-plane noise reduction using active and passive approaches.

2. Developed an efficient suite of computational tools for the accurate prediction of in-plane noise by replacing the acoustic module in AVINOR by an improved and efficient acoustic module HELINOIR (HELIcopter NOIse Reduction) that is suitable for in-plane noise reduction studies using active and passive approaches.

3. Validated and verified the new computational framework employing the new AVINOR/HELINOIR code suite by comparing results obtained from the new framework against experimental and computational results for both in-plane noise as well as out-of-plane BVI noise predictions.

4. Studied closed-loop active in-plane noise reduction using single and dual plain flaps, employing an adaptive version of the Higher Harmonic Control (HHC) algorithm.

5. Explored a variety of feedback microphone locations for in-plane noise reduction.

6. Determined the vibration penalties associated with active control of in-plane noise in level flight at moderate advance ratios.

7. Applied the aeroelastic-aeroacoustic framework to passive noise reduction, while tracking the effect of noise reduction on hub vibrations.

8. Compared performance of active OBC approaches to passive approaches based on various tip geometries (sweep, anhedral and dihedral) for in-plane noise reduction while tracking the effects of noise reduction on hub vibrations.

By accomplishing these objectives the fundamental understanding of the physical mechanism underlying in-plane noise control at moderate advance ratio was substantially enhanced.

CHAPTER II

DESCRIPTION OF THE ROTORCRAFT AEROELASTIC ANALYSIS CODE

The comprehensive rotorcraft simulation code AVINOR (Active VIbration and NOise Reduction) is used for all the active and passive noise and vibration reduction studies in this dissertation [41]. AVINOR has been extensively validated in earlier studies [22, 88]. A brief description of the principal components of the code is provided in this chapter, except for the acoustic model which will be described in detail in Chapter III.

2.1 Structural Dynamics Model

The rotor can be modeled as a four or five-bladed rotor with fully coupled flap-lag-torsional dynamics for each blade. The moderate deflection, nonlinear structural dynamic model is used. Two different structural dynamic models can be used for generating the solution. A global Galerkin model for the straight blade with an OBC device for active control and a Galerkin type finite element model for

the rotor blade with swept tip for passive control.

2.1.1 Global Galerkin Model

For active control, the rotor blade is modeled as a slender cantilever beam composed of a linearly elastic homogeneous material undergoing moderate deflections with fully coupled flap-lag-torsional dynamics. The structural dynamic equations are discretized using the global Galerkin method, employing three flap, two lead-lag, and two torsional free vibration modes of the rotating blade. Each rotating mode is obtained from nine non-rotating uniform beam modes. The effect of control surfaces on the structural properties of the blade is neglected. Thus, the control surfaces influence blade behavior only through their effect on the aerodynamic and inertial loads. This structural model is computationally more efficient compared to the finite element model, especially when coupled with OBC devices. This structural dynamic model is similar to that in Ref. 95 and is described in detail in Appendix A, along with the modeling assumptions, coordinate systems and coordinate transformation relations used in the aeroelastic analysis model.

2.1.2 Galerkin Type Finite Element Model

The finite element model is based on an analysis developed by Yuan and Friedmann (Ref. 125, 126), which is capable of modeling composite blades with transverse shear deformations, cross sectional warping, and swept tips. In the structural dynamic analysis, the rotor blade is modeled as an elastic rotating beam. The blade is modeled by a series of five straight beam finite elements along the

elastic axis of the blade. A single finite element is used to model the tip. Three different tip geometries, namely sweep, anhedral, and dihedral are studied in this dissertation. Pre-cone, control pitch setting, pre-twist and root offset are included in the model. The equations of motion are formulated using a finite element discretization of Hamilton's principle, with the assumption that the blade undergoes moderate deflections. The beam-type finite elements used for the discretization have 23 nodal degrees of freedom. In this study, modal reduction employing eight normal modes, namely the first three flap modes, first two lead-lag modes, first two torsional modes, and the first axial mode, is used to reduce the structural degrees of freedom. This structural dynamic model is similar to that developed in Refs. 59, 125, 126 and is described in detail in Appendix B.

2.2 Aerodynamic Model

The unsteady aerodynamic model consists of three basic components, (a) *attached flow* blade or blade/OBC surface 2D cross-sectional aerodynamic loads, (b) *separated* flow 2D cross-sectional aerodynamics, and (c) a free wake model that is driven by the 2D aerodynamic load distribution along the blade span.

The *attached* flow 2D sectional aerodynamic loads for the blade or blade/OBC surface combination are calculated using a computational fluid dynamics (CFD) based reduced order model (ROM) (Refs. 60, 61). The ROM is obtained by using a compressible unsteady Reynolds-Averaged Navier-Stokes (RANS) CFD solver, CFD++, to generate frequency domain aerodynamic response to generalized mo-

tions. A rational function approximations (RFA) approach is used to represent the least squares fit to the aerodynamic load response data obtained using CFD simulations. Subsequently, the frequency domain loads are converted to the time-domain using the RFA approach, resulting in the final state space representation

$$\begin{aligned}\dot{\mathbf{x}}(t) &= \frac{U(t)}{b}\mathbf{R}(M,\alpha,\delta_f)\mathbf{x}(t) + \mathbf{E}(M,\alpha,\delta_f)\dot{\mathbf{h}}(t),\\ \mathbf{f}(t) &= \frac{1}{U(t)}\Big(\mathbf{C}_0(M,\alpha,\delta_f)\mathbf{h}(t)\\ &\quad + \mathbf{C}_1(M,\alpha,\delta_f)\frac{b}{U(t)}\dot{\mathbf{h}}(t) + \mathbf{D}\mathbf{x}(t)\Big).\end{aligned} \tag{2.1}$$

Equation (2.1) relates the time domain generalized motions $\mathbf{h}(t)$ to the generalized loads $\mathbf{f}(t)$, where the vector $\mathbf{x}(t)$ represents the vector of augmented aerodynamic states. This model accurately predicts the unsteady aerodynamic lift, moment, and drag forces while taking a fraction of computational time compared to CFD. Accounting for both unsteady lift and drag forces is critical for accurate in-plane noise prediction. For the tip sweep/anhedral/dihedral region, the chordwise component of the freestream flow velocity experienced at the blade tip section is used to determine the unsteady aerodynamic loads.

The second component of the aerodynamic model is a 2D model for separated flow that represents the dynamic stall (DS) condition on the blade. The DS model used in AVINOR is the Office National d'Etudes et Recherches Aérospatiale (ONERA) dynamic stall model (Ref. 89).

The third component of the aerodynamic model is a free wake analysis, which is critical for properly capturing BVI effects on vibratory loads and noise. The wake

analysis used has been extracted from the comprehensive code CAMRAD/JA (Refs. 46, 47) and subsequently has undergone significant improvements for modeling BVI noise (Refs. 87, 88). These consist of a finer azimuthal wake resolution, of 5° or less, combined with a dual vortex model used when the tip loading becomes negative. Additional details on the wake model can be found in Ref. 41. The aerodynamic model is described in detail in Appendix C.

2.3 Coupled aeroelastic response/trim solution

The equation of motion for the blade representing an equilibrium between the inertia, aerodynamic, and structural loads is discretized using a finite element approach (Ref. 125). The finite element degrees of freedom are reduced by a normal mode transformation using coupled free vibration modes of the rotating blade. For the global Garlerkin model, the aeroelastic equation of motion is discretized spatially using Galerkin's method of weighted residuals (Ref. 72). This process results in a system of coupled nonlinear differential equations with periodic coefficients that can be written as

$$[M(\mathbf{y})]\ddot{\mathbf{y}} + [C(\mathbf{y}, \dot{\mathbf{y}})]\dot{\mathbf{y}} + [K(\mathbf{y}, \dot{\mathbf{y}}, \ddot{\mathbf{y}})]\mathbf{y} + \mathbf{F}(\mathbf{y}, \dot{\mathbf{y}}, \ddot{\mathbf{y}}) = 0 \tag{2.2}$$

The equations are rewritten in a first-order state variable form and integrated in the time domain using the Adams-Bashforth predictor corrector algorithm (Ref. 102). In the response solution process, the equations of motion (Eqn. 2.2) are fully coupled with the trim equations. Two different trim procedures are available in AVI-

NOR: a propulsive trim procedure (Ref. 70), where six equilibrium equations (three forces and three moments) for the entire helicopter in a steady level flight condition are enforced, and a wind tunnel trim option (Ref. 59), where zero pitching and rolling moments on the rotor are maintained for a specified shaft angle. It is also important to note that in the response solution, the augmented aerodynamic states $\mathbf{x}(t)$ in Eqn. (2.1) are added to the physical degrees of freedom $\mathbf{y}$. Using the response solution, the vibratory hub shears and moments are obtained from the integration of the distributed inertial and aerodynamic loads over the entire blade span in the rotating frame. Subsequently, the resulting loads at the blade root are transformed to the hub-fixed nonrotating system, and the contributions from the individual blades are combined (Ref. 125). In this process, when the blades are assumed to be identical, cancellation of various terms occurs and the dominant components of the hub shears and moments have a frequency of N_b/rev, which is the blade passage frequency. This is described in detail in Appendix D.

2.4 Control Approach

In the AVINOR code, active control of vibration and noise is implemented using the adaptive version HHC algorithm, used extensively for closed-loop vibration and noise control in rotorcraft [85, 88]. The algorithm is based on the assumption that the helicopter can be represented by a linear model relating the output of interest $\mathbf{z}$ to the control input $\mathbf{u}$. The measurement of the plant output and update of the control input are performed at specific times $t_k = k\tau$, where τ is the time

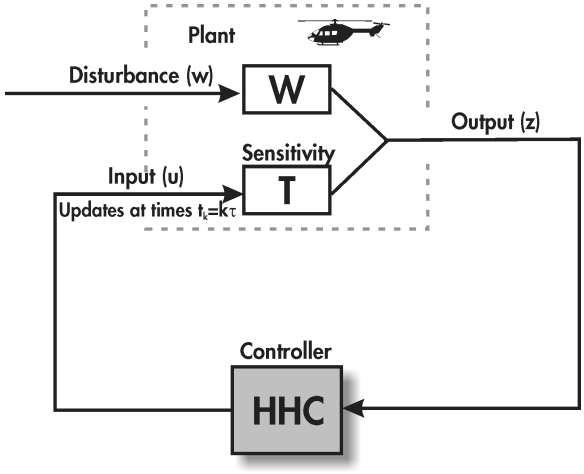

Fig. 2.1. Higher harmonic control architecture

interval between updates during which the plant output reaches a steady state. In actual implementation of the algorithm, this time interval may be one or more revolutions. A schematic of the HHC architecture implemented on a helicopter is shown in Fig. 2.1. The disturbance $\mathbf{w}$ represents the helicopter operating condition. The output vector at the k^{th} time step is given by

$$\mathbf{z}_k = \mathbf{T}\mathbf{u}_k + \mathbf{W}\mathbf{w} \tag{2.3}$$

where the sensitivity matrix $\mathbf{T}$ represents a linear approximation of the helicopter response to the control and is given by

$$\mathbf{T} = \frac{\partial \mathbf{z}}{\partial \mathbf{u}}. \tag{2.4}$$

At the initial condition, $k = 0$,

$$\mathbf{z}_0 = \mathbf{T}\mathbf{u}_0 + \mathbf{W}\mathbf{w}. \tag{2.5}$$

Subtracting Eqn. (2.5) from Eqn. (2.3) to eliminate the unknown $\mathbf{w}$ yields

$$\mathbf{z}_k = \mathbf{z}_0 + \mathbf{T}(\mathbf{u}_k - \mathbf{u}_0). \tag{2.6}$$

The controller is based on the minimization of a general quadratic cost function

$$J(\mathbf{z}_k, \mathbf{u}_k) = \mathbf{z}_k^{\mathrm{T}} \mathbf{Q} \mathbf{z}_k + \mathbf{u}_k^{\mathrm{T}} \mathbf{R} \mathbf{u}_k. \tag{2.7}$$

The optimal control input is determined from the requirement

$$\frac{\partial J(\mathbf{z}_k, \mathbf{u}_k)}{\partial \mathbf{u}_k} = 0, \tag{2.8}$$

which yields the optimal control law $\mathbf{u}_{k,\mathrm{opt}}$, given by

$$\mathbf{u}_{k,\mathrm{opt}} = -(\mathbf{T}^{\mathrm{T}} \mathbf{Q} \mathbf{T} + \mathbf{R})^{-1} (\mathbf{T}^{\mathrm{T}} \mathbf{Q})(\mathbf{z}_0 - \mathbf{T}\mathbf{u}_0). \tag{2.9}$$

Combining Eqs. (2.6), (2.7) and (2.9), the minimum cost is

$$\begin{aligned} &J(\mathbf{z}_k, \mathbf{u}_{k,\mathrm{opt}}) \\ &\quad = (\mathbf{z}_0 - \mathbf{T}\mathbf{u}_0)^{\mathrm{T}} \left[\mathbf{Q} - (\mathbf{Q}\mathbf{T}) \mathbf{D}^{-1} (\mathbf{T}^{\mathrm{T}} \mathbf{Q}) \right] (\mathbf{z}_0 - \mathbf{T}\mathbf{u}_0). \end{aligned} \tag{2.10}$$

where

$$\mathbf{D} = \mathbf{T}^{\mathrm{T}} \mathbf{Q} \mathbf{T} + \mathbf{R} \tag{2.11}$$

This is a classical version of the HHC algorithm that yields an explicit relation for the optimal control input.

Another version of the HHC algorithm where the sensitivity matrix $\mathbf{T}$ is updated using least-squares methods after every control update is known as the adaptive or recursive HHC [85]. In order to describe the adaptive HHC algorithm, relative output and input vectors are defined, $\Delta\mathbf{z}_k$, and $\Delta\mathbf{u}_k$ as

$$\Delta\mathbf{z}_k = \mathbf{z}_k - \mathbf{z}_{k-1}, \;\; \Delta\mathbf{u}_k = \mathbf{u}_k - \mathbf{u}_{k-1}, \tag{2.12}$$

and, $\Delta\mathbf{Z}_k$ and $\Delta\mathbf{U}_k$ as

$$\begin{aligned} \Delta\mathbf{Z}_k &= \begin{bmatrix} \Delta\mathbf{z}_1 & \cdots & \Delta\mathbf{z}_k \end{bmatrix}^T, \\ \Delta\mathbf{U}_k &= \begin{bmatrix} \Delta\mathbf{u}_1 & \cdots & \Delta\mathbf{u}_k \end{bmatrix}^T. \end{aligned} \tag{2.13}$$

The relation between the successive updates of vibration levels $\mathbf{z}_k$ is

$$\mathbf{z}_k = \mathbf{z}_{k-1} + \mathbf{T}(\mathbf{u}_k - \mathbf{u}_{k-1}). \tag{2.14}$$

This can be represented in another form,

$$\Delta\mathbf{z}_k = \mathbf{T}\Delta\mathbf{u}_k. \tag{2.15}$$

Hence, it follows from Eqs. (2.15) and (2.13) that

$$\Delta \mathbf{Z}_k = \mathbf{T} \Delta \mathbf{U}_k. \tag{2.16}$$

Assuming $\Delta \mathbf{U}_k \Delta \mathbf{U}_k^{\mathrm{T}}$ is nonsingular, one can define

$$\mathbf{P}_k = (\Delta \mathbf{U}_k \Delta \mathbf{U}_k^{\mathrm{T}})^{-1}, \tag{2.17}$$

and from Eqn. (2.16) the least squares estimate $\hat{\mathbf{T}}_{\mathrm{LS}_k}$ of $\mathbf{T}$ is given by

$$\hat{\mathbf{T}}_{\mathrm{LS}_k} = \Delta \mathbf{Z}_k \Delta \mathbf{U}_k^{\mathrm{T}} \mathbf{P}_k. \tag{2.18}$$

The recursive least squares method is used to iteratively update $\hat{\mathbf{T}}_{\mathrm{LS}_k}$ based on the past and current values of $\Delta \mathbf{z}_k$ and $\Delta \mathbf{u}_k$. The updated estimate $\hat{\mathbf{T}}_{\mathrm{LS}_k}$ is used at each control update step to calculate the optimal control input $\mathbf{u}_{k,\mathrm{opt}}$ given in Eqn. (2.9). The adaptive HHC algorithm has been shown to perform better than the classical HHC when the model nonlinearities are significant and the sensitivity matrix $\mathbf{T}$ is a poor approximation of the model [85]. The adaptive HHC algorithm is used for all the active vibration and noise reduction simulation in this study.

2.4.1 Implementation of the HHC Algorithm

Previous research [34] has indicated that for a four-bladed rotor, an effective control input $\mathbf{u}_k$, representing the control surface deflection consists of a combina-

tion of 2/rev, 3/rev, 4/rev, and 5/rev harmonic amplitudes:

$$\mathbf{u}_k = [\delta_{2c}, \delta_{2s}, ..., \delta_{5c}, \delta_{5s}]^T, \tag{2.19}$$

where the term 'control surface' is used to denote both a conventional plain trailing-edge flap, Fig. 1.4, or the microflap, Fig. 1.5.The total control surface deflection is given by

$$\delta(\psi, \mathbf{u}_k) = \sum_{n=2}^{5} [\delta_{nc} \cos(n\psi) + \delta_{ns} \sin(n\psi)] \tag{2.20}$$

where the quantities δ_{nc} and δ_{ns} correspond to the cosine and sine components of the n/rev control input harmonic, respectively. The control surface deflection δ corresponds to either the angular deflection of the plain flap or vertical displacement in the case of the microflap. When multiple control surfaces are used, such as in the dual flap configuration, the control surface deflections are given by

$$\delta_i(\psi, \mathbf{u}_k) = \sum_{n=2}^{5} [\delta_{nci} \cos(n\psi) + \delta_{nsi} \sin(n\psi)] \,, \tag{2.21}$$

where $i = 1, 2$. The control vector $\mathbf{u}_k$ is then comprised of the harmonic components from both the flaps given by

$$u_k = [\delta_{2c1}, \delta_{2s1}, ..., \delta_{5c1}, \delta_{5s1}, \delta_{2c2}, \delta_{2s2}, ..., \delta_{5c2}, \delta_{5s2}] \tag{2.22}$$

.

For noise reduction studies, the output vector, $\mathbf{z}_{\text{NR}}$, is dependent on the type of

noise being investigated. For in-plane noise reduction using a *single feedback microphone*, $\mathbf{z}_{\text{NR}}$ consists of the 1$^{\text{st}}$-6$^{\text{th}}$ blade passage frequency harmonic components of the rotor noise, as sensed at the microphone and is given by

$$\mathbf{z}_{\text{NR}} = \begin{bmatrix} N_{H01} \\ N_{H02} \\ \vdots \\ N_{H06} \end{bmatrix} \tag{2.23}$$

where $N_{H01} - N_{H06}$ represent the 1$^{\text{st}}$-6$^{\text{th}}$ blade passage frequency harmonic components of in-plane acoustic pressure level which are the principal components of the in-plane low frequency noise [105]. For multiple feedback microphones, the output vector, $\mathbf{z}_{\text{NR}}$ is comprised of the 1$^{\text{st}}$-6$^{\text{th}}$ harmonics for all the feedback microphones. The goal is to obtain the best configuration of feedback microphones for producing the largest amount of in-plane noise reduction.

As part of the study, out-of-plane BVI noise is also calculated in order to validate the AVINOR/HELINOIR code against experimental results, Section 5.2, and verify the code for the BVI noise reduction results obtained in our previous studies [83], Section 5.3. For BVI noise reduction, $\mathbf{z}_{\text{NR}}$ consists of the 6$^{\text{th}}$-17$^{\text{th}}$ blade passage frequency harmonic components of the rotor noise, which represent approximately the principal part of BVI noise, calculated at a microphone installed on the right rear skid of the helicopter.

For the vibration reduction studies used in the code verification, the output

vector $\mathbf{z}_k$ consists of 4/rev vibratory hub shears and moments represented as:

$$\mathbf{z}_{\text{VR}} = \begin{bmatrix} F_{HX4} \\ F_{HY4} \\ F_{HZ4} \\ M_{HX4} \\ M_{HY4} \\ M_{HZ4} \end{bmatrix}. \tag{2.24}$$

The vibratory hub shears and moments needed for estimating the vibration penalty that accompany noise reduction are obtained by integrating the distributed inertial and aerodynamic loads over the entire blade span in the rotating frame. Subsequently, the loads are transformed to the hub-fixed non-rotating system, and the contributions from the individual blades are combined. When the blades are assumed to be identical, this leads to cancellation of various components so that 4/rev vibratory shears and moments are the dominant components for a 4 bladed rotor. For a 5 bladed rotor, the vibratory hub loads are 5/rev.

The weighting matrix $\mathbf{Q}$ in the cost function in Eqn. (2.7) is a diagonal matrix consisting of weights penalizing the elements in the output vector. For vibration control, $\mathbf{Q}$ is described by six weights corresponding to the three vibratory hub shears and the three vibratory hub moments, shown in Eqn. (2.25). The hub moments are an order of magnitude smaller compared to the hub shears, therefore,

the weights on the moments are 10 times larger those on the hub shears.

$$\mathbf{Q}_{\text{VR}} = \begin{bmatrix} 1 & 0 & 0 & 0 & 0 & 0 \\ 0 & 1 & 0 & 0 & 0 & 0 \\ 0 & 0 & 1 & 0 & 0 & 0 \\ 0 & 0 & 0 & 10 & 0 & 0 \\ 0 & 0 & 0 & 0 & 10 & 0 \\ 0 & 0 & 0 & 0 & 0 & 10 \end{bmatrix}. \tag{2.25}$$

For noise control, the number of weights is dependent on the number of harmonic components considered. For in-plane noise reduction using a far-field feedback microphone, all the six low frequency noise components are weighted equally at 100, whereas a weight of 1 is used in the case of a near-field feedback. The weights were chosen by trial and error. The far-field noise feedback signal needs a higher weight in order to retain control effectiveness. The weighting matrix $\mathbf{R}$ is a diagonal matrix consisting of weights penalizing the elements in the control inputs vector. A value of 1×10^{-6} is used in this study.

2.4.2 Actuator Saturation

Most actuation devices used for on blade control of rotorcraft vibrations and noise are subject to amplitude saturation. Furthermore the actuation amplitudes have to be limited so as to avoid undesirable interactions between the primary flight control system and the on blade controller. For a microflap, the maximum

deflection is constrained by its size, usually 1.5% of the chord. For a conventional trailing-edge flap the maximum deflection is set to 4°. There are four different approaches to implementing actuator saturation in the HHC algorithm, namely truncation, scaling, auto-weighting, and optimization. The optimized approach developed in Ref. 81 is used for this study.

This approach overcomes the limitations associated with the other approaches. Recall that the HHC algorithm is based on the minimization of a quadratic cost function, given by Eqn. (2.7). The saturation limits can be combined with the minimization of the cost function to yield a constrained optimization problem:

$$\begin{aligned} \underset{\mathbf{u}_k}{\text{minimize}} \quad & J(\mathbf{z}_k, \mathbf{u}_k) = \mathbf{z}_k^{\mathrm{T}} \mathbf{Q} \mathbf{z}_k + \mathbf{u}_k^{\mathrm{T}} \mathbf{R} \mathbf{u}_k, \\ \text{subject to} \quad & |\delta_i(\psi, \mathbf{u}_k)| \leq \delta_{\text{limit}}, \quad i = 1, \ldots, n_\delta \end{aligned} \tag{2.26}$$

where n_δ is the total number of control surfaces.

The optimization problem given by Eqn. (2.26) is a nonlinear constrained optimization problem with a quadratic objective function and nonlinear inequality constraints, representing a Nonlinear Programming (NP) problem. This saturation approach involves direct modifications to the HHC algorithm to account for the presence of saturation in an *a priori* manner. The resulting optimal control input always satisfies the saturation limits irrespective of the values of $\mathbf{R}$ and $\mathbf{Q}$.

A NP method, Sequential Quadratic Programming (SQP) [32], available in the FMINCON tool in MATLAB, is used to solve the optimization problem given by Eqs. (2.26). The SQP method solves a quadratic programming subproblem based

on a quadratic approximation of the Lagrangian function. A stand-alone application (a *.exe* file) capable of performing the optimization is generated using the *mcc -m* command in Matlab. Subsequently, this application is invoked from the AVINOR code, written in FORTRAN, in order to evaluate the optimum $\mathbf{u}_k$. The stand-alone application requires approximately 1 sec to run on a 2.53 GHz Intel Xeon processor in the case of a single control surface. Note that the nonlinear constraints described in Eqn. (2.26) have to be satisfied for all values of the azimuth angle $\psi \in [0^\circ \;\; 360^\circ]$. In actual numerical implementation, the nonlinear constraints are evaluated and enforced at every integer value of ψ over the range $[0^\circ \;\; 360^\circ]$ during the control update performed by the external Matlab script.

CHAPTER III

ACOUSTIC MODEL

An overview of the different sources and classification of rotor noise is presented first. This is followed by a discussion of the governing equations, the Ffowcs Williams-Hawkings (FW-H) equations, and its casting into Farrasat's Formulation 1A, that can be implemented in a computationally efficient manner. Two implementation approaches of Formulation 1A, namely the *retarded time* algorithm and the *source time dominant* algorithm are compared. The aeroelastic-aeroacoustic code, AVINOR/WOPWOP, has been extensively validated for accurate out-of-plane BVI noise prediction and control. However, there are limitations in the implementation of WOPWOP that makes it difficult for active in-plane noise prediction. Therefore, a new acoustic methodology, as implemented in the HELIcopter NOIse Reduction (HELINOIR) code, was adopted. This acoustic framework is described next.

3.1 Rotor Noise Sources

There are several approaches for classifying rotor noise [39, 65, 116]. The one followed here follows that presented by Schmitz [98], who classified rotor noise based on its aerodynamic origins. This classification is illustrated using the noise spectrum of a two-bladed UH-1A shown in Fig. 3.1. In this figure, the spectrum is classified according to its source as the (1) main rotor rotational noise, (2) tail rotor rotational noise, (3) main rotor broadband noise due to interaction of the moving blade with shed turbulence and (4) gearbox noise. From Fig. 3.1, it is clear that the main rotor rotational noise is the primary contributor to the overall sound pressure level and is the only source that will be simulated in this study.

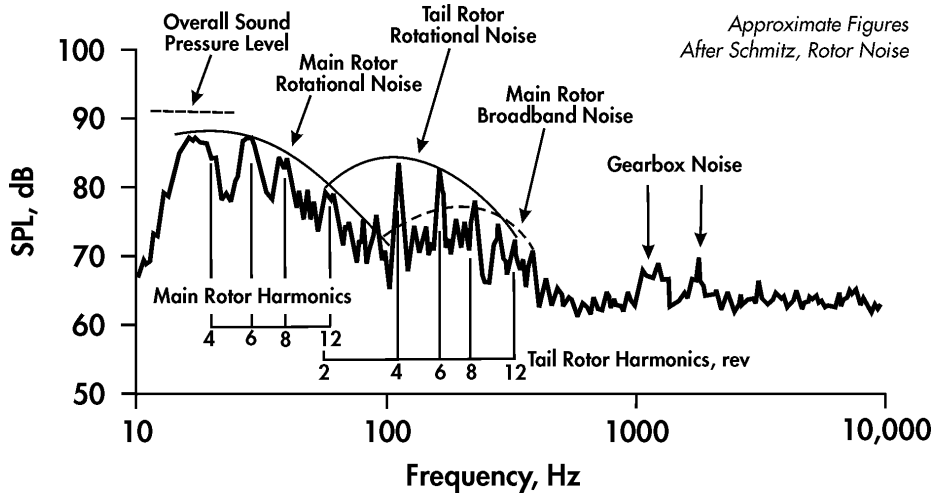

Fig. 3.1. External noise spectrum of UH-1A [98].

The main rotor rotational noise can be broadly divided into in-plane and out-of-plane noise. These two noise planes are further divided into its various sources, shown earlier in Fig. 1.6

In-plane noise is the noise in the plane of the rotor and it is the focus of this

dissertation. It consists of three main components, namely thickness, loading, and HSI noise. The relative contribution of each in-plane noise component is dependent on the advancing tip Mach number, M_{AT} [99].

Thickness Noise The thickness or monopole noise is generated by the displacement of surrounding fluid by the rotating blade [23]. The governing parameters are the blade thickness distribution and the advancing tip Mach number, M_{AT}. A symmetrical negative pulse shape is characteristic of this noise source. Thickness noise is the dominant contributor to the in-plane noise, when compared to the loading noise, particularly at high speed [98]. This is due to the fact that the thickness noise contribution is amplified by the Doppler factor terms which are raised to the second or third power ($\frac{1}{(1-M_r)^2}$ or $\frac{1}{(1-M_r)^3}$). This amplification is evident at high speeds when M_r approaches unity.

In-plane Loading Noise The loading or dipole noise is generated due to the force exerted by the moving blade surface on the surrounding fluid. The in-plane component of the force, which is largely due to airfoil drag, is the major contributor to in-plane noise. The low frequency noise in forward flight is governed by the low frequency air loads on the rotor. There is no characteristic pulse shape associated with this noise source [98]. The shape depends predominantly on the character of the harmonic air loads of the rotor.

High Speed Impulsive Noise The HSI noise is generated by aerodynamic flow nonlinearities, such as transonic flow regions and shocks that appear at the

advancing blade tip at high advance ratios. HSI noise manifests itself as a narrow negative acoustic pulse with impulsive character and high harmonic content, radiating large amounts of in-plane acoustic energy. In the case of $M_{AT} \geq 0.9$, the weak shock front at the tip of the rotor blade radiates to the far-field along a radial direction. This phenomenon is known as delocalization. The HSI noise is the dominant source of in-plane rotor harmonic noise at high speed flight, especially after delocalization [98]. This is an extreme form of thickness noise and is accounted for by the nonlinear quadrupole source term.

Out-of-plane noise consists of two main components, namely BVI and out-of-plane loading noise. Extensive research has been done on the out-of-plane BVI noise. While BVI noise is not the focus of this dissertation, nevertheless, it is used in the parametric study in Section 5.1, as well as the code verification in Section 5.3.

Out-of-plane Loading Noise The out-of-plane force component acting on the rotor, which is largely due to airfoil lift, contributes to the out-of-plane loading noise. The origin and characteristics of this noise source are the same as in-plane loading noise.

Blade Vortex Interaction Noise BVI noise is a specific type of loading noise. It is a source of high frequency unsteady periodic loading noise and is one of the most widely studied sources of rotor noise. This noise is due to impulsive aerodynamic events that occur when tip vortices from preceding blades interact with the subsequent blades, resulting in unsteady pressure fluctua-

tions on the rotor blade. The strength of each BVI event is governed by the local tip vortex strength, tip vortex core size, local interaction angle between the blade and the vortex line, and the vertical separation between the vortex and the blade. The BVI noise contains many harmonics of noise, and is typically represented by including the 6th - 40th harmonic of the Blade Passage Frequency (BPF). It is considered to be the major source of annoyance caused by rotorcraft operations.

3.2 Governing Equations

Rotor noise is most efficiently predicted using integral methods that separate the computation of the noise source and its propagation. This is particularly true for far-field noise calculation. If finite difference CFD methods are used for far-field noise prediction, the large computational domain increases the computational resource requirements dramatically. The two most commonly used integral methods are the FW-H Equation method and the Kirchoff method. The Kirchoff method has been shown to be inaccurate for aeroacoustic problems with moving blade surfaces and therefore the FW-H method is used in this study [11].

3.2.1 Ffowcs William-Hawkings (FW-H) Equation

The Ffowcs Williams-Hawkings [31] equation, Eqn. (3.1a), is used for aeroacoustic predictions in this study. This is an exact reformulation of the Navier Stokes equation using generalized functions and it expresses the noise propagated to an

observer point in terms of a distribution of monopole and dipole sources over a control surface and a distribution of quadrupole sources over the volume outside the control surface. This is shown in Fig. 3.2.

$$\begin{aligned} \Box^2 p'(\vec{x},t) &= \frac{\partial}{\partial t}[\rho_0 U_n \delta(f)] - \frac{\partial}{\partial x_i}[L_i \delta(f)] \\ &+ \frac{\partial^2}{\partial x_i \partial x_j}[T_{ij} H(f)], \end{aligned} \tag{3.1a}$$

where $\Box^2$ is the d' Alembertian or wave operator, $\Box^2 = \frac{1}{a_0^2}\frac{\partial^2}{\partial t^2} - \nabla^2$, U_n is a redefined "velocity" vector normal to the integration surface defined by $f = 0$,

$$U_n = \left(1 - \frac{\rho}{\rho_0}\right) v_n + \frac{\rho u_n}{\rho_0}, \tag{3.1b}$$

u_n is the velocity vector of the fluid normal to the surface, and v_n is the normal velocity of the surface.

L_i are the components of the redefined "loading" vector on the surface,

$$L_i = p\delta_{ij} n_j + \rho u_i (u_n - v_n), \tag{3.1c}$$

p is the local gage pressure relative to the atmospheric pressure, δ_{ij} is the Kronecker delta, and n_j is a component of the unit outward normal to the integration surface. T_{ij} is the Lighthill stress tensor, and $\delta(f)$ and $H(f)$ are the Dirac delta and Heaviside functions, respectively.

The first two terms on the right side of Eqn. (3.1a), namely the monopole and

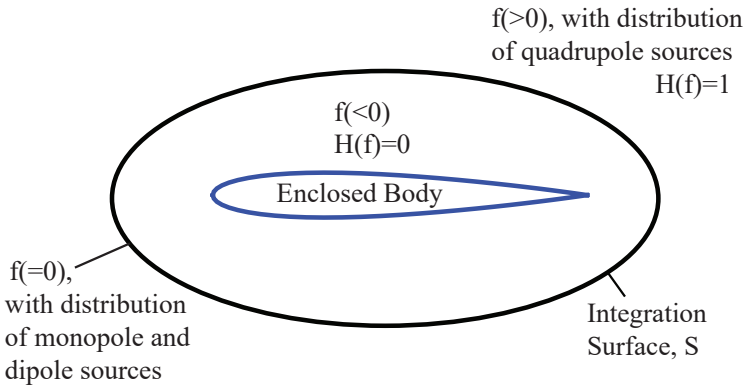

Fig. 3.2. Control surface.

dipole terms are surface source terms considered only on the integration surface, $f(0)$, as indicated by the Dirac delta function $\delta(f)$. These can be solved analytically as described in Section 3.2.2. The third (or quadrupole) term is a volume source term that acts throughout the volume that is exterior to the data surface, as indicated by the Heaviside function, $H(f)$. The quadrupole source term models the nonlinearities due to fluid velocity in the volume surrounding the integration surface and is required for accurate prediction of HSI noise. However, it has often been neglected for subsonic applications because of the high computational costs associated with determining the flow field with sufficient accuracy and the volume integration required in the acoustic analysis.

3.2.2 Farrasat's Formulation 1 and 1A

There are several approaches to solving the FW-H equation, Eqn. (3.1a), as discussed in Ref. 27. However, the most widely implemented approach for rotorcraft aeroacoustic prediction is that developed by Farassat, known as Formulation 1 and

1A [28]. It is the reformulation of the FW-H equation accounting only for surface sources, when the surface moves at subsonic speed.

In this formulation, the integration surface, $f(0)$, is first assumed to be the blade surface which is an *impermeable* surface. Under this assumption, $u_n = v_n$, and Eqns. (3.1b) and (3.1c) reduce to $U_n = u_n$ and $L_i = pn_i$, respectively. For the purpose of this study, we are concerned with rotor surfaces at subsonic speed with minimal contribution from the quadrupole sources, therefore the FW-H equation, Eqn.(3.1a) reduces to,

$$\Box^2 p' = \Box^2 p'_T + \Box^2 p'_L \tag{3.2a}$$

where

$$\Box^2 p'_T = \frac{\partial}{\partial t}[\rho_0 v_n \delta(f)] \tag{3.2b}$$

$$\Box^2 p'_L = -\frac{\partial}{\partial x_i}[p n_i \delta(f)] \tag{3.2c}$$

The thickness noise, Eqn.(3.2b), from the monopole source term is caused by the displacement of the fluid by the moving blade. The loading noise, Eqn.(3.2c), from the dipole source term is caused by the unsteadiness in the load that the blade surface exerts on the surrounding fluid. Note that the use of the terminology thickness and loading noise source is only appropriate if the control surface corresponds to a solid (impermeable) surface.

To derive Formulation 1, the general solution to an arbitrary wave equation is

used. This general solution to the arbitrary wave equation,

$$\Box^2 p' = Q(\vec{x}, t)\delta(f), \tag{3.3}$$

using the free space Green's function, $\delta(g)/4\pi r$, where $g = \tau - t + |\vec{x} - \vec{y}|/a_0$, is given as,

$$p'(x,t) = \frac{1}{4\pi} \int_{-\infty}^{t} \int_{-\infty}^{\infty} \left[\frac{Q(\vec{y}, \tau)\delta(f)\delta(g)}{r} \right] d^3 y d\tau. \tag{3.4}$$

Using the variable transformation $d^3 y d\tau = \frac{dy_1 dy_2 df dg}{|\partial f/\partial y_3|(1-M_r)} = \frac{dS df dg}{(1-M_r)}$, the generic retarded time integral formulation is obtained,

$$p'(x,t) = \frac{1}{4\pi} \int_{f=0} \left[\frac{Q(y,\tau)}{r(1-M_r)} \right]_{ret} dS. \tag{3.5}$$

Further, given the identity

$$\frac{\partial}{\partial x_i} \left(\frac{\delta(g)}{r} \right) = -\frac{1}{a_0} \frac{\partial}{\partial t} \left(\frac{\hat{r}_i \delta(g)}{r} \right) - \frac{\hat{r}_i \delta(g)}{r^2}, \tag{3.6}$$

Formulation 1 is the solution to the FW-H equation, Eqn. (3.2a), based on the general solution, Eqn. (3.5), and algebraic manipulations with the identity, Eqn. (3.6), resulting in:

$$p'(\vec{x}, t) = p'_T(\vec{x}, t) + p'_L(\vec{x}, t) \tag{3.7a}$$

where

$$p'_T(\vec{x},t) = \frac{1}{4\pi}\frac{\partial}{\partial t}\int\limits_{f=0}\left[\frac{\rho_0 v_n}{r(1-M_r)}\right]_{\text{ret}} dS, \tag{3.7b}$$

$$p'_L(\vec{x},t) = \frac{1}{4\pi a_0}\frac{\partial}{\partial t}\int\limits_{f=0}\left[\frac{p n_i \hat{r}_i}{r(1-M_r)}\right]_{\text{ret}} dS + \frac{1}{4\pi}\int\limits_{f=0}\left[\frac{p n_i \hat{r}_i}{r^2(1-M_r)}\right]_{\text{ret}} dS. \tag{3.7c}$$

To improve the speed and accuracy of the solution, mathematical manipulations are performed to move the time derivative inside the first integral of Eqns.(3.7b) and (3.7c) by using the following relation,

$$\frac{\partial}{\partial t}[q(\vec{x},\vec{y},\tau)]_{ret} = \left[\frac{1}{1-M_r}\frac{\partial q(\vec{x},\vec{y},\tau)}{\partial \tau}\right]_{\text{ret}}. \tag{3.8}$$

This results in Formulation 1A,

$$p'_T(\vec{x},t) = \frac{1}{4\pi}\int\limits_{f=0}\left[\frac{\rho_0 \dot{v}_n}{r\cdot(1-M_r)^2}\right]_{\text{ret}} dS + \frac{1}{4\pi}\int\limits_{f=0}\left[\frac{\rho_0 v_n(r\dot{M}_r + a_0(M_r - M^2))}{r^2\cdot(1-M_r)^3}\right]_{\text{ret}} dS \tag{3.9a}$$

$$p'_L(\vec{x},t) = \frac{1}{4\pi a_0}\int_{f=0}\left[\frac{\dot{p}n_i\hat{r}_i}{r(1-M_r)^2}\right]_{\text{ret}} dS \tag{3.9b}$$
$$+\frac{1}{4\pi}\int_{f=0}\left[\frac{p(n_i\hat{r}_i - M_i n_i)}{r^2(1-M_r)^2}\right]_{\text{ret}} dS$$
$$+\frac{1}{4\pi a_0}\int_{f=0}\left[pn_i\hat{r}_i\frac{r\dot{M}_r + a_0(M_r - M^2)}{r^2(1-M_r)^3}\right]_{\text{ret}} dS$$

3.3 Modified WOPWOP

Accurate aerodynamic loads and a high fidelity aeroelastic analysis are prerequisites for reliable noise computations. In this study, the loading and blade kinematic information required by the aeroacoustic solver is obtained from AVINOR, a comprehensive rotorcraft aeroelastic analysis code described earlier in Chapter II. The nonlinear CFD+RFA aerodynamic model used in AVINOR [61] has been shown to be accurate, efficient and suitable for aeroacoustic calculations [82]. A modified version of the WOPWOP code [12] was first incorporated into the AVINOR code by Patt, Liu and Friedmann [87, 88] for BVI predictions.

WOPWOP employs a *retarded time* algorithm, based on the numerical implementation approach in Ref. 10. In this approach, the solution procedure starts with a choice of the observer time, t, at which the solution is desired. To determine each source point location associated with the chosen observer time, the blade is iteratively repositioned through a series of coordinate transformation, while satisfying the retarded time equation, $\tau = t - |\vec{x} - \vec{y}(\tau)|/a_0$. The loading data is also interpolated, to determine the associated loads data, when the source is emitted. Figure 3.3 shows a schematic of the retarded time algorithm implemented in

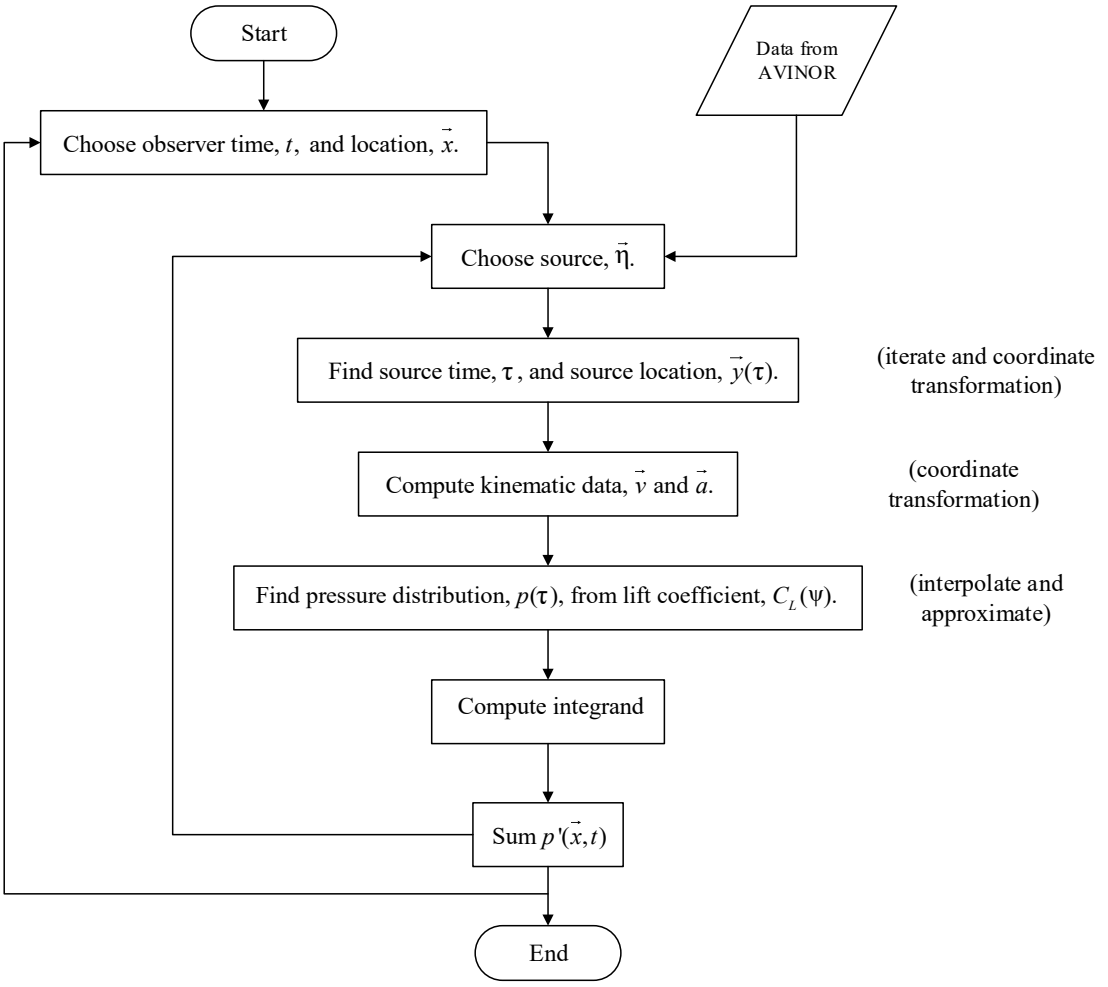

Fig. 3.3. Schematic of the WOPWOP algorithm (Adapted from Ref. 10).

WOPWOP. Note that the coordinate transformations are involved not only in the computation of the blade position, but also in the calculation of the source point velocity and acceleration as well. The iterations, coordinate transformation, and interpolation for each source point contributing to the chosen observer time adds to the computational costs.

The integrand in Fig. 3.3 is based on the Farassat's Formulation 1A of the FW-H equation with the quadrupole term neglected, Eqns.(3.9a), (3.9b). The acoustic computations require chordwise pressure distribution, p, on the blade surface.

Generating CFD based pressure distributions is computationally expensive. To reduce the cost, the blade pressure distribution is obtained using a velocity superposition method based on the potential flow theory [1,55], given as:

$$\Delta C_p = C_{p,Lower} - C_{p,Upper} \tag{3.10a}$$

where

$$C_{p,Upper} = 1 - (\frac{v_t}{V_\infty} + \frac{v_c}{V_\infty} + \frac{v_a}{V_\infty} C_L(\psi))^2 \tag{3.10b}$$

$$C_{p,Lower} = 1 - (\frac{v_t}{V_\infty} - \frac{v_c}{V_\infty} - \frac{v_a}{V_\infty} C_L(\psi))^2 \tag{3.10c}$$

The velocity ratios, $\frac{v_t}{V_\infty}$, $\frac{v_c}{V_\infty}$ and $\frac{v_a}{V_\infty}$ represent the contributions due to the airfoil thickness, camber and angle of attack respectively. For the symmetric NACA 0012 airfoil used in the study, $\frac{v_c}{V_\infty} = 0$. The other two velocity ratio values, $\frac{v_t}{V_\infty}$ and $\frac{v_a}{V_\infty}$, can be obtained from the tables in Ref. 1. Further modifications were made to the WOPWOP code and incorporated into the AVINOR code by Patt, Liu and Friedmann [87,88] for BVI predictions. The modifications to the code account for flexible blade model with coupled flap, lag and torsional dynamics. This model is an acceptable approximation for BVI noise prediction because the lift coefficients from which the pressure distributions are obtained, are based on the CFD model that accounts for compressibility, viscosity, and unsteady effects and that lift is the

main contributor to the out-of-plane BVI noise. Therefore, the AVINOR /WOP-WOP code is used for the out-of-plane BVI noise prediction at low speed descending flight in the initial parametric study in Section 5.1 and verification studies in Section 5.3.

However, this approach is not suitable at higher advance ratios, as the velocity superposition method is accurate only at low freestream velocities [55]. It is also computationally intensive to compute the loading noise contribution from the pressure distribution due to the *retarded time* algorithm implementation approach, and the chordwise discretization of the panel. Another limitation of the WOPWOP code is its incomplete treatment of in-plane aerodynamic loads that have a major role for in-plane noise calculations.

3.4 HELIcopter NOise Reduction (HELINOIR)

To overcome the limitations of the AVINOR/WOPWOP code for in-plane noise prediction and control, a new aeroacoustic solver, named HELINOIR (HELIcopter NOise Reduction), developed by Duraisamy et al is used (Ref. 48–50, 111). Similar to WOPWOP, the aeroacoustic computations in HELINOIR are based on the solution of the Ffowcs-Williams and Hawkings equations (Ref. 31) , using the Farassat 1A formulation (Ref. 29, 30). Only monopole and dipole sources of noise are considered, corresponding to the thickness and loading noise, respectively. Quadrupole, or volume noise sources that arise due to phenomena such as shock-waves and separated flows, are neglected. For the problems of interest in this

work, it is reasonable to expect that quadrupole noise sources are relatively unimportant compared to the loading and thickness noise sources.

It is a *source time dominant* algorithm, unlike WOPWOP which is a *retarded time* algorithm [11, 12]. In this approach, the retarded time integral is evaluated by regarding the source time as the primary or dominant time. A source time-location is first chosen from the input data to determine the observer time, t, when the signal will reach an observer. For a moving observer, this is determined analytically by solving the equation $t - \tau - |\vec{x} - \vec{y}_j|/a_0 = 0$, where the subscript j is an index to the jth source panel. A sequence of prescribed, equally spaced, source times contribute to a sequence of *unequally* spaced observer times. Interpolation in time is necessary so that the contributions from all source panels can be added together at the same observer time. HELINOIR uses a chordwise compact loading model of the airfoil so that the loading data from the aeroelastic analysis, arising from both lift and drag, can be used directly without the pressure distribution approximation in Eqns. (3.10a-3.10c). Figure 3.4 shows a schematic of the source time dominant algorithm implemented in HELINOIR.

In HELINOIR, the Farassat 1A formulation for the acoustic pressure from thickness (p_T) and loading (p_L) noise sources at an observer locations $\vec{x}$ and time t is represented by the following:

$$\begin{aligned} p_T(\vec{x},t) &= \frac{1}{4\pi}\sum_j \left[\frac{\rho_o \dot{v}_n}{r(1-M_r)^2}\right]_{ret,j} \Delta S_j + \\ &\quad \frac{1}{4\pi}\sum_j \left[\frac{\rho_o v_n (r\dot{M}\hat{r}_i + a_o M_r - a_o M^2)}{r^2(1-M_r)^3}\right]_{ret,j} \Delta S_j, \end{aligned} \tag{3.11}$$

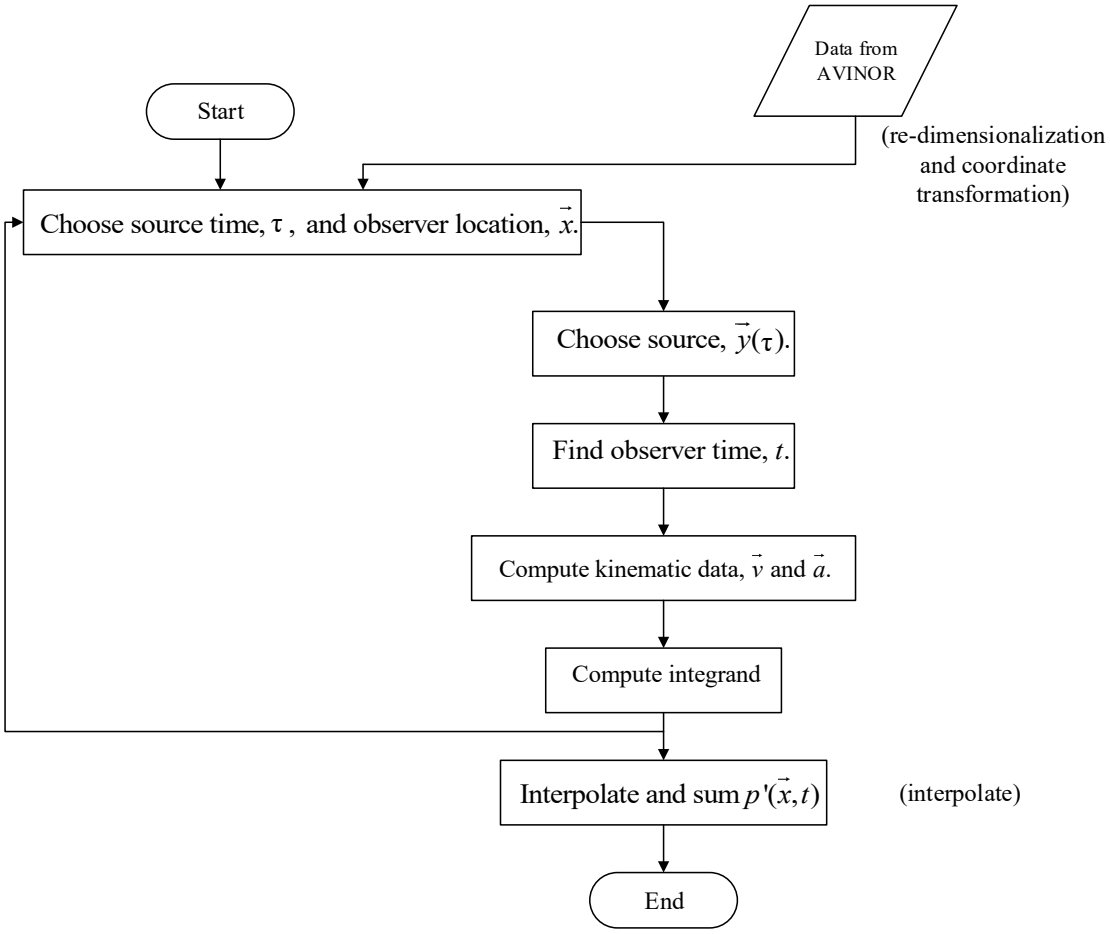

Fig. 3.4. Schematic of the HELINOIR algorithm.

$$
\begin{aligned}
p_L(\vec{x},t) \;=\; & \frac{1}{4\pi a_o}\sum_j \left[\frac{\dot{l}_i \hat{r}_i}{r(1-M_r)^2}\right]_{ret,j} \Delta S_j + \\
& \frac{1}{4\pi}\sum_j \left[\frac{l_i \hat{r}_i - l_i M_i}{r^2(1-M_r)^2}\right]_{ret,j} \Delta S_j + \\
& \frac{1}{4\pi a_o}\sum_j \left[\frac{l_r(r\dot{M}_i \hat{r}_i + a_o M_r - a_o M^2)}{r^2(1-M_r)^3}\right]_{ret,j} \Delta S_j. \qquad (3.12)
\end{aligned}
$$

The blade is discretized into a number of flat panels of surface area ΔS_j and the contribution of each panel j to the noise is recorded in retarded time (subscript ret) and interpolated to the desired observer time.

In Eqns. (3.11) and (3.12), ρ_o, a_o represent the ambient density and speed of sound, respectively. v_n is the velocity of the quarter-chord point of the panel, projected in a direction normal to the airfoil camber. l_i is the sectional load in the i direction, M_i is the Mach number of the source in the i direction, r is the distance from the source to the observer and $\hat{r} = r/|r|$. $\dot{(\cdot)}$ denotes the rate of change of the quantity $(\cdot)$ with respect to source time. The subscript $(\cdot)_r$ or $(\cdot)_n$ indicate a dot product of the vector quantity $(\cdot)$ with the unit vector in the radiation direction, $\hat{r}$, or outward surface normal direction, $\hat{n}$, respectively.

As conceptualized by Schmitz (Ref. 97), the forward section of an airfoil displaces fluid outwards and acts as a pressure source, while the aft part of the aerofoil acts as a pressure sink; this is illustrated in Fig. 3.5. The strength of the source is equal to the mass flux of fluid being displaced by the blade section as it moves through space. For the single source shown in Fig. 3.5, the mass flux is equal to $\rho_0 v_n$ and is positive for the leading edge of the blade section. The sink is the negative source and represents the mass flux of the fluid, that is required for representing

the trailing edge of the rotor blade section. In this work, the mass displacement is represented by a single source at $x/c = 1/8$ and a single sink at $x/c = 5/8$ for each airfoil section. The sectional loads are assumed to be point forces collocated at $x/c = 1/4$.

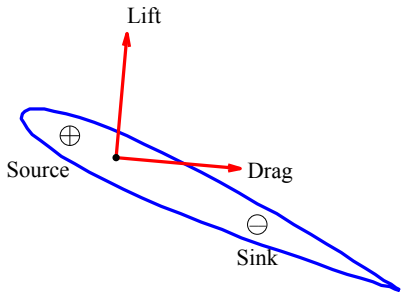

Fig. 3.5. Source/sink representation for thickness noise generation.

This compact acoustic model is a reasonable approximation for far-field noise calculations because the distance of the observer from the noise source, is typically larger by more than an order of magnitude than the blade chord. Extensive validation studies of thickness and loading noise signatures (Ref. 48–50, 111) have been performed with this model. To further demonstrate and verify the accuracy of this formulation, the compact chord model presented above is compared to a version that uses the full blade pressure distributions and geometry obtained from the SUmB/CDP CFD Code (Ref. 43). The configuration chosen is the UH-60 rotor in high-speed forward flight (Ref. 63) (advance ratio $\mu = 0.3$, $M_{tip} = 0.63$). Figure 3.6 shows a sample solution where the observer is located three rotor radii in front of the rotor plane, confirming the good agreement between the compact loading and full geometry models.

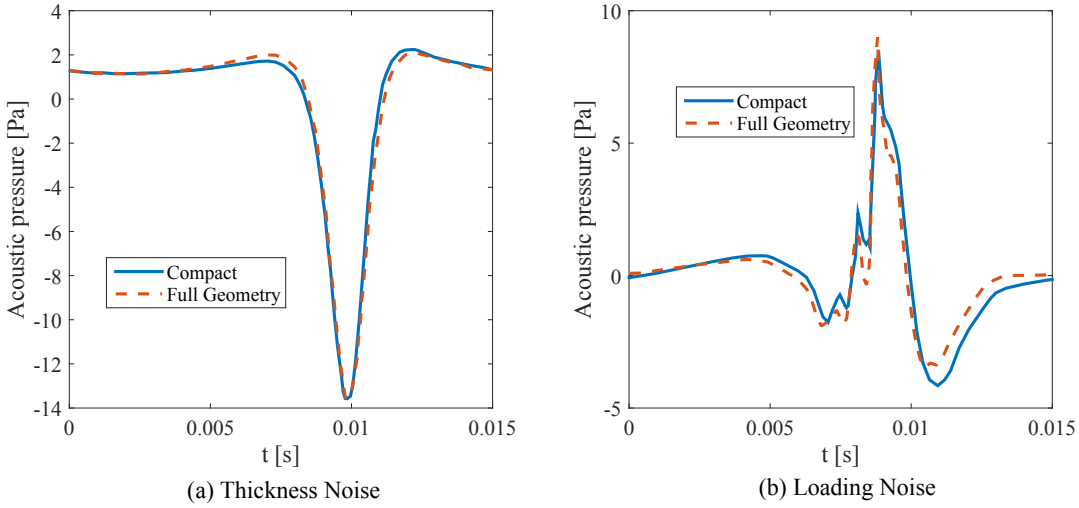

Fig. 3.6. Verification of the compact model acoustic pressure predictions for a UH-60 rotor at μ=0.30, M_{tip}=0.63, at an observer located 3R in front of the rotor plane.

The advantages of HELINOIR for the in-plane noise study are summarized next:

1. It is computationally less expensive since it is a compact model. The coordinate transformations are performed only once for each source time, τ, since the transformation matrices are the same for each source point input data.

2. Input data need not be interpolated and the data from the CFD ROM can be used directly.

3. The drag data from the CFD ROM is utilized for in-plane loading noise predictions to improve accuracy.

4. The solution process is parallel and the algorithm can be parallelized.

CHAPTER IV

THE AEROELASTIC-AEROACOUSTIC FRAMEWORK

The aeroelastic simulation code, AVINOR, was coupled with the modified version of WOPWOP [12, 87]. However, limitations associated with the code restrict its applicability to in-plane noise prediction, as discussed in Section 3.3. Therefore, a new aeroelastic-aeroacoustic framework was developed by coupling the AVINOR code with the new aeroacoustic solver, HELINOIR. The framework, its implementation, and required code modifications are described in this Chapter.

4.1 Data Flow

Figure 4.1 shows the data flow between the AVINOR and HELINOIR codes for the case of active on-blade control and is an extension of the schematic in Fig. 3.4. A set of coupled trim/aeroelastic equations is solved in AVINOR to determine the blade aeroelastic response and unsteady aerodynamic loading at each blade panel and time step. This time domain data is the input for the acoustic source

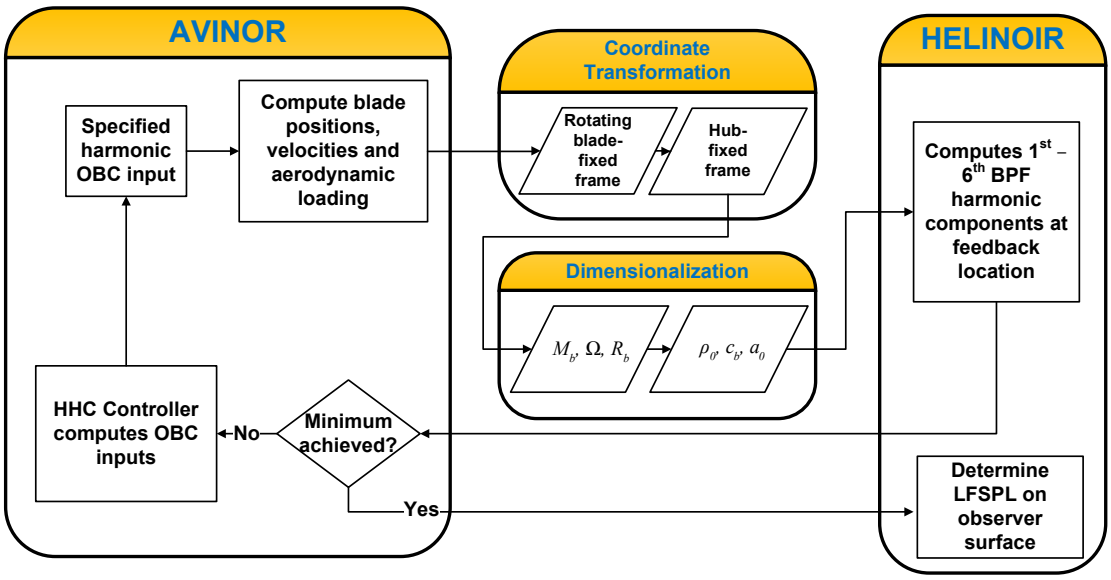

Fig. 4.1. Data flowchart between AVINOR and HELINOIR for active control.

computations in HELINOIR. To ensure data consistency between AVINOR and HELINOIR, a series of coordinate transformations and re-dimensionalization is performed, that are described in Section 4.2.

The HELINOIR code computes the acoustic pressure, using the blade loads and kinematic data obtained from AVINOR, as a post processing step after the aeroelastic analysis. For the noise control loop, the observer location corresponds to the feedback microphone position. The observer time is determined for each panel source by solving the quadratic equation $t - \tau - |\vec{x} - \vec{y}(\tau)|/a_0 = 0$, which relates the propagation distance, $|\vec{x} - \vec{y}|$, and the propagation time, $t - \tau$. The pressure contribution of the loading and thickness source terms from each panel, at the observer location and time are computed. The acoustic pressure contribution from a single blade at the observer location is obtained by summing up the acoustic pressure contribution from all the panels. To reduce computational costs, the total

acoustic pressure contribution from each of the N_b blades is obtained by summing the phase shifted acoustic pressure contribution from each blade.

After the acoustic pressure time history at the feedback location has been computed, the harmonic components of the 1st - 6th BPF are calculated using a conventional Fourier analysis. The BPF harmonic components are sent back to the Higher Harmonic Controller (HHC). The HHC computes the OBC inputs that minimize a quadratic cost function, Eqn. (2.7), based on the feedback microphone noise levels and control input magnitudes. This procedure is repeated until a control input that minimizes the quadratic cost function is achieved. The sound pressure levels on the observer surface are then evaluated using the fully converged, trim aeroelastic solution with this control input. For passive control, a similar framework is used except that the feedback loop with the HHC is absent.

4.2 Computational Implementation

The data in AVINOR and HELINOIR are represented using different coordinate systems, time steps, and are non-dimensionalized using different physical quantities. To achieve compatibility between the two codes, the following modifications were made.

4.2.1 Coordinate System

A blade fixed coordinate system is used to define the deformed blade position and loading data in AVINOR. On the other hand, HELINOIR uses a hub fixed

frame. A series of seven coordinate transformations are performed to transform the blade loading and position vectors from the rotating blade frame to the hub frame. Five of these eight coordinate systems, namely the “1 System", “2 System", “3 System", “4 System" and the “5 System", are described in Appendix A. Three coordinate systems were introduced into the current framework to ensure data consistency between AVINOR and HELINOIR.

“4B" System. This is the blade attached, rotating, deformed reference frame with the y_{4B} axis aligned with the airfoil chord line. The principal axes of the blade cross section lie in the $y_{4B}z_{4B}$ plane. The x_4 axis is coincident with both the x_{4A} and x_{4B} axis. This is the starting point for the basis transformation of the blade aeroelastic response data data from AVINOR.

“4A" System. This is the blade attached, rotating, deformed reference frame with the twist angle, $\theta_{tw}(x)$, removed. The principal axes of the blade cross section lie in the $y_{4A}z_{4A}$ plane, rotated by the input pitch control angle, $\theta_{PC}(\psi)$, about the x_4 axis. The x_4 axis is coincident with the x_{4A} axis. The relationship between the “4B”, “4A”, and “4” systems is depicted in Fig. 4.2.

“1A" System. This is the hub fixed non-rotating reference frame used in HELINOIR. Unlike AVINOR, $-y_{1A}$ is the forward flight direction and x_{1A} is coincident with the left side of the rotor. See Figure 4.3.

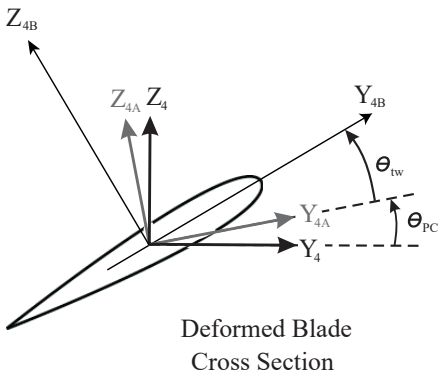

Fig. 4.2. The transformation from the “4B", “4A", to the “4" system.

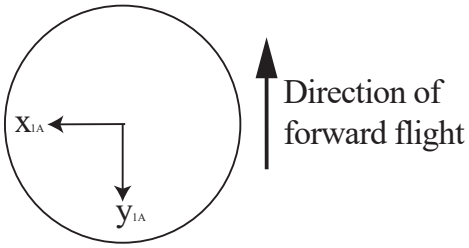

Fig. 4.3. “1A" System.

4.2.1.1 Transformation Matrices

The following coordinate transformation matrices were introduced to change the representation of the deformed blade position and loading in AVINOR to that required in HELINOIR are as follows.

“4B" system to “4A" system

$$\begin{Bmatrix} \hat{e}_{x4A} \\ \hat{e}_{y4A} \\ \hat{e}_{z4A} \end{Bmatrix} = \begin{bmatrix} 1 & 0 & 0 \\ 0 & \cos\theta_{tw} & -\sin\theta_{tw} \\ 0 & \sin\theta_{tw} & \cos\theta_{tw} \end{bmatrix} \begin{Bmatrix} \hat{e}_{x4B} \\ \hat{e}_{y4B} \\ \hat{e}_{z4B} \end{Bmatrix}$$

$$\hat{e}_{4A} = T_{4A4B}\hat{e}_{4B} \tag{4.1}$$

“4A" system to “4" system

$$\begin{Bmatrix} \hat{e}_{x4} \\ \hat{e}_{y4} \\ \hat{e}_{z4} \end{Bmatrix} = \begin{bmatrix} 1 & 0 & 0 \\ 0 & \cos\theta_{PC} & -\sin\theta_{PC} \\ 0 & \sin\theta_{PC} & \cos\theta_{PC} \end{bmatrix} \begin{Bmatrix} \hat{e}_{x4A} \\ \hat{e}_{y4A} \\ \hat{e}_{z4A} \end{Bmatrix}$$
$$\hat{e}_4 = T_{44A}\hat{e}_{4A} \tag{4.2}$$

“1" system to “1A" system

$$\begin{Bmatrix} \hat{e}_{x1A} \\ \hat{e}_{y1A} \\ \hat{e}_{z1A} \end{Bmatrix} = \begin{bmatrix} 0 & -1 & 0 \\ 1 & 0 & 0 \\ 0 & 0 & 1 \end{bmatrix} \begin{Bmatrix} \hat{e}_{x1} \\ \hat{e}_{y1} \\ \hat{e}_{z1} \end{Bmatrix}$$
$$\hat{e}_{1A} = T_{1A1}\hat{e}_1 \tag{4.3}$$

4.2.1.2 Coordinate Transformation for Deformed Blade Position

The data from AVINOR is in the “4B" system. Assuming that the feathering axis is at the quater chord position, the representation of the location of the thickness source term at the $\frac{1}{8}$ chord position in the “4B" system is expressed by Eqn. (4.4).

$$\mathbf{r}_{4B} = \begin{bmatrix} 0 \\ \frac{c}{8} \\ 0 \end{bmatrix} \tag{4.4}$$

The following coordinate transformations are performed to represent the deformed blade position in the non rotating, hub fixed “1A" system for HELINOIR.

$$\mathbf{r}_3 = T_{34}.T_{44A}.T_{4A4B}\mathbf{r}_{4B} + \begin{Bmatrix} x(\psi) \\ v(x,\psi) \\ w(x,\psi) \end{Bmatrix} \tag{4.5}$$

$$\mathbf{r}_{1A} = T_{1A1}.T_{12}.T_{23}\mathbf{r}_3 \tag{4.6}$$

where T_{34}, T_{23}, T_{12} are the transpose of Eqns. (A.8), (A.6), (A.4) respectively. A similar sequence of transformations is performed to obtain the thickness sink location at $\frac{5}{8}c$ in the “1A" system. Similar transformation is performed for the quater chord location, $\frac{1}{4}c$, which is the point at where the aerodynamic load is assumed to act.

For the Galerkin type FEM, based on the coordinate systems defined in Appendix B, the following coordinate transformations are performed.

$$\mathbf{r}_b = T_{be}.T_{ed}\mathbf{r}_{4B} + T_{be}\begin{Bmatrix} x(\psi) + u(x,\psi) - x_J \\ v(x,\psi) \\ w(x,\psi) \end{Bmatrix} + \begin{Bmatrix} x_J \\ 0 \\ 0 \end{Bmatrix} \tag{4.7}$$

$$\mathbf{r}_{1A} = T_{1A1}.T_{nr}.T_{rb}\mathbf{r}_b \tag{4.8}$$

where , $x_J = 0.9R$ is the radial position of the junction between the straight segment and the tip sweep, T_{be}, T_{ed} and T_{rb} are the transposes of Eqns. (B.5), (B.14), (B.4)

respectively, and $T_{nr} = T_{21}$.

4.2.1.3 Coordinate Transformation for Blade Loading

The lift force acting on a blade section is perpendicular to the resultant air velocity $\mathbf{V}_A$ [84] as shown in Figure 4.4 .

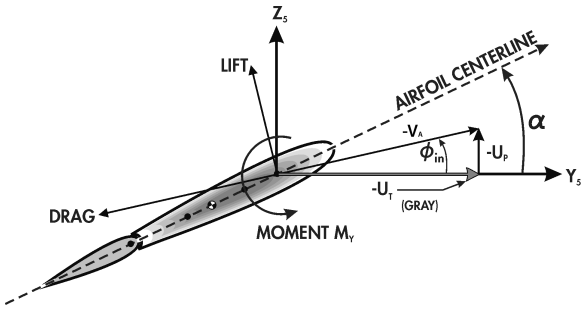

Fig. 4.4. Orientation of tangential and perpendicular air velocities and aerodynamic loads

The radial flow and the forces are assumed to be small and neglected. Therefore the representation of the sectional blade loading in the “5" system at the quater chord position is expressed as Eqn. (4.9).

$$\mathbf{p}_5 = \begin{bmatrix} 0 & 0 & 0 \\ 0 & -\sin\phi_{in} & -\cos\phi_{in} \\ 0 & \cos\phi_{in} & -\sin\phi_{in} \end{bmatrix} \begin{Bmatrix} 0 \\ L(x,\psi) \\ D(x,\psi) \end{Bmatrix} \tag{4.9}$$

where $\phi_{in} = \tan^{-1}\frac{U_p}{U_T}$. The subsequent coordinate transformations to represent the blade loading in the “1A" system is shown in Eqn. (4.10).

$$\mathbf{p}_{1A} = T_{1A1}.T_{12}.T_{23}.T_{35}\mathbf{p}_5 \tag{4.10}$$

where T_{35} is the transpose of Eqn. (A.9).

For the Galerkin type FEM, the coordinate transformation to represent the blade loading in the “1A" system is shown in Eqn. (4.11)

$$\mathbf{p}_{1A} = T_{1A1}.T_{nr}.T_{rb}.T_{be}.T_{ed}.T_{4B4A}.T_{4A4}.T_{45}\mathbf{p}_5 \tag{4.11}$$

where T_{ed}, T_{4B4A}, T_{4A4}, T_{45} are the transposes of Eqns. (B.15), (4.1), (4.2), and (A.10) respectively.

4.2.2 Time Steps

Gaussian quadrature time-steps were used for the time-marching solution of the coupled aeroelastic equations in AVINOR. This is not compatible with HELINOIR, which requires the blade loads and positions at equally spaced time steps. A simple interpolation of the data at equal time step data resulted in inaccurate acoustic predictions, especially on the retreating side. Therefore, the aeroelastic code was modified so that aerodynamic loads and blade positions are computed at equally spaced time steps. This resulted in an accurate acoustic solution, which is validated in Section 5.2.

4.2.3 Inboard Shed Wake Core Radius

The inboard shed wake line is the spanwise component of the inboard vortex sheet, and is parallel to the trailing edge. It is depicted as the dashed arrows in Fig. 4.5. A dimensionless vortex core radius of $\frac{r_c}{R_b}$ =0.4 was used for the validation

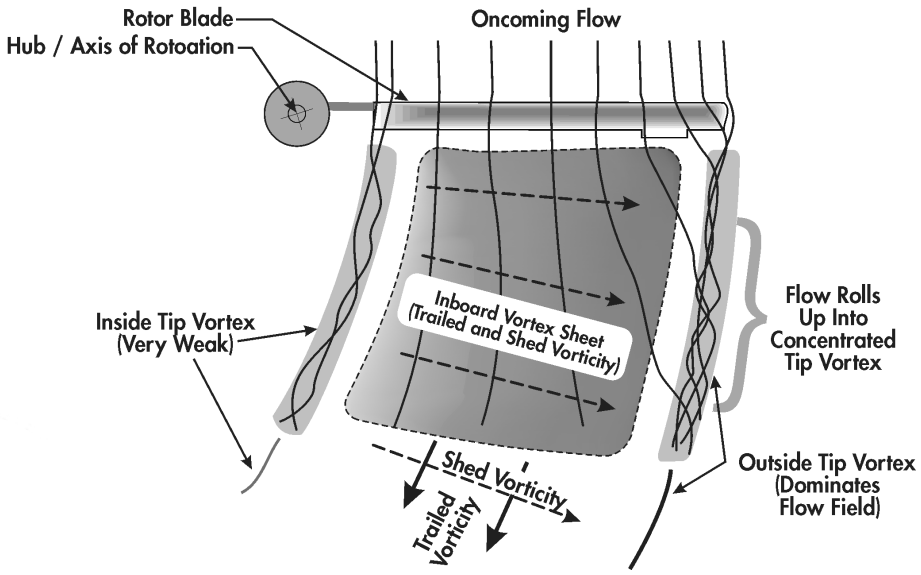

Fig. 4.5. Vortex classification in the rotor flow field [84].

carried out by Padthe et al [82]. Increasing the core size reduces the influence of the inboard shed vortex, and therefore the wake induced velocity at the blade section [46]. The dimensionless vortex core radius was changed to $\frac{r_c}{R_b}$ =0.6 to improve the correlation of the acoustic results using the new AVINOR/HELINOIR code with experimental results.

4.2.4 Dimensional Parameters

The dimensional parameters used in AVINOR and HELINOIR are different. The data in AVINOR is non-dimensionalized using M_b, Ω, and R_b, whereas the data in HELINOIR is non-dimensionalized using ρ_0, a_0, and c_b. Therefore, the non-dimensional data output from AVINOR is dimensionalized by M_b, Ω and/or R_b, and subsequently non-dimensionalized by ρ_0, a_0 and/or c_b before the data is provided as input into HELINOIR.

CHAPTER V

RESULTS

The preceding chapters laid the theoretical foundations for the dissertation and the AVINOR/HELINOIR aerolastic-aeroacoustics framework to be used for in-plane noise prediction at level cruise flight. In this Chapter, the results are presented in four broad sections. First, a parametric study was conducted to determine the optimum stiffness and OBC configuration for active noise and vibration control. Using this configuration, the AVINOR/HELINOIR code was validated against experimental results from two different wind tunnel tests. Subsequently, the active and passive control results from the AVINOR/HELINOIR code are verified against the AVINOR/WOPWOP code. Finally, in-plane noise control using active/passive methods is studied. The resulting effects on the vibratory hub loads and the mid frequency noise levels were also examined.

5.1 Parametric Study of OBC Configuration

The performance of on-blade control devices is linked to blade flapping and torsional stiffness. A parametric study is first conducted to determine the (1) optimal blade torsional stiffness, (2) placement of OBC device (3) type of OBC device and (4) number of OBC devices, that yield the best vibration and noise reduction performance. Two OBC devices, a plain trailing edge flap and a microflap, were considered.

5.1.1 Validation of Microflap CFD Setup

Two different chordwise placements of the microflap, located at 6%c and 10%c from the trailing edge, shown in Fig. 5.5, are studied in the parametric study. The aerodynamic models of these two microflap configurations are first validated [83]. The plain trailing edge flap model was previously validated in Ref. 72. The CFD grids used for the validation are shown in Fig. 5.1. The overall computational domain is shown in Fig. 5.1(a), which contains approximately 90,000 grid points. The CFD grids are generated using the overset approach, which is a convenient method for modeling complex geometries and moving components with large relative motions, Fig. 5.1(b) and 5.1(c). The grids are clustered at the airfoil boundaries such that the dimensionless distance y^+ of the first grid point off the wall is less than 1, and the equations are solved directly to the walls without assuming wall functions [80].

The simulations are carried out at a freestream Mach number , $M_\infty = 0.1$, and

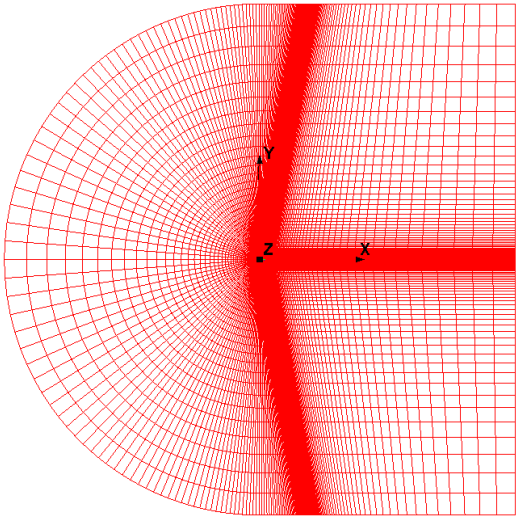

(a) C-grid around airfoil section.

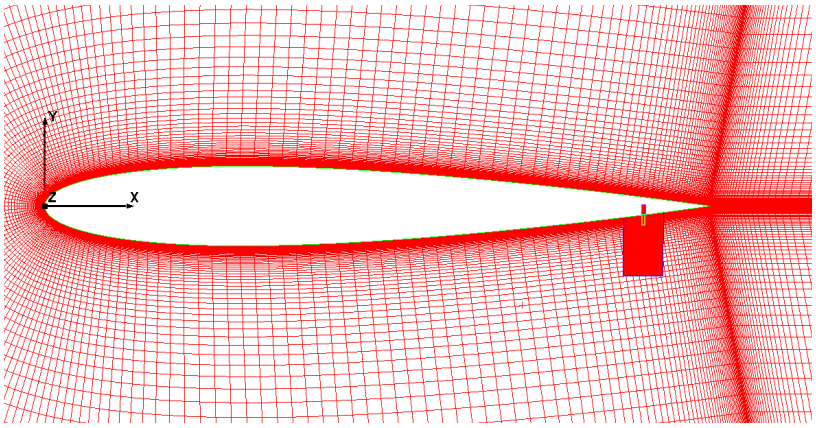

(b) Close-up grid for airfoil section with 10%c microflap.

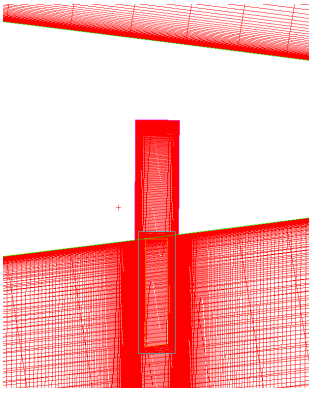

(c) Overset grid showing the trailing-edge of a NACA0012 airfoil with 1.5%c microflap that can slide in and out of the gap located at 10%c from the trailing edge of the airfoil.

Fig. 5.1. Grids used for CFD simulations.

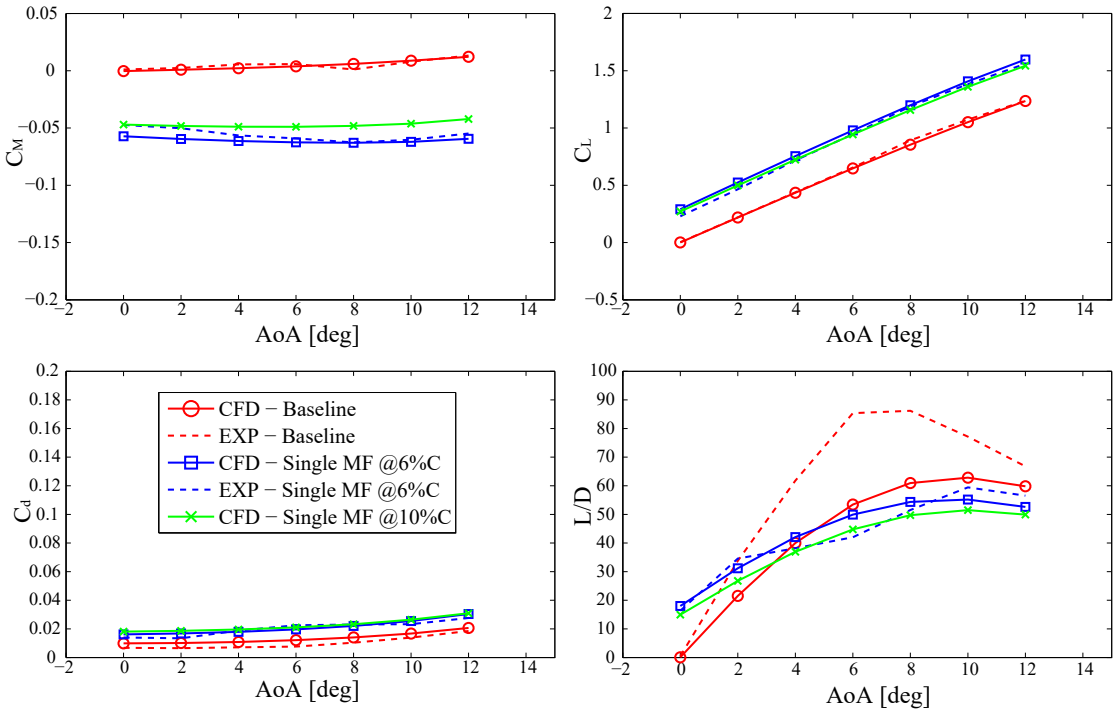

Fig. 5.2. Steady state aerodynamic loads of baseline and microflap airfoils at $M_\infty = 0.1$

at Reynolds number 2.1×10^6 for steady state aerodynamic loads over a range of angles of attack (AoA) for a baseline airfoil as well as airfoils with microflap at $6\%c$ and $10\%c$ from the trailing edge, as shown in Fig. 5.2. The simulation results are compared against experimental results from Ref. [56] for validation. There is good agreement between the CFD and experimental results for both the baseline and 6%c microflap. The CFD results for the airfoil with a microflap at the 10%c location are consistent with the validated 6%c MF case. Note that there is a marginal reduction in the magnitude of the moment and lift coefficient and an increase in the drag coefficient, resulting in a reduction in the lift to drag ratio as the microflap is shifted upstream to the 10%c location.

The CFD simulation was repeated at a higher freestream Mach number, $M_\infty =$

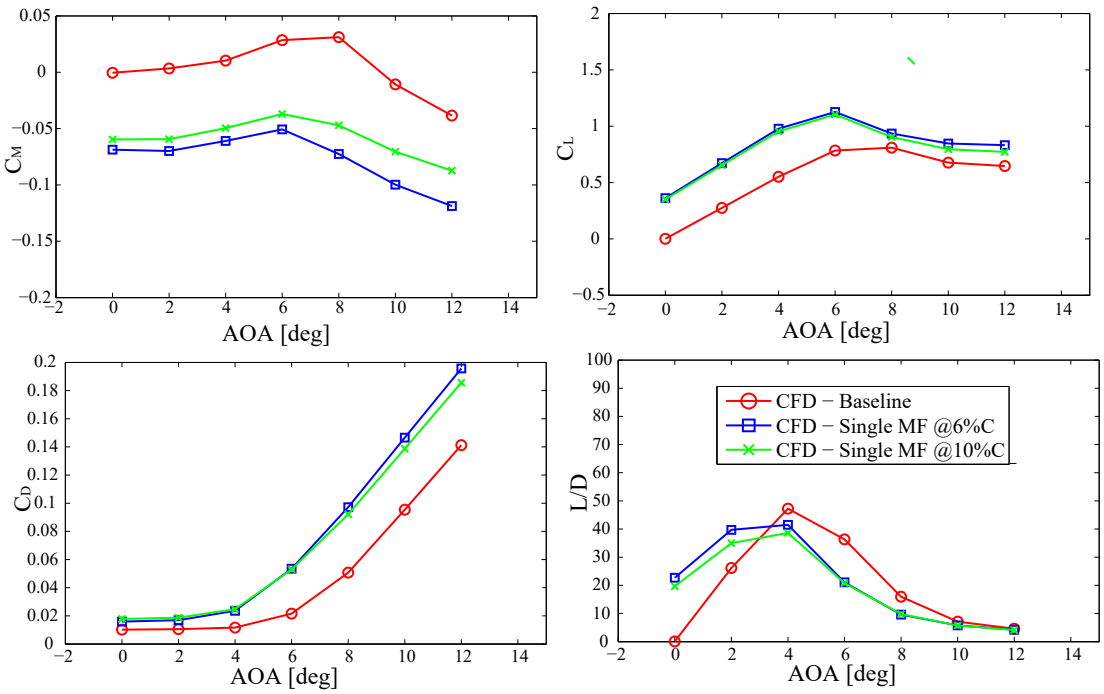

Fig. 5.3. Steady state aerodynamic loads of baseline and microflap airfoils at $M_\infty = 0.6$

0.6, so that the flow condition is more representative of that on an actual blade. As shown in Fig. 5.3, there is a reduction in the lift to drag ratio at the 10%c location compared to the 6%c location, which is similar to the earlier simulations at $M_\infty = 0.1$.

The CFD simulation was also performed for unsteady aerodynamic conditions. Figure 5.4, shows a comparison of the unsteady lift and moment generated by the two microflap configurations at $M_\infty = 0.6$, $\alpha = 0°$, and reduced frequency of microflap oscillation, $k = 0.02$. The difference in the unsteady lift amplitude is small, whereas there is a signficant difference in the the moment. The unsteady moment generated by the microflap at 6%c is 16% larger than that generated by the the microflap at 10%c. This reinforces the observation that the control effectiveness

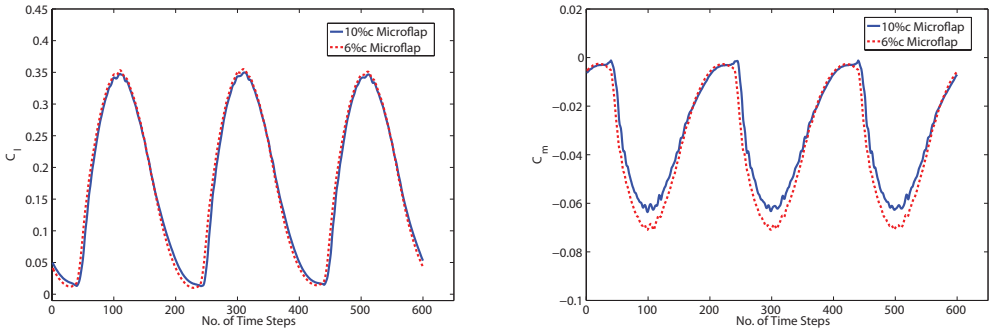

(a) Lift (b) Moment

Fig. 5.4. Comparison of unsteady lift and moment generated by the 6%c and 10%c microflaps at M=0..6, $\alpha = 0°$, and reduced frequency of microflap oscillation $k = 0.02$.

of the microflap is reduced as it is shifted upstream, in both steady and unsteady freestream conditions.

5.1.2 OBC Configuration for Parametric Study

With the microflap model validated, and a better understanding of the sensitivity of the microflap chordwise location on its control effectiveness, a parametric study was performed. The simulation results used in the parametric study are for a helicopter configuration resembling a full-scale 4-bladed MBB BO-105 hingeless rotor at an advance ratio, $\mu = 0.15$ and descent angle of 6.5° representing high BVI conditions. The baseline rotor parameters are provided in Table 5.1. All the values in the table (except C_W, γ, and σ) have been nondimensionalized using M_b, L_b, and $1/\Omega$ for mass, length and time, respectively. The mass and stiffness distributions are assumed to be constant along the span of the blade. The rotor is trimmed using a propulsive trim procedure.

Two OBC devices are considered, the ACF and the microflap. The ACF de-

Table 5.1. Baseline rotor parameters.

Dimensional Rotor Data	
R = 4.91 m	
M_b = 27.35 kg	
Ω = 425 RPM	
Nondimensional Rotor Data	
N_b = 4	L_b = 1.0
c/R = 0.05498	θ_{tw} = -8°
e = 0	
X_A = 0	X_{Ib} = 0
ω_F = 1.124, 3.40, 7.60	ω_L = 0.732, 4.458
ω_T = 3.17, 9.08	
γ = 5.5	σ = 0.07
β_p = 2.5°	
Helicopter Data	
C_W = 0.005	C_{df} = 0.031
X_{FA} = 0.0	Z_{FA} = 0.3
X_{FC} = 0.0	Z_{FC} = 0.3
μ=0.3	M_∞=0.191
M_{tip}=0.637	
Trim Values	
α_R = -5.50°	θ_0=8.76°
θ_{1c}=0.606°	θ_{1s}=-5.08°
θ_{0t}=2.30°	ϕ_R=3.08°

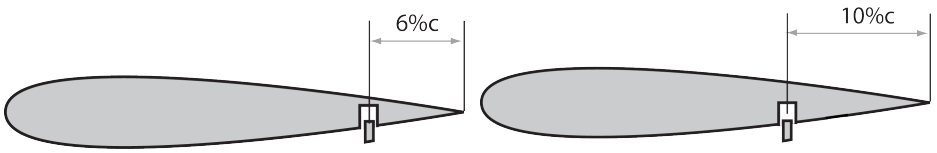

(a) A 1.5%c microflap placed at 6%c from the trailing edge.

(b) A 1.5%c microflap placed at 10%c from the trailing edge.

Fig. 5.5. Microflap placement on airfoil section.

vice is a 20%c conventional plain flap, shown in Fig. 1.4 . The microflap is 1.5%c in height, slides in and out of a cavity near the trailing edge. Two chordwise locations of the microflap are considered, one at 6%c from the sharp trailing edge of the airfoil as shown in Fig. 5.5(a) and the other at 10%c from the trailing edge as shown in Fig. 5.5(b). Two different spanwise flap configurations on the rotor blade are considered for the noise and vibration reduction studies. The first configuration, a single flap configuration, shown in Fig. 5.6(a), consists of a flap with 0.12R spanwise length centered at 0.75R. The second configuration shown in Fig. 5.6(b), is a dual flap configuration, and consists of two flaps each 0.06R in spanwise length. The single and dual microflap configurations are also considered and shown in Fig. 5.7.

The effect of variation in torsional frequency on the vibration and noise reduction effectiveness of single flap and microflap configurations is examined first. The first two torsional frequencies are modified by changing the structural properties. The torsional stiffness, GJ, is uniform over the entire span of the blade and the torsional stiffness values used are provided in Table 5.2. The flap and lead-lag frequencies are kept constant in this procedure. This approach was also used in Ref. 45.

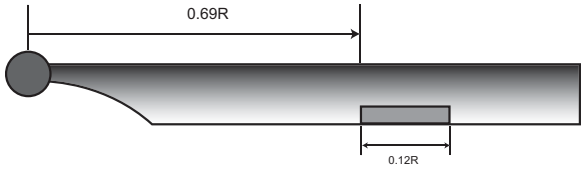

(a) Single flap

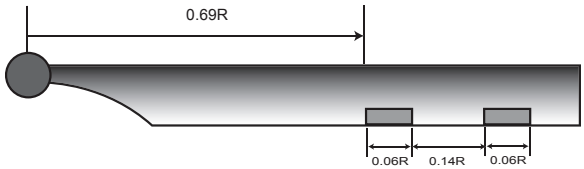

(b) Dual flap

Fig. 5.6. Spanwise configurations of the plain flap on the rotor blade.

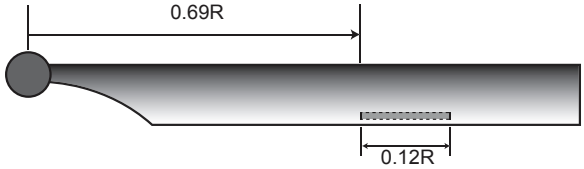

(a) Single microflap

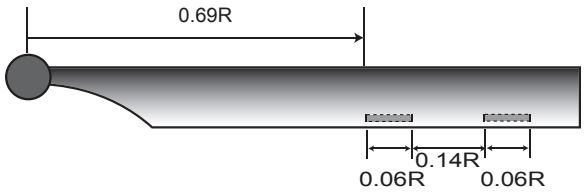

(b) Dual microflap

Fig. 5.7. Spanwise configurations of the microflap on the rotor blade.

Table 5.2. First two torsional frequencies (/rev) and the corresponding nondimensional torsional stiffness.

Case	Frequencies	Stiffness
1	2.50, 6.95	8.50x10^{-4}
2	3.17, 9.08	1.47x10^{-3}
3	4.50,13.20	3.13x10^{-3}
4	6.00, 17.78	5.08x10^{-3}
5	8.00, 23.83	1.02x10^{-2}

The vibratory hub shears and moments are obtained from the integration of the distributed inertial and aerodynamic loads over the entire blade span in the rotating frame. Subsequently, the loads are transformed to the hub-fixed non-rotating system, and the contributions from the individual blades are combined. In this process, the blades are assumed to be identical. Reduction is performed on the N_b/rev components, which are the dominant components, of the hub shears and moments.

The acoustic environment in the vicinity of the helicopter is characterized by the noise decibel levels computed on a carpet plane located 1.15R beneath the rotor, as depicted in Fig. 5.8, where the direction of forward flight is in the negative x direction and the axis of rotor rotation is in the positive z direction following the rotational sense based on the right-hand rule. It was found in Ref. 88 that feedback microphone implemented on the rear right skid works well for BVI noise reduction. Therefore, noise measured by a microphone located at this location is used as the feedback signal to the controller.

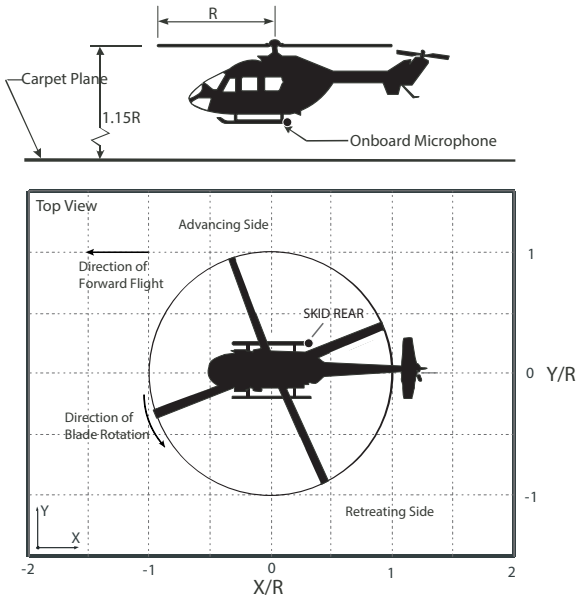

Fig. 5.8. Skid microphone location and carpet plane used for noise simulation.

5.1.3 Vibration Reduction

The baseline 4/rev non-dimensional vibratory hub loads for the various torsional stiffness values are shown in Fig. 5.9. The blade torsional stiffness does not have a significant effect on the baseline vibratory loads.

The controlled non-dimensional vibratory loads for the single flap and the single microflap located at 6%c are shown in Fig. 5.10. The controlled vibratory loads for the dual flap and the dual microflap at 6%c are shown in Fig. 5.11. For the single flap configuration, the lowest vertical hub shear is obtained for a torsional frequency of 4.5/rev, whereas for the dual flap configuration, the lowest vertical hub shear is obtained for a torsional frequency of 3.17/rev. The single flap deflection history for blades of various tosional stiffness values are shown in Fig. 5.12. For a blade with ω_{T1}=2.5/rev, the optimal flap deflection for vibration reduction has a high 3/rev harmonic component. On the other hand, the flap deflections

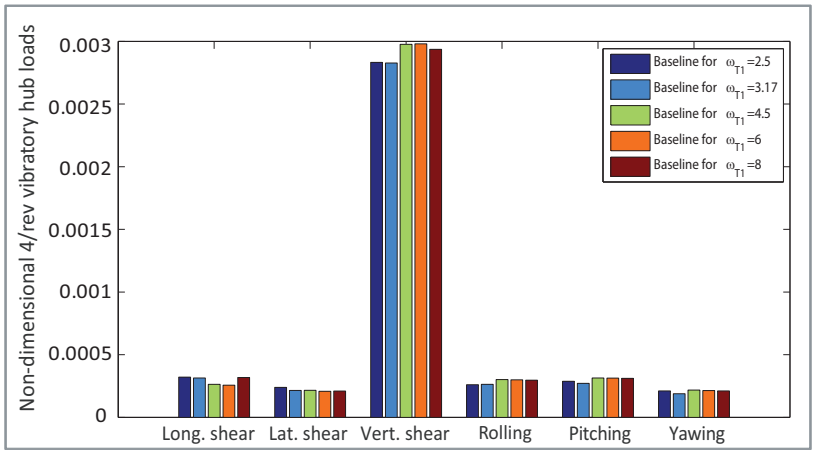

Fig. 5.9. Baseline rotor hub loads for various torsional frequencies.

for blades with ω_{T1}=3.17/rev and 4.5/rev have a higher 4/rev harmonic component, although at different phase angles. The flap deflections for blades of higher torsional frequencies are not shown as they are similar to that of a blade with $\omega_{T1} = 4.5$/rev.

The vibratory cost function, J, is the weighted sum of the squares of the vibratory hub shears and moments, with the weights given in Eqn. 2.25. The percentage reduction in the vibratory cost function at various torsional stiffness values for the single flap configuration is shown in Fig. 5.13, while those for the dual flap configuration is shown in Fig. 5.14. Optimal vibration reduction is achieved at a torsional frequency of 3.17/rev for all the configurations, except for the single flap for which the optimal reduction is at a torsional frequency of 4.5/rev. Both the control devices show similar trends in vibration reduction performance and are consistent with those found in Ref. 70, where the maximum torsional frequency considered was only 5/rev. The results in Fig. 5.13 show that the single microflap and single flap performance initially degrades but levels off for high ($>$ 5/rev) torsional

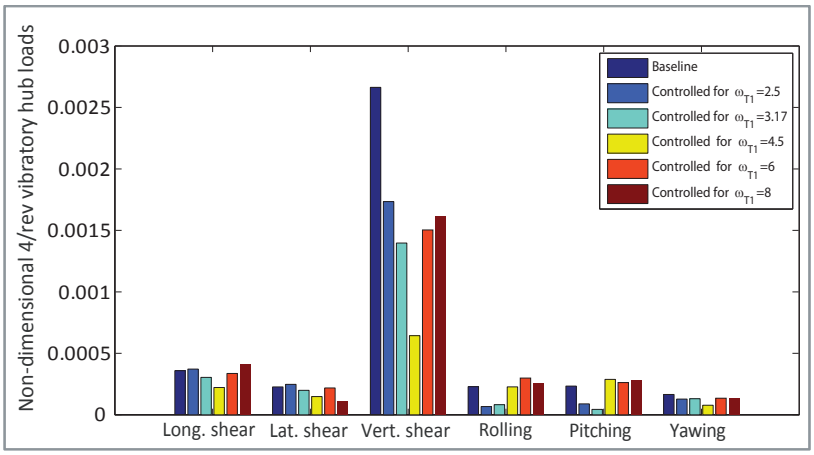

(a) Single flap

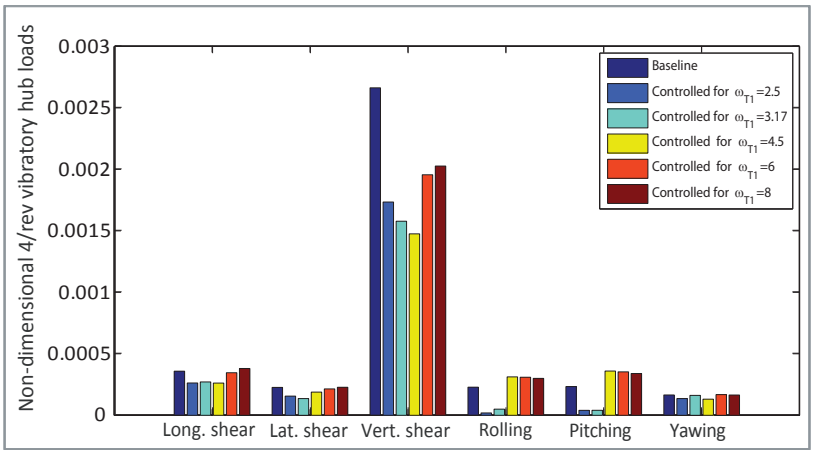

(b) Single microflap

Fig. 5.10. Load reduction for single flap/microflap configurations.

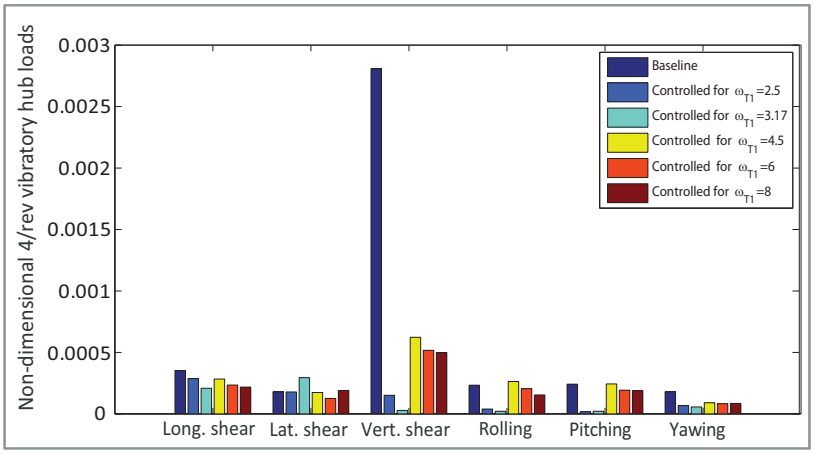

(a) Dual flap

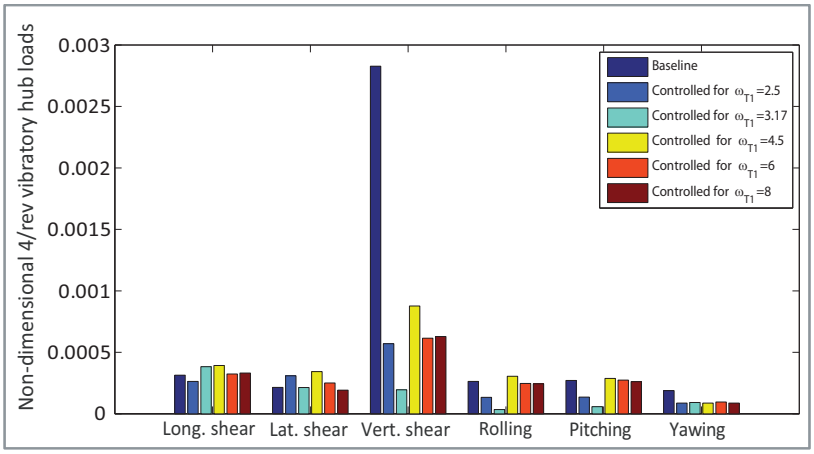

(b) Dual microflap

Fig. 5.11. Load reduction of dual flap/microflap Configurations.

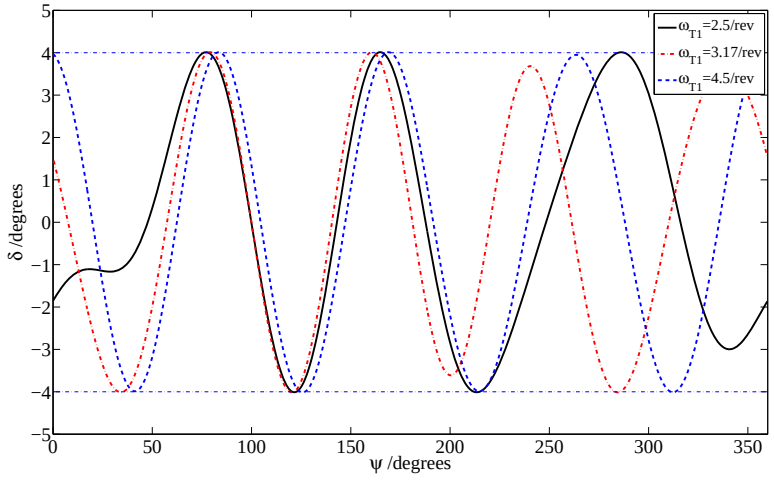

Fig. 5.12. Single flap deflection history.

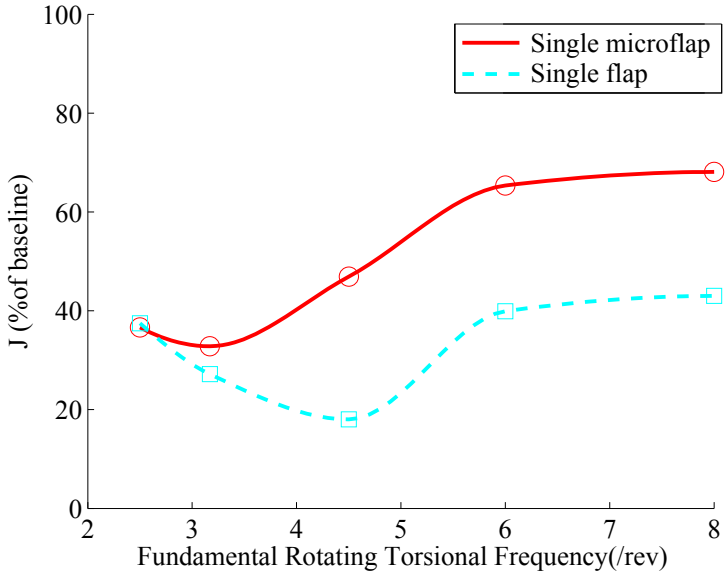

Fig. 5.13. Percentage reduction in the vibration cost function using a single flap and a single microflap.

frequencies. This is attributed to the limitations in the operation of the control surfaces as lift devices at high torsional frequencies. As the blade becomes stiffer in torsion, the ability of the control flap to affect the twist distribution at the blade is reduced, thus reducing its effectiveness in controlling vibrations [70]. Up to 40% vibration reduction is obtained for the single microflap, and up to 60% vibration reduction is obtained in the case of the single flap at high torsional frequency values.

Similar results are shown in Fig. 5.14 for the dual flap/microflap configurations. Both the dual flap and dual microflap yield optimal performance at a torsional frequency of 3.17/rev. Again, the vibration reduction capability degrades and then levels off at high values of torsional stiffness. Up to 80% vibration reduction is obtained for the dual microflap, and up to 90% vibration reduction is

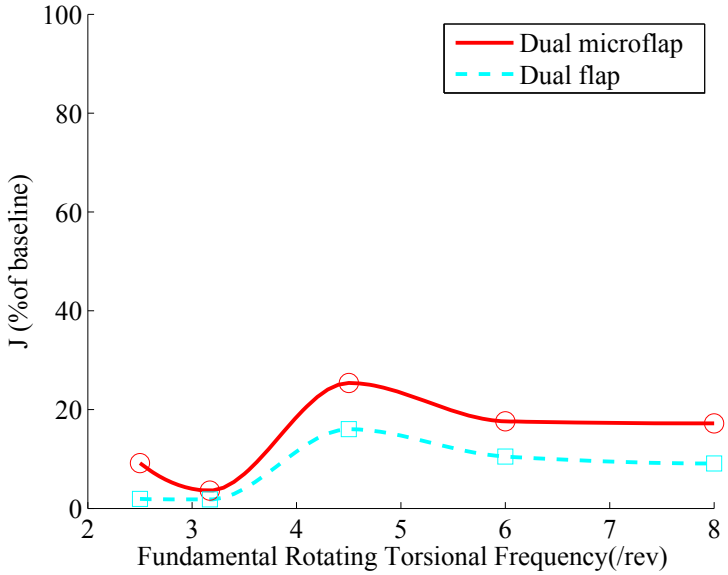

Fig. 5.14. Percentage reduction in the vibration cost function using a dual flap and a dual microflap.

obtained in the case of the dual flap at high torsional frequency values. Thus, the dual flap configuration is effective even at high torsional frequencies. The dual flap configuration consistently yields better vibration reduction compared to the single flap configuration with the same spanwise length, which is attributed to the high dynamic pressure on the outboard flap. Further, for the 20%c plain flap and 1.5%c microflap configurations considered, the plain flap achieves better vibration reduction than the microflap.

5.1.4 Influence of Microflap Chordwise Position on Vibration Reduction

The effect of chordwise location of the microflap on the vibration reduction performance was also studied. A microflap placed at 10%c from the trailing edge is considered in addition to the original microflap located at 6%c. The controlled non-dimensional vibratory loads for the single microflap at 10%c from the trailing edge

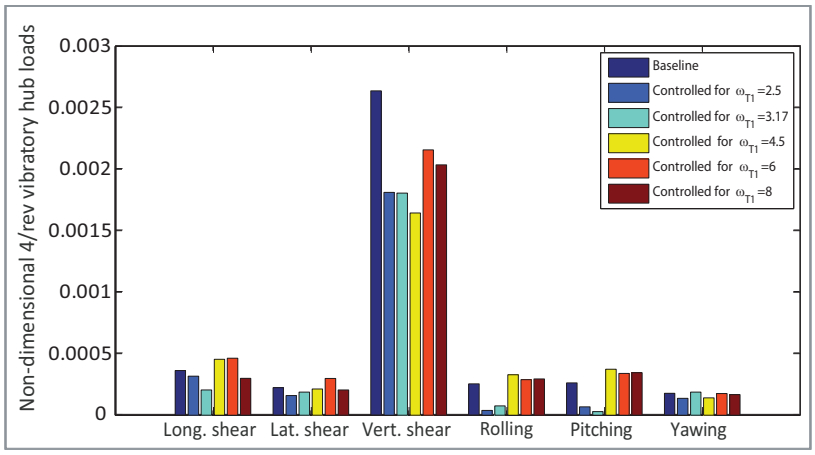

Fig. 5.15. Load reduction for single microflap at 10%c.

are shown in Fig. 5.15. The lowest vertical hub shear is obtained for a torsional frequency of 4.5/rev, which is similar to that obtained for a single microflap at 6%c. However, there is an 11% decrease in hub shear reduction when the microflap is shifted forward.

The percentage reduction in the vibratory cost function at various torsional stiffness values for the single microflap at 6%c and 10%c is shown in Fig. 5.16. There is a consistent decrease in vibration reduction performance of 10% when the microflap is shifted upstream, except at the high torsional stiffness values where the vibration reduction performance seems to reach a limit. Optimal vibration reduction is now obtained at $\omega_{T1} = 2.5$/rev, compared to $\omega_{T1} = 3.17$/rev for a microflap at 6%c. At the higher torsonal frequency values, a vibratory load reduction of 40% is achieved. It is evident that a microflap at 6%c has better vibration reduction performance than a microflap at 10%c. This is attributed to the superior control authority of the former configuration, due to its placement nearer the trailing edge [4, 40]. This is consistent with the steady and unsteady CFD simulation

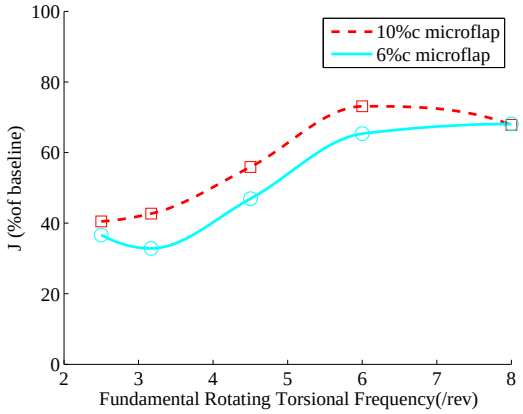

Fig. 5.16. Percentage reduction in the vibration cost function using a single microflap at different chordwise positions.

results from Section 5.1.1.

5.1.5 Noise Reduction

The effect of varying torsional frequency on the noise reduction capabilities of the 20%c flap and 1.5%c microflap at 6%c is presented next. Carpet plots are generated for the range of torsional frequencies shown in Table 5.2 and for the various spanwise, plain and microflap configurations. The noise carpet plot for the baseline blade with fundamental torsional frequency of $\omega_{T1} = 3.17$/rev is shown in Fig. 5.17 (a). The carpet plots corresponding to the dual microflap configuration are shown in Fig. 5.17 (b)-(f).

From the baseline simulation, the maximum BVI level on the advancing side is 119dB at an azimuth of about $\psi = 117°$ and the maximum BVI level in the retreating side is 117dB at an azimuth of approximately $\psi = 315°$, near the end of the retreating cycle. Reduction in noise levels obtained at these locations using the single flap and single microflap are plotted against torsional frequency in Fig. 5.18.

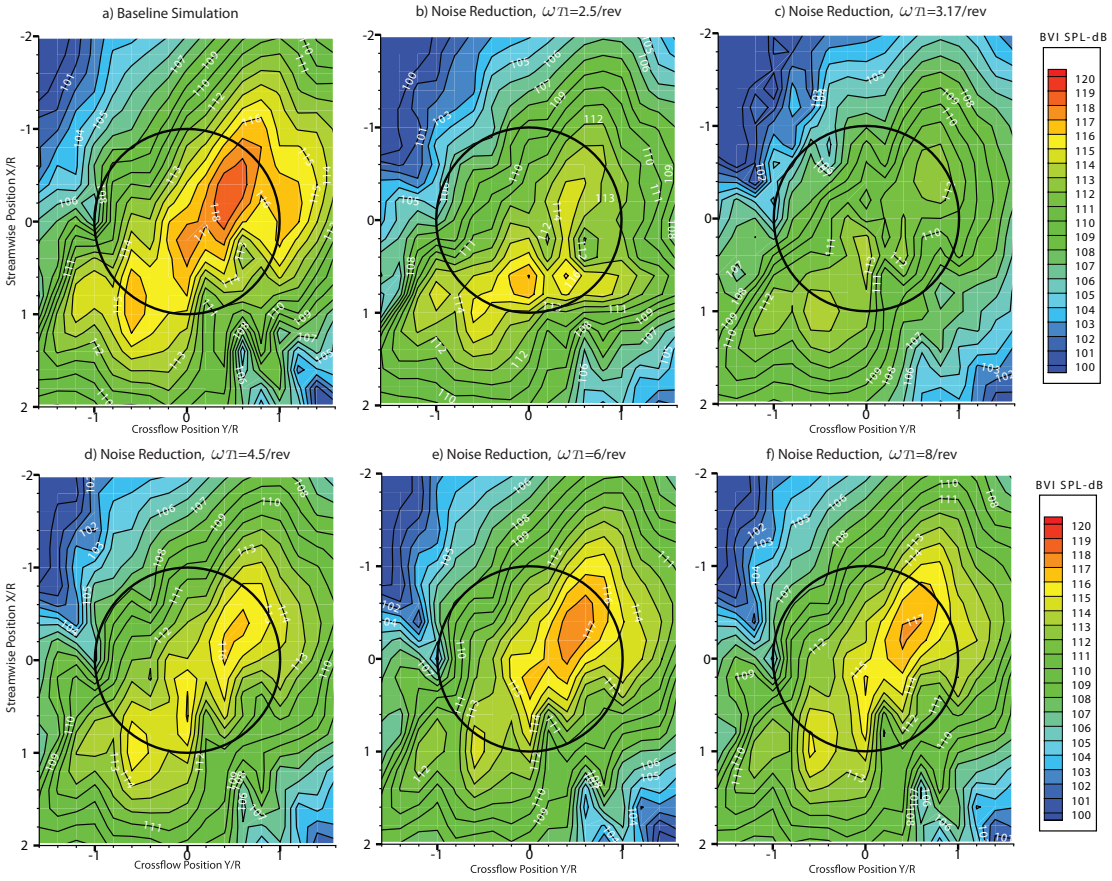

Fig. 5.17. Carpet plots for dual microflap noise reduction at various blade torsional frequencies.

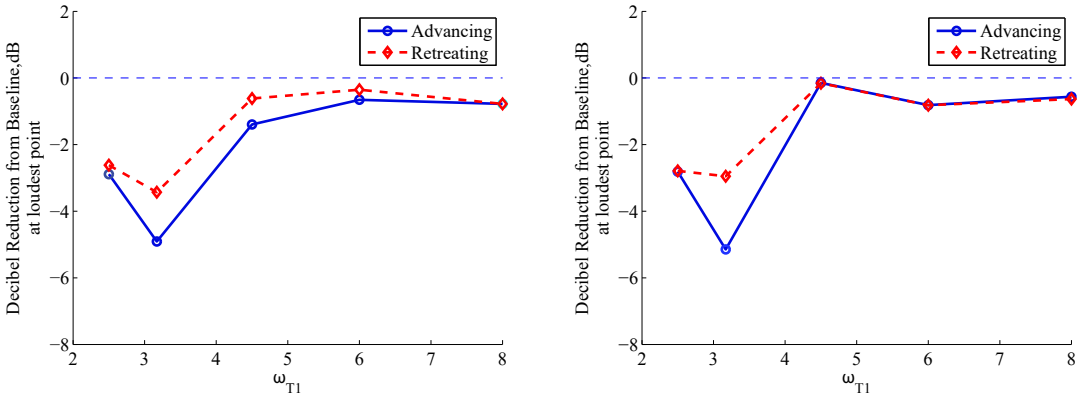

(a) Single flap (b) Single microflap

Fig. 5.18. Maximum BVI reduction for single flap/microflap configurations.

Reduction in noise levels obtained at these locations using the dual flap and dual microflap is plotted against torsional frequency in Fig. 5.19. It can be seen that the noise reduction performance of the ACF varies significantly with the torsional stiffness of the blade. Maximum noise reduction of 7.5 dB is achieved on the advancing side using the dual microflap configuration at a torsional frequency of 3.17/rev as seen in Fig. 5.19(b). In all the cases, the maximum noise reduction is also obtained at $\omega_{T1} = 3.17$/rev. Beyond this optimal torsional stiffness, the noise reduction performance is reduced significantly.

The average values of the BVI levels on the advancing side, bounded within the area $-1 \leq \frac{x}{R} \leq 1$ and $0 \leq \frac{y}{R} \leq 1$, and the retreating side, bounded within the area $-1 \leq \frac{x}{R} \leq 1$ and $-1 \leq \frac{y}{R} \leq 0$, see Fig. 5.8, are also used to characterize the noise levels. The difference in average BVI levels between the baseline and controlled rotor is used to quantify the noise reduction performance. The results are shown in Fig. 5.20 for the single flap configuration and in Fig. 5.21 for the dual flap configuration. Again, optimal reduction is observed at $\omega_{T1} = 3.17$/rev. In general

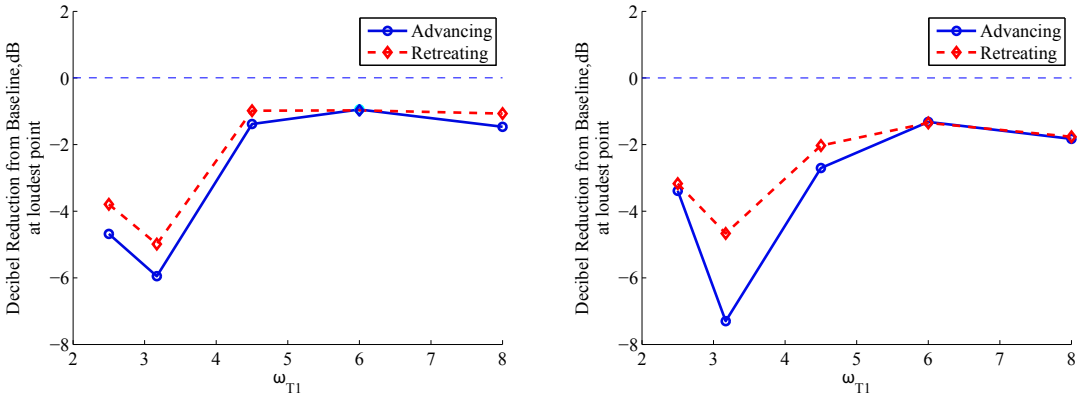

(a) Dual flap (b) Dual microflap

Fig. 5.19. Maximum BVI reduction for dual flap/microflap configurations.

the dual flap configurations, Fig. 5.21, achieves better noise reduction performance than the single flap configurations, Fig. 5.20. On average, noise reduction from the former is 1 dB larger than the latter. This is most apparent on the advancing side at $\omega_{T1} = 3.17$/rev where the single microflap configuration achieves an average noise reduction of approximately 3dB compared to that of the dual microflap configuration with an average 4.8dB reduction. This similarity in performance trend mirrors that noticed for the vibration reduction results. As mentioned earlier, the primary reason is that the outboard flap in the dual flap configuration has more control authority over the twist of the entire blade span as it operates in higher dynamic pressures. It is also interesting to note that on the retreating side, the microflaps yield better noise reduction than the plain flaps. This is evident in the single flap configurations shown in Fig. 5.20 and is consistent with the observations made in Ref. 79.

Based on the parametric study, a rotor blade with a torsional frequency of $\omega_{T1} = 3.17$, outfitted with a plain flap or microflap in a dual flap configuration is capable

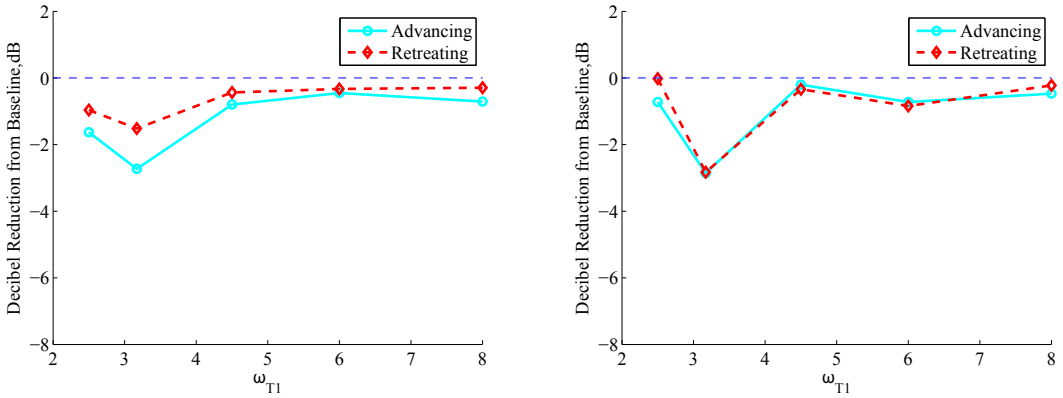

(a) Single flap (b) Single microflap

Fig. 5.20. Average BVI reduction for single flap/microflap configurations.

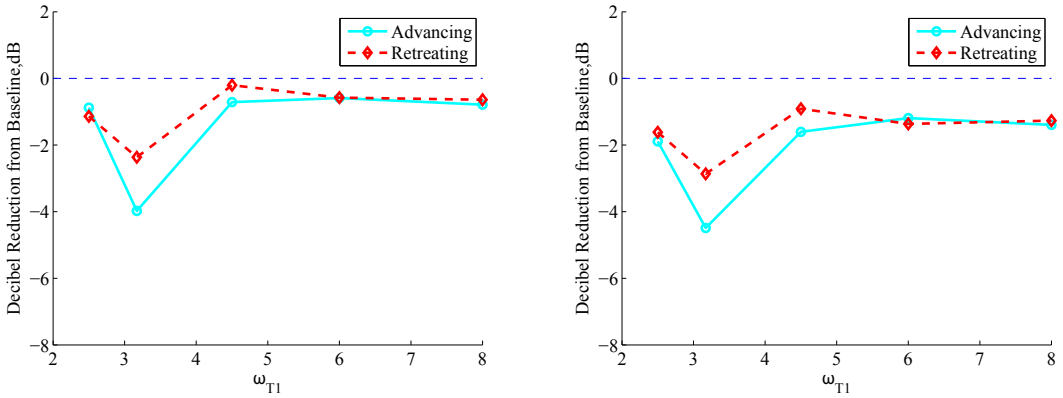

(a) Dual flap (b) Dual microflap

Fig. 5.21. Average BVI reduction for dual flap/microflap configurations.

of achieving maximum noise or vibration reduction. This torsional stiffness will be taken as the baseline configuration for investigating in-plane noise reduction in the subsequent phase of the study.

5.2 Validation Studies

The AVINOR/HELINOIR code combination employing the CFD based ROM was validated against experimental data obtained in two major wind tunnel tests:

1) the Higher-harmonic-control Aeroacoustic Rotor Test (HART) (Ref. 107) and 2) the Boeing-SMART rotor wind tunnel test conducted in the 40'x80' Wind Tunnel of the NFAC at NASA Ames Research Center (Ref. 105). A wind tunnel trim procedure, described in Section 2.3, was used in all the validation studies.

5.2.1 HART Wind Tunnel Test

5.2.1.1 Background

The HART program was a multi-national, comprehensive wind tunnel study on a 40% dynamically and Mach scaled model of a 4-bladed hingeless MBB BO-105 main rotor, with a -8° linear twist and standard rectangular tip shape [107]. It was conducted in the open-jet anechoic test section of the German-Dutch Wind Tunnel (DNW) in 1994. The test setup is depicted in Fig. 5.22. One of the blades was equipped with pressure transducers so that the blade airloads could be measured at various radial locations. Microphone arrays were placed on a traverse stand at a distance of 1.15 rotor radius underneath the rotor hub, and moved across the horizontal plane to measure the rotor noise at various locations. The rotor was trimmed for a given advance ratio μ, thrust coefficient C_T, and rotor shaft angle α_R, using collective and 1/rev cyclic pitch inputs.

The main objective of the program was to improve the physical understanding and mathematical modeling of Higher Harmonic Control on BVI noise and vibration. During the HART wind tunnel test, a "minimum noise" (MN) case was demonstrated to be capable of a maximum of 6dB in BVI noise reduction, which

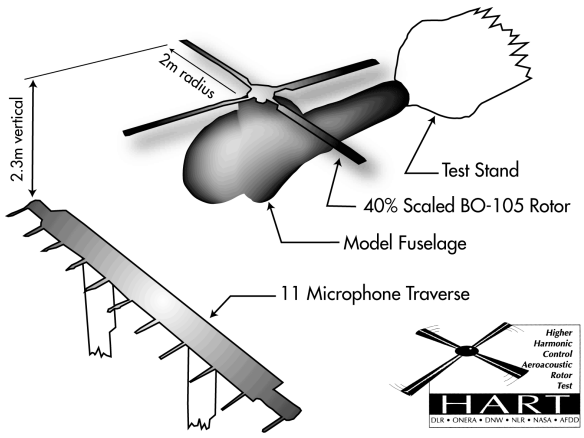

Fig. 5.22. HART test setup.

was accompanied by an increase in vibration levels. In the “minimum vibration" (MV) case, a 30% vibration reduction was achieved, however, this was accompanied by an increase in the BVI noise of up to 2.5dB on the advancing side. A key conclusion was that at maximum noise reduction, increased levels for low frequency noise and vibrations were observed, and vice versa.

Besides these key experimental outcomes, the HART wind tunnel test provided a comprehensive database, which was used for the improvement of wake prediction codes and validation of rotorcraft simulation code. The new AVINOR /HELINOIR code was validated against the HART wind tunnel experimental results. The approach taken is similar to the validation done on the AVINOR/WOPWOP code in Ref. 87.

5.2.1.2 HART Validation Test Case

The validation of the AVINOR/HELINOIR code suite was performed using the baseline condition (i.e. no active control) in the HART experiments. The blade

loading, which serves as an input to the HELINOIR code, was validated first. This was followed by the BVI Sound Pressure Levels (BVISPL) distribution on a carpet plane to validate the magnitude and locations of the noise peaks, as well as the acoustic pressure time history of selected observer locations on the advancing and retreating side.

The baseline flight condition corresponds to a strong BVI descending flight, at $\mu = 0.15$, $C_T = 0.0044$, and shaft angle $\alpha_R = 5.3°$. The rotor parameters are listed in Table 5.3.

Table 5.3. Baseline HART rotor parameters [59].

Nondimensional Rotor Data	
N_b = 4	c/R = 0.0605
ω_L=0.73,4.46	ω_F=1.11,3.21,6.90
ω_T=3.93,11.44	
$\sigma = 0.077$	θ_{tw} = -8°
Helicopter Data	
C_T/σ = 0.057	μ=0.15
M_∞=0.096	M_{tip}=0.64
$\alpha_R = 5.3°$ (backward tilt)	
Trim Values	
θ_0 = 4.04°	θ_{1c}=2.06°
θ_{1s}=-2.13°	

5.2.1.3 Blade Aerodynamic Loads

The aerodynamic loads acting at a location $r/R = 0.87$ along the span of the blade were obtained by integrating the blade pressure distribution along the chord. Figure 5.23 shows the sectional normal coefficient ($C_N M^2$) from the experiment compared against the prediction from the AVINOR/HELINOIR code. The plot

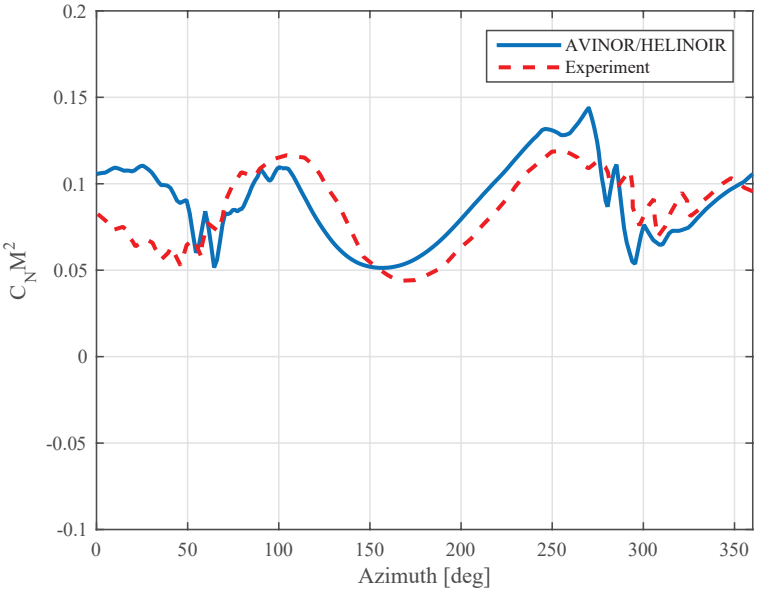

Fig. 5.23. Baseline HART blade loading using AVINOR/HELNOIR compared against experimental results [107] at x=0.87R

can be interpreted as a superposition of two effects, (1) a high magnitude, low frequency oscillation typified by the central valley at $\psi \approx 180°$ and (2) the low magnitude, high frequency oscillations in the first quadrant on the advancing side, $\psi \approx 50°$, and the fourth quadrant on the retreating side, $\psi \approx 300°$, which are attributed to BVI events. Both these effects are well captured by the AVINOR/HELINOIR code.

5.2.1.4 BVISPL on Carpet Plane

The BVISPL in the HART experiments were measured on a carpet plane located 1.15R below the rotor hub and parallel to the hub plane. The carpet plane is similar to that shown in Fig. 5.8. The noise levels measured during the experiment for the baseline blade are shown in Fig. 5.24(a) and the results from the simulation with

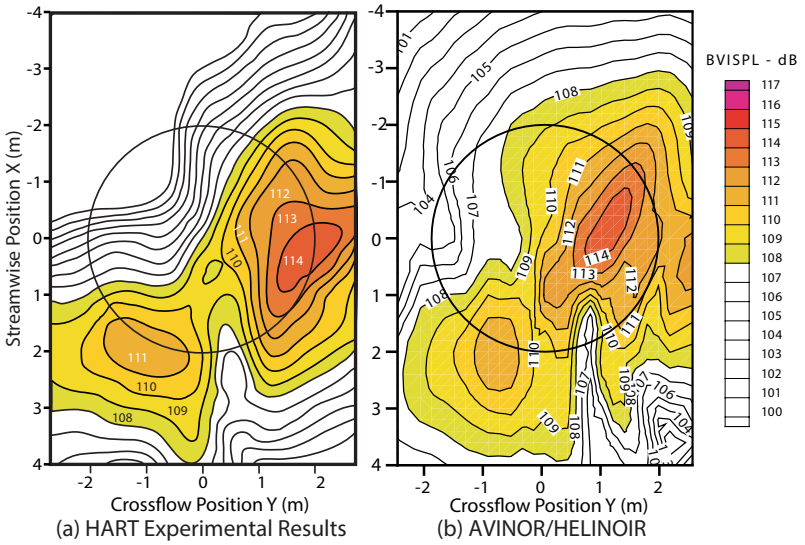

Fig. 5.24. Validation of the acoustic computations against the HART experimental data.

AVINOR/HELINOIR are shown in Fig. 5.24(b). Both carpet plots show a noise footprint which is characteristic of BVI noise, high noise levels concentrated on a pattern extended slightly forward and towards the advancing side of the rotor disk, and another lobe on the retreating side. On the retreating side, the magnitude and location of the 111 dB noise peak is well captured. For the advancing side, the magnitude of the 114 dB noise peak is also well captured, although the location is marginally shifted inboard for the simulation. Overall, there is a good agreement betwen the predicted BVISPL and the experiment.

5.2.1.5 Acoustic Pressure History

In the HART test, the acoustic pressure time histories were recorded at the noise peak locations on the advancing side, $(x, y, z) = (-0.02, 1.64, -2.30)$, and retreating side, $(x, y, z) = (2, -1.07, -2.30)$, shown in Fig. 5.25(a) and (c). The predicted

pressure histories from AVINOR/HELINOIR are shown in Fig. 5.25 (b) and (d) for comparison. The magnitude and phase of the noise signatures are well captured at both locations.

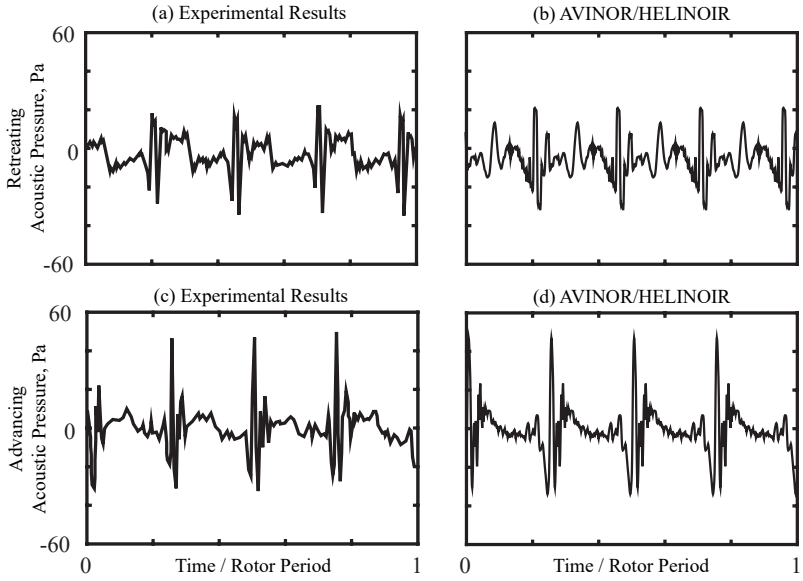

Fig. 5.25. Validation of AVINOIR/HELNOIR by comparing acoustic pressure histories at two locations, one on the advancing side and the other on the retreating side.

5.2.2 Boeing SMART Rotor Wind Tunnel Test

5.2.2.1 Background

The Boeing Smart Material Actuated Rotor Technology (SMART) Wind Tunnel Test was a program jointly funded by DARPA, NASA, Army and Boeing that lasted approximately nine years and culminated in a full scale test conducted in the 40- by 80-foot wind tunnel at the National Full-Scale Aerodynamic Complex at NASA Ames Research Center in early 2008 [109]. The Boeing SMART active flap rotor was a full-scale, five bladed bearingless MD 900 helicopter rotor modi-

fied with a piezoelectric-actuated trailing edge flap on each blade. The objective of the test was to demonstrate the effectiveness of active flap control for out-of-plane BVI noise, in-plane noise, and vibration for a range of flight conditions from moderate speed level cruise to low speed descending flight. Vibration reduction was performed with closed-loop control, implemented using a continuous-time HHC controller. Noise reduction was evaluated in the open-loop mode by conducting phase sweeps at each flap actuation harmonics in the 2-5/rev range, with a flap amplitude of $1.5°$. The results showed that the active flap was capable of achieving noise reduction in BVI and in-plane noise of up to 6dB and reduction of the vibratory hub loads by up to 80%.

5.2.2.2 Boeing SMART Rotor Validation Test Case

The in-plane acoustic prediction capability of AVINOR/HELINOIR in level cruise at moderate advance ratio was validated using results from the SMART Rotor test. This differs from the validation of the code using the HART rotor, discussed in Section 5.2.1, since the SMART rotor test was performed for noise reduction in a different plane, and flight condition. Therefore, this validation provides additional evidence regarding the predictive capability of the AVINOR/HELINOIR code.

The flight condition was a level cruise, at $\mu = 0.30$ and $C_T = 0.006$ for the baseline blade without active control. The rotor parameters are listed in Table 5.4. The rotor was modeled as a slender cantilever beam composed of a linearly elastic homogeneous material undergoing moderate deflections. The structural properties

of the blade model were chosen to match the first modal frequencies, $\omega_{L1}, \omega_{F1}, \omega_{T1}$, of the SMART rotor [110], following the procedure described in Ref. 59, and the torque tube was not modeled. Therefore, this is an approximate structural dynamic model of the rotor blade tested.

Table 5.4. Baseline SMART rotor parameters.

Nondimensional Rotor Data	
N_b = 5	c/R = 0.04924
ω_L=0.58, 3.63	ω_F=1.05, 2.70, 4.92
ω_T=6.4, 19.0	
$\sigma = 0.078$	θ_{tw} = -10°
Helicopter Data	
C_T/σ = 0.075	μ=0.3
M_∞=0.189	M_{tip}=0.623
$\alpha_R = -9.1°$ (forward tilt)	
Trim Values	
θ_0 = 9.86°	θ_{1c}=1.19°
θ_{1s}=-6.49°	

Three in-plane microphones (M13, M15 and M14), positioned along a straight line originating from the advancing blade tip to the tunnel centerline, were used for low frequency, in-plane noise measurements, as shown in Fig. 5.26.

5.2.2.3 In-Plane Acoustic Pressure Histories

The predicted and measured acoustic pressure histories at the M13, M15, and M14 microphones are shown in Fig. 5.27. For the M13 and M15 microphones, there is good agreement between the predicted and measured magnitude of the acoustic pressure history. There is a phase difference of approximately $18°$ between the predicted and measured pressure history at the M13 position, Figs. 5.27(a) and 5.27(b),

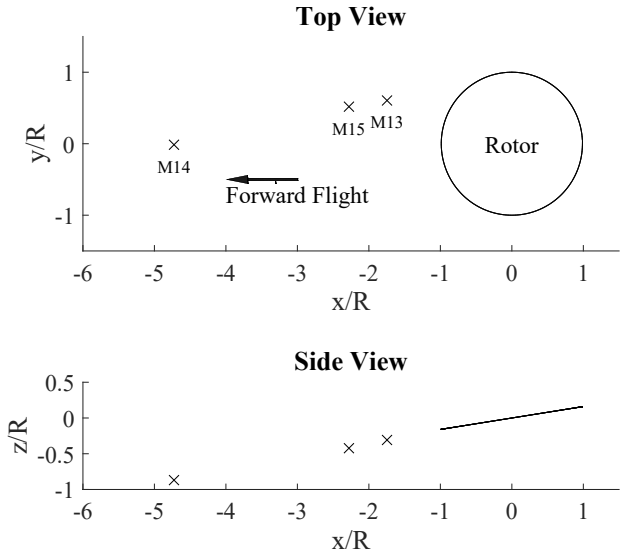

Fig. 5.26. In-plane microphone layout for the Boeing-SMART rotor wind tunnel test. (Data from Ref. 105)

and a phase difference of approximately 5° at the M15 position, Figs. 5.27(c) and 5.27(d). This phase difference is attributed to the approximate structural dynamic model used for the bearingless rotor, where the structural properties were selected so as to match the first 3 modal frequencies of the SMART rotor, thus affecting the blade aeroelastic deformation. For the M14 microphone, the differences in the acoustic pressure magnitude and phase prediction is attributed to the inaccuracy of the sound measurements recorded during the test. The M14 microphone was not located in the acoustically treated portion of the wind tunnel and there were concerns over the quality and therefore accuracy of the sound measurements at that location (Refs. 105, 109). Therefore the comparison between the predicted and experimental results at the M14 location had considerable limitations.

The loading and thickness noise contributions to the overall acoustic pressure at M15 are shown in Fig. 5.28. It is evident that the negative peak pressure gener-

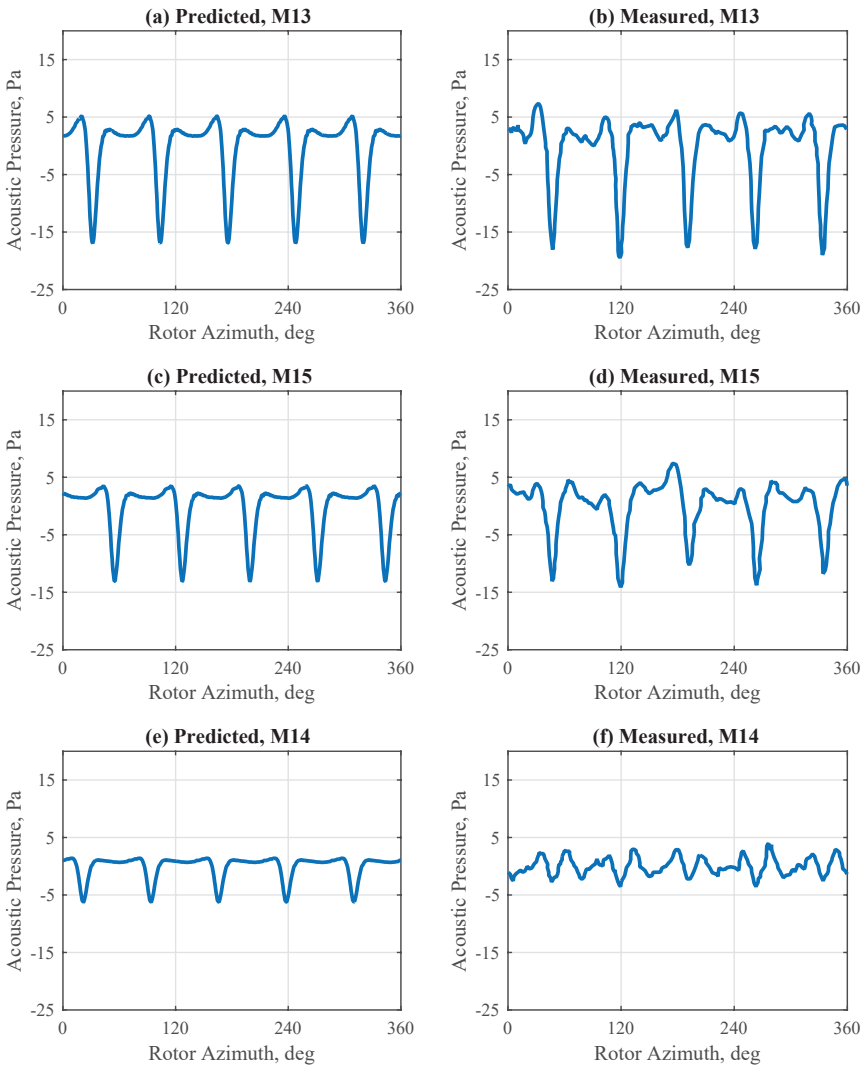

Fig. 5.27. Validation of the acoustic computations against the Boeing SMART experimental data. (Experimental data from Ref. 105)

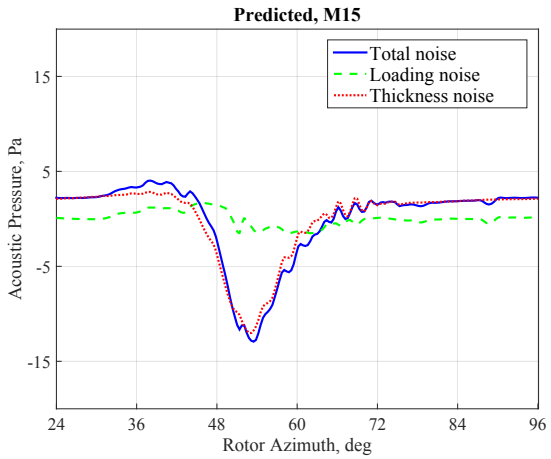

Fig. 5.28. Predicted acoustic pressure components at Microphone M15.

ated by the thickness noise is the dominant contributor to the in-plane noise, when compared to the loading noise [98].

5.3 Verification Studies

The AVINOR/HELINOIR code was validated against the HART rotor and the Boeing SMART rotor in Section 5.2. In this section, the MBB BO105 rotor is modeled using the AVINOR/HELINOIR code and verified by comparing the results with the AVINOR/WOPWOP code. Recall that the AVINOR/WOPWOP code has been separately validated in Refs. 83, 88. The rotor parameters were provided in Table 5.1. The baseline flight condition is descending flight at an advance ratio $\mu = 0.15$, thrust coefficient $C_T = 0.005$, and descent angle $\alpha_D = 6.5°$, representing strong BVI conditions. A propulsive trim procedure was used for all the verification studies. Two versions of the AVINOR/HELINOIR code were verified, one employing the global Galerkin structural dynamic model that is employed for

modeling active control as described in Sec. 2.1.1, and the second version is the Galerkin type FEM used for modeling passive control as described in Sec. 2.1.2.

5.3.1 Global Galerkin Model

The AVINOR/HELINOIR code employing the global Galerkin structural dynamic model is verified by comparing with results obtained from the AVINOR/WOPWOP code in this section. The baseline flight, without active control, was verified first. For the verification of active control, two types of OBC devices were used, a 20%c conventional plain flap, shown in Fig. 1.4, and a 1.5%c microflap located 6%c from the trailing edge, shown in Fig. 1.5. These OBC devices were modeled as a single plain flap and single microflap configuration, with a span of 0.12R and centered at 0.75R, as shown in Fig. 5.6(a) and Fig. 5.7(a), respectively. The active closed-loop noise and vibration control studies were performed using the adaptive higher harmonic control (HHC) algorithm. The comparisons of the acoustic environment for the verification is limited to the BVISPL computed on a carpet plane located 1.15R beneath the rotor. A saturation algorithm [80] was used to constrain the microflap deflection between $0\%c$ and $1.5\%c$ and the plain flap deflection to $\pm 4^{\circ}$.

5.3.1.1 Baseline Flight Condition

The baseline noise level on the carpet plane predicted using the AVINOR/HELINOIR code suite is shown in Fig. 5.29(b). The similar baseline prediction from the AVINOR /WOPWOP code [59] is shown in Fig. 5.29(a). There is good agreement for

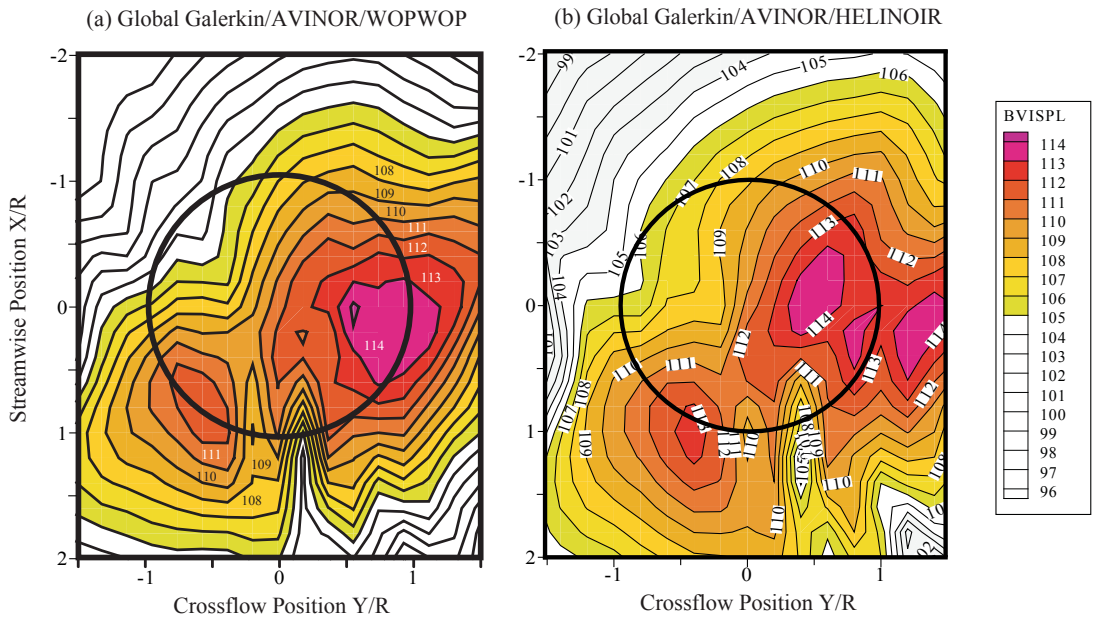

Fig. 5.29. Comparison of the baseline noise levels on the carpet plane using different aeroelastic-aeroacoustic code combination

the overall BVISPL distribution, particularly the noise peak of 114dB and shape of the noise lobe on the advancing side. On the retreating side, there is a good agreement on the location of the noise peak. The discrepancy in the noise magnitude on the retreating side is attributed to the pressure distribution approximation used in the AVINOR/WOPWOP code.

5.3.1.2 Active Noise Reduction

The carpet noise levels obtained in the carpet plane when using the AVINOR/HELINOIR code during active noise reduction implemented by a single plain flap are shown in Fig. 5.30(c), while noise levels obtained by a single microflap are shown in Fig. 5.30(b). These results are also compared to the baseline carpet plane noise levels shown in Fig. 5.30(a). Both the single plain flap and single microflap

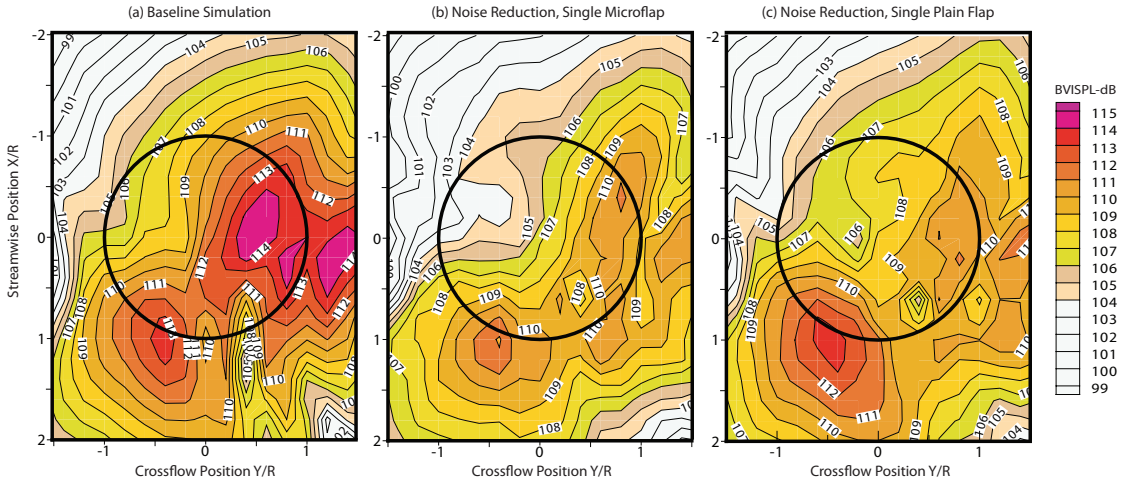

Fig. 5.30. Comparison of the noise levels computed on the carpet plane using HELINOIR during active noise control employing a single microflap (b) and a single plain flap (c), at $\mu = 0.15$, $C_T = 0.005$ and $\alpha_D = 6.5°$.

configuration produced approximately 3 dB noise reduction on the advancing side. On the retreating side, the microflap produced approximately 2dB noise reduction while the plain flap did not produce any appreciable reduction. These active noise reduction trends are similar to those obtained while using the AVINOR/WOPWOP code [83].

The vibration levels during active noise control using the single plain flap and the single microflap configurations are compared to the baseline levels in Fig. 5.31. The vertical hub shear increases by 91% in the case of the microflap and 70% in the case of the plain flap. This trend of vibration penalty accompanying noise reduction, with the microflap incurring a higher penalty, is consistent with the results obtained using the AVINOR/WOPWOP code [82].

The control surface deflection histories for the single microflap and the single plain flap configurations during a revolution are shown in Figs. 5.32(a) and 5.32(b),

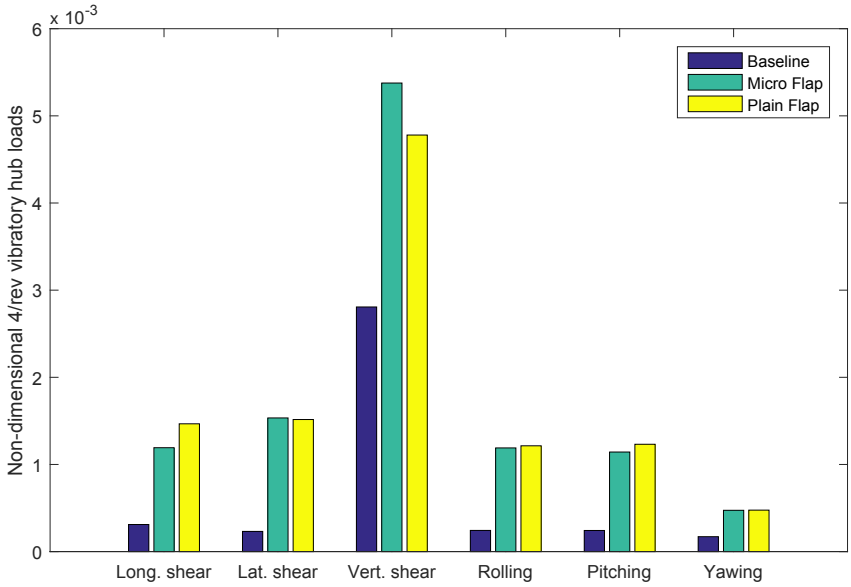

Fig. 5.31. Comparison of the vibration levels computed using the AVINOR/HELINOIR during active noise control using a single microflap and a single plain flap for a heavy BVI descending flight condition.

respectively. It is relevant to note that the strong 3/rev component during active noise reduction is consistent with the minimum noise case in the HART experiment [107].

5.3.1.3 Active Vibration Reduction and Noise Penalty

Closed-loop vibration reduction implemented by a plain flap and microflap are shown in Fig. 5.33. The plain flap and the microflap produced 73% and 63% reduction in the vibration objective function respectively. The noise penalty during active vibration reduction is shown in Fig. 5.34. Both the plain flap and microflap produce a 2dB increase in the noise levels on the advancing side. However, neither OBC device had any significant effect on the retreating side noise levels. This trend agrees well with the results from the AVINOR/WOPWOP code presented in

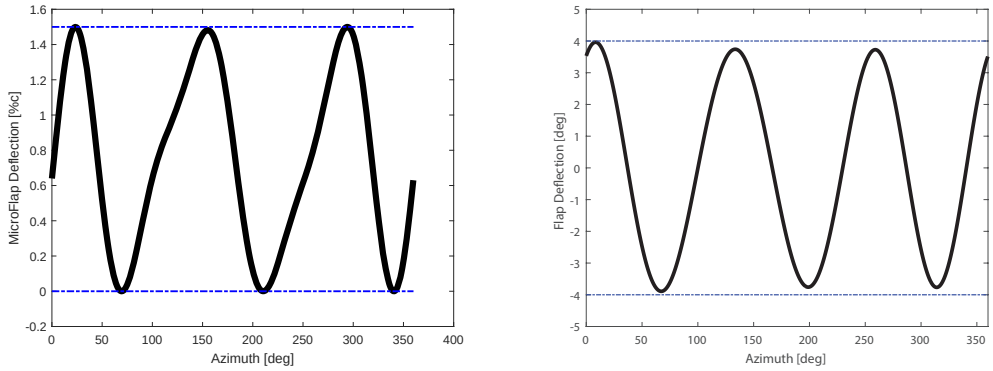

(a) Microflap (b) Plain Flap

Fig. 5.32. Flap deflection histories over a rotor revolution during active noise reduction.

Ref. 83.

5.3.2 Galerkin Type FEM

In order to model the advanced tip geometry used for passive control, a beam type finite element model of a rotor blade, described in Section 2.1.2, was developed and implemented in AVINOR/HELINOIR as part of this study. To verify the new structural model, the acoustic and vibration calculations are compared against the results from the AVINOR/WOPWOP code (Ref. 59) based on the global Galerkin method.

A helicopter configuration resembling a full-scale four bladed MBB BO-105 hingeless rotor with a rectangular tip plan form is used, similar to that used in Section 5.3.1. Constant mass and stiffness distributions are assumed along the blade span. Using these parameters, it was found that six beam-type finite elements are needed to match the modal frequencies, $\omega_{Fi}, \omega_{Li}, \omega_{Ti}$ used in the global Galerkin model. The vibration and acoustic environment represented by BVISPL computed

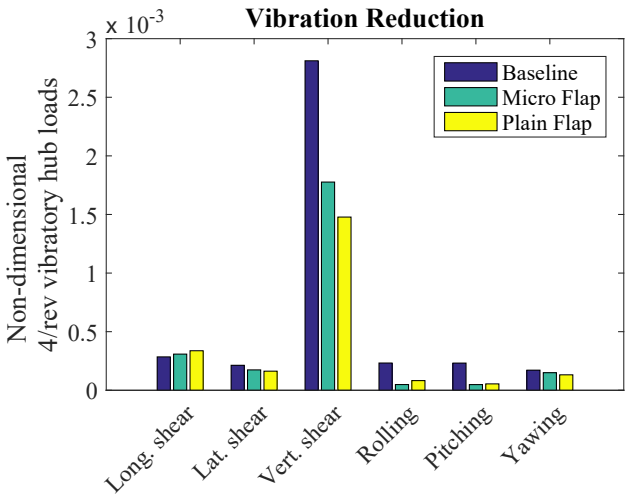

Fig. 5.33. Comparison of the vibration levels computed during active vibration control using a single microflap and a single plain flap at $\mu = 0.15$, $C_T = 0.005$ and $\alpha_D = 6.5°$.

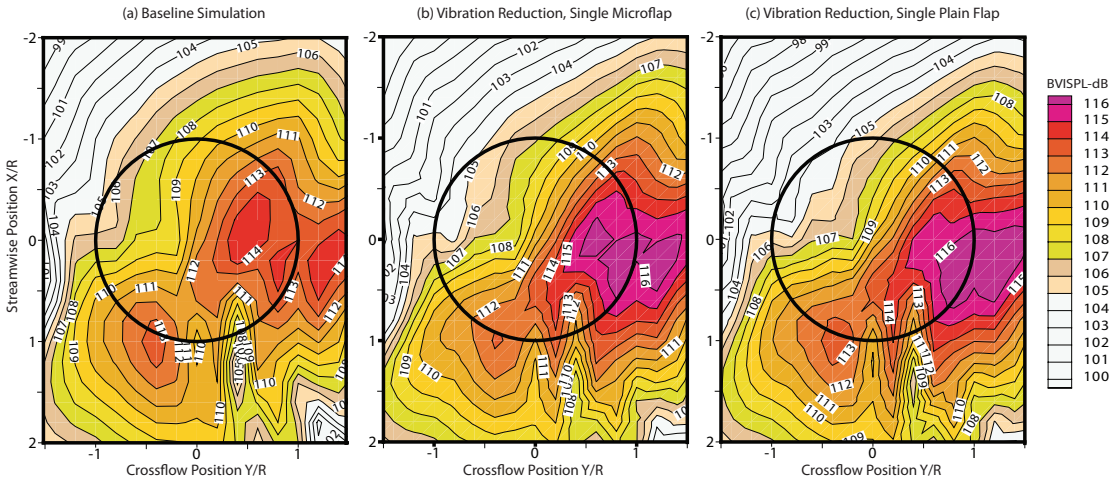

Fig. 5.34. Comparison of the noise levels computed on the carpet plane using HELINOIR during active vibration control using a single microflap (b) and a single plain flap (c) at $\mu = 0.15$, $C_T = 0.005$ and $\alpha_D = 6.5°$.

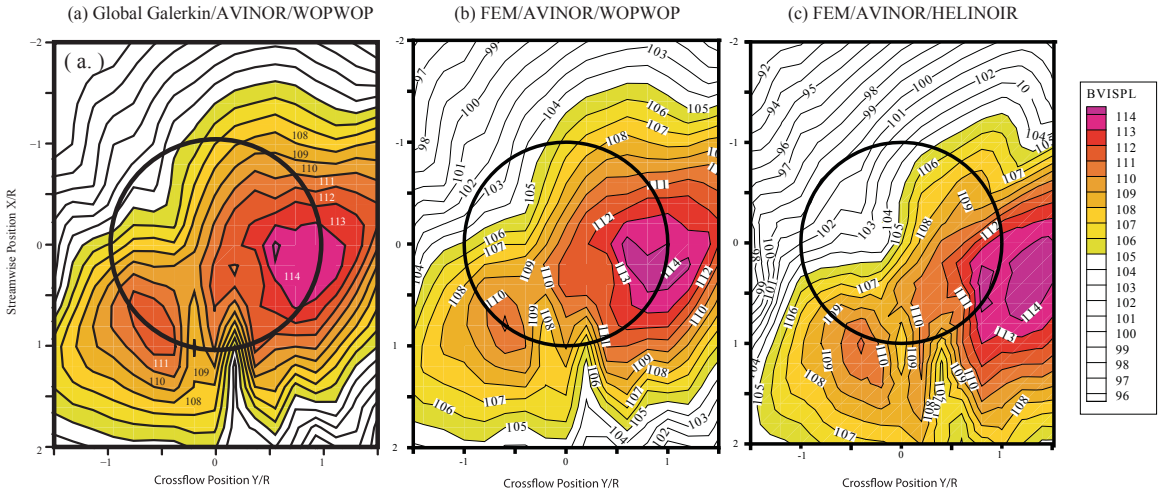

Fig. 5.35. Comparison of the noise levels from a straight blade computed on the carpet plane employing a global Galerkin model (a) and Galerkin type FEM (b) and (c) at $\mu = 0.15, C_T = 0.005$ and $\alpha_D = 6.5°$

on a carpet plane located 1.15R beneath the rotor were also compared for this verification.

5.3.2.1 Baseline Noise and Vibration

The baseline noise level on the carpet plane computed using the AVINOR/ WOPWOP code employing the global Galerkin model is shown in Fig. 5.35(a). Results from simulations performed using the FEM AVINOR code in combination with WOPWOP and HELINOIR codes are shown in Figs. 5.35(b) and (c), respectively. It is evident that the finite element model, whether it is coupled with WOPWOP or HELINOIR, predicts the BVI noise levels on the carpet plane well, capturing the magnitude and location of the noise peaks of 114dB on the advancing side and 111dB on the retreating side.

The associated baseline 4/rev non-dimensional vibratory hub loads for the

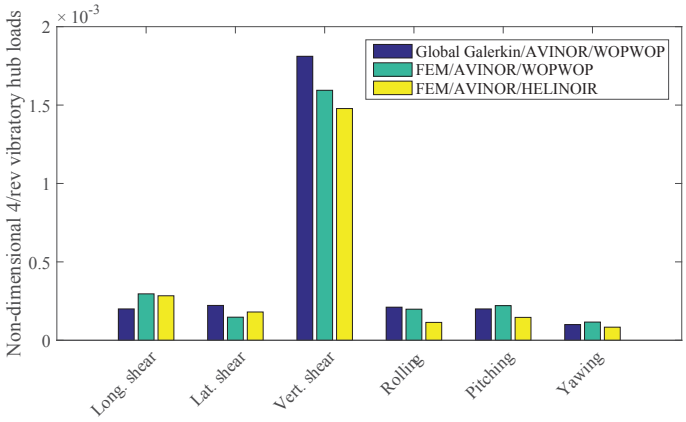

Fig. 5.36. Comparison of the vibration levels from a baseline blade employing a global Galerkin model and Galerkin type FEM at $\mu = 0.15, C_T = 0.005$ and $\alpha_D = 6.5°$

three code combinations are shown in Fig. 5.36. There is good agreement in all six components of the vibratory hub loads. It is evident that both the acoustic and vibratory load predictions from the finite element structural model, coupled with HELINOIR agrees well with the global Galerkin AVINOR/WOPWOP code combination.

5.4 Results - In-Plane Noise Control

The AVINOR/HELINOIR code was validated against experimental results in Section 5.2 and verified against the the AVINOR/WOPWOP code in Section 5.3. The objective of this section is to employ the code for an in-plane noise control study of the MBB BO-105 helicopter at level cruise at a moderate advance ratio. Both active and passive means of control are used, and the impact of noise control on the vibratory hub loads is carefully examined. The effect of noise control on performance is also considered.

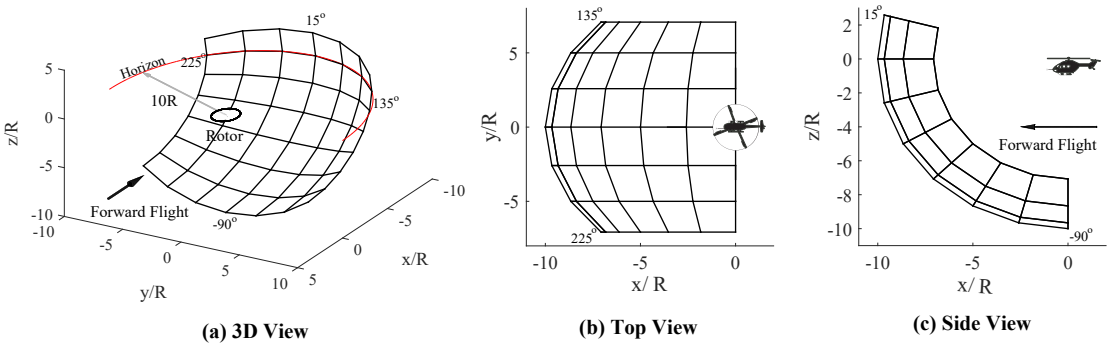

Fig. 5.37. In plane observer surface located at 10R in front of the helicopter. Azimuthal variation is shown in (b) and elevational variation is shown in (c).

5.4.1 Baseline Flight Condition

The results presented in this section are for a helicopter resembling a full-scale four-bladed MBB BO-105 hingeless rotor in level flight at an advance ratio, $\mu = 0.3$. The baseline rotor parameters are provided in Table 5.1. The rotor is trimmed using a propulsive trim procedure during the in-plane noise control simulations.

The acoustic environment in the far-field in front of the helicopter is characterized by the Low Frequency Sound Pressure Level (LFSPL), which consists of the 1st - 6th BPF harmonic components (28 - 170Hz) of the rotor noise, computed on a spherical segment located at a distance of 10R in front of the rotor hub, with an azimuth angle between $135°$ to $225°$ and an elevation angle between $-90°$ to $15°$, as shown in Fig. 5.37. This surface includes the observer locations in the forward in-plane direction where noise reduction is considered. For selected observer locations of interest, the Mid Frequency Sound Pressure Level (MFSPL) is used to characterize the higher frequency components of the in-plane far-field noise. The MFSPL consists of the harmonic components higher than the 6th BPF (>170Hz).

5.4.2 Active Control of In-Plane Noise

Active control of in-plane noise is modeled using the global Galerkin structural model. Different feedback locations are considered and in-plane noise reduction is studied for different advance ratios and OBC configurations.

The OBC is implemented using a 20%c plain flap, shown in Fig. 1.4. Two spanwise configurations are used, a single and a dual flap, shown in Fig. 5.6. The single flap has a span of 0.12R and is centered at 0.75R, shown in Fig. 5.6(a). The dual flap consists of two flaps each with the same span of 0.06R and centered at 0.72R and 0.92R, as shown in Fig. 5.6(b).

5.4.2.1 Baseline Noise

The baseline LFSPL noise, without active control, is shown in Fig. 5.38(a). A region of high noise levels, above 95dB, is predicted around $(\frac{y}{r}, \frac{z}{r}) = (0, 0)$ or 0° elevation angle and 180° azimuth angle. It is this directivity and the low frequency content of the LFSPL noise that increases the range at which the helicopter can be detected in forward flight.

5.4.2.2 Noise Reduction Using Far-Field Feedback

Various feedback microphone locations were explored so as to examine and develop an understanding of closed-loop control of in-plane noise. First, hypothetical feedback locations were chosen within the high noise region on the observer surface. A single microphone feedback and three different arrays of feedback mi-

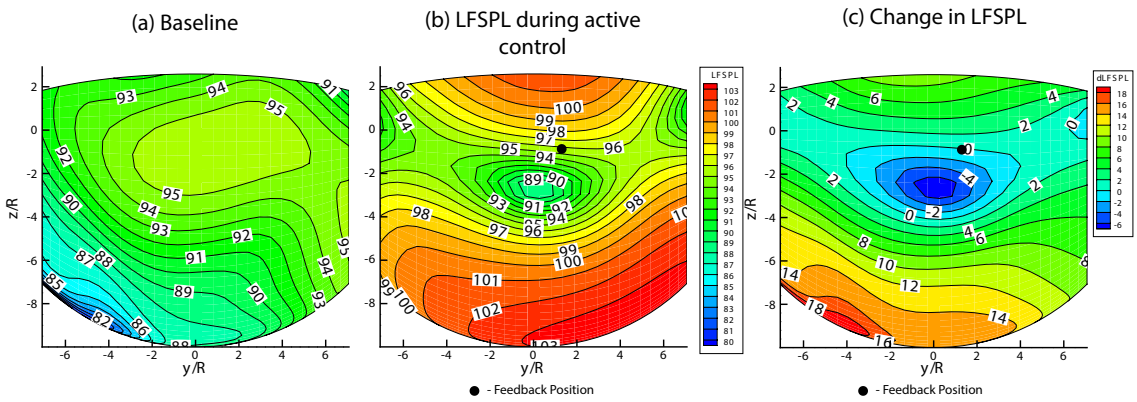

Fig. 5.38. Baseline and the reduced in-plane noise levels obtained using a single plain flap and a single feedback microphone located on the observer surface at 10R.

Table 5.5. Far-field feedback microphone locations.

Number of Microphones	Name	Cartesian Coordinates x/R	y/R	z/R
1		-9.88	1.30	-0.87
3	Config 1	-9.96	0.0	-0.87
		-9.88	1.3	-0.87
		-9.62	2.58	-0.87
3	Config 2	-9.88	-1.30	-0.87
		-9.88	1.30	-0.87
		-9.20	3.18	-0.87
3	Config 3	-9.62	-2.58	-0.87
		-9.88	1.30	-0.87
		-8.63	4.98	-0.87

crophones defined in Table 5.5, were examined. These are hypothetical feedback locations in the far-field. This is employed so as to conduct a numerical experiment that will provide physical insight on closed-loop control for in-plane noise reduction.

The LFSPL noise reduction obtained using a single plain flap with a single far-field feedback microphone is shown in Fig 5.38(b). The change in the LFSPL from the baseline is shown in Fig. 5.38(c). It is evident from Fig. 5.38(c) that significant

noise reduction of up to 6dB was achieved between $-4 \leq \frac{y}{R} \leq 4, -4 \leq \frac{z}{R} \leq -1$ or an elevation angle of between -24° to 4° from the horizon and azimuth angle between 156° to 204°. This direction corresponds to the forward, slight downward tilt of the main rotor tip path plane and is the most significant for reducing the range at which the helicopter can be detected. A reduction of 6 dB is similar to that obtained in Ref. 105. However, a noise increase of up to 18 dB is generated in the left, out-of-plane location. This suggests that the reduction of in-plane noise can result in a severe noise penalty in the out-of-plane direction. Although not specifically studied here, the use of OBC for in-plane noise reduction may also result in a marginal rotor performance penalty (Ref. 106) and a minor amount of additional power requirement to operate the OBC system (Refs. 82,88).

The mechanism behind in-plane noise reduction can be better understood by comparing the acoustic pressure history at an in-plane observer location before and after active control. Figures 5.39(a) and 5.39(b) show the acoustic pressure history for the baseline and the controlled case, respectively, at the observer location where maximum LFSPL reduction is achieved: $(\frac{x}{R}, \frac{y}{R}, \frac{z}{R}) = (-9.70, -0.27, -2.41)$. It is evident that thickness noise is the dominant component in the baseline pressure history, Fig. 5.39(a) resembles Fig. 5.28 for the Boeing SMART rotor test. By comparing Figs. 5.39(a) and 5.39(b), it is evident that there is no change in the thickness noise shown by the dotted red line. However, the overall LFSPL noise is reduced during active control via the generation of an appropriately phased positive peak loading noise, which cancels the negative peak thickness noise. This waveform is consistent with the ”antinoise" profile proposed in Ref. 105 for in-plane noise re-

duction. This result implies that closed-loop active control, implemented through a plain flap, is capable of generating an “antinoise" signal required for in-plane noise reduction.

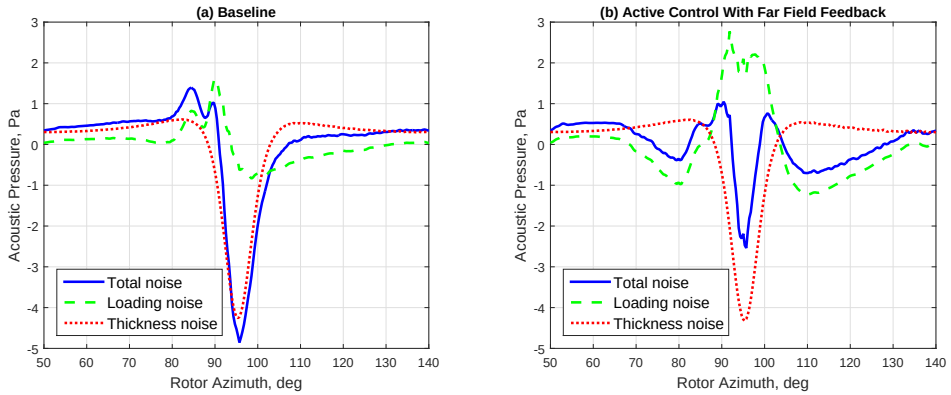

Fig. 5.39. Acoustic pressure histories at observer location, $(\frac{x}{R}, \frac{y}{R}, \frac{z}{R}) = (-9.70, -0.27, -2.41)$, before and after active control.

To further understand in-plane noise reduction performance, an array of three in-plane feedback microphones was considered. A similar three-microphone feedback array was used in the AATD/Sikorsky/UTRC active flap wind tunnel demonstration rotor in Ref. 106. The locations of the feedback microphones for the three different configurations used are provided in Table 5.5 and illustrated by the black circular dots in Figs. 5.40(b)-(d). All three microphones in the feedback array were given equal weights in the cost function of the HHC algorithm.

The reduced in-plane noise levels produced using the three-microphone array are shown in Fig. 5.40 (b)-(d). All three configurations exhibit similar levels of noise reduction. A maximum noise reduction of 6dB near in-plane below the horizon was obtained with an out-of-plane noise increase of approximately 18dB. The noise reduction achieved using multiple feedback microphones resemble that

obtained using a single feedback microphone, shown in Fig. 5.40(a) for comparison. Therefore, no significant improvement in performance is obtained when using multiple feedback microphones, when compared to a single feedback microphone.

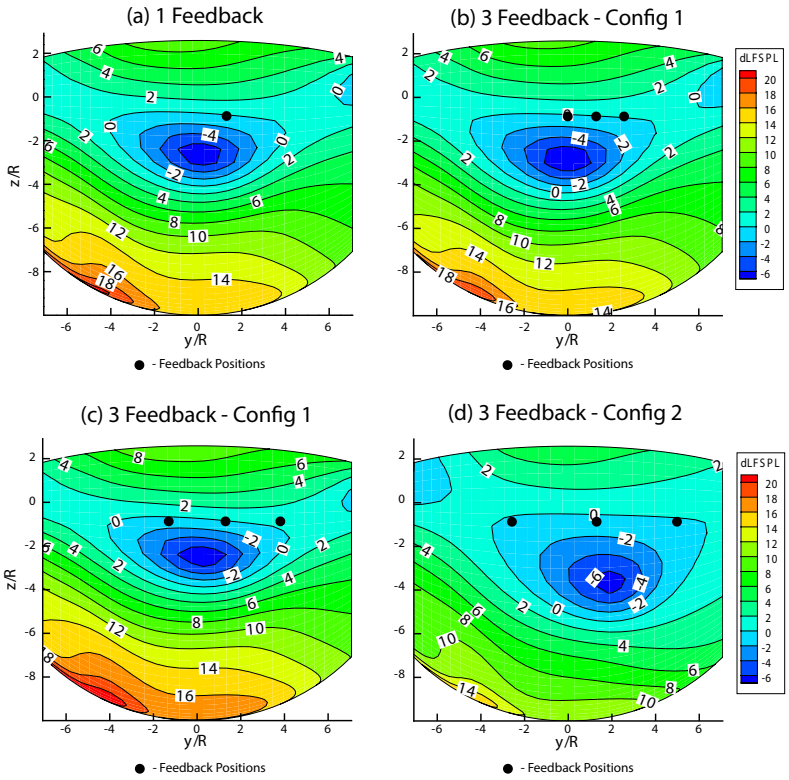

Fig. 5.40. Reduction in the in-plane noise levels obtained at 10R using various far-field feedback configurations.

The vibration levels obtained during active in-plane noise control using the single plain flap for the four different feedback microphone array locations are compared to the baseline levels in Fig. 5.41. It is evident that a vibration penalty is induced during in-plane noise reduction for all the six vibratory hub load components. The vertical hub shear increased by 70.1% for the one feedback configuration and an average of 58.2% for the three feedback configurations. This trend of vibration penalty accompanying in-plane noise reduction is consistent with the

observations in Ref. 105 and is analogous to the vibration penalty incurred during BVI noise reduction during low speed descending flight conditions [34].

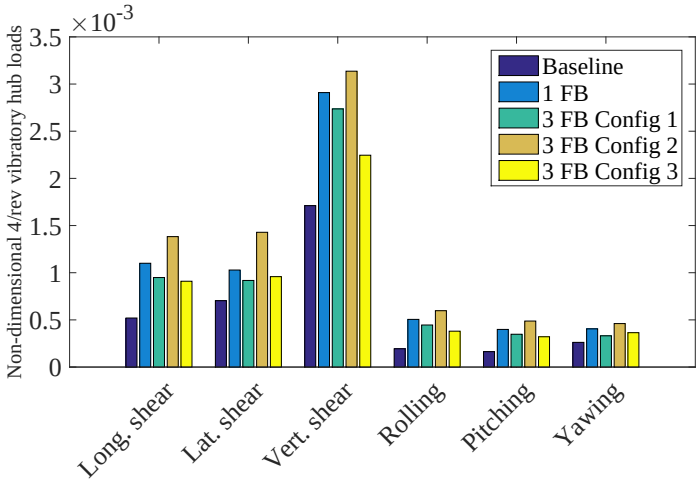

Fig. 5.41. Vibration penalty during closed-loop in-plane noise reduction using various feedback microphone configurations for single plain flap.

The flap deflection history for one feedback configuration is shown in Fig. 5.42. Two observations are in order. First, the active flap is moving from a flap up to flap down position between $80° - 125°$, suggesting that the flap is generating extra lift and drag, and therefore an anti-noise signal at this azimuthal location. Second, a strong 3/rev flap deflection component is produced by the HHC controller for in-plane noise reduction for the 4-bladed MBB BO105 rotor. By contrast, a 4/rev flap deflection was identified using open-loop sweep studies during a wind tunnel test to achieve the best in-plane noise reduction performance for the 5-bladed Boeing-SMART rotor [105] suggesting that the (N-1)/rev harmonic input may be the most effective for in-plane noise reduction.

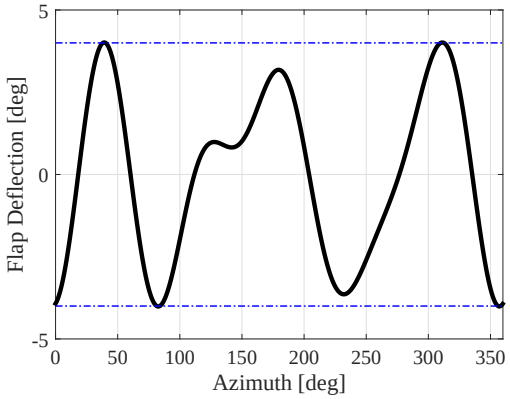

Fig. 5.42. Flap deflection history for active in-plane noise reduction using a single feedback location.

5.4.2.3 Noise Reduction Using Near-Field Feedback

In order to implement closed-loop in-plane noise reduction on a helicopter, the feedback microphone has to be located on the vehicle and its noise measurement has to be representative of far-field noise. In the case of BVI noise reduction, flight tests have demonstrated that there is a strong correlation between BVI noise reduction measured by microphones on the ground in far-field and those measured by microphones located on the skid in the near-field [34]. In Ref. 88, feedback microphone implemented on the rear right skid was found to work well for BVI noise reduction. However, there are no equivalent far-field, near-field noise correlation studies for in-plane noise reduction. To examine this issue, five near-field on-vehicle feedback locations listed in Table 5.6, were considered for in-plane noise reduction. Two of these locations, the left boom and tip of the right skid, are illustrated in Fig. 5.43.

In-plane noise reduction obtained using a feedback location at the tip of the left skid is shown in Fig. 5.44(a) and that obtained using a feedback location at

Table 5.6. Near-field feedback microphone locations.

	Cartesian Coordinates		
Name	x/R	y/R	z/R
Tip of Left Skid	-0.40	-0.32	-0.60
Tip of Right Skid	-0.40	0.32	-0.60
Left Boom	-0.70	-0.20	-0.40
Center Boom	-0.70	0.0	-0.40
Right Boom	-0.70	0.20	-0.40

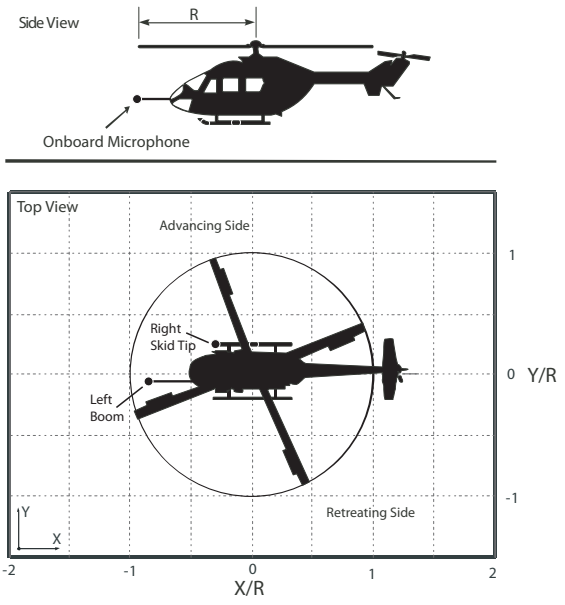

Fig. 5.43. Near-field onboard microphone feedback location on left boom and tip of the right skid.

the tip of the right skid is shown in Fig. 5.44(b). A noise reduction of 4 dB was found, which was significantly lower than that obtained using the far-field feedback, shown in Fig. 5.40. Furthermore, noise reduction is not directed in the forward in-plane direction. However, it is interesting to note that the out-of-plane noise penalty is reduced significantly when compared to the far-field feedback location.

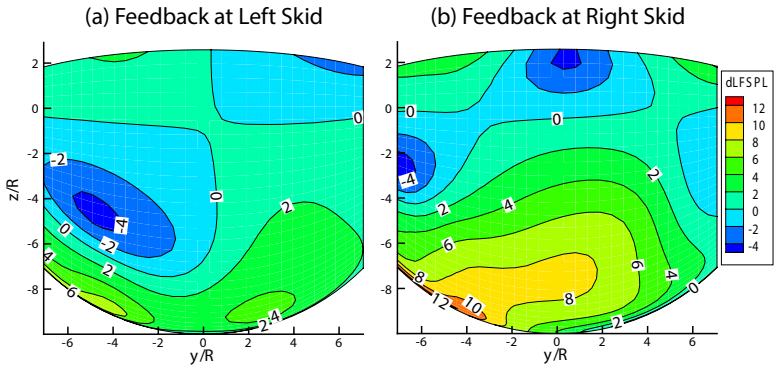

Fig. 5.44. Reduction in LFSPL at 10R using skid feedback.

The correlation between far-field noise radiation pattern and near-field feedback is examined further using three different boom positions as feedback locations. The in-plane noise reduction obtained by using feedback microphone locations at the left, center, and right boom is shown in Fig. 5.45. In all three cases, an in-plane noise reduction of 6dB was achieved with an approximately 18 dB noise increase out-of-plane, which is similar to the results obtained using far-field feedback, Fig. 5.40. More importantly, the azimuthal directivity of the noise reduction shifted with the boom feedback position. From Fig. 5.45(a), it is evident that a microphone located on the left boom position provided the best feedback for near in-plane noise reduction below the horizon.

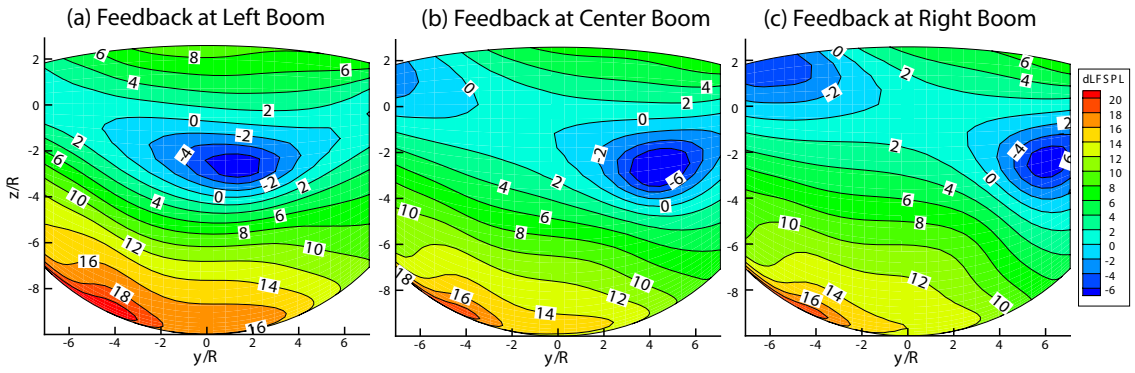

Fig. 5.45. Reduction in LFSPL at 10R using various boom feedback locations.

The sound pressure levels of the 1st-40th BPF harmonics for the baseline blade and the actively controlled case with the feedback at the left boom position is shown in Fig. 5.46. The SPL is computed at the observer location, $(\frac{x}{R}, \frac{y}{R}, \frac{z}{R})=(-9.70, -0.27, -2.41)$ corresponding to the forward, slight downward tilt of the main rotor tip path plane. The insertion loss is defined as the reduction in the sound pressure level due to the insertion of an active/passive control device. This is obtained by taking the difference between the SPL of the baseline and controlled case in Fig. 5.46. The insertion loss at the specified observer location due to active control is shown in Fig. 5.47. It is evident that the insertion loss in the 1st - 6th BPF harmonics contributed to the in-plane LFSPL reduction. There is also significant insertion loss at the higher harmonics from 16th - 23rd BPF harmonics indicating that active control is capable of noise reduction over a broad range of audible frequencies.

The vibration levels during active noise control using the single plain flap with near-field feedback at the left boom location is compared to the baseline levels in Fig. 5.48. As expected, there is a vibration penalty due to in-plane noise reduction

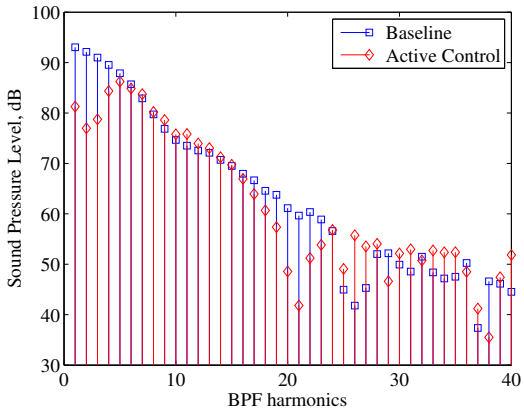

Fig. 5.46. Sound Pressure Levels before and after active control.

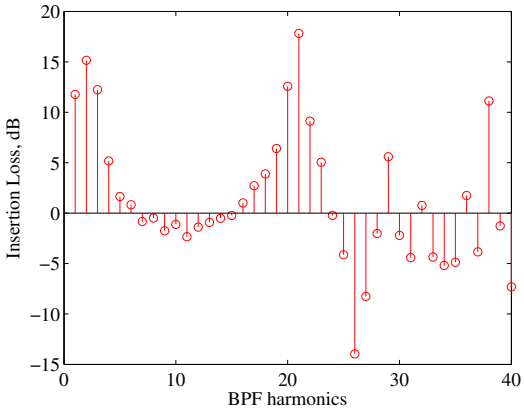

Fig. 5.47. Insertion Loss due to active control.

in all the six components of hub shears and moments, with a maximum increase of 60.6% in the vertical hub shear. The associated flap deflection schedule obtained using the left boom feedback is shown in Fig. 5.49.

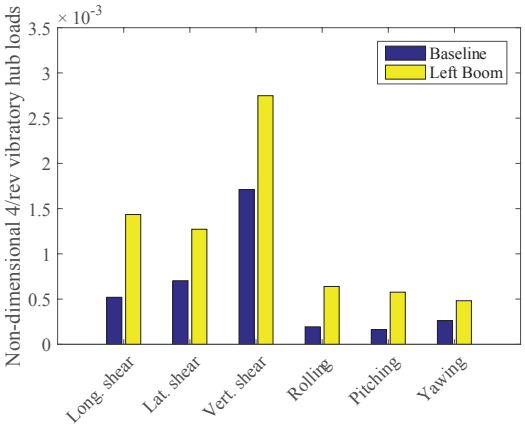

Fig. 5.48. Vibration penalty during in-plane noise reduction using a single plain flap with a left boom feedback.

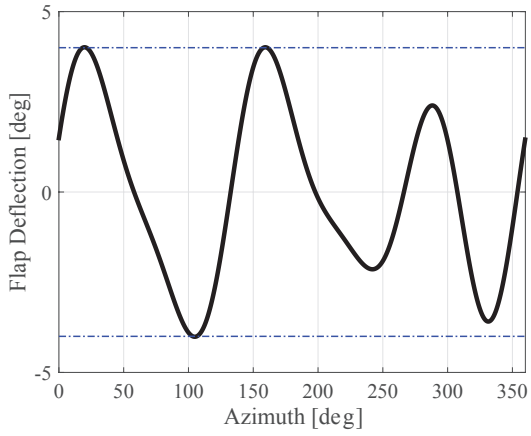

Fig. 5.49. Flap deflection history for active in-plane noise reduction with a left boom feedback.

The variation of the cost function J during the adaptive control loop for in-plane reduction with the feedback at the left boom position is shown in Fig. 5.50. The adaptive HHC algorithm approaches a stable solution after about 10 control

updates.

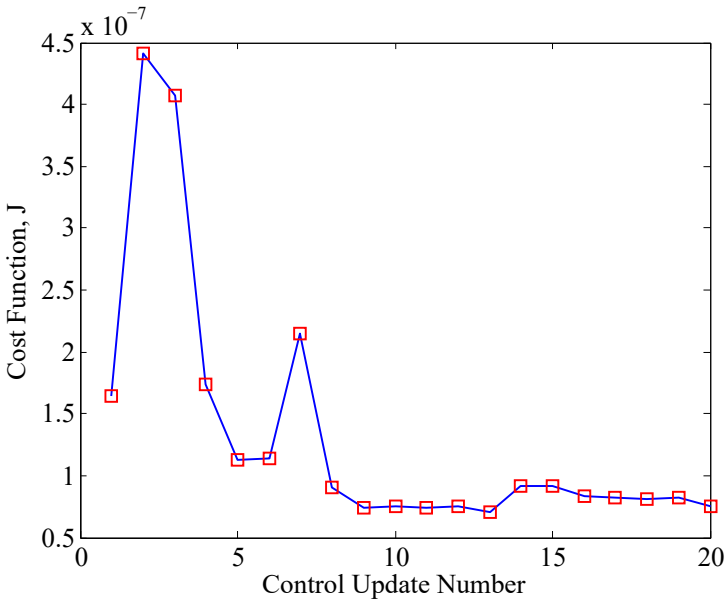

Fig. 5.50. Adaptive controller performance during in-plane noise reduction with feedback at left boom position at level cruise, $\mu = 0.3$.

5.4.2.4 Effects of Advance Ratio

To investigate the feasibility of using a near-field feedback location for in-plane LFSPL reduction at other flight conditions, simulation was performed for a single plain flap rotor at level cruise, $\mu = 0.2$. The LFSPL on the observer surface for the new flight condition before and after active control is shown in Figs. 5.51(a) and (b). A noise reduction of up to 8dB was achieved in the forward near in-plane location below the horizon, Fig. 5.51(c), similar to that achieved for level cruise at an advance ratio of $\mu = 0.3$, Fig. 5.45(a).

The pressure time histories at the near-field left boom feedback position and an in-plane far-field location where maximum LFSPL reduction was achieved,

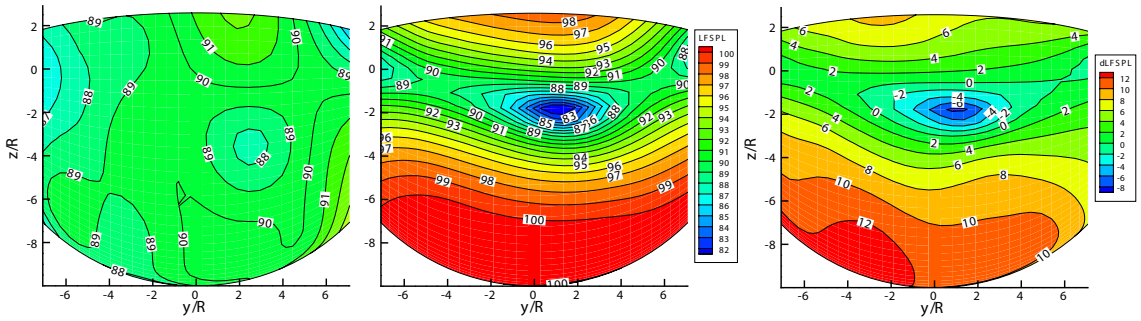

(a) Baseline

(b) LFSPL during active control

(c) Change in LFSPL

Fig. 5.51. Baseline and the reduced in-plane noise levels obtained using a single plain flap and near-field feedback microphone at the left boom for level cruise, $\mu = 0.2$.

$(\frac{x}{R}, \frac{y}{R}, \frac{z}{R})$ = (-9.70, -0.27,-2.41), before and after control at level cruise, $\mu = 0.3$ are shown in Fig. 5.52. The analogous data for level cruise at $\mu = 0.2$, is shown in Fig. 5.53. By comparing Figs. 5.52(c) and 5.52(d), it is evident that the dominant mechanism for LFSPL reduction at the near-field feedback location is by reducing the magnitude of loading noise contribution. A similar observation can also be made by comparing Figs. 5.53(c) and 5.53(d) for level cruise at $\mu = 0.2$. On the other hand, at the far-field location, the LFSPL noise is reduced by an increased loading noise signal that cancels the thickness noise, as in the anti-noise approach. This phenomenon can be observed by comparing Figs. 5.52(a) and 5.52(b) for $\mu = 0.3$ and similarly Figs. 5.53(a) and 5.53(b) for $\mu = 0.2$. It is interesting to note that the controller is only reducing the loading noise at the near-field feedback location. It is not clear how this results in an "anti-noise" signal at the far-field location and it requires further study. The OBC device only affects the loading noise in order to reduce the overall noise both in the near-field and far-field locations, whereas the

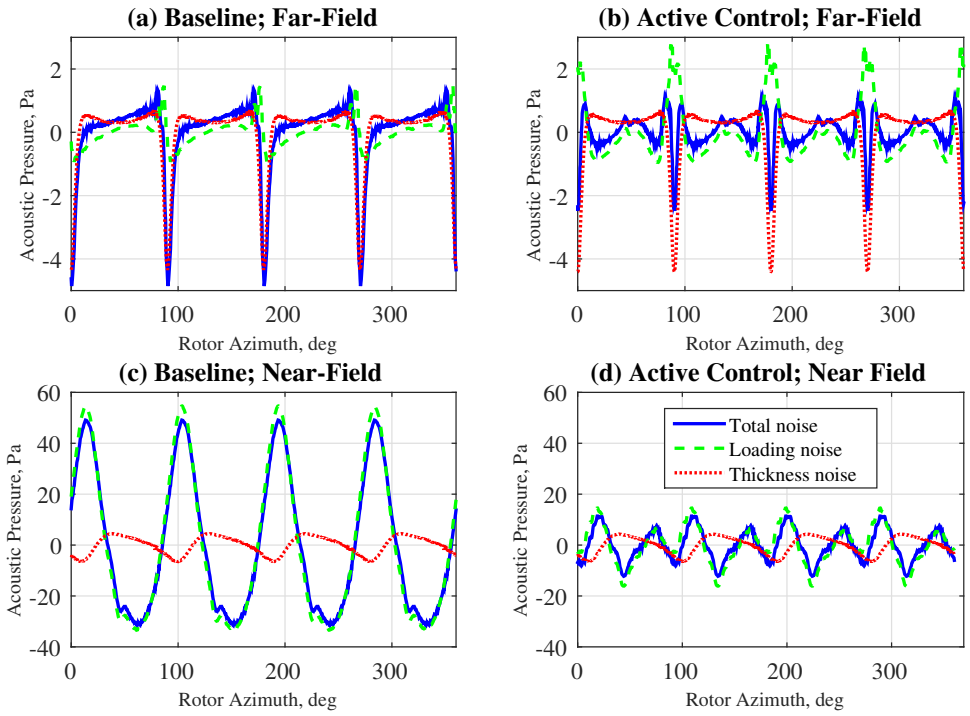

Fig. 5.52. Baseline and the reduced in-plane noise levels obtained using a single plain flap and near-field feedback microphone at the left boom for level cruise, $\mu = 0.3$.

thickness noise contribution is not significantly affected.

5.4.2.5 Noise Reduction Using a Dual Plain Flap Configuration

It was shown in Ref. 19 that the dual flap configuration, shown in Fig. 5.6(b), is more effective than a single flap configuration for vibration and BVI noise reduction. This was attributed to the higher dynamic pressure at the outboard flap location combined with enhanced control authority over the blade twist and aerodynamic loads. Therefore, active in-plane noise reduction is examined using a dual plain flap configuration so as to understand better this type of noise reduction.

In-plane noise reduction obtained using a dual plain flap configuration with a

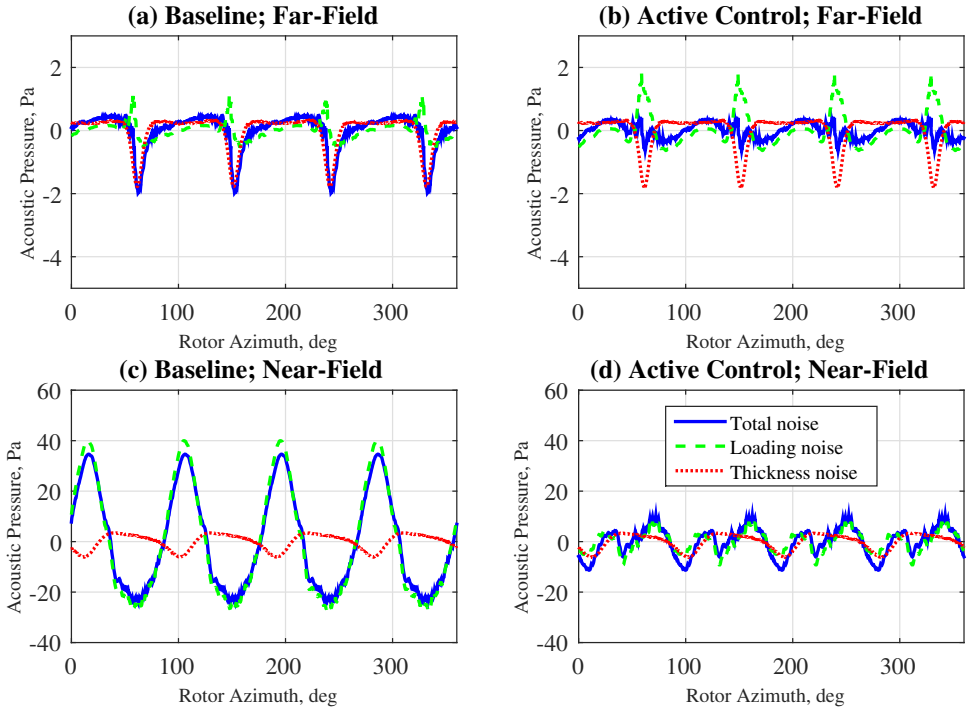

Fig. 5.53. Baseline and the reduced in-plane noise levels obtained using a single plain flap and near-field feedback microphone at the left boom for level cruise, $\mu = 0.2$.

far-field feedback is shown in Fig. 5.54(a). The effect of near-field feedback at the left boom is shown in Fig. 5.54(b). By comparing Figs. 5.54(a) and Fig. 5.38(c), it is evident that the maximum LFSPL reduction is similar for the dual and single flap configurations when far-field feedback microphone is used. However the out-of-plane noise penalty is lower and the noise reduction was achieved over a larger region for the dual flap case. When the left boom feedback is used, Fig. 5.54(b), the dual flap configuration also produced noise reduction over a wider azimuth than the single flap configuration, Fig. 5.45(a).

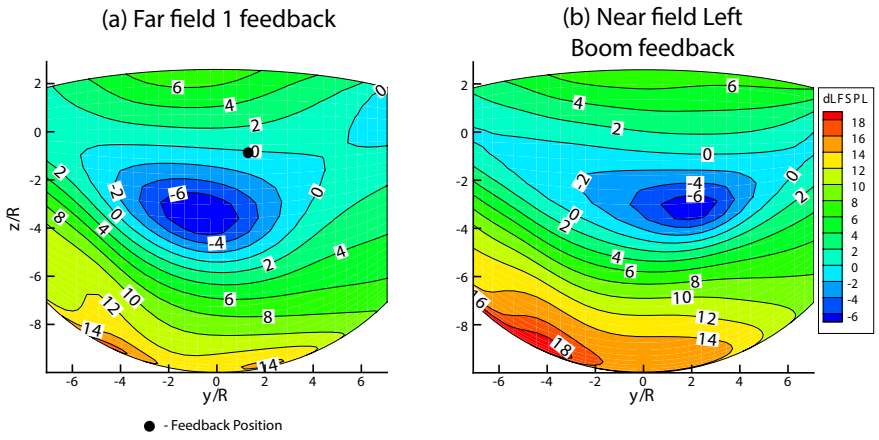

Fig. 5.54. Comparison of the noise levels computed on the 10R observer surface using a dual plain flap configuration with different feedback locations.

The vibration penalty associated with in-plane noise reduction using the dual flap configuration with far-field and near-field left boom feedback locations is shown in Fig. 5.55. The vertical hub shear increased by 14% with far-field feedback and 47.1% with the near-field left boom feedback. This implies that the dual plain flap configuration produces similar, and in some cases better noise reduction, with a smaller vibration penalty than the single plain flap configuration. The flap

deflection schedule for the dual plain flap with near-field feedback is shown in Fig. 5.56. A strong 3/rev component is apparent, which is consistent with findings from the previous sections.

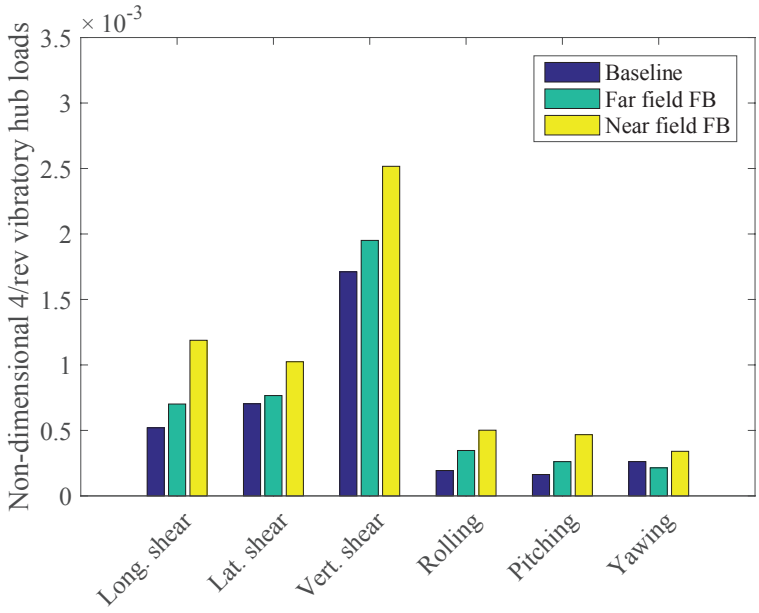

Fig. 5.55. Vibration penalty for the dual plain flap configuration with near and far-field feedback locations.

5.4.3 Passive Control of In-Plane Noise

In this section, the AVINOR/HELINOIR code employing the Galerkin type FEM is used to study in-plane noise control using passive tip geometry modification.

Passive in-plane noise control is implemented through a sweep, dihedral or anhedral tip spanning the outboard 10% of the blade. The orientation of the tip sweep relative to the straight portion is described by a sweep angle Λ_s, and is defined positive backward, as shown in Fig. 5.57(a). The tip inclination angle from

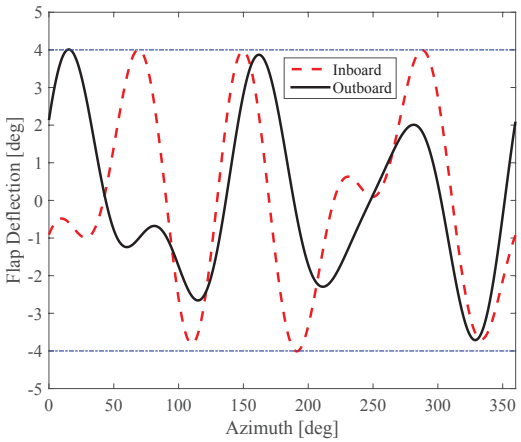

Fig. 5.56. Flap deflection history for dual flap configuration during active in-plane noise reduction using near-field Left Boom feedback.

the horizontal Λ_a is defined positive upward as shown in Fig. 5.57(b), therefore $\Lambda_a > 0°$ for a dihedral tip and $\Lambda_a < 0°$ for an anhedral tip. The blade is modeled using six beam-type finite elements along the elastic axis. Five elements are used to model the straight segment of the blade which spans 90% of the blade length, and remaining 10% is represented using a single finite element. A range of sweep, dihedral, and anhedral angles up to a maximum of $6°$ are considered.

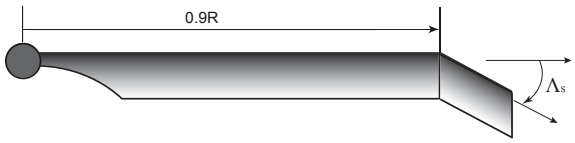

(a) Rotor blade with a swept tip geometry.

(b) Rotor blade with a dihedral tip geometry.

Fig. 5.57. Rotor blade with passive control.

5.4.3.1 Baseline Noise

The baseline LFSPL noise obtained using the finite-element based AVINOR /HELINOR code combination is shown in Fig. 5.58(a). Two regions of high noise levels, above 95dB, are predicted in front of the rotor, at around $(\frac{y}{r}, \frac{z}{r}) = (2, 0)$ and $(\frac{y}{r}, \frac{z}{r}) = (-7, 6)$. It is this directivity and the low frequency content of the LFSPL noise that increases the range at which the helicopter can be detected in forward flight. This is similar to the baseline obtained from global Galerkin structural model, Fig. 5.38(a). The differences could be attributed to the differences in the implementation of the wake model. The wake model used with the active control model was further modified to account for a higher wake resolution and the dual vortex structure [59, 87].

5.4.3.2 Impact of Tip Geometry Modification on Noise

The LFSPL obtained using a rotor blade with swept tip, $\Lambda_s = 6°$, is shown in Fig. 5.58(b). The change in the LFSPL from the baseline with the introduction of swept tip, obtained by taking the difference between the controlled and baseline case, is shown in Fig. 5.59(a). Similarly, the change in the LFSPL with a dihedral tip, $\Lambda_a = 6°$, is shown in Fig. 5.59(b) and the change in the LFSPL with an anhedral tip, $\Lambda_a = -6°$, is shown in Fig. 5.59(c).

For the case of the swept tip, Fig. 5.59(a), there is no significant change in the LFSPL in the in-plane direction on the horizon, $\frac{z}{R} = 0$ or $0°$ elevation angle. Therefore the swept tip does not contribute significantly to the in-plane noise on the

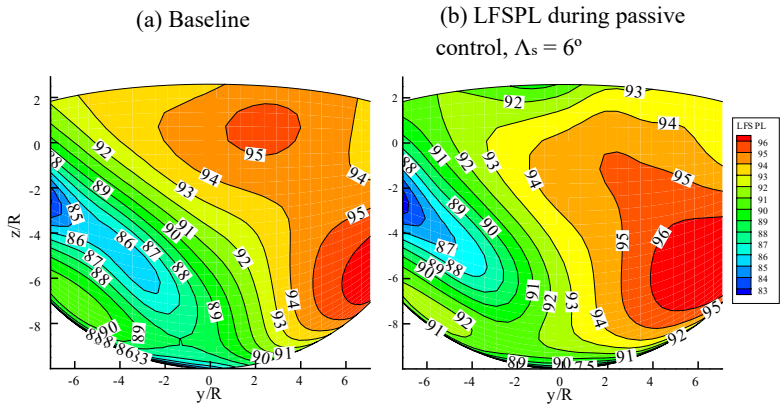

Fig. 5.58. In-plane LFSPL noise levels obtained using a baseline blade and blade with tip sweep, $\Lambda_s = 6°$, on the observer surface at 10R, $\mu = 0.3$.

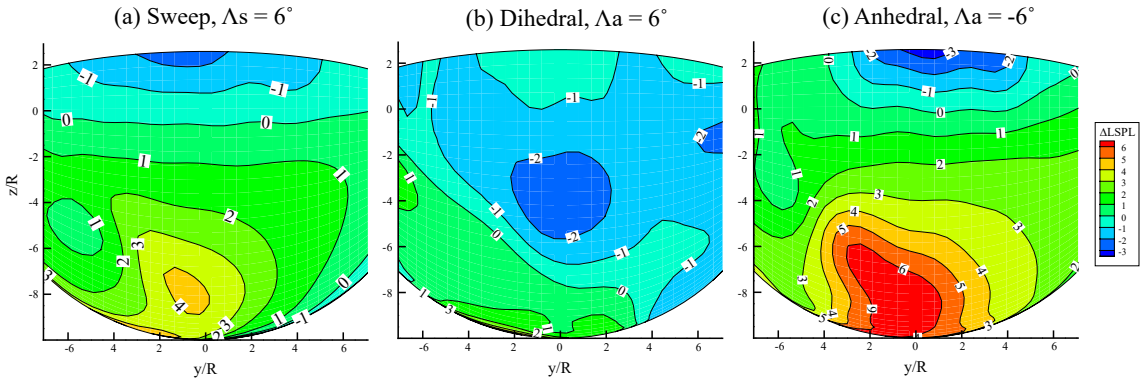

Fig. 5.59. Change in the LFSPL obtained at 10R for different tip geometries at $\mu = 0.3$.

horizon at moderate tip speed when quadrupole noise is not significant. This result is in agreement with Ref. 66. However, the swept tip reduces noise by up to 2 dB above the horizon, $\frac{z}{R} = 2$ or 15° elevation angle and more significantly causes a noise increase of up to 4dB below the horizon, $\frac{z}{R} = -7$ or -45° elevation angle. Similarly for the anhedral tip, Fig. 5.59(c), there is a noise reduction of up to 3dB above the horizon and a noise increase of up to 6dB below the horizon. This increase in the LFSPL noise below the horizon increases the range at which rotorcraft can be detected and is not desirable.

On the other hand, a dihedral tip, Fig. 5.59(b) achieved a noise reduction of up to 2dB for $\frac{z}{R} > -6$, or an elevation angle above -37°. This direction corresponds to the forward, slight downward tilt of the main rotor tip path plane and is significant for reducing the range at which the helicopter can be detected. However, a noise increase of up to 3dB is also generated in the left out-of-plane direction. These results suggest that the reduction of in-plane LFSPL noise can result in a severe noise penalty in the out-of-plane direction, which is consistent with the results obtained for the actively controlled case.

Noise Reduction Mechanism

To gain an improved understanding of the reason behind in-plane noise increase/decrease below the horizon, the acoustic pressure histories at an in-plane observer location for a rotor blade with and without tip geometry modifications are compared. Figure 5.60(a) shows the acoustic pressure history for the baseline blade at the observer location, $(\frac{x}{R}, \frac{y}{R}, \frac{z}{R}) = (-9.70, -0.27, -2.41)$. Figures 5.60(b), (c)

and (d) show the acoustic pressure history with tip geometry modifications at the same location. In all three cases, there are only marginal changes in the thickness noise. For the tip sweep and tip anhedral, there is an increase in the loading noise component in phase with the negative peak thickness noise component, resulting in an overall increase in the magnitude of the total acoustic pressure and in-plane LFSPL noise below the horizon. On the other hand, for a tip dihedral, there is an out-of-phase increase in the loading noise component, which cancels the negative peak thickness noise, resulting in an overall decrease in the magnitude of the total acoustic pressure.

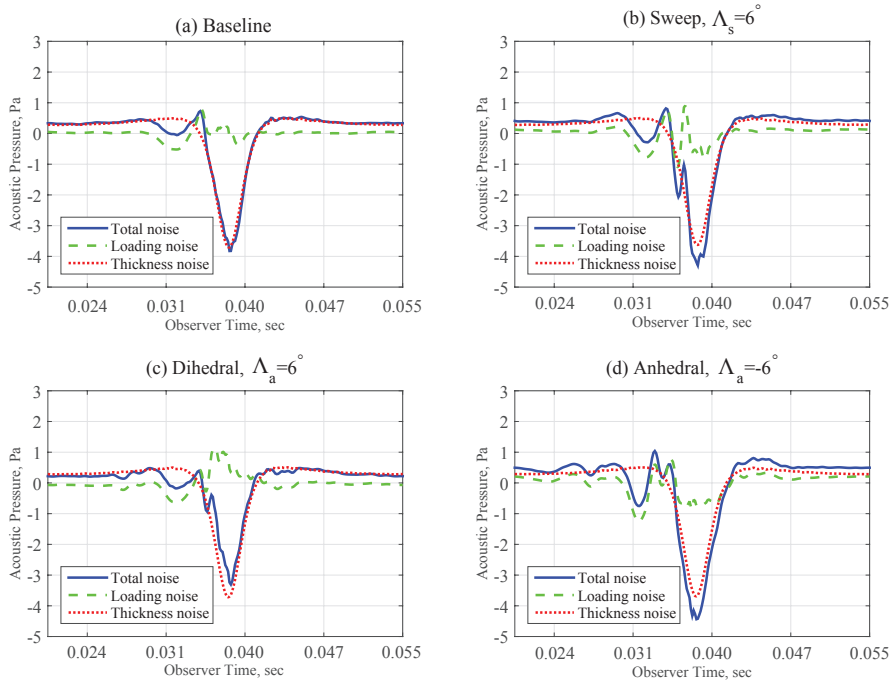

Fig. 5.60. Acoustic pressure histories at observer location $(\frac{x}{R}, \frac{y}{R}, \frac{z}{R}) = (-9.70, -0.27, -2.41)$ with baseline blade (a), swept tip (b), dihedral tip (c) and anhedral tip (d).

Insertion Loss

The insertion loss at the observer location,$(\frac{x}{R}, \frac{y}{R}, \frac{z}{R}) = (-9.70, -0.27, -2.41)$, for the sweep, dihedral and anhedral tip relative to the baseline blade is shown in Fig. 5.61. It is evident that the reduction in LFSPL for the dihedral tip, Fig 5.59(b), is reflected in the insertion loss of the 1st-6th BPF harmonics in Fig. 5.61(b). Conversely, the increase in LFSPL for the swept and anhedral tip, Fig 5.59(a) and (c), is reflected in the negative insertion loss, or insertion gain, of the 1st-6th BPF harmonics in Fig. 5.61(a) and (c). In all three cases, there is a overall insertion gain in the MFSPL, >6th BPF harmonic components, which is the frequency range of BVI noise. This suggests that passive control can add acoustic energy to the higher BPF harmonic components, contributing to near-field noise.

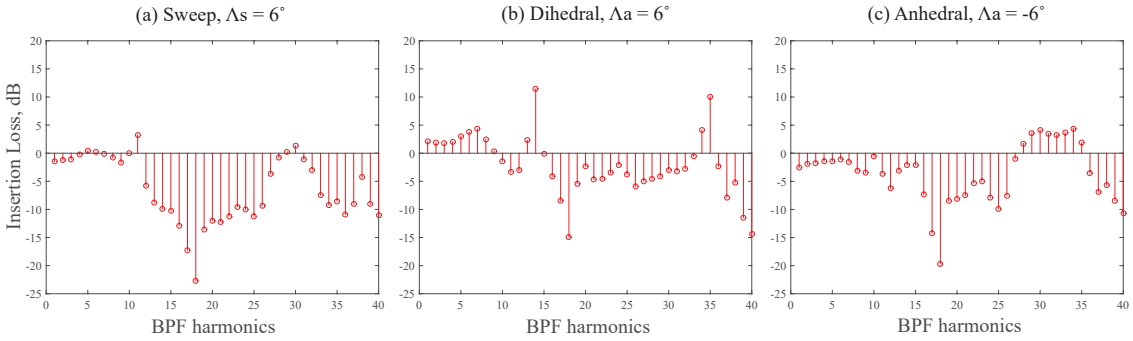

Fig. 5.61. Insertion loss due to passive control.

5.4.3.3 Impact of Tip Geometry Modification on Vibration

Fig 5.62 shows the associated 4/rev vibratory hub loads for the three tip geometries compared to the baseline blade. There is a reduction in all six components of

the vibratory hub loads for the swept and dihedral tip. For a tip sweep, $\Lambda_s = 6°$, the vertical hub shear was reduced by up to 32% and tip dihedral, $\Lambda_a = 6°$, the vertical hub shear was reduced by up to 19%. For tip anhedral, there is a reduction in the vertical hub shear of up to 9%, however, this was accompanied by an increase in the other vibratory hub load components. The reduction in the vibratory vertical hub shear, with the introduction of a tip sweep or tip anhedral is consistent with the findings in Ref. 21.

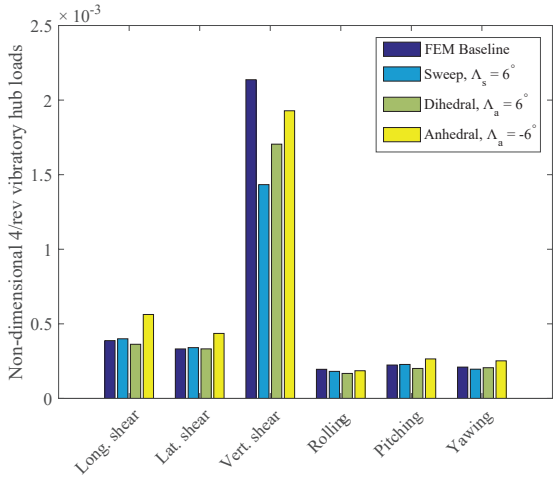

Fig. 5.62. Vibration levels for different tip geometries at $\mu = 0.3$

From the simulation results obtained, it is evident that a judicious choice of tip sweep and dihedral is required to obtain the optimum benefits of in-plane LF-SPL noise and vibration reduction. A tip dihedral reduces in-plane noise with a reduction in vibratory hub loads. A tip sweep results in a maximum reduction in vibratory hub loads. Although not simulated in this study, a tip sweep is also beneficial in delaying and therefore reducing HSI noise at high advance ratio [98]. A tip anhedral resulted in an increase in the in-plane LFSPL noise accompanied

by an increase in the in-plane, and side-to-side hub shears and moments, while generating a relatively marginal reduction in the vertical hub shears compared to the other passive control means. It is interesting to note that in the blade shape optimization study performed in Ref. 118, the blade design that improves aerodynamic performance and reduces overflight noise during forward flight is also one with backward sweep and mild dihedral.

5.4.4 Comparison Between Active and Passive Control

5.4.4.1 Noise Reduction Performance

By comparing the change in LFSPL due to passive control, Fig. 5.59, and active control using a single plain flap, Fig. 5.45(a), it can be seen that the reduction of in-plane LFSPL below the horizon, can best be achieved using active control where a reduction of up to 6dB was achieved. Active control also resulted in insertion loss over a broad BPF spectrum. On the other hand, a LFSPL reduction of only 2dB could be achieved using tip dihedral, $\Lambda_a = 6^\circ$. Passive control also resulted in insertion gain at the > 6th BPF harmonics, Fig. 5.61. In all cases, there is a LFSPL increase in the out-of-plane direction.

5.4.4.2 Impact on Vibration

It should be noted that there is a trade-off between in-plane LFSPL noise reduction performance, MFSPL, and vibration performance. For OBC, in-plane LFSPL reduction below the horizon is accompanied by an increase in vibratory hub loads,

Fig. 5.48. For tip sweep and tip anhedral, the increase in LFSPL is accompanied by a reduction in vibratory hub loads, Fig. 5.62. For the tip dihedral, even though LFSPL reduction is also accompanied by vibration reduction, the benefits are also offset by the increase in the MFSPL.

5.4.4.3 Noise Control Mechanism

The loading noise plays a critical role in in-plane noise reduction/amplification, even though the negative peak pressure generated by the thickness noise is the dominant contributor to the in-plane noise. In the case of a swept tip blade, Fig. 5.60, the magnitude of total noise increased due to the in-phase reduction of the loading noise, while the negative peak thickness noise was reduced marginally. On the other hand, a positive peak, anti-phase loading noise generated, as in the case of active control (Ref. 18), would cancel the dominant negative peak thickness noise to reduce the total in-plane noise.

The loading noise changes can be traced back to the rotor source using the loading noise source density before and after control. For a given observer location, the loading noise source density plot shows the loading noise source location on the rotor disk at source time [49]. The loading source density for the baseline blade and the blade with tip sweep is shown in Fig. 5.63. The two noise peaks at the observer time, t=0.035s and t=0.037s, in Figs 5.60(a) and (b) can be identified as the two elongated regions of concentrated loading source density at $\psi \approx 90^{\circ}$.

Figure 5.64 shows the changes in the loading noise source density of the noise due to tip sweep, $\Lambda_s = 6^{\circ}$, and active control, obtained by taking the difference

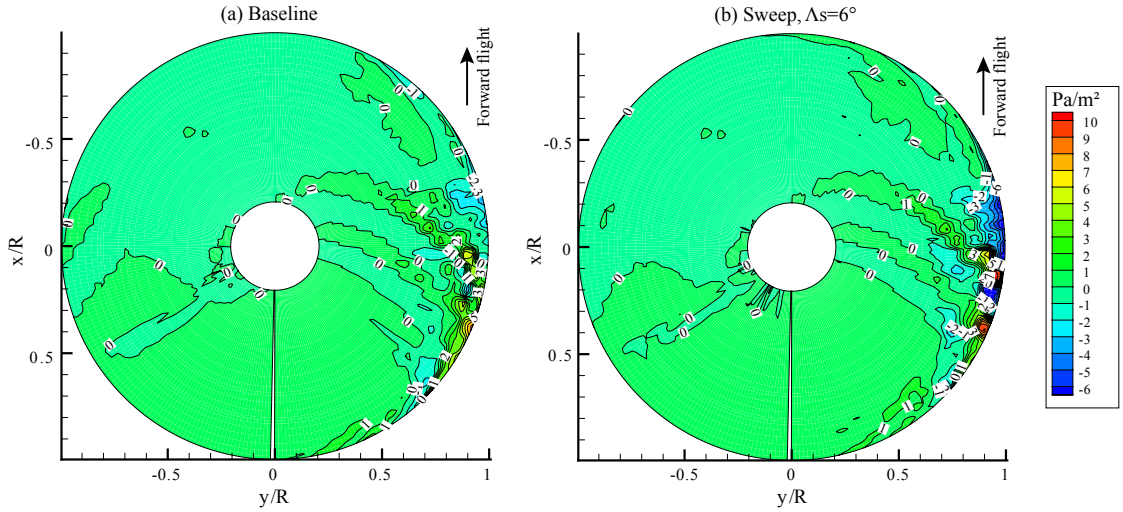

Fig. 5.63. Loading noise source density of baseline blade and blade with tip sweep, $\Lambda_s = 6°$.

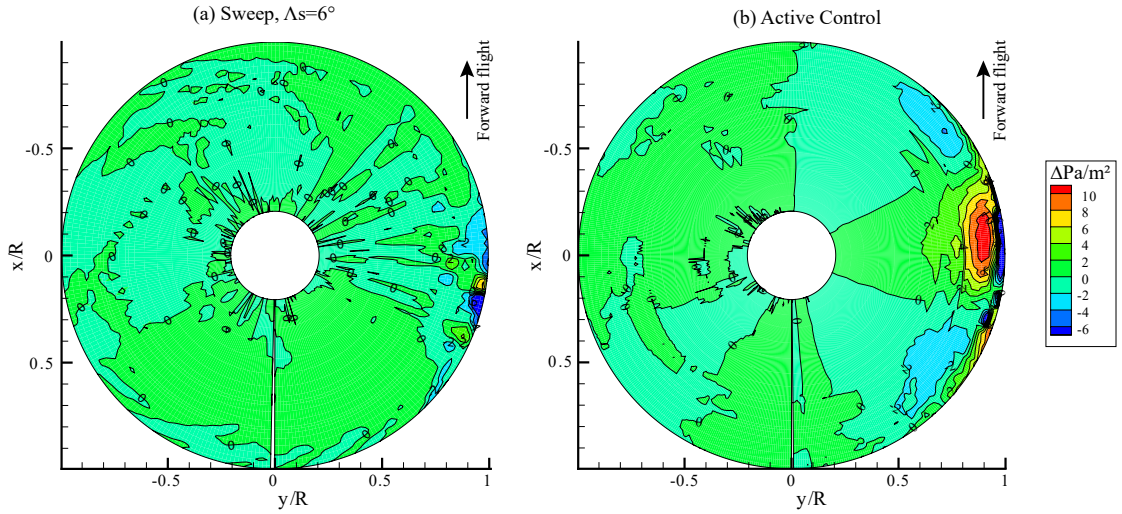

Fig. 5.64. Change in loading noise source density due to implementation of passive /active control.

between the controlled and baseline case. The reduction of loading noise at the forward observer location using tip sweep, Fig. 5.60(b), can be attributed to the reduction of the loading noise source at the tip sweep, >0.9R, when the blade is at the $\psi \approx 90^{\circ}$ location, Fig. 5.64(a). The positive loading noise [18], or anti-noise, can be attributed to effects of the active flap and the blade tip segment on the advancing side, when the blade is at the $\psi \approx 90^{\circ}$ location. By comparing Fig. 5.64(a) and (b), it is evident that a $12\%c$ plain flap is capable of exercising greater control authority than a 6°, 10%R tip sweep, over the loading noise source contribution to reduce the thickness noise source.

CHAPTER VI

SUMMARY AND CONCLUSIONS

This dissertation demonstrated the use of active and passive approaches for in-plane noise reduction on a hingeless rotor configuration resembling the MBB BO-105 rotor, while tracking the vibrations induced during noise reduction. First a parametric study was performed to examine the impact of varying torsional stiffness on the vibration and noise performance of plain trailing edge flaps and microflaps. Simulations were performed at a low speed descending flight condition with significant BVI effects using the AVINOR code, combined with a CFD-based unsteady reduced order aerodynamic model, coupled with an aeroacoustic code WOPWOP.

Subsequently, to overcome the limitations of WOPWOP, a new suite of computational tools capable of predicting in-plane low frequency rotorcraft noise and its control was developed. This was achieved by coupling AVINOR with a compact noise prediction code named HELINOIR, in a new aeroelastic-aeracoustic framework. The acoustic calculations are based on a compact loading model, which takes into account both the airfoil lift and drag forces. Acoustic predictions from

this new code combination were validated against the HART and Boeing SMART Rotor experimental results. The comparisons show that the new code is capable of accurately predicting both in-plane and out-of-plane noise.

The new combined AVINOR/HELINOIR code suite was used for in-plane LF-SPL noise prediction and control, employing either actively controlled plain flaps operating in closed-loop mode or passive blade tip geometry modifications, for level flight at moderate advance ratios. For active control, various far-field and on-board near-field feedback microphone locations were examined using single and dual flap configurations. For passive control, three tip geometries, namely sweep, dihedral, and anhedral, were studied. Noise reduction and the associated vibration penalty were examined.

6.1 Conclusions

The principal conclusions obtained from the research conducted in this dissertation are summarized next:

1. From the parametric study conducted at the beginning of this dissertation, it was found that the OBC devices considered (flaps and microflaps) yielded the best vibration reduction performance when the blade torsional frequency is in the vicinity of 3.17/rev. An exception to this rule is a single plain flap that yields the best performance at a torsional frequency of 4.5/rev. The performance of OBC devices degrades as the torsional frequency increases.

2. Changing the single microflap location from 6%c to 10%c from the trailing

edge results in a 10% decrease in vibration reduction performance.

3. The best noise reduction is also achieved at a torsional frequency of 3.17/rev for both the single and dual flap/ microflap configurations. The noise reduction performance also degrades significantly with increasing torsional stiffness. Furthermore, the noise reduction performance displays a higher sensitivity to changes in torsional frequency.

4. The dual flap configuration is more effective than a single flap configuration with the same span for both active noise and vibration reduction.

5. A 20%c trailing edge flap has superior vibration reduction performance compared to a sliding microflap with a height of 1.5%c, for the same spanwise location and blade structural properties.

6. A sliding microflap with height of 1.5%c achieves better noise reduction when compared to a 20% plain trailing edge flap for the same spanwise location and blade structural properties.

7. The acoustic and blade loads predictions obtained from the new AVINOR/ HELINOIR code suite were validated against experimental results from the HART I and Boeing SMART Rotor program tests. The agreement between the computed results and the experiments was good.

8. The acoustic predictions from the AVINOR/HELINOIR code suite were verified against computations performed using the previous AVINOR employing the WOPWOP acoustic module and the results obtained from the two

codes were similar.

9. The compact acoustic model used in the HELINOIR code provides efficient and accurate prediction of far-field in-plane noise, compared to the full pressure distribution and geometry model obtained from CFD.

10. A feedback microphone in the near-field, on the left boom tip, was found to be an ideal location for implementing active closed-loop control of in-plane noise for the level cruise flight at moderate advance ratios ($\mu = 0.2$ and $\mu = 0.3$). The noise reduction obtained using feedback at this location was comparable to the far-field feedback locations considered. For the hypothetical feedback microphone located at 10R in front of the helicopter, similar noise reduction performance was achieved regardless whether a single or an array of three feedback microphones was used.

11. Active closed-loop in-plane noise reduction of up to 6dB was obtained below the horizon with plain trailing edge flaps using a feedback microphone located at the left boom tip. The insertion loss in-plane was achieved over a wide range of BPF harmonics. However, this in-plane noise reduction was accompanied by an out-of-plane noise increase of up to 18dB.

12. The flap deflection generated by the HHC controller produced a properly phased loading noise component that canceled the thickness noise component. This finding is consistent with the anti-noise approach used in earlier open-loop studies. The ability to control loading noise is critical to LFSPL

reduction. The flap deflection contained a strong 3/rev component for the 4-bladed MBB BO-105 rotor.

13. There is an inherent vibration penalty associated with active in-plane noise reduction. The increase in the vertical hub shear was about 60% for the single plain flap. This vibration penalty resembles that incurred during BVI noise reduction at low speed descending flight.

14. A dual flap configuration achieved noise reduction over a wider azimuth with a lower vibration penalty when compared to a single flap configuration.

15. A Galerkin type finite element model for the MBB BO105 rotor was implemented in the AVINOR/HELINOIR code suite and verified against the earlier AVINOR/ WOPWOP combination. The results predicted by two codes were similar.

16. Passive control, implemented through a dihedral tip of $\Lambda_a = 6^\circ$, results in an in-plane noise reduction of 2dB below the horizon at a moderate advance ratio $\mu = 0.3$. On the other hand, the anhedral and swept tips produce LFSPL increases of up to 4dB and 6dB respectively, below the horizon. For all three cases, there is an insertion gain at the higher harmonics in-plane and an increase in the out-of-plane LFSPL noise.

17. The swept and dihedral tips reduce the vibratory hub loads for a helicopter in level flight, $\mu = 0.3$. A sweep angle of $\Lambda_s = 6^\circ$ provides the most effective vibratory load reduction, reducing the 4/rev vertical hub shear amplitude by

up to 32%. The anhedral tip increases the vibratory hub loads. Therefore, a combination of tip sweep and dihedral may be ideal for in-plane LFSPL noise and vibration reduction.

18. In most cases there is a trade-off between in-plane LFSPL noise reduction below the horizon, the MFSPL, and vibration performance.

19. The thickness noise component, which is the principal contributor to in-plane noise, is not modified significantly by the passive or active control approaches considered. Controlling the loading noise component is critical for reduction of in-plane LFSPL noise. Active 12%c plain flap has superior greater control authority over the loading noise source, when compared to passive approaches.

6.2 Future Work

It was shown in this dissertation that active control of in plane noise is difficult and it is usually accompanied by a significant vibration penalty. This was also found in another recent experimental study (Ref. 105). Therefore the only feasible approach for designing a rotor with improved lower noise and vibration levels, is by conducting a multi-disciplinary design optimization study where the blade, OBC system and control law are designed simultaneously in an integrated manner. Such an approach has been also suggested in Ref. 118, however carrying out such a detailed computational study would represent an important contribution to the state of the art.

APPENDICES

APPENDIX A

Global Galerkin Model

The global Galerkin stuctural dynamic model is used for modeling the rotor blade with active OBC, implemented by a plain flap or the microflap.

A.1 Modeling Assumptions

The basic assumptions used to develop the aeroelastic analysis model for the rotor blade are as follows:

1. The rotor blade is cantilevered at the hub, with a root offset e from the axis of rotation (see Fig. A.2).

2. The blade has a precone angle β_p (see Fig. A.2) and it has built-in pretwist distribution θ_{tw} about the elastic axis of the blade.

3. The blade has no sweep, droop or torque offset.

4. The blade cross section is assumed to be symmetric with respect to its major principal axes.

5. The blade feathering axis is coincident with the elastic axis.

6. The deflections in the blade are assumed to be moderate and the strains to be small.

7. The blade has completely coupled flap, lead-lag, torsional and axial dynamics.

8. The blade is assumed to be inextensible.

9. The rotor shaft is assumed to be rigid and body degrees of freedom are suppressed.

10. The structural effects of the microflap and the conventional trailing edge flap are neglected.

11. The distributed aerodynamic loads are obtained using CFD-based RFA aerodynamic model.

12. The induced inflow is nonuniform and is obtained by a free wake analysis included in the aeroelastic model.

13. Reverse flow effects are included by setting the lift and moment equal to zero and by changing the sign of the drag force inside the reverse flow region.

14. The speed of rotation Ω of the rotor is constant.

15. The helicopter is in trimmed, steady, level or descending flight. Either propulsive or wind tunnel trim can be implemented.

A.2 Coordinate Systems

The following six coordinate systems are used to formulate the aeroelastic model:

"0" System: This is an inertial reference frame with origin at the hub center O_H oriented such that the gravitational vector is aligned along the negative z_0 axis. The tail of the helicopter is assumed to lie in the $x_0 z_0$ plane in the direction of the positive x_0 axis.

"1" System: This is an inertial reference frame with origin at O_H. The y_1 axis is coincident with the y_0 axis, and the z_1 axis pitched forward at an angle α_R about the y_0 axis so that it is aligned with the rotor axis of rotation. The "1" system provides the non-rotating reference frame. The "0" and "1" systems are depicted in Fig. A.1.

"2" System: This system has its origin at O_H. The z_2 axis is coincident with the z_1 axis but rotates with the blades about the z_1 axis. The "2" system is the rotating reference frame.

"3" System: This system rotates with the blades and has its origin at the blade root located at a distance e away from the axis of rotation along the x_2 axis, as shown in Figure A.2. The x_3 axis is "preconed" by an angle β_p around

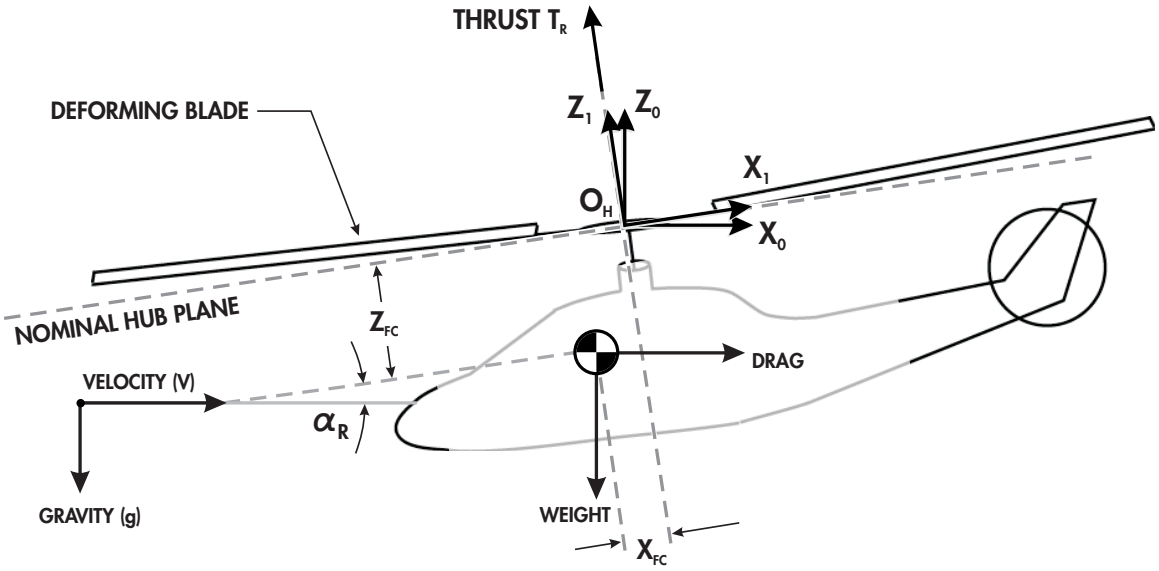

Fig. A.1. Transformation from the "0" system to the "1" system

the y_2 axis such that the x_3 axis lies along the undeformed elastic axis of the blade. The principal axes of the undeformed blade cross-section at any point along the span lie in a plane parallel to the $y_3 z_3$ plane and are oriented at an angle $\theta_G(x)$ about the x_3 axis. Angle $\theta_G(x)$ is the sum of collective and cyclic pitch inputs at the root and geometric pretwist of the blade at the particular point along the span, Eqn. A.1.

$$\theta_G(x) = \theta_{PC}(x) + \theta_{tw}(x) \tag{A.1}$$

The "3" system provides the undeformed reference frame.

"4" System: This is a blade attached system. Before deformation, the "3" and "4" systems are parallel. After deformation, the "4" system is translated and rotated such that the x_4 axis is tangent to the elastic axis of the blade at each blade cross-section along the span. The principal axes of the blade cross-

section lie in the $y_4 z_4$ plane, rotated at an angle $\theta_G(x)$ about the x_4 axis. The "4" system provides the deformed reference frame. The relationships between the "2", "3" and "4" systems are depicted on Fig. A.2.

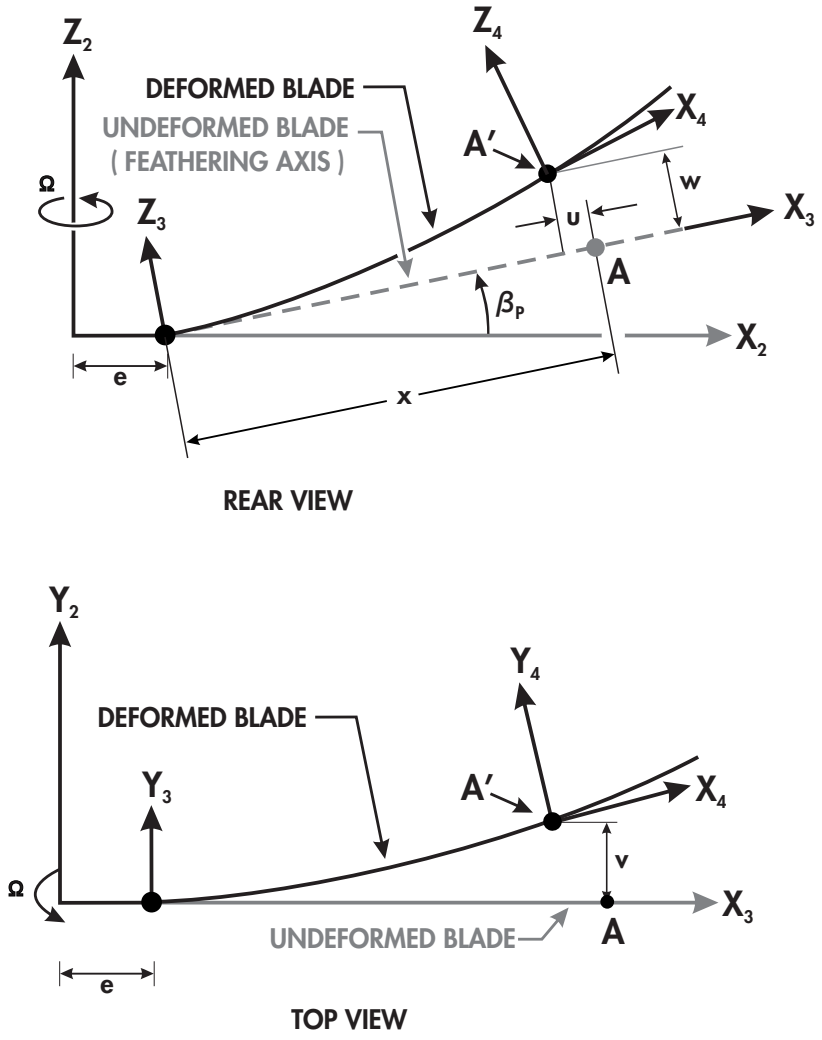

Fig. A.2. The transformation from the "2" system to the "4" system

"5" System: This is also a blade attached system and represents the "4" system with the torsional deformation removed, as shown in Figure A.3. Thus, the principal axes of the blade cross section are rotated at an angle $\theta_G(x) + \phi(x)$ about the x_5 axis where $\phi(x)$ is the elastic twist. This reference frame is conve-

nient in the derivation of the aerodynamic loads. The relationships between the "3", "4" and "5" systems are depicted on Fig. A.3.

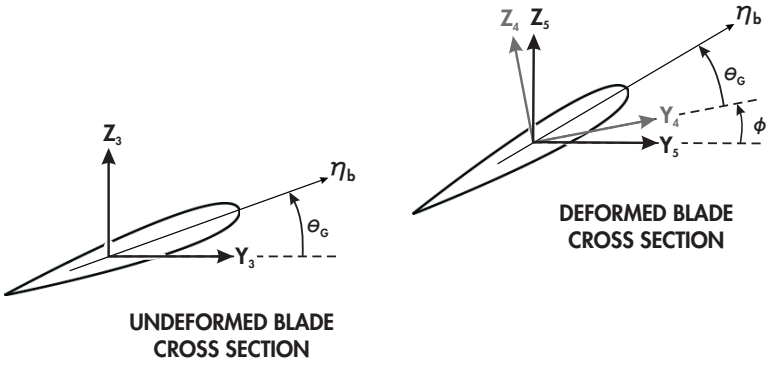

Fig. A.3. The transformation from the "3" system to the "5" system

A.3 Coordinate Transformations

The set of coordinate transformation matrices that were used to move between the various systems listed above are presented below [Ref. 72, Eqn. (4.1)-(4.20)]:

"0" system to "1" system

$$\begin{Bmatrix} \hat{e}_{x1} \\ \hat{e}_{y1} \\ \hat{e}_{z1} \end{Bmatrix} = \begin{bmatrix} \cos\alpha_R & 0 & \sin\alpha_R \\ 0 & 1 & 0 \\ -\sin\alpha_R & 0 & \cos\alpha_R \end{bmatrix} \begin{Bmatrix} \hat{e}_{x0} \\ \hat{e}_{y0} \\ \hat{e}_{z0} \end{Bmatrix} \tag{A.2}$$

"1" system to "2" system

$$\begin{Bmatrix} \hat{e}_{x2} \\ \hat{e}_{y2} \\ \hat{e}_{z2} \end{Bmatrix} = \begin{bmatrix} \cos\psi & \sin\psi & 0 \\ -\sin\psi & \cos\psi & 0 \\ 0 & 0 & 1 \end{bmatrix} \begin{Bmatrix} \hat{e}_{x1} \\ \hat{e}_{y1} \\ \hat{e}_{z1} \end{Bmatrix} \tag{A.3}$$

$$\begin{Bmatrix} \hat{e}_{x2} \\ \hat{e}_{y2} \\ \hat{e}_{z2} \end{Bmatrix} = \begin{bmatrix} \cos\psi & \sin\psi & 0 \\ -\sin\psi & \cos\psi & 0 \\ 0 & 0 & 1 \end{bmatrix} \begin{Bmatrix} \hat{e}_{x1} \\ \hat{e}_{y1} \\ \hat{e}_{z1} \end{Bmatrix}$$

$$\hat{e}_2 = T_{21}\hat{e}_1 \tag{A.4}$$

"2" system to "3" system

$$\begin{Bmatrix} \hat{e}_{x3} \\ \hat{e}_{y3} \\ \hat{e}_{z3} \end{Bmatrix} = \begin{bmatrix} 1 & 0 & \beta_p \\ 0 & 1 & 0 \\ -\beta_p & 0 & 1 \end{bmatrix} \begin{Bmatrix} \hat{e}_{x2} \\ \hat{e}_{y2} \\ \hat{e}_{z2} \end{Bmatrix} \tag{A.5}$$

$$\hat{e}_3 = T_{32}\hat{e}_2 \tag{A.6}$$

"3" system to "4" system The coordinate transformation from the undeformed "3" system to the deformed "4" system is obtained using a sequence of angular rotations. The sequence used in this study is flap-lag-torsion, and consists of 1) a flap rotation by the angle $w_{,x}$ clockwise about the y_3 axis, 2) a lead-lag rotation by the angle $v_{,x}$ counterclockwise about the z_3 axis, and 3) a torsional rotation given by the twist angle ϕ counterclockwise about the x_4 axis, in that order. Hence, the coordinate transformation from the undeformed "3"

system to the deformed "4" system is given by the matrix product:

$$\left\{\begin{array}{c}\hat{e}_{x4}\\ \hat{e}_{y4}\\ \hat{e}_{z4}\end{array}\right\} = \left[\begin{array}{ccc}1 & 0 & 0\\ 0 & \cos\phi & \sin\phi\\ 0 & -\sin\phi & \cos\phi\end{array}\right] \cdot \left[\begin{array}{ccc}1 & v_{,x} & 0\\ -v_{,x} & 1 & 0\\ 0 & 0 & 1\end{array}\right] \cdot \left[\begin{array}{ccc}1 & 0 & w_{,x}\\ 0 & 1 & 0\\ -w_{,x} & 0 & 1\end{array}\right] \left\{\begin{array}{c}\hat{e}_{x3}\\ \hat{e}_{y3}\\ \hat{e}_{z3}\end{array}\right\} \tag{A.7}$$

Note that the small angle assumptions $\cos v_{,x} \cong 1$, $\cos w_{,x} \cong 1$, $\sin v_{,x} \cong v_{,x}$, and $\sin w_{,x} \cong w_{,x}$ have been made. Performing the matrix multiplication yields:

$$\left\{\begin{array}{c}\hat{e}_{x4}\\ \hat{e}_{y4}\\ \hat{e}_{z4}\end{array}\right\} = \left[\begin{array}{ccc}1 & v_{,x} & w_{,x}\\ -v_x\cos\phi - w_{,x}\sin\phi & \cos\phi & \sin\phi - v_{,x}\,w_{,x}\cos\phi\\ v_{,x}\sin\phi - w_{,x}\cos\phi & -\sin\phi & \cos\phi + v_{,x}\,w_{,x}\sin\phi\end{array}\right] \left\{\begin{array}{c}\hat{e}_{x3}\\ \hat{e}_{y3}\\ \hat{e}_{z3}\end{array}\right\}$$

$$\hat{e}_4 = T_{43}\hat{e}_3 \tag{A.8}$$

"3" system to "5" system

$$\left\{\begin{array}{c}\hat{e}_{x5}\\ \hat{e}_{y5}\\ \hat{e}_{z5}\end{array}\right\} = \left[\begin{array}{ccc}1 & v_{,x} & w_{,x}\\ -v_{,x} & 1 & -w_{,x}\,v_{,x}\\ -w_{,x} & 0 & 1\end{array}\right] \left\{\begin{array}{c}\hat{e}_{x3}\\ \hat{e}_{y3}\\ \hat{e}_{z3}\end{array}\right\}$$

$$\hat{e}_5 = T_{53}\hat{e}_3 \tag{A.9}$$

"4" system to "5" system

$$\begin{Bmatrix} \hat{e}_{x5} \\ \hat{e}_{y5} \\ \hat{e}_{z5} \end{Bmatrix} = \begin{bmatrix} 1 & 0 & 0 \\ 0 & \cos\phi & -\sin\phi \\ 0 & \sin\phi & \cos\phi \end{bmatrix} \begin{Bmatrix} \hat{e}_{x4} \\ \hat{e}_{y4} \\ \hat{e}_{z4} \end{Bmatrix}$$

$$\hat{e}_5 = T_{54}\hat{e}_4 \tag{A.10}$$

A.4 Ordering Scheme

An ordering scheme is applied to eliminate the higher order nonlinear terms in the structural equations of motion, in a consistent manner. This is accomplished by assigning orders of magnitude to various commonly encountered nondimensional physical terms and then neglecting terms with an order higher than a predetermined threshold value.

It is assumed the slopes of the deformed rotor blades are of the order ϵ ($0.10 \leq \epsilon \leq 0.20$), based on the moderate deflection assumption. The ordering scheme assumes the terms of order ϵ^2 or higher can be neglected with respect to terms of order 1, i. e.

$$O(1) + O(\epsilon^2) \cong 1 \tag{A.11}$$

A careful and systematic application of this ordering scheme yields expressions of manageable size and with sufficient accuracy for rotor stability and response calculations.

To assign orders of magnitude to individual terms, they must first be expressed

in nondimensional form. This is performed using the following reference quantities:

$$\begin{aligned} \text{[length]} &= R, \quad \text{rotor radius,} \\ \text{[mass]} &= M_b, \quad \text{mass of one blade,} \\ \text{[time]} &= \frac{1}{\Omega}, \quad \text{inverse of the rotor speed.} \end{aligned}$$

Orders of magnitude have been assigned to common nondimensional quantities as follows:

$$\begin{aligned} O(1): &\quad \frac{x}{R}, \frac{L_b}{R}, \frac{m_b}{(M_b/R)}, \frac{\rho_b}{(M_b/R^3)}, \mu, \psi, \cos\psi, \sin\psi, \\ &\quad a_o, R\frac{\partial}{\partial x}, \frac{1}{\Omega}\frac{\partial}{\partial t}, \frac{\partial}{\partial \psi} \\ O(\epsilon^{1/2}): &\quad \frac{L_{cs}}{R}, \theta_G, \delta \\ O(\epsilon): &\quad \frac{c_b}{R}, \frac{e}{R}, \frac{c_{cs}}{R}, \frac{m_c}{(M_b/R)}, \frac{X_h}{R}, \theta_{pt}, \lambda, \alpha_R, \beta_p, \\ &\quad \frac{v}{R}, \frac{w}{R}, v_{,x}, w_{,x}, \phi \\ O(\epsilon^{3/2}): &\quad \frac{M_c}{M_b}, \frac{X_A}{R}, \frac{X_{Ib}}{R}, \frac{X_{Ic}}{R}, \frac{X_{IIb}}{R}, \frac{X_{IIc}}{R}, C_{d0} \\ O(\epsilon^2): &\quad \frac{u}{R}, \frac{EI_{\zeta\zeta}}{M_b R^3 \Omega^2}, \frac{EI_{\eta\eta}}{M_b R^3 \Omega^2}, \frac{fC_{df}}{R^2}, \\ O(\epsilon^{5/2}): &\quad \frac{I_{MB2}}{M_b R}, \frac{I_{MB3}}{M_b R} \\ O(\epsilon^3): &\quad \frac{g}{\Omega^2 R}, \frac{GJ_b}{M_b R^3 \Omega^2} \\ O(\epsilon^{7/2}): &\quad \frac{I_{MC2}}{M_b R}, \frac{I_{MC3}}{M_b R} \end{aligned}$$

The orders of magnitude presented here are consistent with those used in Refs. [70, 73, 95].

A.5 Equations of Motion for the Elastic Blade

The hingeless blades are modeled as slender rods of linearly elastic, homogeneous material, cantilevered at an offset e from the rotor hub, using a blade model taken from Ref. 70. This blade model describes the fully coupled flap-lag-torsional dynamics of an isotropic blade. The blade model described in Ref. 70 was derived to reflect the deformation sequence flap-lag-torsion.

The equations of motion for the elastic blade consist of a set of nonlinear partial differential equations of motion, with the distributed loads left in general symbolic form. The distributed loads on the blade, not including control surface loads, can be expressed in the "3" system as:

$$\mathbf{p_b} = p_{bx3}\hat{e}_{x3} + p_{by3}\hat{e}_{y3} + p_{bz3}\hat{e}_{z3}, \tag{A.12}$$

$$\mathbf{q_{Mb}} = q_{bx3}\hat{e}_{x3} + q_{by3}\hat{e}_{y3} + q_{bz3}\hat{e}_{z3}, \tag{A.13}$$

where $\mathbf{p_b}$ and $\mathbf{q_{Mb}}$ represent the total distributed spanwise force and moment, respectively. The equations of motion for the elastic blade, derived in Ref. 72, Eqs. (4.23)-(4.25), are then given by:

Flap Equation

$$
\begin{aligned}
&- [(EI_{\zeta\zeta} - EI_{\eta\eta}) \sin\theta_G \cos\theta_G (v_{,xx} + 2\phi w_{,xx}) \\
&+ (EI_{\zeta\zeta} - EI_{\eta\eta}) \phi v_{,xx} \cos 2\theta_G + (EI_{\zeta\zeta} \sin^2\theta_G + EI_{\eta\eta} \cos^2\theta_G) w_{,xx} \\
&- TX_{IIb} (\sin\theta_G + \phi \cos\theta_G)]_{,xx} + (GJ_b \phi_{,x} v_{,xx})_{,x} + (w_{,x} T)_{,x} \\
&- (v_{,x} q_{bx3})_{,x} + q_{by3,x} + p_{bz3} = 0.
\end{aligned}
\tag{A.14}
$$

Lag Equation

$$
\begin{aligned}
&- [(EI_{\zeta\zeta} \cos^2\theta_G + EI_{\eta\eta} \sin^2\theta_G) v_{,xx} + (EI_{\zeta\zeta} - EI_{\eta\eta}) \phi w_{,xx} \cos 2\theta_G \\
&+ (EI_{\zeta\zeta} - EI_{\eta\eta}) \sin\theta_G \cos\theta_G (w_{,xx} - 2\phi v_{,xx}) \\
&- TX_{IIb} (\cos\theta_G - \phi \sin\theta_G)]_{,xx} - (GJ_b \phi_{,x} w_{,xx})_{,x} + (v_{,x} T)_{,x} \\
&+ (w_{,x} q_{bx3})_{,x} - q_{bz3,x} + p_{by3} = 0.
\end{aligned}
\tag{A.15}
$$

Torsional Equation

$$
\begin{aligned}
&[GJ_b (\phi_{,x} - v_{,x} w_{,xx})]_{,x} \\
&+ (EI_{\zeta\zeta} - EI_{\eta\eta}) [({v_{,xx}}^2 - {w_{,xx}}^2) \sin\theta_G \cos\theta_G - v_{,xx} w_{,xx} \cos 2\theta_G] \\
&+ TX_{IIb} (w_{,xx} \cos\theta_G - v_{,xx} \sin\theta_G) + q_{bx3} + v_{,x} q_{by3} + w_{,x} q_{bz3} = 0,
\end{aligned}
\tag{A.16}
$$

where T is the axial tension.

A.6 Incorporation of the Control Surfaces in the Blade Equations of Motion

The following assumptions have been used for incorporating the effects of the microflap and the active plain flap in the dynamic equations of equilibrium:

1. The microflap and the plain flap are constrained to slide or rotate only in the plane of the blade cross section;

2. The control surfaces are assumed to be inextensible;

3. The inertial and aerodynamic effects of the control surfaces are included in the model. The effect of the microflap/flap on the structural properties of the blade is assumed to be negligible. Thus, the control surfaces influence the behavior of the blade only through their contribution to the spanwise distributed loads on the blade.

The distributed force and moment on the blade due to the control surfaces can be represented in the "3" system by [Ref. 72, Eqs. (4.26)-(4.27)]:

$$\mathbf{p_c} = p_{cx3}\hat{e}_{x3} + p_{cy3}\hat{e}_{y3} + p_{cz3}\hat{e}_{z3}, \tag{A.17}$$

$$\mathbf{q_c} = q_{cx3}\hat{e}_{x3} + q_{cy3}\hat{e}_{y3} + q_{cz3}\hat{e}_{z3}. \tag{A.18}$$

For a single microflap/flap configuration, with the center of the microflap/flap control surface located at a distance x_{cs}^1 from the blade root, the distributed loads are given by:

$$\mathbf{p_c}, \mathbf{q_c} = \begin{cases} 0 & for \quad x < x_{cs}^1 - \frac{L_{cs}}{2} \\ \mathbf{p_c^1}, \mathbf{q_c^1} & for \quad x_{cs}^1 - \frac{L_{cs}}{2} \leq x \leq x_{cs}^1 + \frac{L_{cs}}{2} \\ 0 & for \quad x > x_{cs}^1 + \frac{L_{cs}}{2} \end{cases}$$

where $\mathbf{p_c^1}$ and $\mathbf{q_c^1}$ represent the distributed loads due to the single microflap/flap, and are described in the next section. For a dual microflap/flap configuration, with the center of the second microflap/flap control surface located at a distance x_{cs}^2 from the blade root, the distributed loads are given by:

$$\mathbf{p_c}, \mathbf{q_c} = \begin{cases} 0 & for \quad x < x_{cs}^1 - \frac{L_{cs}}{2} \\ \mathbf{p_c^1}, \mathbf{q_c^1} & for \quad x_{cs}^1 - \frac{L_{cs}}{2} \leq x \leq x_{cs}^1 + \frac{L_{cs}}{2} \\ 0 & for \quad x_{cs}^1 + \frac{L_{cs}}{2} < x < x_{cs}^2 - \frac{L_{cs}}{2} \\ \mathbf{p_c^2}, \mathbf{q_c^2} & for \quad x_{cs}^2 - \frac{L_{cs}}{2} \leq x \leq x_{cs}^2 + \frac{L_{cs}}{2} \\ 0 & for \quad x > x_{cs}^2 + \frac{L_{cs}}{2} \end{cases}$$

where $\mathbf{p_c^1}$, $\mathbf{q_c^1}$ and $\mathbf{p_c^2}$, $\mathbf{q_c^2}$ represent distributed loads due to the first and second control surfaces, respectively.

The effect of the control surfaces is included in the blade equations of motion by adding the distributed loads due to the control surfaces, given in Eqs. (A.17)-(A.18), to the distributed loads for the blade alone. The equations of motion for the

blade, Eqs. (A.14)-(A.15), can be rewritten to reflect this change as:

Flap Equation

$$
\begin{aligned}
&-[(EI_{\zeta\zeta}-EI_{\eta\eta})\sin\theta_G\cos\theta_G(v_{,xx}+2\phi w_{,xx})\\
&+(EI_{\zeta\zeta}-EI_{\eta\eta})\phi v_{,xx}\cos 2\theta_G+(EI_{\zeta\zeta}\sin^2\theta_G+EI_{\eta\eta}\cos^2\theta_G)w_{,xx}\\
&-TX_{IIb}(\sin\theta_G+\phi\cos\theta_G)]_{,xx}+(GJ_b\phi_{,x}\,v_{,xx})_{,x}+(w_{,x}\,T)_{,x}\\
&-(v_{,x}\,(q_{bx3}+q_{cx3}))_{,x}+(q_{by3}+q_{cy3})_{,x}+(p_{bz3}+p_{cz3}) \;=\; 0.
\end{aligned}
\tag{A.19}
$$

Lag Equation

$$
\begin{aligned}
&-[(EI_{\zeta\zeta}\cos^2\theta_G+EI_{\eta\eta}\sin^2\theta_G)v_{,xx}+(EI_{\zeta\zeta}-EI_{\eta\eta})\phi w_{,xx}\cos 2\theta_G\\
&+(EI_{\zeta\zeta}-EI_{\eta\eta})\sin\theta_G\cos\theta_G(w_{,xx}-2\phi v_{,xx})\\
&-TX_{IIb}(\cos\theta_G-\phi\sin\theta_G)]_{,xx}\\
&-(GJ_b\phi_{,x}\,w_{,xx})_{,x}+(v_{,x}\,T)_{,x}+(w_{,x}\,(q_{bx3}+q_{cx3}))_{,x}\\
&-(q_{bz3}+q_{cz3})_{,x}+(p_{by3}+p_{cy3}) \;=\; 0.
\end{aligned}
\tag{A.20}
$$

Torsion Equation

$$
\begin{aligned}
[GJ_b(\phi_{,x} - v_{,x}\, w_{,xx}\,)]_{,x} + (EI_{\zeta\zeta} - EI_{\eta\eta})[(v_{,xx}{}^2 - w_{,xx}{}^2)\sin\theta_G \cos\theta_G \\
- v_{,xx}\, w_{,xx} \cos 2\theta_G] + TX_{IIb}(w_{,xx}\cos\theta_G - v_{,xx}\sin\theta_G) \\
+ (q_{bx3} + q_{cx3}) + v_{,x}\,(q_{by3} + q_{cy3}) + w_{,x}\,(q_{bz3} + q_{cz3}) \;=\; 0,
\end{aligned}
\tag{A.21}
$$

A.7 Distributed Loads

A complete description of the aeroelastic equations governing the motion of the rotor blade requires a derivation of the distributed inertial, aerodynamic, gravitational, and the structural damping loads. Distributed inertial, gravitational, and damping loads on a flapped rotor blade were derived as explicit expressions of blade displacement in Ref. 70. Expressions for distributed aerodynamic loads were derived in Ref. 72. These expressions have been used in the present analysis. The purpose of this section is to show how the complete equations of motion are formulated. This will be accomplished by establishing the blade kinematics first and subsequently the distributed loads.

A.7.1 Blade Kinematics

To formulate explicit expressions of the distributed loads acting on the blade, the position of an arbitrary point on the blade or control surface must be defined in terms of the blade degrees of freedom. The approach described in this chapter

is taken from Ref. 72. The kinematic description of the blade used in the derivation of the distributed loads is based on the assumptions of Euler-Bernoulli beam theory: plane sections normal to the elastic axis of the beam before deformation remain plane after deformation, and strains within cross-sections are neglected. Accordingly, an arbitrary point on the beam before deformation, represented by the vector

$$\mathbf{R_p} = e\hat{e}_{x2} + x\hat{e}_{x3} + y_o\hat{e}_{y3} + z_o\hat{e}_{z3}, \tag{A.22}$$

is described after deformation by the vector

$$\mathbf{r_p} = e\hat{e}_{x2} + (x+u)\hat{e}_{x3} + v\hat{e}_{y3} + w\hat{e}_{z3} + y_o\hat{e}_{y4} + z_o\hat{e}_{z4}. \tag{A.23}$$

where u, v, and w represent the displacement of a point on the elastic axis of the blade as illustrated in Fig. A.2. If the coordinate pair $(\bar{y}_o, \bar{z}_o)$ can be interpreted as the pair (y_o, z_o) expressed in the “5" coordinate system, i.e.

$$y_o\hat{e}_{y4} + z_o\hat{e}_{z4} = \bar{y}_o\hat{e}_{y5} + \bar{z}_o\hat{e}_{z5}, \tag{A.24}$$

then

$$\mathbf{r_p} = e\hat{e}_{x2} + (x+u)\hat{e}_{x3} + v\hat{e}_{y3} + w\hat{e}_{z3} + \bar{y}_o\hat{e}_{y5} + \bar{z}_o\hat{e}_{z5}. \tag{A.25}$$

The velocity and acceleration of a point in a reference frame that is translating and rotating relative to an inertial frame can be found using the classical relations:

$$\mathbf{v_p} = \dot{\mathbf{R}}_\mathbf{o} + \dot{\mathbf{r}} + \omega \times \mathbf{r}, \tag{A.26}$$

$$\mathbf{a_p} = \ddot{\mathbf{R}}_\mathbf{o} + \ddot{\mathbf{r}} + 2\omega \times \dot{\mathbf{r}} + \dot{\omega} \times \mathbf{r} + \omega \times (\omega \times \mathbf{r}), \tag{A.27}$$

where $\mathbf{R_o}$ is the position of the origin of the moving reference frame in the inertial frame, and ω the vector of angular velocity. The time derivatives of $\mathbf{R_o}$ are taken in the inertial frame, while those for $\mathbf{r}$ are taken in the rotating frame. For the rotor case, the inertial frame is that of the hub, described by the "1" system. The rotating frame rotates with the blades and corresponds to the "2" system. The origin of the rotating frame is assumed to coincide with the that of the non-rotating frame. Thus:

$$\ddot{\mathbf{R}}_\mathbf{o} = \dot{\mathbf{R}}_\mathbf{o} = \mathbf{R_o} = \mathbf{0}. \tag{A.28}$$

Also, $\omega = \Omega\hat{e}_{z2}$, and since Ω is constant, $\dot{\omega} = \mathbf{0}$. Hence, the velocity and acceleration of any point in the rotating reference frame ("2" system) are given by:

$$\mathbf{v_p} = \dot{\mathbf{r}}_\mathbf{p} + \Omega\hat{e}_{z2} \times \mathbf{r_p}, \tag{A.29}$$

$$\mathbf{a_p} = \ddot{\mathbf{r}}_\mathbf{p} + 2\Omega\hat{e}_{z2} \times \dot{\mathbf{r}}_\mathbf{p} + \Omega\hat{e}_{z2} \times (\Omega\hat{e}_{z2} \times \mathbf{r_p}). \tag{A.30}$$

Equations (A.29) and (A.30), taken from Ref. 72, are the fundamental kinematic relations used in the derivation of the distributed loads.

A.7.2 Inertial Loads

The inertial loads are obtained using D'Alembert's principle. Expressions for the inertial loads will first be formulated in the "2" system, and then transformed to the "3" system to be compatible with the blade elastic equations of motion. Given an arbitrary point in the rotating frame ("2" system), represented by the vector:

$$\mathbf{r_p} = r_{px2}\hat{e}_{x2} + r_{py2}\hat{e}_{y2} + r_{pz2}\hat{e}_{z2}, \tag{A.31}$$

the acceleration of this point can be found using Eqn. (A.30). Expressed in the "2" system, this is given by:

$$\mathbf{a_p} = a_{px2}\hat{e}_{x2} + a_{py2}\hat{e}_{y2} + a_{pz2}\hat{e}_{z2}, \tag{A.32}$$

where:

$$a_{px2} = \ddot{r}_{px2} - 2\Omega\dot{r}_{py2} - \Omega^2 r_{px2}, \tag{A.33}$$

$$a_{py2} = \ddot{r}_{py2} + 2\Omega\dot{r}_{px2} - \Omega^2 r_{py2}, \tag{A.34}$$

$$a_{pz2} = \ddot{r}_{pz2}, \tag{A.35}$$

with time derivatives of $\mathbf{r_p}$ taken in the "2" system.

From Eqn. (A.25), a point on the deformed blade can be expressed as:

$$\mathbf{r_b} = e\hat{e}_{x2} + (x+u)\hat{e}_{x3} + v\hat{e}_{y3} + w\hat{e}_{z3} + \bar{y}_{ob}\hat{e}_{y5} + \bar{z}_{ob}\hat{e}_{z5}. \tag{A.36}$$

The inertial forces and moments taken about the elastic axis of the blade at a given spanwise location are given by:

$$\mathbf{p_{Ib}} = -\int_{A_b} \rho_b \mathbf{a_b} dA, \tag{A.37}$$

$$\mathbf{q_{Ib}} = -\int_{A_b} \mathbf{r_{ob}} \times \rho_b \mathbf{a_b} dA, \tag{A.38}$$

where:

$$\mathbf{r_{ob}} = \bar{y}_{ob}\hat{e}_{y5} + \bar{z}_{ob}\hat{e}_{z5}. \tag{A.39}$$

The resulting spanwise distributed inertia force is expressed in the "2" system as [Ref. 72, Eqs. (5.36)-(5.39)]:

$$\mathbf{p_{Ib}} = p_{Ibx2}\hat{e}_{x2} + p_{Iby2}\hat{e}_{y2} + p_{Ibz2}\hat{e}_{z2}, \tag{A.40}$$

where the components of $\mathbf{p_{Ib}}$ are given by:

$$\begin{aligned} p_{Ibx2} &= m_b\Omega^2(x+e) + 2m_b\Omega\dot{v} + m_b\beta_p(\ddot{w} - w\Omega^2) \\ &\quad + m_b(u\Omega^2 - \ddot{u}) - 2m_bX_{Ib}\Omega\sin(\theta_G+\phi)(\dot{\theta}_G+\dot{\phi}), \end{aligned} \tag{A.41}$$

$$\begin{aligned} p_{Iby2} &= 2m_b\Omega\dot{w}\beta_p + m_b(v\Omega^2 - \ddot{v}) - 2m_b\Omega\dot{u} \\ &\quad + m_bX_{Ib}\cos(\theta_G+\phi)((\dot{\theta}_G+\dot{\phi})^2 + \Omega(\Omega + 2\dot{v}_{,x}) + 2\Omega(\dot{\theta}_G+\dot{\phi})(w_{,x}+\beta_p)) \\ &\quad + m_bX_{Ib}\sin(\theta_G+\phi)((\ddot{\theta}_G+\ddot{\phi}) + 2\Omega\dot{w}_{,x} - 2\Omega(\dot{\theta}_G+\dot{\phi})v_{,x}), \end{aligned} \tag{A.42}$$

$$\begin{aligned} p_{Ibz2} &= -m_b\ddot{u}\beta_p - m_b\ddot{w} \\ &\quad + m_bX_{Ib}\cos(\theta_G+\phi)(-(\ddot{\theta}_G+\ddot{\phi}) + \ddot{v}_{,x}(w_{,x}+\beta_p) + 2\dot{w}_{,x}\dot{v}_{,x} + \ddot{w}_{,x}v_{,x}) \\ &\quad + m_bX_{Ib}\sin(\theta_G+\phi)((\dot{\theta}_G+\dot{\phi})^2 - (\ddot{\theta}_G+\ddot{\phi})(w_{,x}+\beta_p)v_{,x}). \end{aligned} \tag{A.43}$$

Similarly, distributed spanwise moment is expressed in the "2" system as [Ref. 72, Eqs. (5.40)-(5.43)]:

$$\mathbf{q_{Ib}} = q_{Ibx2}\hat{e}_{x2} + q_{Iby2}\hat{e}_{y2} + q_{Ibz2}\hat{e}_{z2}, \tag{A.44}$$

where:

$$
\begin{aligned}
q_{Ibx2} &= m_b X_{Ib}\cos(\theta_G+\phi)((v\Omega^2-\ddot{v})(w_{,x}+\beta_p)v_{,x}-\ddot{w}-\ddot{u}\beta_p) \\
&\quad m_b X_{Ib}\sin(\theta_G+\phi)((\ddot{v}-v\Omega^2)+2\Omega\dot{u}-2\Omega\dot{w}\beta_p) \\
&\quad -(I_{MB2}+I_{MB3})(\ddot{\theta}_G+\ddot{\phi}) \\
&\quad +(I_{MB2}-I_{MB3})\cos(\theta_G+\phi)\sin(\theta_G+\phi)\Omega((\Omega+2\dot{v}_{,x})+2(\dot{\theta}_G+\dot{\phi})(w_{,x}+\beta_p) \\
&\quad +2(I_{MB2}\cos^2(\theta_G+\phi)+I_{MB3}\sin^2(\theta_G+\phi))\Omega((\dot{\theta}_G+\dot{\phi})v_{,x}-\dot{w}_{,x}) \\
&\quad +(I_{MB2}\sin^2(\theta_G+\phi)+I_{MB3}\cos^2(\theta_G+\phi)) \\
&\quad (2\dot{v}_{,x}\,\dot{w}_{,x}+v_{,x}\,\ddot{w}_{,x}+(w_{,x}+\beta_p)(\Omega^2 v_{,x}+\ddot{v}_{,x})), \qquad \text{(A.45)} \\
q_{Iby2} &= -m_b X_{Ib}\cos(\theta_G+\phi)(\Omega^2 x(w_{,x}+\beta_p)+\ddot{w})v_{,x} \\
&\quad +m_b X_{Ib}\sin(\theta_G+\phi)(\Omega^2(x+e)-(\Omega^2 w\beta_p+\ddot{w}w_{,x})+2\Omega\dot{v}+(u\Omega^2-\ddot{u})) \\
&\quad -(I_{MB2}+I_{MB3})(\ddot{\theta}_G+\ddot{\phi})v_{,x} \\
&\quad +(I_{MB2}-I_{MB3})\cos(\theta_G+\phi)\sin(\theta_G+\phi)((v_{,x}\,\Omega^2-\ddot{v}_{,x})-2(\dot{\theta}_G+\dot{\phi})\dot{w},x) \\
&\quad +(I_{MB2}\cos^2(\theta_G+\phi)+I_{MB3}\sin^2(\theta_G+\phi)) \\
&\quad (w_{,x}-\Omega^2(w_{,x}+\beta_p)-2(\dot{\theta}_G+\dot{\phi})(\Omega+\dot{v}_{,x})), \qquad \text{(A.46)} \\
q_{Ibz2} &= m_b X_{Ib}\cos(\theta_G+\phi)(-\Omega^2(x+e)-2\Omega\dot{v}+(\ddot{u}-u\Omega^2) \\
&\quad +(w\Omega^2-\ddot{w})\beta_p+(\ddot{v}-v\Omega^2)v_{,x}) \\
&\quad +m_b X_{Ib}\sin(\theta_G+\phi)(\ddot{v}-v\Omega^2)(w_{,x}+\beta_p) \\
&\quad -(I_{MB2}+I_{MB3})(\ddot{\theta}_G+\ddot{\phi})(w_{,x}+\beta_p) \\
&\quad +(I_{MB2}-I_{MB3})\cos(\theta_G+\phi)\sin(\theta_G+\phi)(\ddot{w}_{,x}-2(\dot{\theta}_G+\dot{\phi})(\Omega+\dot{v}_{,x})) \\
&\quad -(I_{MB2}\sin^2(\theta_G+\phi)+I_{MB3}\cos^2(\theta_G+\phi))(\ddot{v}_{,x}+2(\dot{\theta}_G+\dot{\phi})\dot{w}_{,x}). \qquad \text{(A.47)}
\end{aligned}
$$

Using the coordinate transformations described in the previous sections of this chapter, the distributed spanwise inertial force can be expressed in the "3" system as:

$$\mathbf{p_{Ib}} = p_{Ibx3}\hat{e}_{x3} + p_{Iby3}\hat{e}_{y3} + p_{Ibz3}\hat{e}_{z3}, \tag{A.48}$$

where:

$$p_{Ibx3} = p_{Ibx2} + \beta_p p_{Ibz2}, \tag{A.49}$$

$$p_{Ibx3} = p_{Iby2}, \tag{A.50}$$

$$p_{Ibx3} = -\beta_p p_{Ibx2} + p_{Ibz2}. \tag{A.51}$$

Similarly, the distributed spanwise moment can be expressed in the "3" system as:

$$\mathbf{q_{Ib}} = q_{Ibx3}\hat{e}_{x3} + q_{Iby3}\hat{e}_{y3} + q_{Ibz3}\hat{e}_{z3}, \tag{A.52}$$

where:

$$q_{Ibx3} = q_{Ibx2} + \beta_p q_{Ibz2}, \tag{A.53}$$

$$q_{Ibx3} = q_{Iby2}, \tag{A.54}$$

$$q_{Ibx3} = -\beta_p q_{Ibx2} + q_{Ibz2}. \tag{A.55}$$

The derivation of the inertia loads due to a control surface is identical to that for the blade and can be found in Ref. 72.

A.7.3 Gravitational Loads

The distributed gravitational loads can be derived by integrating the gravitational force and moment per unit volume over the blade cross-section. Gravitational acceleration g is directed along the negative z_0 axis:

$$\mathbf{g} = -g\hat{e}_{z0}. \tag{A.56}$$

Expressed in the "2" system, this becomes:

$$\mathbf{g} = g_{x2}\hat{e}_{x2} + g_{y2}\hat{e}_{y2} + g_{z2}\hat{e}_{z2}, \tag{A.57}$$

where:

$$g_{x2} = -g\sin\alpha_R\cos\psi, \tag{A.58}$$

$$g_{y2} = g\sin\alpha_R\sin\psi, \tag{A.59}$$

$$g_{z2} = -g\cos\alpha_R. \tag{A.60}$$

These expressions are then used to derive the distributed force and moment.

The distributed gravitational force is derived by integrating the gravitational force per unit volume over the blade cross-section:

$$\mathbf{p_{Gb}} = \int_{A_b} \rho_b \mathbf{g} dA. \tag{A.61}$$

This can be expressed in the "2" system as [Ref. 72, Eqs. (5.103)-(5.106)]:

$$\mathbf{p_{Gb}} = p_{Gbx2}\hat{e}_{x2} + p_{Gby2}\hat{e}_{y2} + p_{Gbz2}\hat{e}_{z2}, \tag{A.62}$$

where:

$$p_{Gbx2} = \int_{A_b} \rho_b g_{x2} dA = -m_b g \sin\alpha_R \cos\psi, \tag{A.63}$$

$$p_{Gby2} = \int_{A_b} \rho_b g_{y2} dA = m_b g \sin\alpha_R \sin\psi, \tag{A.64}$$

$$p_{Gbz2} = \int_{A_b} \rho_b g_{z2} dA = -m_b g \cos\alpha_R. \tag{A.65}$$

Similarly, the distributed gravitational moment about the elastic axis is derived by integrating the gravitational moment per unit volume over the blade cross-section:

$$\mathbf{q_{Gb}} = \int_{A_b} (\bar{y}_{0b}\hat{e}_{y5} + \bar{z}_{0b}\hat{e}_{z5}) \times \rho_b \mathbf{g} dA, \tag{A.66}$$

Expressed in the "2" system, this becomes [Ref. 72, Eqs. (5.108)-(5.111)]:

$$\mathbf{q_{Gb}} = q_{Gbx2}\hat{e}_{x2} + q_{Gby2}\hat{e}_{y2} + q_{Gbz2}\hat{e}_{z2}, \tag{A.67}$$

where:

$$q_{Gbx2} = \int_{A_b} \rho_b(\bar{y}_{0b}(g_{z2} + (w_{,x} + \beta_p)v_{,x}\, g_{y2}) - \bar{z}_{0b} g_{y2})dA, \tag{A.68}$$

$$q_{Gby2} = \int_{A_b} \rho_b(\bar{y}_{0b}(g_{z2} - (w_{,x} + \beta_p)v_{,x} + \bar{z}_{0b}((w_{,x} + \beta_p)g_{z2} + g_{x2}))dA, \tag{A.69}$$

$$q_{Gbz2} = \int_{A_b} \rho_b(-\bar{y}_{0b}(v_{,x}\, g_{y2} + g_{x2}) - \bar{z}_{0b}(w_{,x} + \beta_p)g_{y2})dA. \tag{A.70}$$

Substituting (A.58)-(A.60) into (A.68)-(A.70) leads to:

$$\begin{aligned} q_{Gbx2} &= -m_b g X_{Ib} \cos(\theta_G + \phi)(\cos\alpha_R - (w_{,x} + \beta_p)v_{,x} \sin\alpha_R \sin\psi) \\ &\quad -m_b g X_{Ib} \sin(\theta_G + \phi) \sin\alpha_R \sin\phi, \end{aligned} \tag{A.71}$$

$$\begin{aligned} q_{Gby2} &= -m_b g X_{Ib} \cos(\theta_G + \phi)(\cos\alpha_R - (w_{,x} + \beta_p) \sin\alpha_R \cos\psi)v_{,x} \\ &\quad -m_b g X_{Ib} \sin(\theta_G + \phi)((w_{,x} + \beta_p)\cos\alpha_R + \sin\alpha_R \cos\phi), \end{aligned} \tag{A.72}$$

$$\begin{aligned} q_{Gbz2} &= -m_b g X_{Ib} \cos(\theta_G + \phi) \sin\alpha_R (v_{,x} \sin\phi - \cos\phi) \\ &\quad -m_b g X_{Ib} \sin(\theta_G + \phi) \sin\alpha_R \sin\phi). \end{aligned} \tag{A.73}$$

These expressions are then transformed to the "3" system to be compatible with the blade equations of motion. The derivation of the distributed gravitational loads due to a control surface is identical to that described for the blade and can be found in Ref. 72.

A.7.4 Damping Loads

Distributed structural damping loads are assumed to be of viscous type, and act only on the blade. Define the distributed damping force as:

$$\mathbf{p_D} = -g_{S_L}\dot{v}\hat{e}_{y3} - g_{S_F}\dot{w}\hat{e}_{z3}. \tag{A.74}$$

The distributed damping moment is given by:

$$\mathbf{q_D} = -g_{S_T}\dot{\phi}\hat{e}_{x4}, \tag{A.75}$$

which can be expressed in the "3" system as [Ref. 72, Eqn. (5.196)]:

$$\mathbf{q_D} = -g_{ST}\dot{\phi}(\hat{e}_{x3} - v_{,x}\,\hat{e}_{y3} - w_{,x}\,\hat{e}_{z3}). \tag{A.76}$$

g_{S_L}, g_{S_F}, and g_{S_T} are the distributed structural damping factors in lag, flap and torsion, respectively.

A.7.5 Total Distributed Loads

The total distributed loads are found by summing the inertial, gravitational, aerodynamic, and damping contributions. The distributed aerodynamic loads are derived in Appendix C. The total distributed load per unit length on the blade, Eqn. A.12, is given by:

$$\mathbf{p_b} = \mathbf{p_{Ib}} + \mathbf{p_{Gb}} + \mathbf{p_A} + \mathbf{p_D}. \tag{A.77}$$

where the subscripts I, G, A, and D correspond to the inertial, gravitational, aerodynamic, and damping loads respectively. The distributed moment per unit length about the elastic axis, Eqn. A.13, is given by:

$$\mathbf{q_{Mb}} = \mathbf{q_{Ib}} + \mathbf{q_{Gb}} + \mathbf{q_{A}} + \mathbf{q_{D}}. \tag{A.78}$$

The distributed force per unit length on the blade due to the control surface, Eqn. A.17, is given by:

$$\mathbf{p_c} = \mathbf{p_{Ic}} + \mathbf{p_{Gc}}. \tag{A.79}$$

The distributed moment per unit length about the elastic axis due to the control surface, Eqn. A.18, is given by:

$$\mathbf{q_c} = \mathbf{q_{Ic}} + \mathbf{q_{Gc}}. \tag{A.80}$$

Aerodynamic loads due to control surfaces are not included in Eqn. (A.79) or (A.80). Instead, these loads are contained in the expressions for the aerodynamic blade loads appearing in (A.77) and (A.78).

APPENDIX B

Galerkin Type Finite Element Model

The Galerkin type finite element model is used for modeling the rotor blade with tip geometry modification, implemented through a tip sweep, anhedral or dihedral.

B.1 Modeling Assumptions

The basic assumptions used to develop the aeroelastic analysis model for the rotor blade are as follows:

1. The rotor blade root offset, e, precone angle β_p, built-in pretwist distribution τ_0, sweep, droop and torque offset assumptions are similar to that in Appendix A.

2. The blade consists of a straight portion and a swept tip whose orientation relative to the straight portion is described by a sweep angle (Λ_s) and an anhedral angle (Λ_a) (see Fig. B.1).

3. The blade is modeled by beam type finite elements along the elastic axis of the blade.

4. A single finite element is used to model the swept tip.

5. The blade cross section can have arbitrary shape with distinct shear center, aerodynamic center, tension center and center of mass.

6. The blade feathering axis is coincident with the elastic axis of the straight portion of the blade, which is approximated by a straight line.

7. The effects of transverse shear deformations are included, however deformation of the cross in its own plane are neglected. Out-of-plane warping are included, however higher order warping terms are neglected.

8. The deflections in the blade are assumed to be moderate and the strains to be small compared to unity. No assumption is made regarding the relative magnitude between the axial and shear strains.

9. The blade has completely coupled flap, lead-lag, torsional and axial dynamics.

10. The distributed aerodynamic loads are obtained using CFD-based RFA aerodynamic model.

11. The induced inflow is nonuniform and is obtained by a free wake analysis included in the aeroelastic model.

12. Reverse flow effects are included by setting the lift and moment equal to zero and by changing the sign of the drag force inside the reverse flow region.

13. The speed of rotation, Ω, of the rotor is constant.

14. The helicopter is in trimmed, steady, level or descending flight. Either propulsive or wind tunnel trim can be implemented.

B.2 Coordinate Systems

The following six coordinate systems, similar to those used in Ref. 70, are used to formulate the aeroelastic model:

Non Rotating, Hub-fixed Coordinate System: The $(\hat{\mathbf{i}}_{nr}, \hat{\mathbf{j}}_{nr}, \hat{\mathbf{k}}_{nr})$ system is an inertial reference frame and has its origin at the hub center. The vector $\hat{\mathbf{i}}_{nr}$ point towards the helicopter tail, $\hat{\mathbf{j}}_{nr}$ points to the right of the helicopter, and $\hat{\mathbf{k}}_{nr}$ coincides with the rotation vector of the rotor. $\hat{\mathbf{i}}_{nr}$ and $\hat{\mathbf{j}}_{nr}$ are in the plane of rotation. Hub shears and moments are defined in this coordinate system. This is similar to the "1" system described in Appendix A.

Rotating Hub-fixed Coordinate System: The $(\hat{\mathbf{i}}_r, \hat{\mathbf{j}}_r, \hat{\mathbf{k}}_r)$ system also has its origin at the hub center but rotates with a constant angular velocity $\Omega\hat{\mathbf{k}}_r$. The vector $\hat{\mathbf{i}}_r$ coincides with the azimuth position of the blade, while $\hat{\mathbf{k}}_r$ is coincident with the vector $\hat{\mathbf{k}}_{nr}$. The vectors $\hat{\mathbf{i}}_r$ and $\hat{\mathbf{j}}_r$ are also in the plane of the rotation of the rotor. This is similar to the "2" system described in Appendix A.

Preconed, Pitched, Blade-fixed Coordinate System The $(\hat{\mathbf{i}}_b, \hat{\mathbf{j}}_b, \hat{\mathbf{k}}_b)$ system rotates with the blade and has its origin at the blade root, offset fromt he hub center by $e\hat{\mathbf{i}}_r$. The vector $\hat{\mathbf{i}}_b$ coincides with the pitch axis, which is also the undeformed elastic axis of the straight portion of the blade. The $(\hat{\mathbf{i}}_b, \hat{\mathbf{j}}_b, \hat{\mathbf{k}}_b)$ system is oriented by rotating the $(\hat{\mathbf{i}}_r, \hat{\mathbf{j}}_r, \hat{\mathbf{k}}_r)$ system about the $-\hat{\mathbf{j}}_r$ by the precone angle β_p, and subsequently introducing a second rotation about the rotated $\hat{\mathbf{i}}_r$ axis by the pitch control angle θ_{pc}. In the finite element model of the blade, the $(\hat{\mathbf{i}}_b, \hat{\mathbf{j}}_b, \hat{\mathbf{k}}_b)$ is the global coordinate system.

Undeformed Element Coordinate System The $(\hat{e}_x, \hat{e}_y, \hat{e}_z)$ has its origin at the inboard node of the finite element. See Fig. B.1. The vector $\hat{e}_x$ is aligned with the beam elastic axis, while the vectors $\hat{e}_y$ and $\hat{e}_z$ are defined in the cross section of the beam. For the straight portion of the blade, the $(\hat{e}_x, \hat{e}_y, \hat{e}_z)$ system has the same orientation as the $(\hat{\mathbf{i}}_b, \hat{\mathbf{j}}_b, \hat{\mathbf{k}}_b)$ system. For the swept tip element, the $(\hat{e}_x, \hat{e}_y, \hat{e}_z)$ system is oriented by rotating the $(\hat{\mathbf{i}}_b, \hat{\mathbf{j}}_b, \hat{\mathbf{k}}_b)$ system about $-\hat{k}_b$ by the sweep angle Λ_s and then about $-\hat{j}_b$ by the anhedral angle Λ_a. The $(\hat{e}_x, \hat{e}_y, \hat{e}_z)$ is also the local coordinate system for the blade finite element model. The displacement components and the applied loads of the finite element are defined in this coordinate system.

Undeformed Curvilinear Coordinate System In the $(\hat{e}_x, \hat{e}_\eta, \hat{e}_\zeta)$ system, the vectors $\hat{e}_\eta$ and $\hat{e}_\zeta$ are defined parallel to the modulus principal axes of the cross section. The pretwist angle $\beta(x)$ is defined as the the change in the orientation of $\hat{e}_\eta, \hat{e}_\zeta$ with respect to $\hat{e}_y, \hat{e}_z)$, repectively, at any location along the beam

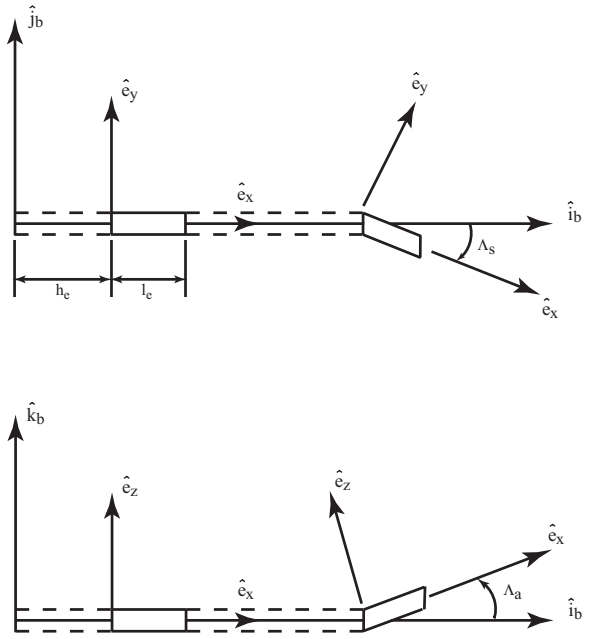

Fig. B.1. Undeformed element coordinate system.

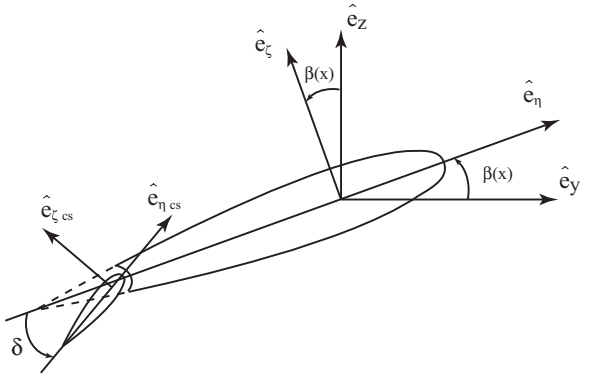

Fig. B.2. Undeformed curvilinear coordinate system.

element, as shown in Fig. B.2. The strain components, the material properties, and the cross section warping function are all derived in this coordinate system.

Deformed Curvilinear Coordinate System The $(\hat{e}'_x, \hat{e}'_\eta, \hat{e}'_\zeta)$ system represents the orientation of the local blade geometry after deformation. The orientation of the $(\hat{e}'_x, \hat{e}'_\eta, \hat{e}'_\zeta)$ system is obtained by rotating the $(\hat{e}_x, \hat{e}_\eta, \hat{e}_\zeta)$ system through

three Euler angles in the order of θ_{zeta},θ_η and θ_x about $\hat{e}_\zeta$, rotated $\hat{e}_\eta$ and rotated $\hat{e}_x$, respectively. The vector $\hat{e}'_x$ is chosen to be tangent to the local deformed elastic axis. This is equivalent to the "4B" system in Chapter IV.

B.3 Coordinate Transformations

The coordinate transformations between the various coordinate systems described above are presented in this section [Ref. 125, Eq. (2.1)-(2.17)].

Rotating to Nonrotating Transformation

$$\begin{Bmatrix} \hat{\mathbf{i}}_r \\ \hat{\mathbf{j}}_r \\ \hat{\mathbf{k}}_r \end{Bmatrix} = [T_{rn}] \begin{Bmatrix} \hat{\mathbf{i}}_{nr} \\ \hat{\mathbf{j}}_{nr} \\ \hat{\mathbf{k}}_{nr} \end{Bmatrix} \tag{B.1}$$

the transformation matrix $[T_{rn}]$ is given by

$$[T_{rn}] = \begin{bmatrix} \cos\psi & \sin\psi & 0 \\ -\sin\psi & \cos\psi & 0 \\ 0 & 0 & 1 \end{bmatrix} \tag{B.2}$$

Blade-fixed to Hub-fixed Transformation

$$\begin{Bmatrix} \hat{\mathbf{i}}_b \\ \hat{\mathbf{j}}_b \\ \hat{\mathbf{k}}_b \end{Bmatrix} = [T_{br}] \begin{Bmatrix} \hat{\mathbf{i}}_r \\ \hat{\mathbf{j}}_r \\ \hat{\mathbf{k}}_r \end{Bmatrix} \tag{B.3}$$

the transformation matrix $[T_{br}]$ is given by

$$[T_{br}] = \begin{bmatrix} 1 & 0 & 0 \\ 0 & \cos\theta_{pc} & \sin\theta_{pc} \\ 0 & -\sin\theta_{pc} & \cos\theta_{pc} \end{bmatrix} \begin{bmatrix} \cos\beta_p & 0 & \sin\beta_p \\ 0 & 1 & 0 \\ -\sin\beta_p & 0 & \cos\beta_p \end{bmatrix} \tag{B.4}$$

Element to Blade Transformation

$$\begin{Bmatrix} \hat{e}_x \\ \hat{e}_y \\ \hat{e}_z \end{Bmatrix} = [T_{eb}] \begin{Bmatrix} \hat{\mathbf{i}}_b \\ \hat{\mathbf{j}}_b \\ \hat{\mathbf{k}}_b \end{Bmatrix} \tag{B.5}$$

For the straight portion of the blade

$$[T_{eb}] = \begin{bmatrix} 1 & 0 & 0 \\ 0 & 1 & 0 \\ 0 & 0 & 1 \end{bmatrix} \tag{B.6}$$

For the swept-tip element

$$
\begin{aligned}
[T_{eb}] &= \begin{bmatrix} \cos\Lambda_s & -\sin\Lambda_s & 0 \\ \sin\Lambda_s & \cos\Lambda_s & 0 \\ 0 & 0 & 1 \end{bmatrix} \begin{bmatrix} \cos\Lambda_a & 0 & \sin\Lambda_a \\ 0 & 1 & 0 \\ -\sin\Lambda_a & 0 & \cos\Lambda_a \end{bmatrix} \\
&= \begin{bmatrix} \cos\Lambda_s\cos\Lambda_a & -\sin\Lambda_s & \cos\Lambda_s\sin\Lambda_a \\ \sin\Lambda_s\cos\Lambda_a & \cos\Lambda_s & \sin\Lambda_s\sin\Lambda_a \\ -\sin\Lambda_a & 0 & \cos\Lambda_a \end{bmatrix}
\end{aligned} \tag{B.7}
$$

Undeformed Curvilinear to Undeformed Element Transformation

$$
\begin{Bmatrix} \hat{e}_x \\ \hat{e}_\eta \\ \hat{e}_\zeta \end{Bmatrix} = [T_{ce}] \begin{Bmatrix} \hat{e}_x \\ \hat{e}_y \\ \hat{e}_z \end{Bmatrix} \tag{B.8}
$$

the transformation matrix $[T_{ce}]$ is given by

$$
[T_{ce}] = \begin{bmatrix} 1 & 0 & 0 \\ 0 & \cos\beta & \sin\beta \\ 0 & -\sin\beta & \cos\beta \end{bmatrix} \tag{B.9}
$$

Differentiating Eq. (B.8) with respect to x gives

$$\begin{Bmatrix} \hat{e}_{x,x} \\ \hat{e}_{\eta,x} \\ \hat{e}_{\zeta,x} \end{Bmatrix} = \begin{Bmatrix} 0 \\ \tau_0 \hat{e}_\zeta \\ -\tau_0 \hat{e}_\eta \end{Bmatrix} \tag{B.10}$$

where

$$\tau_0 = \beta_{,x} \tag{B.11}$$

Deformed to Undeformed Curvilinear Transformation

$$\begin{Bmatrix} \hat{e}'_x \\ \hat{e}'_\eta \\ \hat{e}'_\zeta \end{Bmatrix} = [T_{dc}] \begin{Bmatrix} \hat{e}_x \\ \hat{e}_\eta \\ \hat{e}_\zeta \end{Bmatrix} \tag{B.12}$$

the transformation matrix $[T_{dc}]$ is given by

$$[T_{dc}] = \begin{bmatrix} 1 & 0 & 0 \\ 0 & \cos\theta_x & \sin\theta_x \\ 0 & -\sin\theta_x & \cos\theta_x \end{bmatrix} \begin{bmatrix} \cos\theta_\eta & 0 & \sin\theta_\eta \\ 0 & 1 & 0 \\ -\sin\theta_\eta & 0 & \cos\theta_\eta \end{bmatrix} \begin{bmatrix} \cos\theta_\zeta & \sin\theta_\zeta & 0 \\ -\sin\theta_\zeta & \cos\theta_\zeta & 0 \\ 0 & 1 & 0 \end{bmatrix} \tag{B.13}$$

Deformed Curvilinear to Undeformed Element Transformation

$$\left\{ \begin{array}{c} \hat{e}'_x \\ \hat{e}'_\eta \\ \hat{e}'_\zeta \end{array} \right\} = [T_{de}] \left\{ \begin{array}{c} \hat{e}_x \\ \hat{e}_y \\ \hat{e}_z \end{array} \right\} \tag{B.14}$$

the transformation matrix $[T_{de}]$ is given in terms of the displacement variables u, v, w and ϕ

$$[T_{de}] = [T_{dc}][T_{ce}] = \left[\begin{array}{ccc} 1 & v_{,x} & w_{,x} \\ -v_{,x}c\beta\phi - w_{,x}s\beta\phi & c\beta\phi & s\beta\phi \\ v_{,x}s\beta\phi - w_{,x}c\beta\phi & -s\beta\phi + \tau'_c c\beta & c\beta\phi + \tau'_c s\beta \end{array} \right] \tag{B.15}$$

where

$$\tau'_c = (v_{,x}\sin\beta - w_{,x}\cos\beta)(v_{,x}\cos\beta + w_{,x}\sin\beta)$$

and the notations $c\beta\phi, s\beta\phi, c\beta$ and $s\beta$ used in Eq. (B.15) are defined as

$$c\beta\phi \equiv \cos(\beta+\phi),\ c\beta \equiv \cos\beta,\ s\beta\phi \equiv \sin(\beta+\phi),\ s\beta \equiv \sin\beta$$

B.4 Ordering Scheme

The purpose of the ordering scheme and reference quantities used are detailed in Appendix A. The orders of magnitude assigned to common nondimensional quantities in the finite element model are as follows:

$$
\begin{aligned}
O(1): \quad & \frac{x}{l}, \frac{R}{l}, \frac{h_e}{l}, \frac{l_e}{l}, l\frac{\partial}{\partial x}, \psi, \frac{\partial}{\partial \psi} = \frac{1}{\Omega}\frac{\partial}{\partial t}, \sin\psi, \cos\psi, \\
& \Lambda_s, \Lambda_a, \sin\Lambda_s, \cos\Lambda_s, \sin\Lambda_a, \cos\Lambda_a \\
O(\epsilon^{1/2}): \quad & \theta_p, \beta \\
O(\epsilon): \quad & \frac{\eta}{l}, \frac{\zeta}{l}, \frac{v}{l}, \frac{w}{l}, v_{,x}, w_{,x}, \phi, \alpha l, \frac{\Psi_{,\eta}}{l}, \frac{\Psi_{,\zeta}}{l}, \frac{e_1}{l}, \beta_p, \theta_x, \theta_\eta, \theta_\zeta \\
O(\epsilon^2): \quad & \frac{u}{l}, u_{,x}, \bar{\epsilon}_{xx}, \bar{\gamma}_{x\eta}, \bar{\gamma}_{x\zeta}, \frac{\Psi}{l^2}, \frac{m\Omega^2 l^2}{EA}
\end{aligned}
\tag{B.16}
$$

In general, it is assumed that rotation terms such as $v_{,x}$, $w_{,x}$ and ϕ are of the order ϵ, while strain terms such as $u_{,x}$, $\bar{\gamma}_{x\eta}$ and $\bar{\gamma}_{x\zeta}$ are of the order ϵ^2. The warping amplitude α is assumed to have the same oder of magnitude as $\phi_{,x}$. This scheme is consistent with a moderate deflection theory (small strains and moderate rotations).

B.5 Beam Kinematics

The nonlinear kinematics of deformation is based on the mechanics of curved rods [114, 115]. The strain components are first derived in a curvilinear coordinate system so that the effects of pretwist is properly accounted for. These strain components are then transformed to a local cartesian coordinate system. The stress-strain relations are assumed to be defined in this local cartesian coordinate system.

The position vector of a point $\mathbf{P}$ on the undeformed beam is written as

$$
\mathbf{r}(x, \eta, \zeta) = e_1\hat{\mathbf{i}}_r + h_e\hat{\mathbf{i}}_b + x\hat{e}_x + \eta\hat{e}_\eta + \zeta\hat{e}_\zeta \tag{B.17}
$$

Equation (B.17) can be used to represent the undeformed position vector both for

a point on the straight portion as well as a point on the swept-tip portion. For a point on the swept-tip element, h_e, equals the length of the straight portion of the blade. The corresponding undeformed base vectors at point $\mathbf{P}$ are defined by

$$\mathbf{g}_x = \mathbf{r}_{,x} = \hat{e}_x - \zeta\tau_0\hat{e}_\eta + \eta\tau_0\hat{e}_\zeta \tag{B.18a}$$

$$\mathbf{g}_\eta = \mathbf{r}_{,\eta} = \hat{e}_\eta \tag{B.18b}$$

$$\mathbf{g}_\zeta = \mathbf{r}_{,\zeta} = \hat{e}_\zeta \tag{B.18c}$$

where the derivatives of the orthonormal triad $(\hat{e}_x, \hat{e}_\eta, \hat{e}_\zeta)$ are related to the initial twist, τ_0, of the undeformed beam by

$$\begin{Bmatrix} \hat{e}_{x,x} \\ \hat{e}_{\eta,x} \\ \hat{e}_{\zeta,x} \end{Bmatrix} = \begin{bmatrix} 0 & 0 & 0 \\ 0 & 0 & \tau_0 \\ 0 & -\tau_0 & 0 \end{bmatrix} \begin{Bmatrix} \hat{e}_x \\ \hat{e}_\eta \\ \hat{e}_\zeta \end{Bmatrix} \tag{B.19}$$

and

$$\tau_0 = \beta_{,x} \tag{B.20}$$

Since the in-plane deformations of the beam cross-section are neglected, the position vector of the point $\mathbf{P}$ in the deformed configuration can be written as

$$\mathbf{R}(x,\eta,\zeta) = \mathbf{R}_0(x) + \eta\mathbf{E}_\eta + \zeta\mathbf{E}_\zeta + \alpha(x)\mathbf{\Psi}(\eta,\zeta)\hat{e}'_x \tag{B.21}$$

where

$$\mathbf{R}_0(x) = \mathbf{R}(x, 0, 0) \tag{B.22}$$

is the corresponding position vector of a point on the deformed elastic axis; and

$$\mathbf{E}_i(x) = \mathbf{R}_{,i}(x, 0, 0), \ i = x, \eta, \zeta \tag{B.23}$$

are the base vectors of a point on the deformed elastic axis. In Eq. (B.21), the first three terms represent translations and rotations of the cross-section, while the last term is the out-of-plane warping of the cross-section. $\alpha(x)$ is the unknown amplitude of warping; $\mathbf{\Psi}(\eta, \zeta)$ is the out-of-plane warping function of the cross-section, with

$$\mathbf{\Psi}(0, 0) = \mathbf{\Psi}_{,\eta}(0, 0) = \mathbf{\Psi}_{,\zeta}(0, 0) = 0 \tag{B.24}$$

With the assumption that in-plane deformations of the beam cross-section are neglected, the base vectors of the deformed elastic axis are expressed by the following definition [115]

$$\mathbf{E}_x = (1 + \bar{\varepsilon}_{xx})\hat{e}'_x \tag{B.25a}$$

$$\mathbf{E}_\eta = \bar{\gamma}_{x\eta}\hat{e}'_x + \hat{e}'_\eta \tag{B.25b}$$

$$\mathbf{E}_\zeta = \bar{\gamma}_{x\zeta}\hat{e}'_x + \hat{e}'_\zeta \tag{B.25c}$$

where $\bar{\varepsilon}_{xx}, \bar{\gamma}_{x\eta}$ and $\bar{\gamma}_{x\zeta}$ can be shown to be the axial and the transverse shear strains, respectively, at the elastic axis. Equation (B.25) imply that cross sections which are

normal to the elastic axis before deformation (e. g. $\hat{e}'_\eta - \hat{e}'_\zeta$ plane) will no longer be normal to the elastic axis after deformation (e. g. $\mathbf{E}_\eta - \mathbf{E}_\zeta$ plane) due to the presence of transverse shear strains. The deformed base vectors at point $\mathbf{P}$ are defined as

$$\mathbf{G}_x = \mathbf{R}_{,x},\ \mathbf{G}_\eta = \mathbf{R}_{,\eta},\ \mathbf{G}_\zeta = \mathbf{R}_{,\zeta} \tag{B.26}$$

where the derivatives of the orthonormal triad $(\hat{e}'_x, \hat{e}'_\eta, \hat{e}'_\zeta)$ are related to the curvatures, $\kappa_\eta, \kappa_\zeta$, and twist, τ, of the deformed beam by

$$\begin{Bmatrix} \hat{e}'_{x,x} \\ \hat{e}'_{\eta,x} \\ \hat{e}'_{\zeta,x} \end{Bmatrix} = \begin{bmatrix} 0 & \kappa_\eta & \kappa_\zeta \\ -\kappa_\eta & 0 & \tau \\ -\kappa_\zeta & -\tau & 0 \end{bmatrix} \begin{Bmatrix} \hat{e}'_x \\ \hat{e}'_\eta \\ \hat{e}'_\zeta \end{Bmatrix} \tag{B.27}$$

B.6 Strain Components and Strain-Displacement Relations

The set of coordinates (x, η, ζ) are, in general, non-orthogonal curvilinear coordinates since the base vector $\mathbf{g}_x$, expressed in Eq. (B.18a) is neither a unit vector nor orthogonal to the base vectors $\mathbf{g}_\eta$ and $\mathbf{g}_\zeta$ for an arbitrary point on the beam with nonzero initial twist τ_0. In the derivation that follows, the notations (x_1, x_2, x_3) will be used in place of (x, η, ζ) whenever convenient.

The components of the strain tensor in the curvilinear coordinates are defined by [114]

$$f_{ij} = \frac{1}{2}(\mathbf{G}_i \cdot \mathbf{G}_j - \mathbf{g}_i \cdot \mathbf{g}_j),\ i, j = x, \eta, \zeta \tag{B.28}$$

Define a system of local cartesian coordinates (y_1, y_2, y_3) at point $\mathbf{P}$ with its unit

vectors parallel to the orthonormal triad $(\hat{e}_x, \hat{e}_\eta, \hat{e}_\zeta)$ of the cross section, respectively. The stress-strain relations of the beam are assumed to be given in the local cartesian coordinate system. The transformation relation between the curvilinear coordinates (x_1, x_2, x_3) and the local cartesian coordinates (y_1, y_x, y_3) is given in matrix form by

$$\left[\frac{\partial x_i}{\partial y_j}\right] = [\mathbf{g}_k \cdot \mathbf{g}_i]^{-1}[\mathbf{g}_k \cdot \hat{e}_j] = \begin{bmatrix} 1 & 0 & 0 \\ \zeta\tau_0 & 1 & 0 \\ -\eta\tau_0 & 0 & 1 \end{bmatrix} \tag{B.29}$$

The strain tensor defined in the local cartesian coordinates, ε_{ij}, is obtained from the transformation

$$\varepsilon_{ij} = \sum_{k=1}^{3}\sum_{l=1}^{3} \frac{\partial \mathrm{x_k}}{\partial y_i}\frac{\partial \mathrm{x_l}}{\partial y_j} f_{kl} \tag{B.30}$$

Combining Eqs. (B.18), (B.21), and (B.25) through (B.30), the strain components in the local cartesian coordinates become

$$\begin{aligned} \varepsilon_{xx} &= \bar{\varepsilon}_{xx} - \eta\kappa_\eta - \zeta\kappa_\zeta + \alpha_{,x}\mathbf{\Psi} + \alpha\tau_0(\zeta\mathbf{\Psi}_{,\eta} - \eta\mathbf{\Psi}_{,\zeta}) \qquad \text{(B.31a)} \\ &\quad + \frac{1}{2}(\eta^2 + \zeta^2)(\tau - \tau_0)^2 + \eta(\bar{\gamma}_{x\eta,x} - \tau_0\bar{\gamma}_{x\zeta}) + \zeta(\bar{\gamma}_{x\zeta,x} + \tau_0\bar{\gamma}_{x\eta}) \\ \gamma_{x\eta} &= \bar{\gamma}_{x\eta} + \alpha\mathbf{\Psi}_{,\eta} - \zeta(\tau - \tau_0) \qquad \text{(B.31b)} \\ \gamma_{x\zeta} &= \bar{\gamma}_{x\zeta} + \alpha\mathbf{\Psi}_{,\zeta} + \eta(\tau - \tau_0) \qquad \text{(B.31c)} \\ \varepsilon_{\eta\eta} &\simeq \varepsilon_{\zeta\zeta} \simeq \gamma_{\eta\zeta} \simeq 0 \qquad \text{(B.31d)} \end{aligned}$$

where

$$\gamma_{x\eta} \equiv 2\varepsilon_{x\eta},\ \gamma_{x\zeta} \equiv 2\varepsilon_{x\zeta},\ \gamma_{\eta\zeta} \equiv 2\varepsilon_{\eta\zeta}$$

The strain components in Eqs. (B.31) are valid for small strains and large deflections and are expressed in terms of seven unknown functions of the axial coordinate x : $\bar{\varepsilon}_{xx}, \bar{\gamma}_{x\eta}, \bar{\gamma}_{x\zeta}, \kappa_\eta, \kappa_\zeta, \tau$ and α. The first three are the axial and transverse shear strains, respectively, at the elastic axis; the next three are curvatures and twist, respectively, of the deformed beam; α is the amplitude of warping.

In developing an aeroelastic model, it is desirable to express the strain components in terms of the displacement components (u, v, w) of the elastic axis and the elastic twist (ϕ) so that the structural model can be more conveniently combined with the inertial and aerodynamic models. After applying an ordering scheme that is consistent with a moderate deflection theory (small strains and moderate rotations), it is shown that the strain components can be expressed in terms of u, v, w and ϕ as follows:

$$\begin{aligned}
\varepsilon_{xx} &= u_{,x} + \frac{1}{2}(v_{,x})^2 + \frac{1}{2}(w_{,x}^2) - v_{,xx}[\eta\cos(\beta+\phi) - \zeta\sin(\beta+\phi)] \qquad \text{(B.32a)}\\
&\quad -w_{,xx}[\eta\sin(\beta+\phi) + \zeta\cos(\beta+\phi)] + \frac{1}{2}(\eta^2+\zeta^2)(\phi_{,x})^2\\
&\quad +\alpha_{,x}\mathbf{\Psi} + \alpha\tau_0(\zeta\mathbf{\Psi}_{,\eta} - \eta\mathbf{\Psi}_{,\zeta}) + \eta(\bar{\gamma}_{x\eta,x} - \tau_0\bar{\gamma}_{x\zeta}) + \zeta(\bar{\gamma}_{x\zeta,x} + \tau_0\bar{\gamma}_{x\eta})\\
\gamma_{x\eta} &= \bar{\gamma}_{x\eta} + \alpha\mathbf{\Psi}_{,\eta} - \zeta(\phi_{,x} + \phi_0) \qquad \text{(B.32b)}\\
\gamma_{x\zeta} &= \bar{\gamma}_{x\zeta} + \alpha\mathbf{\Psi}_{,\zeta} + \eta(\phi_{,x} + \phi_0) \qquad \text{(B.32c)}
\end{aligned}$$

The seven unknown functions of the axial coordinate, x, in the strain-displacement relations, Eqs. (B.32), become: u, v, w, ϕ, α, $\bar{\gamma}_{x\eta}$ and $\bar{\gamma}_{x\zeta}$.

B.7 Constitutive Relations

The constitutive relations are defined based on the assumptions that the material properties are linear elastic and generally orthotropic (anisotropic behavior) and that the stress components within the cross section are set to zero ($\sigma_{\eta\eta} = \sigma_{\zeta\zeta} = \sigma_{\eta\zeta} = 0$). The anisotropic stress-strain relations for a linearly elastic body are written as

$$\begin{bmatrix} \sigma_{xx} \\ \sigma_{\eta\eta} \\ \sigma_{\zeta\zeta} \\ \sigma_{\eta\zeta} \\ \sigma_{x\zeta} \\ \sigma_{x\eta} \end{bmatrix} = \begin{bmatrix} C_{11} & C_{12} & C_{13} & C_{14} & C_{15} & C_{16} \\ C_{12} & C_{22} & C_{23} & C_{24} & C_{25} & C_{26} \\ C_{13} & C_{23} & C_{33} & C_{34} & C_{35} & C_{36} \\ C_{14} & C_{24} & C_{34} & C_{44} & C_{45} & C_{46} \\ C_{15} & C_{25} & C_{35} & C_{45} & C_{55} & C_{56} \\ C_{16} & C_{26} & C_{36} & C_{46} & C_{56} & C_{66} \end{bmatrix} \begin{bmatrix} \varepsilon_{xx} \\ \varepsilon_{\eta\eta} \\ \varepsilon_{\zeta\zeta} \\ \gamma_{\eta\zeta} \\ \gamma_{x\zeta} \\ \gamma_{x\eta} \end{bmatrix} \tag{B.33}$$

Setting the three stress components within the cross section equal to zero and applying back substitution, the constitutive relations are

$$\begin{Bmatrix} \sigma_{xx} \\ \sigma_{x\zeta} \\ \sigma_{x\eta} \end{Bmatrix} = \begin{bmatrix} Q_{11} & Q_{15} & Q_{16} \\ Q_{15} & Q_{55} & Q_{56} \\ Q_{16} & Q_{56} & Q_{66} \end{bmatrix} \begin{Bmatrix} \varepsilon_{xx} \\ \gamma_{x\zeta} \\ \gamma_{x\eta} \end{Bmatrix} \tag{B.34}$$

where

$$[Q] = [C_{bb}] - [C_{bs}][C_{ss}]^{-1}[C_{sb}]$$

$$[C_{bb}] = \begin{bmatrix} C_{11} & C_{15} & C_{16} \\ C_{15} & C_{55} & C_{56} \\ C_{16} & C_{56} & C_{66} \end{bmatrix}$$

$$[C_{ss}] = \begin{bmatrix} C_{22} & C_{23} & C_{24} \\ C_{23} & C_{33} & C_{34} \\ C_{24} & C_{34} & C_{44} \end{bmatrix}$$

$$[C_{bs}] = [C_{sb}]^T = \begin{bmatrix} C_{12} & C_{13} & C_{14} \\ C_{25} & C_{35} & C_{45} \\ C_{26} & C_{36} & C_{46} \end{bmatrix}$$

B.8 Equations of Motion

The nonlinear equations of motion and the corresponding finite element matrices are derived for each beam element using Hamilton's principle

$$\int_{t_1}^{t_2} (\delta U - \delta T - \delta W_e) dt = 0 \tag{B.35}$$

where δU, δT and δW_e represent the strain energy variation, kinetic energy variation, and virtual work of external loads, respectively.

B.8.1 Strain Energy

The variation of the strain energy for each beam element is

$$\delta U = \int_0^{l_e} \int\int_A \begin{Bmatrix} \delta\varepsilon_{xx} \\ \delta\gamma_{x\zeta} \\ \delta\gamma_{x\eta} \end{Bmatrix}^T \begin{bmatrix} Q_{11} & Q_{15} & Q_{16} \\ Q_{15} & Q_{55} & Q_{56} \\ Q_{16} & Q_{56} & Q_{66} \end{bmatrix} \begin{Bmatrix} \varepsilon_{xx} \\ \gamma_{x\zeta} \\ \gamma_{x\eta} \end{Bmatrix} d\eta d\zeta dx \tag{B.36}$$

Integrating Eq. (B.36) over the cross section yields three sets of modulus weighted section constants, which are presented in Ref. 125. These section constants can be calculated by a separate linear, two-dimensional analysis which is decoupled from the nonlinear, one-dimensional global analysis for the beam. The cross sectional analysis as developed in Ref. 52,53 is based upon the solution of Saint Venant's flexure and torsion problems. It uses the principle of minimum potential energy and two-dimensional finite element analysis to solve for the displacement and stress distribution in an anisotropic composite blade cross section. This two-dimensional cross sectional analysis has undergone modifications to account for differences in kinematic assumptions, resulting in a set of modified weighted section constants that are described in Ref. 125. These section constants are given on pages 65-70 of Ref. 125.

B.8.2 Kinetic Energy

The variation of the kinetic energy for each beam element is

$$\delta T = \int_0^{l_e} \int\int_A \rho \mathbf{V} \cdot \delta \mathbf{V} d\eta d\zeta dx \tag{B.37}$$

where the velocity vector, $\mathbf{V}$, is obtained by

$$\mathbf{V} = \dot{\mathbf{R}} + \Omega \hat{\mathbf{k}}_r \times \mathbf{R} \tag{B.38}$$

with the position vector, $\mathbf{R}$, of a point $\mathbf{P}$ on the deformed beam written in the form

$$\mathbf{R} = e_1 \hat{\mathbf{i}}_r + h_e \hat{\mathbf{i}}_b + (x+u)\hat{e}_x + v\hat{e}_y + w\hat{e}_z + \eta \mathbf{E}_\eta + \zeta \mathbf{E}_\zeta + \alpha \mathbf{\Psi} \hat{e}'_x \tag{B.39}$$

All the terms in the expressions of the velocity vector, $\mathbf{V}$, in Eq. (B.38) were transformed to the $(\hat{e}_x, \hat{e}_y, \hat{e}_z)$ system before carrying out the algebraic manipulations. Integrating Eq. (B.37) over the cross section yields mass weighted section constants about the shear center, which are also presented in Ref. 125.

B.8.3 External Work Contributions

The effects of the nonconservative distributed loads are included using the principle of virtual work. The virtual work done on each beam element is

$$\delta W_e = \int_0^{l_e} (\mathbf{P} \cdot \delta \mathbf{u} + \mathbf{Q} \cdot \delta \mathbf{\Theta}) dx \tag{B.40}$$

where $\mathbf{P}$ and $\mathbf{Q}$ are the distributed force and moment vectors, respectively, along the elastic axis; $\delta\mathbf{u}$ and $\delta\mathbf{\Theta}$ are the virtual displacement and virtual rotation vectors, respectively, of a point on the deformed elastic axis. In the aeroelastic analysis, components of $\mathbf{P}$ and $\mathbf{Q}$ are replaced by the corresponding components of aerodynamic forces and moments, derived in Appendix C.

B.9 Finite Element Discretization

The spatial discretization of the blade equations of motion is achieved by using the finite element method. The straight portion of the blade is divided into a number of beam elements, while the swept tip is modeled as a single beam element. The discretized form of Hamilton's principle as given in Eq. (B.35) is written as

$$\int_{t_1}^{t_2} \sum_{i=1}^{n} (\delta U_i - \delta T_i - \delta W_{ei}) dt = 0 \tag{B.41}$$

Hermite interpolation polynomials are used to discretize the space dependence of the generalized coordinates: cubic polynomials for v and w; quadratic polynomials for ϕ, u, α, $\bar{\gamma}_{x\eta}$ and $\bar{\gamma}_{x\zeta}$. The seven unknown generalized coordinates of the beam finite element can be expressed in the following form

$$\begin{bmatrix} v \\ w \\ \phi \\ u \\ \alpha \\ \bar{\gamma}_{x\eta} \\ \bar{\gamma}_{x\zeta} \end{bmatrix} = \begin{bmatrix} \{\Phi_v\}^T & 0 & 0 & 0 & 0 & 0 & 0 \\ 0 & \{\Phi_w\}^T & 0 & 0 & 0 & 0 & 0 \\ 0 & 0 & \{\Phi_\phi\}^T & 0 & 0 & 0 & 0 \\ 0 & 0 & 0 & \{\Phi_u\}^T & 0 & 0 & 0 \\ 0 & 0 & 0 & 0 & \{\Phi_\alpha\}^T & 0 & 0 \\ 0 & 0 & 0 & 0 & 0 & \{\Phi_\eta\}^T & 0 \\ 0 & 0 & 0 & 0 & 0 & 0 & \{\Phi_\zeta\}^T \end{bmatrix} \begin{bmatrix} \{V\} \\ \{W\} \\ \{\phi\} \\ \{U\} \\ \{\alpha\} \\ \{\Gamma_\eta\} \\ \{\Gamma_\zeta\} \end{bmatrix} \tag{B.42}$$

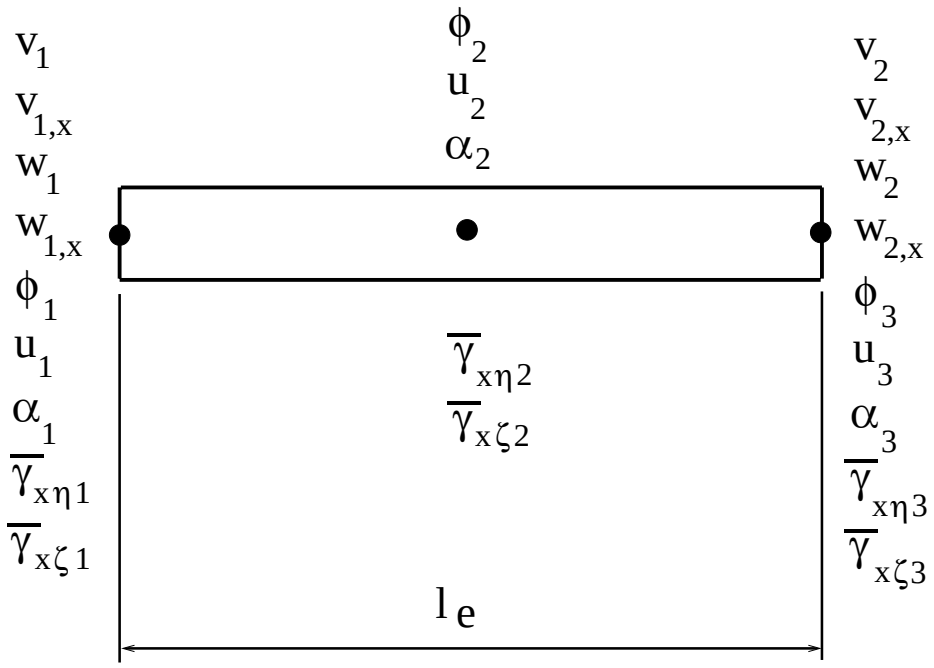

Fig. B.3. Finite element nodal degrees of freedom

where $\{\Phi_v\}$,$\{\Phi_w\}$,$\{\Phi_\phi\}$,$\{\Phi_u\}$,$\{\Phi_\alpha\}$,$\{\Phi_\eta\}$,$\{\Phi_\zeta\}$ are the Hermite interpolation polynomials, and $\{V\},\{W\},\{\phi\},\{U\},\{\alpha\},\{\Gamma_\eta\}$, $\{\Gamma_\zeta\}$ are time dependent nodal parameters for v, w, ϕ, u, α, $\bar{\gamma}_{x\eta}$ and $\bar{\gamma}_{x\zeta}$, respectively. Each beam element consists of two end nodes and one internal node at its mid-point, resulting in a total of 23 nodal degrees of freedom, as shown in Fig. B.3. The quadratic polynomial has the capability of modeling a linear variation of strains along the element length, thus being compatible with the cubic polynomial for transverse deflections v and w. These polynomials also satisfy all inter-element compatibility requirements associated with the variational principle in this formulation.

B.9.1 Element Matrices Associated with the Strain Energy Variation

Using the interpolation of the generalized coordinates with nodal parameters given by Eq. (B.42), the variation of the strain energy in Eq. (B.36) can be expressed in the following form

$$\delta U = \delta \mathbf{q}^T([\mathrm{K}^{\mathrm{L}}] + [\mathrm{K}^{\mathrm{NL}}(\mathbf{q})])\mathbf{q} \tag{B.43}$$

where

$$\mathbf{q} = [\{V\}^T, \{W\}^T, \{\phi\}^T, \{U\}^T, \{\alpha\}^T, \{\Gamma_\eta\}^T, \{\Gamma_\zeta\}^T]^T$$

and $[\mathrm{K}^{\mathrm{L}}]$ and $[\mathrm{K}^{\mathrm{NL}}]$ are the linear stiffness matrix(symmetric) and nonlinear stiffness matrix, respectively. Detailed expressions for the stiffness matrices are presented in Ref. 125.

B.9.2 Element Matrices Associated with the Kinetic Energy Variation

The variation of the kinetic energy in Eq. (B.37) can be expressed in the following form, utilizing Eq. (B.42)

$$\delta T = \delta \mathbf{q}^T([\mathrm{M}]\ddot{\mathbf{q}} + [\mathrm{M}^{\mathrm{C}}]\dot{\mathbf{q}} + [\mathrm{K}^{\mathrm{CF}}]\mathbf{q} + \{\mathrm{F}^{\mathrm{CF}}\}) \tag{B.44}$$

where $[\mathrm{M}]$ is the mass matrix(symmetric), $[\mathrm{M}^{\mathrm{C}}]$ is a Coriolis damping matrix(antisymmetric), $[\mathrm{K}^{\mathrm{CF}}]$ is a centrifugal stiffening matrix(symmetric when $\mathbf{\Omega}$ is constant, and $\{\mathrm{F}^{\mathrm{CF}}\}$ is a centrifugal force vector. Detailed expressions for these matrices are presented in Ref. 125.

B.9.3 Element Matrices Associated with the Virtual Work of External Loads

The virtual work of external loads in Eq. (B.40) has the form

$$\delta W_e = -\delta \mathbf{q}^T([\mathrm{K}^{\mathrm{I}}]\mathbf{q} + \{\mathrm{F}^{\mathrm{I}}\}) \tag{B.45}$$

where $[\mathrm{K}^{\mathrm{I}}]$ is a stiffness type matrix associated with applied distributed moments, and $\{\mathrm{F}^{\mathrm{I}}\}$ is an applied force vector. Detailed expressions for these matrices are presented in Ref. 125.

B.9.4 Summary of the Beam Finite Element Equations of Motion

The finite element equations of motion for a single beam element are obtained by substituting Eqs. (B.43-B.45) into the discretized form of Hamilton's principle, Eq. (B.41)

$$[\mathrm{M_i}]\ddot{\mathbf{q}} + [\mathrm{C_i}]\dot{\mathbf{q}} + [\mathrm{K_i}]\mathbf{q} + \mathbf{F_i} = \mathbf{0} \tag{B.46}$$

where

$$\begin{aligned}
[\mathrm{M_i}] &= [\mathrm{M}]_i \\
[\mathrm{C_i}] &= [\mathrm{M}^{\mathrm{C}}]_i \\
[\mathrm{K_i}] &= [\mathrm{K}^{\mathrm{L}}]_i + [\mathrm{K}^{\mathrm{CF}}]_i + [\mathrm{K}^{\mathrm{I}}]_i + [\mathrm{K}^{\mathrm{NL}}(\mathbf{q})]_i \\
\mathbf{F_i} &= \{\mathrm{F}^{\mathrm{CF}}\}_i + \{\mathrm{F}^{\mathrm{I}}\}_i
\end{aligned}$$

The global mass, damping, stiffness matrices and force vector can then be assembled using standard finite element assembly procedure, using the boundary conditions of the cantilevered blade.

APPENDIX C

Aerodynamic Model

C.1 RFA Model for the Attached Flow Region

The RFA based state-space, time domain unsteady aerodynamic model that accounts for unsteady free-stream and compressibility effects was first developed and used for rotary-wing applications by Myrtle and Friedmann [73]. In the RFA approach, approximate frequency domain transfer functions between the airloads and the generalized motions of a two-dimensional airfoil-flap combination are constructed. These relations are then transformed into the time domain to yield a statespace aerodynamic model. This method accounts for compressibility and unsteady effects due to free stream and blade-flap motions. In Ref. 73, a two-dimensional doublet-lattice (DL) method was used to obtain unsteady aerodynamic loading on an airfoil/trailing-edge flap combination over a range. The DL method is based on linear flow theory and thus cannot predict the drag coeffi-

cient or account for the airfoil thickness effects. Both these effects are crucial for in-plane noise predictions. Further, the DL method is not valid when significant flow nonlinearities associated with viscous effects are present and therefore cannot be used to model the microflap. To overcome this limitations, a CFD based RFA model was developed in Refs. [60, 61, 79]. In this new approach, a compressible unsteady RANS CFD solver is used to generate the frequency domain unsteady aerodynamic loads instead of the DL method.

C.1.1 CFD-Based RFA Reduced Order Model

To construct a ROM for the microflap, the frequency domain solutions required for the construction of the RFA model are obtained from a compressible unsteady RANS solver, CFD++. A schematic description of the new CFD based RFA model is shown in Fig. C.1.

The CFD based aerodynamic load responses to various generalized motions are obtained for Mach number range 0.05 to 0.8 with an increment of 0.05 and an angle of attack range -2° to 15° with an increment of 1°. At each flow condition defined by the free stream Mach number and the airfoil mean angle of attack, simulations are performed to generate frequency domain load responses for reduced frequency values ranging from 0.02 to 0.2 with an increment of 0.02. Note that the 5/rev frequency, which is the highest actuation frequency used for noise and vibration reduction in this study, corresponds to a reduced frequency value of approximately 0.18 based on the average local freestream velocity for a blade section at 0.75R span location. A 1° oscillation amplitude is used for the generalized

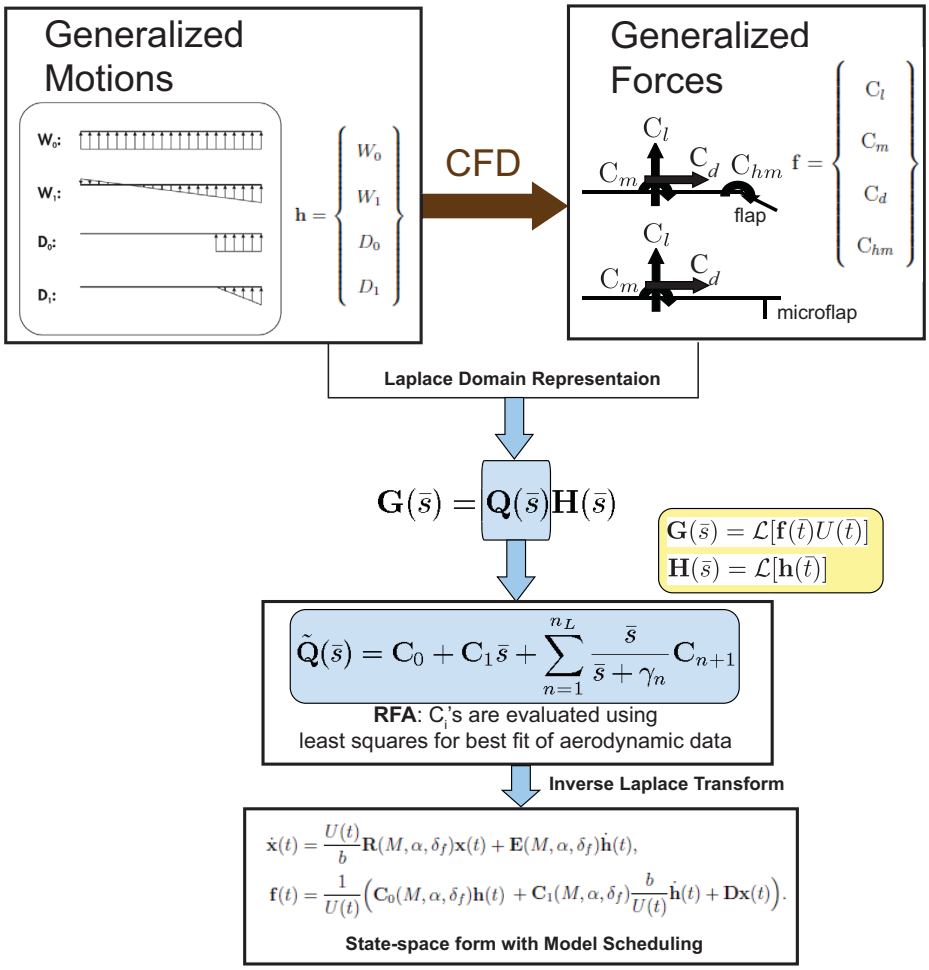

Fig. C.1. A schematic description of the new CFD based RFA model

motions W_0 and W_1. In the case of a conventional plain flap, a 1° flap deflection amplitude is used for the D_0 and D_1 generalized motions and for the microflap, 1.5%c flap deflection amplitude is used for the D_0 generalized motion. The aerodynamic load response data obtained from CFD is processed using the FFT (Fast Fourier Transform) tool in MATLAB. The frequency domain data thus obtained is tabulated and used to generate the coefficients C_0, C_1, ... ,C_{n_L+1} in the Roger's Approximation. The Reynolds number is 2.1×10^6 for all the simulations.

C.1.2 Roger's Approximation

The RFA approach, which is based on a least squares method known as Roger's approximation [94], is employed to convert the tabulated frequency domain response data generated by CFD into the time domain. This process is described below.

Consider an aerodynamic system which is represented in the Laplace domain by the expression

$$\mathbf{G}(\bar{s}) = \mathbf{Q}(\bar{s})\mathbf{H}(\bar{s}), \tag{C.1}$$

where $\mathbf{G}(\bar{s})$ and $\mathbf{H}(\bar{s})$ represent Laplace transforms of the generalized aerodynamic load and generalized motion vectors, respectively. Using the Least Squares approach, the aerodynamic transfer matrix $\mathbf{Q}(\bar{s})$ is approximated using a rational expression of the form

$$\tilde{\mathbf{Q}}(\bar{s}) = \mathbf{C}_0 + \mathbf{C}_1\bar{s} + \sum_{n=1}^{n_L} \frac{\bar{s}}{\bar{s} + \gamma_n}\mathbf{C}_{n+1}. \tag{C.2}$$

The n_L terms in the summation are aerodynamic lag terms and contain an associated set of poles γ_n. These poles are assumed to be positive valued to produce stable open loop roots. The accuracy and numerical efficiency of the approximation depend upon an appropriate choice of the number of lag terms.

The elements of the coefficient matrices $\mathbf{C}_n$ are chosen such that they provide a best fit, in a least squares sense, to the oscillatory response data obtained using CFD. The approximation is constrained at $k = 0$ to recover the steady state response.Numerical optimization techniques are used to find the optimal poles such that the fitting error is minimized. The fitting process is described in detail in Ref. 72.

C.1.3 State Space Model

The arbitrary motions of the airfoil and flap are represented by the four generalized motions depicted in Fig. C.2. These motions produce constant and linearly varying normal velocity distributions on the airfoil and flap, which can be expressed in terms of the classical pitch and plunge motions α and h, the flap deflection δ, and the freestream velocity U:

$$W_0 = U\alpha + \dot{h}, \tag{C.3}$$

$$W_1 = b\dot{\alpha}. \tag{C.4}$$

$$D_0 = U\delta_f, \tag{C.5}$$

$$D_1 = b\dot{\delta}_f. \tag{C.6}$$

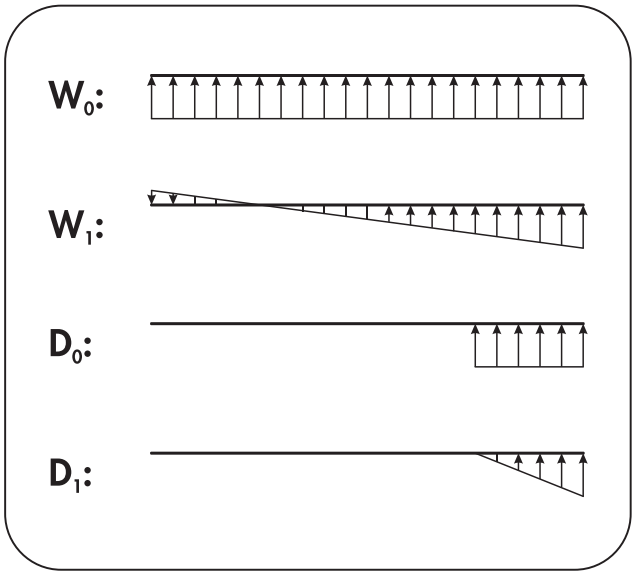

Fig. C.2. Normal velocity distribution corresponding to generalized airfoil and flap motions

For the airfoil and plain flap combination, the generalized motion vector $\mathbf{h}(t)$ and generalized force vector $\mathbf{f}(t)$ are given by:

$$\mathbf{h} = \begin{Bmatrix} W_0 \\ W_1 \\ D_0 \\ D_1 \end{Bmatrix} \tag{C.7}$$

$$\mathbf{f} = \begin{Bmatrix} C_L \\ C_M \\ C_d \\ C_{Hm} \end{Bmatrix}. \tag{C.8}$$

For the airfoil and microflap combination, the generalized motion component D_1 is not used as it primarily represents the apparent mass effect, which is found

to be insignificant for the microflap in the CFD simulations. The generalized force component C_{Hm} defined for a regular flap is not applicable for a microflap. Therefore the generalized motion vector $\mathbf{h}(t)$ and generalized force vector $\mathbf{f}(t)$ are given by:

$$\mathbf{h} = \begin{Bmatrix} W_0 \\ W_1 \\ D_0 \end{Bmatrix} \tag{C.9}$$

where

$$D_0 = \delta_f \tag{C.10}$$

and

$$\mathbf{f} = \begin{Bmatrix} C_L \\ C_M \\ C_d \end{Bmatrix}. \tag{C.11}$$

In order to capture unsteady freestream effects [72], the derivation of the aerodynamic model is carried out in terms of reduced time $\bar{t}$, which is a nondimensional parameter representing the length in semi-chords that the airfoil has traveled.

$$\bar{t} = \frac{1}{b}\int_0^1 U(\tau)d\tau \tag{C.12}$$

The aerodynamic system can then be represented in the form given in Eq. C.1 by taking $\mathbf{G}(\bar{s}) = \mathcal{L}[\mathbf{f}(\bar{t})U(\bar{t})]$ and $\mathbf{H}(\bar{s}) = \mathcal{L}[\mathbf{h}(\bar{t})]$.

To simplify the notation, the lag terms in Eq. C.2 are rewritten in matrix form

[72],

$$\sum_{n=1}^{n_L} \frac{\bar{s}}{\bar{s}+\gamma_n} \mathbf{C}_{n+1} = \mathbf{D}\left(\mathbf{I}\bar{s} - \mathbf{R}\right)^{-1} \mathbf{E}\bar{s}, \tag{C.13}$$

where

$$\mathbf{D} = \begin{bmatrix} \mathbf{I} & \mathbf{I} & \dots & \mathbf{I} \end{bmatrix}, \quad \mathbf{R} = -\begin{bmatrix} \gamma_1\mathbf{I} & & & \\ & \gamma_2\mathbf{I} & & \\ & & \dots & \\ & & & \gamma_{n_L}\mathbf{I} \end{bmatrix}, \quad \mathbf{E} = \begin{bmatrix} \mathbf{C}_2 \\ \mathbf{C}_3 \\ \vdots \\ \mathbf{C}_{n_L+1} \end{bmatrix}. \tag{C.14}$$

Using Eq. C.13, the rational approximant $\tilde{\mathbf{Q}}(\bar{s})$ in Eq. C.2 can be rewritten as

$$\tilde{\mathbf{Q}}(\bar{s}) = \mathbf{C}_0 + \mathbf{C}_1\bar{s} + \mathbf{D}\left(\mathbf{I}\bar{s} - \mathbf{R}\right)^{-1} \mathbf{E}\bar{s}. \tag{C.15}$$

Eq. C.15 is then substituted into Eq. C.1, yielding

$$\mathbf{G}(\bar{s}) = \left(\mathbf{C}_0 + \mathbf{C}_1\bar{s} + \mathbf{D}\left(\mathbf{I}\bar{s} - \mathbf{R}\right)^{-1} \mathbf{E}\bar{s}\right) \mathbf{H}(\bar{s}). \tag{C.16}$$

The lag terms in Eq. C.16 are then used to define a vector of aerodynamic states $\mathbf{X}(\bar{s})$ given by

$$\mathbf{X}(\bar{s}) = \left(\mathbf{I}\bar{s} - \mathbf{R}\right)^{-1} \mathbf{E}\bar{s}\mathbf{H}(\bar{s}). \tag{C.17}$$

Expressing Eq. C.16 in terms of $\mathbf{X}(\bar{s})$ yields

$$\mathbf{G}(\bar{s}) = \mathbf{C}_0\mathbf{H}(\bar{s}) + \mathbf{C}_1\bar{s}\mathbf{H}(\bar{s}) + \mathbf{D}\mathbf{X}(\bar{s}). \tag{C.18}$$

Equations C.17 and C.18 are transformed to the time domain using the inverse Laplace transform. Converting from reduced time $\bar{t}$ to time t using the relation $\frac{d}{d\bar{t}} = \frac{b}{U(t)}\frac{d}{dt}$, yields

$$\dot{\mathbf{x}}(t) = \frac{U(t)}{b}\mathbf{R}\mathbf{x}(t) + \mathbf{E}\dot{\mathbf{h}}(t), \tag{C.19}$$

$$\mathbf{f}(t) = \frac{1}{U(t)}\left(\mathbf{C}_0\mathbf{h}(t) + \mathbf{C}_1\frac{b}{U(t)}\dot{\mathbf{h}}(t) + \mathbf{D}\mathbf{x}(t)\right), \tag{C.20}$$

The aerodynamic loads $\mathbf{f}(t)$ are a function of the aerodynamic states $\mathbf{x}(t)$, which are governed by the set of first order differential equations given by Eq. C.19. Equations C.20 and C.19 are functions of the generalized airfoil and flap motions contained in the vector $\mathbf{h}(t)$.

To account for the large variations in Mach number and large angles of attack encountered in rotary wing applications and the large amplitudes of ACF deflection the RFA model is modified using a technique referred to as *model scheduling* [2]. In this approach, the rational approximants are generated at increments of Mach number, angles of attack and ACF deflection over the range of interest. The resulting coefficient matrices $\mathbf{C}_n(M, \alpha, \delta_f)$ are then functions of the three aforementioned parameters and replace the original coefficients in Eqs. C.19 – C.20, yielding

$$\begin{aligned}\dot{\mathbf{x}}(t) &= \frac{U(t)}{b}\mathbf{R}(M,\alpha,\delta_f)\mathbf{x}(t) + \mathbf{E}(M,\alpha,\delta_f)\dot{\mathbf{h}}(t),\\ \mathbf{f}(t) &= \frac{1}{U(t)}\Big(\mathbf{C}_0(M,\alpha,\delta_f)\mathbf{h}(t)\\ &\quad + \mathbf{C}_1(M,\alpha,\delta_f)\frac{b}{U(t)}\dot{\mathbf{h}}(t) + \mathbf{D}\mathbf{x}(t)\Big).\end{aligned} \tag{C.21}$$

C.2 Dynamic Stall Model for the Separated Flow Regime

Dynamic stall effects due to flow separation are modeled using a semi-empirical dynamic stall model based on a modified version of the ONERA dynamic stall model [24, 25]. The modified aerodynamic state vector for each blade section consists of the CFD based RFA attached flow states and the ONERA separated flow states. Dynamic stall is an important contributor to vibration levels and control loads for the moderate advance ratio ($\mu = 0.3$) considered in this study. In the ONERA model developed by Petot [89], the three second-order differential equations governing the separated flow states are:

$$\ddot{\Pi}_j + a_j\frac{U}{b}\dot{\Pi}_j + r_j\left(\frac{U}{b}\right)^2\Pi_j = -[r_j\left(\frac{U}{b}\right)^2 V\Delta C_j + E_j\frac{U}{b}\dot{W}_0], \tag{C.22}$$

where $j = l, m, d$ represent lift, moment, and drag respectively. The coefficients a_j, r_j, E_j are obtained empirically. The complete two-dimensional sectional airloads are given by:

$$L = L_A + L_S, \;\; M = M_A + M_S, \;\; D = D_A + D_S, \tag{C.23}$$

where L_A, M_A, and D_A are the attached flow lift, moment, and drag, respectively, calculated using the CFD based RFA model. The lift, moment, and drag due to the separated flow are given by:

$$L_S = \frac{1}{2}\rho c_b U \Pi_l, \tag{C.24}$$

$$M_S = \frac{1}{2}\rho c_b^2 U \Pi_m, \tag{C.25}$$

$$D_S = \frac{1}{2}\rho c_b U \Pi_d. \tag{C.26}$$

The flow separation and reattachment criterion is based on the angle of attack and a correction similar to Prandtl-Glauert to account for compressibility. The critical angle of attack for separation and reattachment is $\alpha_{cr} = 15°(1-M^2)$. Contributions to the three sectional airloads from the dynamic stall model, Eqn. C.22, are denoted by $\Delta C_L, \Delta C_M$, and ΔC_D. They can either be zero:

$$\Delta C_L = \Delta C_M = \Delta C_D = 0, \tag{C.27}$$

or take the following values if the flow has separated [24]:

$$\Delta C_L = (p_0 - 0.1M^4)(\alpha - \alpha_{cr}) - 0.7(1-M)[e^{(-0.5+(1.5-M)M^2)(\alpha-\alpha_{cr})} - 1], \tag{C.28}$$

$$\Delta C_M = (-0.11 - 0.19e^{-40(M-0.6)^2})[e^{(-0.4-0.21\arctan[22(0.45-M)])(\alpha-\alpha_{cr})} - 1], \tag{C.29}$$

$$\Delta C_D = (0.008 - 0.3)\left[1 - \left(\frac{25-\alpha}{25-\alpha_{cr}}\right)^{\frac{25-\alpha_{cr}}{18-2\arctan(4M)}-\alpha_{cr}}\right], \tag{C.30}$$

where

$$p_0 = 0.1\frac{1-M^8}{\sqrt{1-M^2}}. \tag{C.31}$$

The separation criteria based on the angle of attack is given by,

1. Case 1: if $\alpha < \alpha_{cr} = 15°(1-M^2)$, $\Delta C_L = \Delta C_M = \Delta C_D = 0$.

2. Case 2: assume that at time $t = t_0$, $\alpha = \alpha_{cr}$, $\dot{\alpha} > 0$; then, for $t > t_0 + \Delta t$, $\Delta C_L, \Delta C_M$, and ΔC_D are given by Eqs. C.28-C.30.

3. Case 3: when $\alpha < \alpha_{cr}$, the flow is reattached and $\Delta C_L, \Delta C_M$, and ΔC_D are set to zero again.

The ONERA model features 18 empirical coefficients, 6 each $(r_{j0}, r_{j2}, a_{j0}, a_{j2}, E_{j2})$ associated with lift $(j = l)$, moment $(j = m)$, and drag $(j = d)$. These quantities can be found in Ref. 24.

C.3 Free Wake Model

The wake analysis consists of two elements: (1) a wake geometry calculation procedure including a free wake analysis developed by Scully [101], which determines the position of the vortices; (2) an induced velocity calculation procedure as implemented in CAMRAD/JA, which calculates the nonuniform induced velocity distribution at the blades.

C.3.1 Wake Geometry

The rotor wake is composed of two main elements: the tip vortex, which is a strong, concentrated vorticity filament generated at the tip of the blade; and the near wake, which is an inboard sheet of trailed vorticity. The near wake is much weaker and more diffused than the tip vortex. The wake vorticity is created in the flow field as the blade rotates, and then convected with the local velocity of the fluid. The local velocity of the fluid consists of the free stream velocity, and the wake self induced velocity. Thus, the wake geometry calculation proceeds as follows: (1) the position of the blade generating the wake element is calculated, this is the point at which the wake vorticity is created; (2) the undistorted wake geometry is computed as wake elements are convected downstream from the rotor by the free stream velocity; (3) distortion of wake due to the wake self-induced velocity is computed and added to the undistorted geometry. The position of a generic wake element is identified by its current azimuth position ψ and its age ϕ_w. Age is the nondimensional time that has elapsed since the wake element's creation. Thus, the position of a generic wake element is written as:

$$\mathbf{r}_w(\psi, \phi_w) = \mathbf{r_b}(\psi - \phi_w) + \phi_w \mathbf{V_A} + \mathbf{D}(\psi, \phi_w) \tag{C.32}$$

where $\mathbf{r_b}(\psi - \phi_w)$ is the position of the blade when it generates the wake element, $\mathbf{V_A}$ is the free stream velocity, and $\mathbf{D}(\psi, \phi_w)$ is the wake distortion.

To evaluate the wake self-induced distortion $\mathbf{D}(\psi, \phi_w)$, a free wake procedure developed by Scully [101] is employed. This procedure is used only to calculate

the distorted geometry of the tip vortices, which is the dominant feature of the rotor wake. The inboard vorticity is determined by a prescribed wake model [46] to save the computational cost.

In the free wake geometry calculation, the distortion $\mathbf{D}$ is obtained by integrating in time the induced velocity at each wake element due to all the other wake elements. The induced velocity $\mathbf{q_I}$ is calculated at all wake elements for a given age ϕ_w, and all azimuth angles ψ. As the wake age increases by $\Delta\psi$, the distortion at ψ is obtained by adding the contribution of the induced velocity to the distortion at previous azimuthal step:

$$\mathbf{D}(\psi, \phi_w) = \mathbf{D}(\psi, \phi_w - \Delta\psi) + \Delta\psi \mathbf{q}(\psi) \tag{C.33}$$

The distortion in the wake at the time of its creation is zero. Hence,

$$\mathbf{D}(\psi, 0) = 0. \tag{C.34}$$

C.3.2 Induced Velocity Calculation

The induced velocity calculation procedure, developed by Johnson [46], is based on a vortex-lattice approximation for the wake. The tip vortex elements are modeled by line segments with a small viscous core radius, while the near wake can be represented by vortex sheet elements or by line segments with a large core radius to eliminate large induced velocities. The near wake vorticity is generally retained for only a number K_{NW} of azimuth steps behind the blade. The wake structure is

illustrated in Fig. C.3.

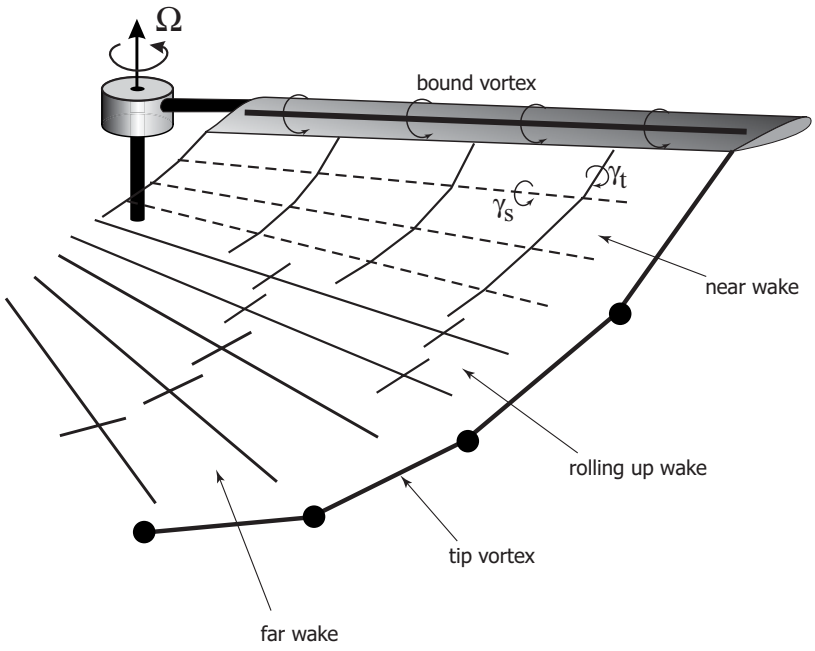

Fig. C.3. Vortex-lattice approximation for rotor wake model

Conservation of vorticity on a three-dimensional blade requires the bound circulation to be trailed into the wake from the blade tip and root. The lift and circulation are concentrated at the tip of the blade, since larger dynamic pressures are present in the tip region. Therefore, a strong, concentrated tip vortex is generated. The vorticity in the tip vortex is distributed over a small but finite region, called the vortex core. The accuracy of a wake model is sensitive to the value of the strength of the tip vortex prescribed. Two different approaches are used, depending on the spanwise distribution of the bound circulation. For helicopters in low speed forward flight, the bound circulation is positive along the entire span of the blade (Fig. C.4). The distribution of the bound circulation has only one peak and is refered to as the single peak model. In the single peak model, the maximum

value of the bound circulation over the blade span, Γ_{max}, is selected for the tip vortex strength. For helicopters in high speed forward flight or under some means of active control, a spanwise circulation distribution with two peaks of opposite sign can be encountered. A large positive peak is generally located inboard and a smaller negative peak on the outboard section of blade (Fig. C.5). The dual peak model represents such a situation. The inboard and outboard peaks Γ_I and Γ_O, respectively, are identified, and the tip vortex strength assumes the value of the outboard peak.

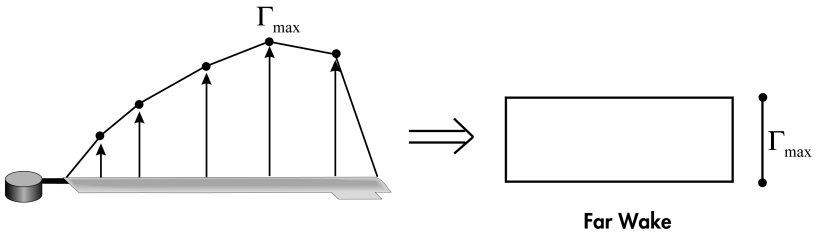

Fig. C.4. Single peak circulation distribution model and the resulting far wake approximation

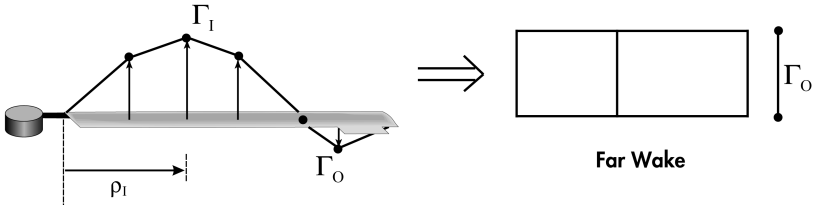

Fig. C.5. CAMRAD/JA dual peak model and the resulting far wake approximation

Given the blade displacements and circulation distribution, the wake geometry is calculated. Once the wake geometry has been determined, the influence coefficients are calculated and stored in the influence coefficient matrix. The induced velocity distribution is obtained by conveniently multiplying the influence coeffi-

cient matrix with the circulation distribution:

$$\mathbf{q} = \sum_{j=1}^{J} \Gamma_{Oj} \mathbf{C}_{Oj} + \sum_{j=1}^{J} \Gamma_{Ij} \mathbf{C}_{Ij} + \sum_{j=1}^{K_{NW}} \sum_{i=1}^{M} \Gamma_{ij} \mathbf{C}_{NWij}, \tag{C.35}$$

where $\Gamma_{I_j}, \Gamma_{O_j}$ are the inboard and outboard peaks, respectively, at the azimuth j; J, M are the numbers of azimuth and spanwise stations, respectively; K_{NW} is the number of azimuth stations on which the near wake extends; $\mathbf{C}_{O_j}, \mathbf{C}_{I_j}$ and $\mathbf{C}_{NW_{ij}}$ are terms of the influence coefficient matrix. For the single peak model, $\Gamma_{O_j} = \Gamma_{\max j}$ and $\Gamma_{I_j} = 0$.

C.3.3 Wake Modeling Improvements

As mentioned earlier, the fidelity of the wake model dictates the accuracy of BVI noise prediction. Therefore, a number of improvements were made to the CAMRAD/JA wake model by Patt, Liu, and Friedmann [59, 84, 87] in order to obtain better correlation with the HART experimental data. Two modifications are discussed below.

C.3.3.1 Wake Resolution

For accurate prediction of BVI noise, a 5° or finer azimuthal wake resolution is required, as compared to the much coarser 15° resolution that is often adequate for vibration reduction studies. The original CAMRAD/JA wake code uses a resolution of 15° for the free wake analysis. This restriction was removed in the current wake code to allow for wake resolution of up to 2°. However, due to some nu-

merical difficulties [101] the free wake model failed to converge for the resolutions finer than 3° and therefore a resolution of 5° was used. This resolution was shown to be adequate for BVI noise prediction through validations against the HART experimental data [59, 84]. An azimuthal wake resolution of 5° is used for the active control simulations in the current study.

C.3.3.2 Dual Vortex Rollup

The free wake model taken from CAMRAD/JA was based on the assumption that the inboard vortices cannot roll up, thus facilitating the use of either a vortex-sheet or an equivalent vortex-line model to model the inboard vortices. This was not compatible with the HART test data where significant increases in BVI noise levels for the "minimum vibration" case have been attributed to a dual vortex structure [107].

A dual vortex model was therefore incorporated by including a possible second inboard vortex line. This feature of the wake model becomes active only when the tip loading becomes negative, as shown in Fig. C.6. The release point of this second vortex line is taken to be at the radial location r_I, where blade bound circulation becomes negative, and the strength of this vortex is assumed to be $\Gamma_I - \Gamma_O$, where Γ_O, the outboard circulation peak, is negative. Furthermore, the free wake distortion computation routine was also modified to include the deformation of this second inboard vortex line, including its interaction with the outer tip vortices. This was realized by evaluating the self-induced velocities by both tip vortices and secondary vortices. Moreover, a threshold criteria, suggested in Ref. 92, can be em-

ployed to determine whether to have inboard vortex line rolled up. Rollup of the inboard vortex is allowed when the radial gradient of the bound circulation $\partial\Gamma/\partial r$ at the inboard vortex release point r_I is greater than a specified threshold value. This condition represents the physical requirement that the shear in the wake be sufficiently strong so as to form a fully rolled-up, concentrated vortex.

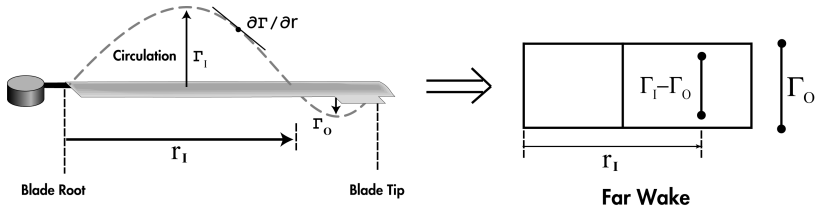

Fig. C.6. Improved dual peak model, leading to dual concentrated vortex lines

C.4 Reverse Flow Model

In forward flight, there exists a reverse flow region on the retreating side of the rotor disk where the airflow encountered by the blade is flowing from the trailing edge to the leading edge. The boundary of this region on the blade span as a function of azimuth ψ and advance ratio μ is given by

$$x_{rev}(\psi) = -(e_1 + \mu R \sin\psi). \tag{C.36}$$

This is illustrated schematically in Fig. C.7. In the present analysis, it is assumed that the aerodynamic lift and moment are zero within the reverse flow region, and that the aerodynamic drag changes direction inside the reverse flow region, remaining parallel to the total air velocity. This is accomplished by multiplying

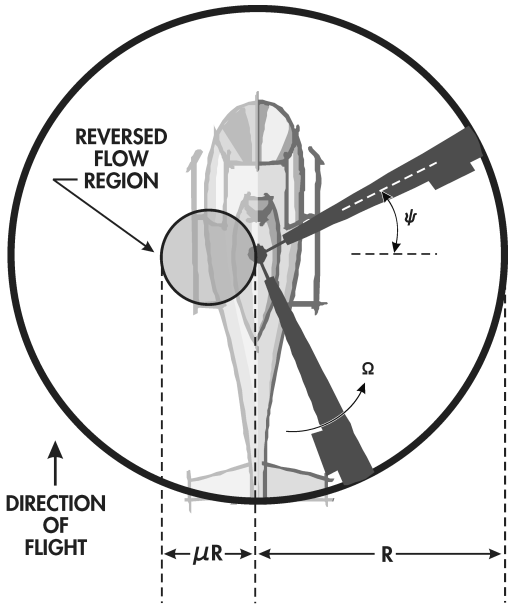

Fig. C.7. Reverse flow region

the aerodynamic lift and moment expressions by the reverse flow parameter R_{LM}, and the drag expression by the reverse flow parameter R_D. These parameters are defined as follows:

$$R_{LM} = \begin{cases} 0 & for \quad 0 \leq x \leq x_{rev}(\psi) \\ 1 & for \quad x > x_{rev}(\psi) \end{cases}$$

$$R_D = \begin{cases} -1 & for \quad 0 \leq x \leq x_{rev}(\psi) \\ 1 & for \quad x > x_{rev}(\psi) \end{cases}$$

C.5 Sectional Airloads

Final expressions for the sectional airloads are obtained by combining the RFA aerodynamic model, the ONERA dynamic stall model, and the reverse flow model.

For non-flapped sections, the sectional lift, moment, and drag are given by

$$L = \rho U^2 b \left(C_{L_A} + C_{L_S}\right) R_{LM}, \tag{C.37}$$

$$M = 2\rho U^2 b^2 \left(C_{M_A} + C_{M_S}\right) R_{LM}, \tag{C.38}$$

$$D = \rho U^2 b \left(C_{d0} + C_{D_S}\right) R_D. \tag{C.39}$$

where C_{L_A} and C_{M_A} are obtained from Eq. C.21, C_{L_S}, C_{M_S}, and C_{D_S} are based on Eqs. C.24, C.25, and C.26 respectively.

For flapped sections,

$$L = \rho U^2 b C_{L_A} R_{LM}, \tag{C.40}$$

$$M = 2\rho U^2 b^2 C_{M_A} R_{LM}, \tag{C.41}$$

$$D = \rho U^2 b C_{d0} R_D. \tag{C.42}$$

Flapped sections have an additional expression for the hinge moment given by

$$H_m = 2\rho U^2 b^2 C_{Hm}, \tag{C.43}$$

In addition, the following simple linear model is used to account for the effect of flap deflection on profile drag [24]:

$$C_{d0} = 0.01 + 0.001 \left|\delta_f\right| \tag{C.44}$$

To incorporate the aerodynamic model in the present analysis, expressions for W_0, W_1, U and α in terms of the blade degrees of freedom and modal parameters are needed:

$$\alpha = \theta_G + \phi \tag{C.45}$$

$$U = U_T \tag{C.46}$$

$$\dot{h} = -U_P \tag{C.47}$$

$$W_0 = U\alpha + \dot{h} \tag{C.48}$$

$$W_1 = b\dot{\alpha} \tag{C.49}$$

where U_T and U_P correspond to the components of the total air velocity $\mathbf{V_A}$ taken in the $-\hat{e}_{y5}$ and $-\hat{e}_{z5}$ directions, respectively, as illustrated in Figure C.8.

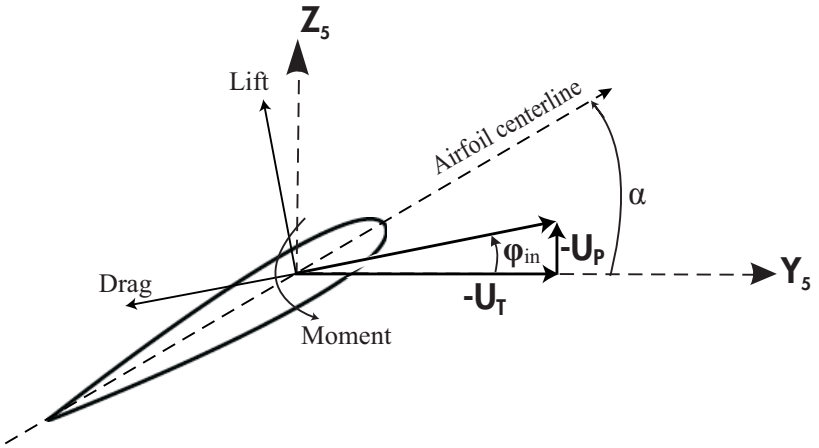

Fig. C.8. Orientation of tangential and perpendicular air velocities and aerodynamic loads.

C.5.1 Blade Velocity Relative to Air

U_T and U_P can be expressed as

$$U_T = -V_{Ay5}, \tag{C.50}$$

$$U_P = -V_{Ay5} \tag{C.51}$$

where V_{Ay5} and V_{Az5} represent the y and z components of the freestream velocity vector at the elastic axis in the “5" system.

The total freestream air velocity $\mathbf{V_A}$ encountered by the blade is calculated as the sum of airflow velocity due to forward flight, blade rotation and induced inflow $\mathbf{V_{A1}}$ and airflow velocity due to blade dynamics $\mathbf{V_{A2}}$ and can be expressed as follows:

$$\mathbf{V_A} = \mathbf{V_{A1}} - \mathbf{V_{A2}}, \tag{C.52}$$

where,

$$\mathbf{V_{A1}} = \Omega R[(\mu + \lambda_x)\hat{e}_{x1} + \lambda_y \hat{e}_{y1} + \lambda_z \hat{e}_{z1}] \tag{C.53}$$

and

$$\mathbf{V_{A2}} = \dot{\mathbf{r}}_{\mathbf{EA}} + \Omega \hat{e}_{z2} \times \mathbf{r_{EA}}. \tag{C.54}$$

The advance ratio μ and inflow ratio λ are given by

$$\mu = \frac{V_F \cos \alpha_R}{\Omega R}, \tag{C.55}$$

$$\lambda = \frac{V_F \sin \alpha_R + \nu}{\Omega R}, \tag{C.56}$$

where V_F is the freestream velocity, α_R is the rotor shaft angle, and ν is the induced flow velocity. The position vector for a point on the elastic axis $\mathbf{r_{EA}}$ is given by:

$$\mathbf{r_{EA}} = e\hat{e}_{x2} + (x+u)\hat{e}_{x3} + v\hat{e}_{y3} + w\hat{e}_{z3}. \tag{C.57}$$

The resultant velocity $\mathbf{V_A}$ is expressed in the $(\hat{e}_{x5}, \hat{e}_{y5}, \hat{e}_{z5})$ coordinate system using appropriate coordinate transformations, described in the previous section. As mentioned earlier, U_T and U_P correspond to the components of the total air velocity $\mathbf{V_A}$ in the $-\hat{e}_{y5}$ and $-\hat{e}_{z5}$ directions, respectively, which are given by the expressions [Ref. [72], Eqs. (5.176)-(5.177)]:

$$\begin{aligned} U_T &= \Omega(x+e+u) + \Omega v v_{,x} - \Omega w \beta_p + \dot{v} \\ &\quad + (\mu+\lambda_x)\Omega R v_{,x}\cos\phi + \lambda_y \Omega R v_{,x}\sin\phi \\ &\quad + (\mu+\lambda_x)\Omega R\sin\phi - \lambda_y \Omega R\cos\phi, \end{aligned} \tag{C.58}$$

$$\begin{aligned} U_P &= \dot{w} + \Omega v(w_{,x} + \beta_p) - \lambda_z \Omega R + (\mu+\lambda_x)\Omega R(w_{,x}+\beta_p)\cos\phi \\ &\quad - \lambda_y \Omega R(w_{,x}+\beta_p)\cos\phi. \end{aligned} \tag{C.59}$$

These expressions for U_T and U_P are then substituted into Eqs. (C.45-C.49) to produce explicit expressions for U, $\dot{h}$, and the generalized airfoil and flap motions.

C.5.2 Distributed Aerodynamic Loads

Expressions for sectional lift and drag have been obtained in Eqns. (C.37) and (C.39), respectively. Lift is assumed to act normal to the total air velocity, and drag

is assumed to act parallel to it. Furthermore, all aerodynamic forces act at the quarter chord, which is assumed to coincide with the elastic axis, thus $X_A = 0$. Following these assumptions, the spanwise distributed aerodynamic force in the "5" system is given by:

$$\mathbf{p_A} = p_{Ay5}\hat{e}_{y5} + p_{Az5}\hat{e}_{z5}, \tag{C.60}$$

where:

$$p_{Ay5} = -D\cos\phi_{in} - L\sin\phi_{in}, \tag{C.61}$$

$$p_{Az5} = -D\sin\phi_{in} + L\cos\phi_{in}, \tag{C.62}$$

The inflow angle ϕ_{in} is the angle between U_T and the resultant air velocity, given by:

$$\cos\phi_{in} = \frac{U_T}{\sqrt{U_T^2 + U_P^2}}. \tag{C.63}$$

The distributed aerodynamic moment in Eq. (A.78) is assumed to act about the elastic axis of the blade. It can be expressed in the "5" system as:

$$\mathbf{q_A} = q_{Ax5}\hat{e}_{x5}, \tag{C.64}$$

where:

$$q_{Ax5} = M. \tag{C.65}$$

Using appropriate transformations, the distributed aerodynamic force in the "3" system is given by:

$$\mathbf{p_A} = p_{Ax3}\hat{e}_{x3} + p_{Ay3}\hat{e}_{y3} + p_{Az3}\hat{e}_{z3}, \tag{C.66}$$

where:

$$p_{Ax3} = -v_{,x}\, p_{Ay5} - w_{,x}\, p_{Az5}, \tag{C.67}$$

$$p_{Ay3} = p_{Ay5}, \tag{C.68}$$

$$p_{Az3} = -v_{,x}\, w_{,x}\, p_{Ay5} + p_{Az5}. \tag{C.69}$$

Similarly, the distributed aerodynamic moment is expressed in the "3" system as:

$$\mathbf{q_A} = q_{Ax3}\hat{e}_{x3} + q_{Ay3}\hat{e}_{y3} + q_{Az3}\hat{e}_{z3}, \tag{C.70}$$

where:

$$q_{Ax3} = q_{Ax5}, \tag{C.71}$$

$$q_{Ay3} = v_{,x}\, q_{Ax5}, \tag{C.72}$$

$$q_{Az3} = w_{,x}\, q_{Ax5}. \tag{C.73}$$

APPENDIX D

Solution Procedure

D.1 Coupled Trim/Aeroelastic Response Solutions

D.1.1 Solution of the Blade Equations of Motion for the global Galerkin Model

The spatial dependence of the equations of motion is removed using Galerkin's method of weighted residuals. Three flap, two lead-lag, and two torsional free vibration modes of a rotating beam are used to represent the flexibility of the blade. Each free vibration mode was calculated using the first nine exact nonrotating modes of a uniform cantilevered beam. The displacements v and w and twist ϕ

are thus represented by:

$$w \cong \sum_{i=1}^{3} q_{wi}(\psi) W_i(x), \tag{D.1}$$

$$v \cong \sum_{i=1}^{2} q_{vi}(\psi) V_i(x), \tag{D.2}$$

$$\phi \cong \sum_{i=1}^{2} q_{\phi i}(\psi) \Phi_i(x), \tag{D.3}$$

where W_i, V_i, and Φ_i are the i-th rotating flap, lead-lag, and torsional uncoupled mode shapes, respectively, with participation coefficients q_{wi}, q_{vi}, and $q_{\phi i}$. These mode shapes satisfy the boundary conditions of a hingeless blade cantilevered to the hub, which implies:

$$w(\psi,0) = v(\psi,0) = \phi(\psi,0) = 0, \tag{D.4}$$

$$w_{,x}(\psi,0) = v_{,x}(\psi,0) = 0, \tag{D.5}$$

$$w_{,xx}(\psi,R) = v_{,xx}(\psi,R) = 0, \tag{D.6}$$

$$w_{,xxx}(\psi,R) = v_{,xxx}(\psi,R) = 0. \tag{D.7}$$

Galerkin's method is applied by substituting (D.1)-(D.3) in (A.19)-(A.21). The error residuals are then multiplied by the appropriate mode shape and integrated over the span of the blade. After having introduced the appropriate boundary conditions, seven equations of motion are obtained [Ref. 72, Eqns. (6.12)-(6.14)]:

Flap Equations $(i = 1, 2, 3)$:

$$\int_0^{L_b} \{-[(EI_{\zeta\zeta} - EI_{\eta\eta}) \sin\theta_G \cos\theta_G (v_{,xx} + 2\phi w_{,xx}) + (EI_{\zeta\zeta} - EI_{\eta\eta})\phi v_{,xx} \cos 2\theta_G + (EI_{\zeta\zeta} \sin^2\theta_G + EI_{\eta\eta} \cos^2\theta_G) w_{,xx} - TX_{IIb}(\sin\theta_G + \phi \cos\theta_G)] W_{i,xx} + (GJ_b \phi_{,x} v_{,xx} + w_{,x} T - v_{,x} (q_{bx3} + q_{cx3}) + (q_{by3} + q_{cy3})) W_{i,x} + (p_{bz3} + p_{cz3}) W_i\} dx = 0. \quad \text{(D.8)}$$

Lag Equations $(i = 1, 2)$:

$$\int_0^{L_b} \{-[(EI_{\zeta\zeta} \cos^2\theta_G + EI_{\eta\eta} \sin^2\theta_G) v_{,xx} + (EI_{\zeta\zeta} - EI_{\eta\eta})\phi w_{,xx} \cos 2\theta_G + (EI_{\zeta\zeta} - EI_{\eta\eta}) \sin\theta_G \cos\theta_G (w_{,xx} - 2\phi v_{,xx}) - TX_{IIb}(\cos\theta_G - \phi \sin\theta_G)] V_{i,xx} + (-GJ_b \phi_{,x} w_{,xx} + v_{,x} T + w_{,x} (q_{bx3} + q_{cx3}) - (q_{bz3} + q_{cz3})) V_{i,x} + (p_{by3} + p_{cy3}) V_i\} dx = 0. \quad \text{(D.9)}$$

Torsional Equations $(i = 1, 2)$:

$$\int_0^{L_b} \{[GJ_b(\phi_{,x} - v_{,x} w_{,xx})] \Phi_{i,x} + (EI_{\zeta\zeta} - EI_{\eta\eta})[({v_{,xx}}^2 - {w_{,xx}}^2) \sin\theta_G \cos\theta_G - v_{,xx} w_{,xx} \cos 2\theta_G] \Phi_i + TX_{IIb}(w_{,xx} \cos\theta_G - v_{,xx} \sin\theta_G) \Phi_i + ((q_{bx3} + q_{cx3}) + v_{,x} (q_{by3} + q_{cy3}) + w_{,x} (q_{bz3} + q_{cz3})) \Phi_i\} dx = 0. \quad \text{(D.10)}$$

The spatial dependence of these equations is eliminated when all mode shape substitutions are made and the integration is performed. The spanwise integrations are carried out numerically in the simulation, using Gaussian quadrature. This process produces a set of seven nonlinear ordinary differential equations in terms of q_{w1}, q_{w2}, q_{w3}, q_{v1}, q_{v2}, $q_{\phi 1}$, and $q_{\phi 2}$. They can be expressed in state variable form, where the vector $\mathbf{q_b}$ of blade degrees of freedom is:

$$\mathbf{q_b} = \begin{bmatrix} q_{w1} & q_{w2} & q_{w3} & q_{v1} & q_{v2} & q_{\phi 1} & q_{\phi 2} \end{bmatrix}^T . \tag{D.11}$$

For integration using Gaussian quadrature, the integrand is evaluated at a set number of stations along the span of the blade at locations corresponding to predefined Gaussian points. At each station, the sectional airloads are provided by the CFD based RFA model which requires solving a set of aerodynamic state equations. These aerodynamic state equations are fully coupled with the blade equations of motion given in Eqns. (D.8)-(D.10) through the blade degrees of freedom and the aerodynamic loads. The structural and aerodynamic equations include a set of trim parameters. The trim parameters are obtained by solving a set of trim equations which enforce force and moment equilibrium at the hub.

D.1.2 Solution of the Blade Equations of Motion from the Galerkin Type Finite Element Model

D.1.2.1 Free Vibration Analysis

The first step in the solution procedure is the calculation of the natural frequencies and mode shapes of the blade. The coupled equations of motion representing the free vibrations of the rotating blade are a set of nonlinear ordinary differential equations obtained from the finite element discretization described in Appendix B. The computation of the natural frequencies and mode shapes of the blade is based on the linear, undamped equations of motion. The equations of motion for the typical element used to model the straight portion of the blade are:

$$[M_i^F]\ddot{\mathbf{q}}_i + [K_i^F]\mathbf{q}_i = \mathbf{0}, \qquad \text{i=1,...,n-1} \; . \tag{D.12}$$

and for the tip element, the equations of motion are given by

$$[\Lambda^L]^T[M_t^F][\Lambda^L]\ddot{\mathbf{q}}_t^G + [\Lambda^L]^T[K_t^F][\Lambda^L]\mathbf{q}_t^G = 0. \tag{D.13}$$

where the linear transformation $[\Lambda^L]$ is used in the local-to-global coordinate transformation.

The n-1 equations represented by Eqns. (D.12) and (D.13) are then assembled using the standard finite clement assembly procedure. The assembled finite ele-

ment equations of motion for the free vibrations of the blade are written as

$$[M^F]\ddot{\mathbf{q}}_i + [K^F]\mathbf{q}_i = \mathbf{0} \tag{D.14}$$

In Eqns. (D.12) and (D.14), the superscript F denotes matrices used in the free vibration analysis. The boundary conditions at the blade root for a cantilevered beam are imposed.

D.1.2.2 Modal Coordinate Transformation and Assembly Procedure

A preliminary step in the solution of the aeroelastic formulation is the modal coordinate transformation performed on the blade equations so as to reduce the number of degrees of freedom, and to assemble the various element matrices into global system mass, damping, and stiffness matrices as well as the system load vector. For the i-th clement, the modal coordinate transformation has the form:

$$\mathbf{q}_i = [Q_i]\mathbf{y} \tag{D.15}$$

where $\mathbf{y}$ is the vector of generalized modal coordinates, which becomes the new unknowns of the problem and has size N_m which is the number of modes used to perform the modal coordinate transformation. In this study, the following 8 modes are used: the first 3 flap modes, first 2 lead-lag modes, first 2 torsional modes, and the first axial mode.

The assembled stiffness, damping and mass matrices of the blade are obtained

by summing the matrices of the individual elements after the modal coordinate transformation has been performed on each of these elements:

$$[K] = \sum_{i=1}^{n-1}[Q_i]^T[K_i][Q_i] + [Q_t]^T[\Lambda_L]^T[K_t]([\Lambda^L] + [\Lambda^K]) \tag{D.16}$$

$$[C] = \sum_{i=1}^{n-1}[Q_i]^T[C_i][Q_i] + [Q_t]^T[\Lambda^L]^T[C_t]([\Lambda^L] + [\Lambda^C]) + [M_t][\Lambda^M][Q_t] \tag{D.17}$$

$$[M] = \sum_{i=1}^{n-1}[Q_i]^T[M_i][Q_i] + [Q_t]^T[\Lambda^L]^T[M_t]([\Lambda^L] + [\Lambda^C])[Q_t] \tag{D.18}$$

where $[\Lambda^K]$, $[\Lambda^C]$, $[\Lambda^M]$ are defined in Ref. 125 and the assembled load vector is given by:

$$\mathbf{F} = \sum_{i=1}^{n-1}[Q_i]^T\mathbf{F}_i + [Q_t]^T[\Lambda^L]^T\mathbf{F_t} \tag{D.19}$$

In Eqns. (D.16) – (D.19), the local-to-global transformation for the tip element has been applied before implementing the modal transformation. The assembled blade equations of motion in the modal space are a set of nonlinear, coupled, ordinary differential equations written as:

$$[M(\mathbf{y})]\ddot{\mathbf{y}} + [C(\mathbf{y}, \dot{\mathbf{y}})]\dot{\mathbf{y}} + [K(\mathbf{y}, \dot{\mathbf{y}}, \ddot{\mathbf{y}})]\mathbf{y} + \mathbf{F}(\mathbf{y}, \dot{\mathbf{y}}, \ddot{\mathbf{y}}) = \mathbf{0} \tag{D.20}$$

D.1.3 Propulsive Trim Procedure

The propulsive trim procedure models actual free-flight conditions. A helicopter in free flight has six degrees of freedom; thus, six equilibrium equations must be satisfied. The trim procedure, taken from Ref. 21, enforces these equilibrium equations in straight and level flight conditions. A modified version of this

procedure developed in Refs. 59, 84 is used for descending flight conditions.

In the case of actual helicopter flight, the pilot inputs consist of collective and cyclic inputs (θ_0, θ_{1s}, θ_{1c}) and the tail rotor pitch (θ_{0t}). For a given flight condition, the quantities C_W and μ are known, and the trim procedure generates the equilibrium values of θ_0, θ_{1s}, θ_{1c}, ϕ_R, α_R, and θ_{0t}. These variables comprise the six-component helicopter trim vector $\mathbf{q_t}$.

Only the average values of the rotor hub forces and moments, identified by overbars, are required. Since non-uniform inflow is used in this study, the trim procedure does not require an explicit inflow relation. The complete six equilibrium equations are enforced in the present trim calculation. A simplified model for the tail rotor, developed in Ref. 21, is used. The vector $\mathbf{q_t}$ of trim variables is defined as

$$\mathbf{q_t} = \{\alpha_R, \theta_0, \theta_{1c}, \theta_{1s}, \theta_{0t}, \phi_R\}^T. \tag{D.21}$$

A schematic of a helicopter in descending flight is depicted in Fig. D.1. The equilibrium equations are formulated in the nonrotating, hub-fixed system (x_1, y_1, z_1). The helicopter weight W acts at the center of gravity of the fuselage, which is offset from the hub center by the distances X_{FC} and Z_{FC} in the $-\hat{e}_{x1}$ and $-\hat{e}_{z1}$ directions respectively. The trim procedure has a provision for accommodating the aerodynamic drag that acts at a location (the aerodynamic center) that is different from the center of gravity. However, in all the cases considered in this study, the flat plate drag always acts at the center of gravity of the fuselage, and $X_{FA} = X_{FC}$, $Y_{FA} = Y_{FC}$, and $Z_{FA} = Z_{FC}$. The lateral center of gravity offset Y_{FC} is also set to

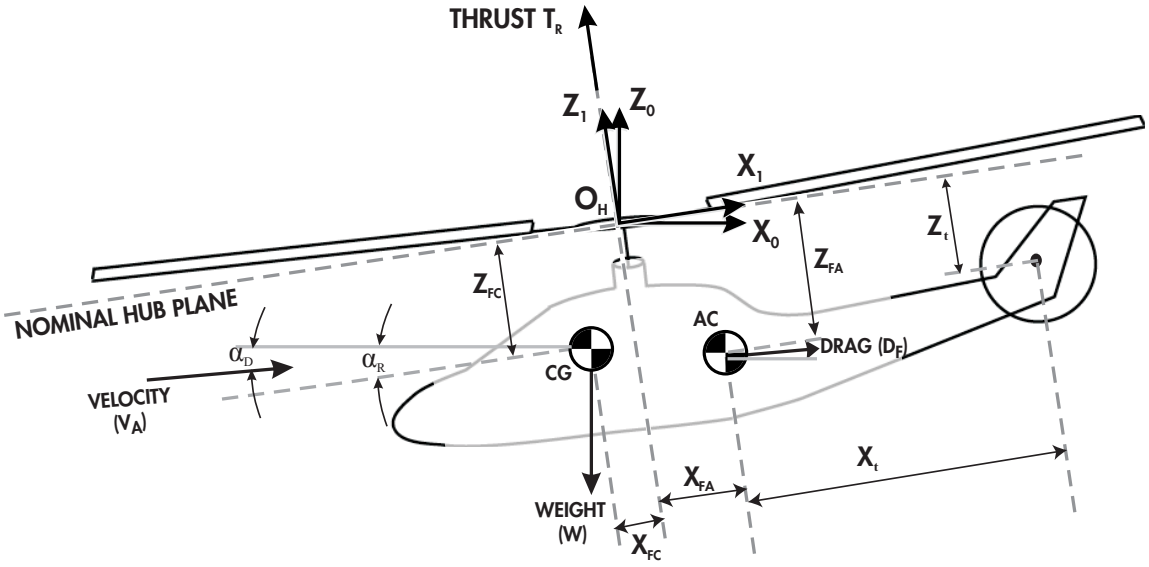

Fig. D.1. A schematic of the helicopter in descending flight

zero for cases considered in this study. The flat-plate drag is given by:

$$D_f = \frac{1}{2}\rho_A \mathbf{V_A}^2 C_{df} \pi R^2. \tag{D.22}$$

A typical value for the flat-plate drag coefficient is

$$C_{df} = 0.01. \tag{D.23}$$

In descending flight, a constant angle α_D is defined as the angle between the forward flight velocity $\mathbf{V_A}$ and the horizontal plane, and is shown in Fig. D.1. The descent angle is a known quantity along with W and μ. Note that the drag force D_f will continue to act parallel to the direction of the resultant velocity $\mathbf{V_A}$. Setting the descent angle $\alpha_D = 0$, trim equations for a level flight condition similar to those found in Ref. 21 can be recovered. The trim equations are:

a. Pitching Moment

Moment equilibrium about the y_1 axis requires:

$$\begin{aligned} \overline{M}^{pt} + W[-X_{FC}\cos\phi_R\cos\alpha_R + Z_{FC}\cos\phi_R\sin\alpha_R] \\ -D_f[-X_{FA}\sin(\alpha_R-\alpha_D) + Z_{FA}\cos(\alpha_R-\alpha_D)] - Q_t &= 0. \end{aligned} \tag{D.24}$$

b. Rolling Moment

Moment equilibrium about the x_1 axis requires:

$$\overline{M}^{rl} - Z_{FC}W\sin\phi_R + T_t Z_t = 0. \tag{D.25}$$

where T_t is the tail rotor thrust and Z_t is the vertical distance between the hub axis and the center of the tail rotor.

c. Yawing Moment

Moment equilibrium about the z_1 axis requires:

$$\overline{M}^{yw} - X_{FC}W\sin\phi_R + T_t X_t = 0. \tag{D.26}$$

where T_t is the tail rotor thrust and X_t is the horizontal distance between the hub axis and the center of the tail rotor (Fig. D.1).

d. Vertical Force

Force equilibrium in the z_1 direction requires:

$$\overline{F_T} - W\cos\alpha_R\cos\phi_R - D_f\sin(\alpha_R-\alpha_D) = 0. \tag{D.27}$$

e. Longitudinal Force

Force equilibrium in the x_1 direction requires:

$$\overline{H} - W \sin\alpha_R \cos\phi_R + D_f \cos(\alpha_R - \alpha_D) = 0. \tag{D.28}$$

f. Lateral Force

Force equilibrium in the y_1 direction requires:

$$\overline{Y} - W \sin\alpha_R \cos\phi_R + T_t = 0. \tag{D.29}$$

The advance ratio μ and inflow ratio λ were defined in Eqns. C.55 and C.56 as

$$\mu = \frac{V_F \cos\alpha_R}{\Omega R} \tag{D.30}$$

$$\lambda = \frac{V_F \sin\alpha_R + \nu}{\Omega R} \tag{D.31}$$

For descending flight, these equations must be modified by replacing α_R with $(\alpha_R - \alpha_D)$. Thus, the modified expressions for advance ratio μ and inflow ratio λ are:

$$\begin{aligned} \mu &= \frac{V_F \cos(\alpha_R - \alpha_D)}{\Omega R} \\ \lambda &= \frac{V_F \sin(\alpha_R - \alpha_D) + \nu}{\Omega R} \end{aligned} \tag{D.32}$$

here ν is the induced inflow velocity. For the free wake analysis, it is replaced by a nonuniform inflow distribution.

D.1.4 Wind-Tunnel Trim Procedure

For wind-tunnel trim, the previous trim procedure can be simplified because the force equilibrium equations are automatically satisfied and the tail rotor is not modeled. The prescribed quantities are α_R, θ_0, μ and the cyclic pitch components are used to trim out the pitching and rolling moments on the rotor. For the coupled wind-tunnel trim analysis implemented in the code, the following moment equations are enforced:

a. Pitching Moment

$$\begin{aligned} \overline{M}^{pt} + W[-X_{FC}\cos\phi_R\cos\alpha_R + Z_{FC}\cos\phi_R\sin\alpha_R] \\ -D_f[-X_{FA}\sin(\alpha_R-\alpha_D) + Z_{FA}\cos(\alpha_R-\alpha_D)] &= 0. \end{aligned} \tag{D.33}$$

b. Rolling Moment

$$\overline{M}^{rl} - Z_{FC}W\sin\phi_R = 0. \tag{D.34}$$

The solution procedure is similar to that for the full vehicle trim equations discussed above, except the cyclic controls (θ_{1S} and θ_{1C}) are adjusted iteratively to satisfy Eqns. (D.33) and (D.34). Thus, for wind-tunnel trim, the trim vector is reduced in size to match the two equilibrium equations. To simulate descent flight using the wind-tunnel trim procedure, the shaft angle α_R is set to chosen value approximating the angle of the rotor in descending flight and the thrust coefficient, C_T, is prescribed to obtain the collective pitch setting, θ_0. This follows the procedure used in the experiment described in Ref. 107.

D.2 Time Integration of the Coupled Trim/Aeroelastic Equations

The complete aeroelastic model for the blade and control surface consists of three sets of equations. These are sets of nonlinear differential equations that describe the final equations of motion in the time domain. The blade equations of motion (Eqns. D.8-D.10) or Eqn. D.20 required for the coupled trim/aeroelastic response, can be written in the vector form:

$$\mathbf{f_b}(\mathbf{q_b}, \dot{\mathbf{q}}_\mathbf{b}, \ddot{\mathbf{q}}_\mathbf{b}, \mathbf{x_a}, \mathbf{q_t}; \psi) = \mathbf{0}. \tag{D.35}$$

where $\mathbf{q_b}$ represents the vector of blade degrees of freedom, described in Eqn. D.11, or the modal participation , $\mathbf{x_a}$ represents the vector of aerodynamic states (Eqn. C.17), , and $\mathbf{q_t}$ represents the trim vector (Eqn. D.21) . To convert Eqn. D.35 to first order form, define a mass matrix given by:

$$\mathbf{M_b} = \frac{\partial \mathbf{f_b}}{\partial \ddot{\mathbf{q}}_\mathbf{b}} \tag{D.36}$$

This allows Eqn. D.35 to be decomposed into the form:

$$\mathbf{f_b} = \mathbf{g_b}(\mathbf{q_b}, \dot{\mathbf{q}}_\mathbf{b}, \mathbf{x_a}, \mathbf{q_t}; \psi) + \mathbf{M_b}(\mathbf{q_b}, \mathbf{q_t}; \psi)\ddot{\mathbf{q}}_\mathbf{b} = \mathbf{0}. \tag{D.37}$$

Solving for $\ddot{\mathbf{q}}_\mathbf{b}$ yields

$$\ddot{\mathbf{q}}_\mathbf{b} = -\mathbf{M_b^{-1}}\mathbf{g_b}. \tag{D.38}$$

Explicit expressions for $\mathbf{M_b}$ and $\mathbf{g_b}$ can be found in Ref. 70. The second order system (D.38) can be written in the following state variable form

$$\dot{\mathbf{x}}_b = \begin{bmatrix} \mathbf{0} & \mathbf{I} \\ \mathbf{0} & \mathbf{0} \end{bmatrix} \mathbf{x_b} + \begin{bmatrix} \mathbf{0} \\ -\mathbf{M_b^{-1}} \mathbf{g_b} \end{bmatrix}, \tag{D.39}$$

where $\mathbf{x_b}$ is the state vector of blade degrees of freedom:

$$\mathbf{x_b} = \begin{bmatrix} \mathbf{q_b} \\ \dot{\mathbf{q}}_\mathbf{b} \end{bmatrix}. \tag{D.40}$$

Similarly, the complete set of aerodynamic state equations is represented by the vector expression

$$\mathbf{f_a}(\mathbf{q_b}, \dot{\mathbf{q}}_\mathbf{b}, \ddot{\mathbf{q}}_\mathbf{b}, \mathbf{x_a}, \dot{\mathbf{x}}_\mathbf{a}, \mathbf{q_t}; \psi) = 0, \tag{D.41}$$

which can be written in the first order form

$$\dot{\mathbf{x}}_\mathbf{a} = \mathbf{g_a}(\mathbf{q_b}, \dot{\mathbf{q}}_\mathbf{b}, \ddot{\mathbf{q}}_\mathbf{b}, \mathbf{x_a}, \mathbf{q_t}; \psi). \tag{D.42}$$

The dependence on $\ddot{\mathbf{q}}_\mathbf{b}$ is eliminated by substituting Eqn. (D.38) into Eqn. (D.42), producing the reduced set of equations

$$\dot{\mathbf{x}}_\mathbf{a} = \mathbf{g_{aR}}(\mathbf{x_b}, \mathbf{x_a}, \mathbf{q_t}; \psi). \tag{D.43}$$

Define a state vector $\mathbf{y}$ as

$$\mathbf{y} = \left\{ \begin{array}{c} \mathbf{x_b} \\ \\ \mathbf{x_a} \end{array} \right\}, \tag{D.44}$$

then, combining Eqns. (D.39) and (D.43) yields a system of coupled first-order state variable equations of the form:

$$\dot{\mathbf{y}} = \mathbf{F}(\mathbf{y}; t). \tag{D.45}$$

This system is solved numerically using the ODE solver DE/STEP, which is a general-purpose predictor-corrector Adams-Bashforth differential system solver [102].

D.2.1 Solution of the Trim Equations

The dependence of the trim equations (D.24)-(D.29) on blade degrees of freedom $\mathbf{q_b}$ and the aerodynamic states $\mathbf{x_a}$ in the trim equations occurs through terms representing the rotor hub loads. However, only the average values of the hub loads are used in the trim equations. When only the steady state response of the system is considered, the average values of the hub loads will depend only on the trim variables $\mathbf{q_t}$ defined in Eqn. D.21. The trim equations are solved using an iterative procedure referred to as the autopilot trim procedure. The trim solution presented here is identical to that of Ref. 24. The trim equations can be written in the form:

$$\mathbf{f_t}(\mathbf{q_t}) = 0. \tag{D.46}$$

Let $\mathbf{R_{ti}}$ be the vector of trim residuals at the trim condition $\mathbf{q_{t_i}}$ at iteration i:

$$\mathbf{f_t}(\mathbf{q_{t_i}}) = \mathbf{R_{t_i}}. \tag{D.47}$$

An iterative optimal control strategy is then used to reduce the value of $\mathbf{R_{t_i}}$; based on the minimization of the performance index:

$$J = \mathbf{R_{t_i}^T R_{t_i}}. \tag{D.48}$$

This algorithm resembles a feedback controller used for vibration reduction. The trim parameters at the i^{th} iteration are then given by:

$$\mathbf{q_{t_i}} = -\mathbf{T_i^{-1}} \mathbf{R_{t_{i-1}}} + \mathbf{q_{t_{i-1}}}, \tag{D.49}$$

where $\mathbf{T_i}$ is a transfer matrix describing the sensitivities of trim residuals to changes in the trim variables:

$$\mathbf{T_i} = \frac{\partial \mathbf{R_{t_i}}}{\partial \mathbf{q_t}}. \tag{D.50}$$

where $\mathbf{T_i}$ is computed using a finite difference scheme. Under certain complex flight conditions, convergence of this procedure can be improved using a relaxation approach:

$$\mathbf{q_{t_i}} = -\alpha \mathbf{T_i^{-1}} \mathbf{R_{t_{i-1}}} + \mathbf{q_{t_{i-1}}}, \tag{D.51}$$

where α is a relaxation parameter less than unity. The use of this relaxation parameter was employed first by Depailler [24].

D.3 Vibratory Hub Shears and Moments

The resultant force and moment at the root of the k-th blade is found by integrating the distributed inertial, gravitational, aerodynamic, and damping loads $\mathbf{p_b}, \mathbf{p_c}, \mathbf{q_b}, \mathbf{q_c}$ given in Eqns. (A.77)-(A.80), over the blade span. Following the procedure used in [Ref. 24, Eqns. (8.48)-(8.50)], the resultant shears and moments of the k-th blade, at azimuth ψ_k, may be expressed in the rotating "2" frame as:

$$\mathbf{F_{Rk}}(\psi_k) = \int_0^{L_b} (\mathbf{p_b} + \mathbf{p_c})\, dr, \tag{D.52}$$

$$\mathbf{M_{Rk}}(\psi_k) = \int_0^{L_b} (\mathbf{q_b} + \mathbf{q_c})\, dr, \tag{D.53}$$

where:

$$\psi_k = \psi + \frac{2\pi(k-1)}{N_b}. \tag{D.54}$$

Then, rotor hub shears and moments in the nonrotating "1" frame $F_H(\psi)$, $M_H(\psi)$ are computed by summing the contribution of each blade $F_{Rk}(\psi_k)$, $M_{Rk}(\psi_k)$ and by converting them from the "2" frame to the "1" frame using a coordinate transformation described in Eqn. (A.4).

In an N_b-bladed helicopter with identical blades, N_b/rev is the dominant harmonic of vibratory loads transferred to the hub. Other harmonics of vibratory loads are also present, but these are of lesser importance and are not considered in the active reduction problems addressed in this study. The quantities $\mathbf{F_{H4c}}$, $\mathbf{F_{H4s}}$,

$\mathbf{F_{H4c}}$, and $\mathbf{F_{H4s}}$ represent the $\sin$ and $\cos$ components of the 4/rev hub shears and moments, and are obtained using

$$\mathbf{F_{H4c}} = \frac{1}{2}\int_0^{2\pi} \mathbf{F_H}(\psi)\cos 4\psi \; d\psi, \tag{D.55}$$

$$\mathbf{F_{H4s}} = \frac{1}{2}\int_0^{2\pi} \mathbf{F_H}(\psi)\sin 4\psi \; d\psi, \tag{D.56}$$

$$\mathbf{M_{H4c}} = \frac{1}{2}\int_0^{2\pi} \mathbf{M_H}(\psi)\cos 4\psi \; d\psi, \tag{D.57}$$

$$\mathbf{M_{H4s}} = \frac{1}{2}\int_0^{2\pi} \mathbf{M_H}(\psi)\sin 4\psi \; d\psi. \tag{D.58}$$

BIBLIOGRAPHY

BIBLIOGRAPHY

[1] I. H. Abbott and A. E. Von Doenhoff. *Theory of Wing Sections*, Dover Publications, Inc., 1959. pp. 77, 321.

[2] D. A. Allwine, J. A. Strahler, D. A. Lawrence, J. E. Jenkins, and J. H. Myatt. "Nonlinear Modeling of Unsteady Aerodynamics at High Angle of Attack". In *Proceedings of the AIAA Atmospheric Flight Mechanics Conference and Exhibit*, Providence, RI, Aug 2004.

[3] J.D. Baeder. "Passive Design for Reduction of High-Speed Impulsive Rotor Noise". *Journal of the American Helicopter Society*, 43(3):222–234, Jul 1998.

[4] J. P. Baker, K. J. Standish, and C. P. van Dam. "Two-Dimensional Wind Tunnel and Computational Investigation of a Microtab Modified Airfoil". *Journal of Aircraft*, 44(2):563–572, March-April 2007.

[5] M. Bebesel, D. Roth, and K. Pongratz. "Reduction of BVI Noise on the Ground - In Flight Evaluation of Closed-Loop Controller". In *Proceedings of the 28th European Rotorcraft Forum*, pages 19.1–19.9, Bristol, England, September 2002.

[6] R. Blackwell and T. A. Millott. "Dynamics Design Characteristics of the Sikorsky X2 Technology Demonstrator Aircraft". In *Proceedings of the 64th American Helicopter Society Annual Forum, Montreal, Canada, Apr-May*, 2008.

[7] E. R. Booth and M. L. Wilbur. "Acoustic Aspects of Active-Twist Rotor Control". In *Proceedings of the American Helicopter Society 58th Annual Forum*, Montreal, Canada, June 2002.

[8] E. R. Booth and M. L. Wilbur. "Acoustic Aspects of Active-Twist Rotor Control". *Journal of the American Helicopter Society*, 49(1), January 2004.

[9] D.A. Boxwell and F.H. Schmitz, *In-Flight Acoustic Comparison of the 540 and K747 Main Rotors for the AH-1S Helicopter.* USAAEFA Project No. 77-38, US Army, Oct 1979.

[10] K. S. Brentner, G. A. Bres, and G. Perez. "Maneuvering Rotorcraft Noise Prediction: A New Code for a New Problem". In *Proceedings of the American Helicopter Society Aerodynamics, Acoustics and Test Evaluation Technical Specialists Meeting*, San Francisco, CA, Jan 2002.

[11] K. S. Brentner and F. Farassat. "Modeling Aerodynamically Generated Sound of Helicopter Rotors". *Progress in Aerospace Sciences*, 39(2–3):83–120, February–April 2003.

[12] K.S. Brentner, *Prediction of Helicopter Rotor Discrete Frequency Noise: A Computer Program Incorporating Realistic Blade Motions and Advanced Acoustic Formulation*. NASA-TM-87721, Oct 1986.

[13] A. Brocklehurst and G.N. Barakos. "A Review of Helicopter Rotor Blade Tip Shapes". *Progress in Aerospace Sciences*, 56:35–74, Jan 2013.

[14] A. Brocklehurst and E. Duque. "Experimental and Numerical Study of the British Experimental Rotor Programme Blade". In *Proceedings of the 8th Applied Aerodynamics Conference*, Portland, Oregon, 1990.

[15] R. Celi. "Recent Applications of Design Optimization to Rotorcraft—A Survey". *Journal of Aircraft*, 36(1):176–189, January-February 1999.

[16] R. Celi and P.P. Friedmann. "Aeroelastic Modeling of Swept Tip Rotor Blades Using Finite Elements". *Journal of the American Helicopter Society*, 33(2):43–52, April 1988.

[17] R. Celi and P.P. Friedmann. "Structural Optimization with Aeroelastic Constraints of Rotor Blades with Straight and Swept Tips". *AIAA Journal*, 28(5):928–936, May 1990.

[18] M.H. Chia, A.K. Padthe, K. Duraisamy, and P.P. Friedmann. "An Efficient Approach for the Simulation and On-Blade Control of Noise and Vibration". In *Proceedings of the 72nd American Helicopter Society Annual Forum*, May 2016.

[19] Miang H. Chia, Ashwani K. Padthe, and Peretz P. Friedmann. "A Parametric Study of On-Blade Control Device Performance for Helicopter Vibration and Noise Reduction". In *Proceedings of the 70th American Helicopter Society Annual Forum*, May 20-22 2014.

[20] D. A. Conner and D. R. Hoad, *Reduction of High-Speed Impulsive Noise by Blade Planform Modification of a Model Helicopter Rotor*. NASA TM84553, 1982.

[21] M. de Terlizzi. *Blade Vortex Interaction and Its Alleviation Using Passive and Active Control Approaches*. PhD Dissertation, UCLA, 1999.

[22] M. de Terlizzi and P. P. Friedmann. "Active Control of BVI Induced Vibrations Using a Refined Aerodynamic Model and Experimental Correlation". In *American Helicopter Society 55th Annual Forum Proceedings*, pages 599–615, Montreal, Canada, May 25-27 1999.

[23] A. F. Deming, *Noise from Propellers with Symmetrical Sections at Zero Blade Angle, II*. NACA TN679, Dec 1938.

[24] G. Depailler. *Alleviation of Dynamic Stall Induced Vibrations on Helicopter Rotors Using Actively Controlled Flaps*. PhD Dissertation, University of Michigan, Ann Arbor, 2002.

[25] G. Depailler and P. P. Friedmann. "Reductions of Vibrations Due to Dynamic Stall in Helicopters Using an Actively Controlled Flap". In *Proceedings of the 43rd AIAA/ASME/ASCE/AHS/ACS Structures, Structural Dynamics and Materials Conference*, Denver, CO, April 2002. AIAA Paper No. 2002-1431.

[26] O. Dieterich, B. Enenkl, and D. Roth. "Trailing Edge Flaps for Active Rotor Control Aeroelastic Characteristics of the ADASYS Rotor System". In *Proceedings of the 62nd American Helicopter Society Annual Forum*, Phoenix, AZ, May 2006.

[27] F. Farassat. "Linear Acoustic Formulas for Calculation of Rotating Blade Noise". *AIAA Journal*, 19(9), September 1981.

[28] F. Farassat, *Derivation of Formulations 1 and 1A of Farassat*. NASA/TM-2007-214853, March 2007.

[29] F. Farassat and G. P. Succi. "A Review of Propeller Discrete Frequency Noise Prediction Technology with Emphasis on Two Current Methods for Time Domain Calculations". *Journal of Sound and Vibration*, 71(3), 1980.

[30] F. Farassat and G.P. Succi. "The Prediction of Helicopter Rotor Discrete Frequency Noise". *Vertica*, 7(4):309–320, October 1983.

[31] J. E. Ffowcs Williams and D. L. Hawkings. "Sound Generation by Turbulence and Surfaces in Arbitrary Motion". *Philosophical Transactions of Royal Soc. London, Series A*, 264(1151):321–342, May 1969.

[32] R. Fletcher. *Practical Methods of Optimization*, John Wiley and Sons, 1987.

[33] P. P. Friedmann. "Helicopter Vibration Reduction Using Structural Optimization with Aeroelastic/Multidisciplinary Constraints - A Survey". *Journal of Aircraft*, 28(1):8–21, 1991.

[34] Peretz P. Friedmann. "On-Blade Control of Rotor Vibration, Noise and Vibration: Just Around the Corner? The 33rd Alexander Nikolsky Honorary Lecture". *Journal of American Helicopter Society*, 59(4):8–21, October 2014.

[35] M. Fulton. "Design of the Active Elevon Rotor for Low Vibration". In *Proceedings of the AHS Aeromechanics Specialist' Meeting, Atlanta, GA, Nov 13-15*, 2000.

[36] R. Ganguli. "Survey of Recent Developments in Rotorcraft Design Optimization". *Journal of Aircraft*, 41(3):493–510, May-June 2004.

[37] R. Ganguli and I. Chopra. "Aeroelastic Optimization of an Advanced Geometry Helicopter Rotor". *Journal of the American Helicopter Society*, 41(1):18–28, January 1996.

[38] R. Ganguli and I. Chopra. "Aeroelastic Tailoring of Composite Coupling and Blade Spanwise Geometry of a Helicopter Rotor Using Optimization Methods". *Journal of the American Helicopter Society*, 42(3):218–228, July 1997.

[39] A.R. George. "Helicopter Noise: State of the Art". *Journal of Aircraft*, 15(11):707–715, 1978.

[40] P. Giguere, J. Lemay, and G. Dumas. "Gurney Flap Effects and Scaling for Low-speed Airfoils". In *Proceedings of the AIAA Applied Aerodynamics Conference*, San Diego, June 1995.

[41] B. Glaz, P. P. Friedmann, L. Liu, D. Kumar, and C. E. S. Cesnik. "The AVINOR Aeroelastic Simulation Code and Its Application to Reduced Vibration Composite Rotor Blade Design". In *Proceedings of the 50th AIAA/ASME/ASCE/AHS/ACS Structures, Structural Dynamics and Materials Conference*, May 2009. AIAA Paper No. 2009-2601.

[42] G. Gopalan and F. H. Schmitz. "Far-Field Near In-Plane Harmonic Main Rotor Helicopter Impulsive Noise Reduction Possibilities". In *Proceedings of the 64th American Helicopter Society Annual Forum*, Apr 2008.

[43] S. Hahn, J. Alonso, K. Duraisamy, G. Iaccarino, S. Lele, P. Moin, F. Schmitz, M. Shoeybi, and Z. Wu. "Progress on Hybrid Unsteady Simulation of Helicopter Rotor Flow". In *Annual Research Briefs, Center for Turbulence Research*, Stanford University, 2005.

[44] S. A. Jacklin, A. Blaas, D. Teves, and R. Kube. "Reduction of Helicopter BVI Noise, Vibration, and Power Consumption through Individual Blade Control". In *Proceedings of the 51st Annual Forum of the American Helicopter Society*, pages 662–680, May 1995.

[45] R. Jain and H. Yeo. "Effects of Torsion Frequencies on Rotor Performance and Structural Loads with Trailing Edge Flap". *Smart Material Structures*, July 2012.

[46] W. Johnson, *CAMRAD/JA - A Comprehensive Analytical Model of Rotorcraft Aerodynamics and Dynamics, Vol I. Theory Manual*. Johnson Aeronautics, Palo Alto, CA, 1988.

[47] W. Johnson, *CAMRAD/JA - A Comprehensive Analytical Model of Rotorcraft Aerodynamics and Dynamics, Vol II. Users' Manual*. Johnson Aeronautics, Palo Alto, CA, 1988.

[48] M. E. Kelly, K. Duraisamy, and R. E. Brown. "Predicting Blade Vortex Interaction, Airloads and Acoustics Using the Vorticity Transport Model". In *Proceedings of the AHS Specialist's Conference on Aeromechanics*, January 2008.

[49] H. W. Kim, K. Duraisamy, and R. E. Brown. "Effect of Rotor Stiffness and Lift Offset on the Aeroacoustics of a Coaxial Rotor in Level Flight". In *Proceedings of the 65th American Helicopter Society Annual Forum*, May 2009.

[50] H.W. Kim, A.R. Kenyon, R.E. Brown, and K. Duraisamy. "Interactional Aerodynamics and Acoustics of a Hingeless Coaxial Helicopter with an Auxiliary Propeller in Forward Flight". *The Aeronautical Journal*, 113(1140):65–78, February 2009.

[51] P. Konstanzer, B. Enenkl, P. Aubourg, and P. Cranga. "Recent Advances in Eurocopter's Passive and Active Vibration Control". In *Proceedings of the 64th Annual Forum of the American Helicopter Society*, Montreal, Canada, May 2008.

[52] J.B. Kosmatka. *Structural Dynamic Modeling of Advanced Composite Propellers by the Finite Element Model*. PhD Dissertation, University of California, Los Angeles, 1986.

[53] J.B. Kosmatka and P.P. Friedmann. "Vibration Analysis of Composite Turbopropellers Using a Nonlinear Beam-Type Finite-Element Approach". *AIAA Journal*, 27(11):1606–1614, November 1989.

[54] A. J. Landgrebe and E.D. Bellinger. "Experimental Investigation of Model Variable - Geometry and Ogee-Tip Rotors". Technical Report CR-2275, NASA, Feb 1974.

[55] J. G. Leishman. *Principles of Helicopter Aerodynamics*, Cambridge University Press, Cambridge, 2006. Chapter 7.5.3.

[56] Y. Li, J. Wang, and P. Zhang. "Influences of Mounting Angles and Locations on the Effects of Gurney Flaps". *Journal of Aircraft*, 40(3):494–498, May-June 2003.

[57] R. H. Liebeck. "Design of Subsonic Airfoils for High Lift". *Journal of Aircraft*, 15(9):547–561, Sept 1978.

[58] C. Lim, C. Tung, Y. Yu, C. Burley, T. F. Brooks, D. Boyd, B. G. van der Wall, O. Schneider, P. Richard, P. Beaumier, Y. Delrieux, and K. Pengel. "Hart-II: Prediction of Blade-Vortex Interaction Loading". In *Proceedings of the 29th European Rotorcraft Forum*, Friedrichschafen, Germany, September 2003.

[59] L. Liu. *BVI Induced Vibration and Noise Alleviation By Active and Passive Approaches*. PhD Dissertation, University of Michigan, Ann Arbor, 2005.

[60] L. Liu, A. Padthe, P. P. Friedmann, E. Quon, and M. Smith. "Unsteady Aerodynamics of an Airfoil/Flap Combination on a Helicopter Rotor Using CFD and Approximate Methods". *Journal of American Helicopter Society*, 56(3):1–13, July 2011.

[61] L. Liu, A. K. Padthe, and P. P. Friedmann. "Computational Study of Microflaps with Application to Vibration Reduction in Helicopter Rotors". *AIAA Journal*, 49(7):1450–1465, July 2011.

[62] Loewy, R.G. "Helicopter Vibrations: A Technological Perspective". *Journal of the American Helicopter Society*, 29(4):4 – 30, October 1984.

[63] P. Lorber. "Aerodynamic Results of Pressure-Instrumented Model Rotor Test at the DNW.". *Journal of American Helicopter Society*, 36(4):66–76, 1991.

[64] P. Lorber, B. Hain, J. Wong, and B. Wake. "Rotor Aeromechanics Results from the Sikorsky Active Flap Demonstration Rotor". In *Proceedings of the 68th American Helicopter Society Annual Forum*, Fort Worth, TX, May 1-3 2012.

[65] M.V. Lowson, *Helicopter Noise: Analysis, Prediction and Methods of Reduction*. AGARD-LS-63-5, March 1973.

[66] A.S. Lyrintzis, J.R. Jameson, and E.K. Koutsavdis. "Technical Note: A Study of Rotorcraft Blade-Tip Shape High Speed Impulsive Noise Characteristics". *Journal of the American Helicopter Society*, 45(1):54–57, Jan 2000.

[67] W. R. Mantay, P. A. Shidler, and R. L. Campbell. "Some Results of the Testing of a Full-Scale Ogee-Tip Rotor". *Journal of Aircraft*, 6(3):215–221, March 1979.

[68] W.R. Mantay and W.T. Yeager Jr, *Parametric Tip Effects for Conformable Rotor Applications*. NASA Technical Memorandum TM-85682, August 1983.

[69] J. H. Milgram and I. Chopra. "A Parametric Design Study for Actively Controlled Trailing Edge Flaps". *Journal of the American Helicopter Society*, 43(2):110–119, April 1998.

[70] T. A. Millott and P. P. Friedmann, *Vibration Reduction in Helicopter Rotors Using an Actively Controlled Partial Span Trailing Edge Flap Located on the Blade*. NASA CR 4611, June 1994.

[71] A. Murashige, N. Kobiki, A. Tsuchihasi, H. Nakamura, K. Inagaki, and E. Yamakawa. "ATIC Aeroacoustic Model Rotor Test at DNW". In *Proceedings of Heli Japan 98*, Gifu, Japan, 1998.

[72] T. F. Myrtle. *Development of an Improved Aeroelastic Model for the Investigation of Vibration Reduction in Helicopter Rotors using Trailing Edge Flaps*. PhD Dissertation, University of California, Los Angeles, 1998.

[73] T. F. Myrtle and P. P. Friedmann. "Application of a New Compressible Time Domain Aerodynamic Model to Vibration Reduction in Helicopters Using an Actively Controlled Flap". *Journal of the American Helicopter Society*, 46(1):32–43, January 2001.

[74] T.F. Myrtle and P.P. Friedmann. "Vibration Reduction in Rotorcraft Using the Actively Controlled Trailing Edge Flap and Issues Related to Practical Implementation". In *Proceedings of the 54th American Helicopter Society Annual Forum*, Washington, DC, May 1998.

[75] H. Nakamura, H. Nishimura, N. Kondo, E. Yamakawa, T. Aoyama, and S. Saito. "Effect of Blade Geometry on BVI Noise in Various Flight Conditions". In *Proceedings of Heli Japan 98*, Gifu, Japan, 1998.

[76] H. Nishimura, N. Kondo, H. Nakamura, T. Tsujiuchi, E. Yamakawa, T. Aoyama, and S. Saito. "Comparison between Calculated Rotor Noise and Experimental Data Obtained by DNW Test". In *Proceedings of the 24th European Rotorcraft Forum*, Marseille, France, September 1998.

[77] Y. Niu, T. Hsu, C. T. Hsieh, C. C. Chang, and C. C. Chu. "How Does a Gurney Flap Enhance the Aerodynamic Forces". *AIAA Journal*, 48(11):2710–2714, November 2010.

[78] T. R. Norman, C Theodore, P Shinoda, D Fuerst, U. T. P. Arnold, S. Makinen, P. Lorber, and J. O'Neill. "Full-Scale Wind Tunnel Test of a UH-60 Individual Blade Control System for Performance Improvement and Vibration, Loads, and Noise Control". In *Proceedings of the 65th American Helicopter Society Annual Forum*, May 2009.

[79] A. Padthe. *Active Vibration and Noise Alleviation in Rotorcraft Using Microflaps*. PhD Dissertation, University of Michigan, Ann Arbor, 2011.

[80] A. Padthe and P. P. Friedmann. "Simultaneous Blade-Vortex Interaction Noise and Vibration Reduction in Rotorcraft Using Microflaps, Including the Effect of Actuator Saturation". *Journal of American Helicopter Society*, 60(4):1–16, October 2015.

[81] A. K. Padthe and P. P. Friedmann. "Simultaneous BVI Noise and Vibration Reduction in Rotorcraft Using Microflaps Including the Effect of Actuator Actuation". In *Proceedings of the AHS 68th Annual Forum, Fort Worth, Texas*, 2012.

[82] A. K. Padthe, L. Liu, and P. P. Friedmann. "Numerical Evaluation of Microflaps for On Blade Control of Noise and Vibration". In *Proceedings of the 52nd AIAA/ASME/ASCE/AHS/ACS Structures, Structural Dynamics and Materials Conference*, Denver, CO, April 2011.

[83] Ashwani K. Padthe, Peretz P. Friedmann, Miang H. Chia, and Li Liu. "A Comprehensive Numerical Assessment of Microflaps for On-Blade Control of Rotorcraft Noise and Vibration". *Journal of Aircraft*, 53(4):1113–1130, October 2016.

[84] D. Patt. *Simultaneous Noise and Vibration Reduction in Rotorcraft Using Actively Controlled Flaps and Including Performance Considerations*. PhD Dissertation, University of Michigan, Ann Arbor, 2004.

[85] D. Patt, L. Liu, J. Chandrasekar, D. S. Bernstein, and P. P. Friedmann. "Higher-Harmonic-Control Algorithm for Helicopter Vibration Reduction Revisited". *Journal of Guidance, Control, and Dynamics*, 28(5):918–930, September-October 2005.

[86] D. Patt, L. Liu, and P. P. Friedmann. "Rotorcraft Vibration Reduction and Noise Prediction Using a Unified Aeroelastic Response Simulation". In *Proceedings of the 59th American Helicopter Society Annual Forum*, Phoenix, AZ, May 2003.

[87] D. Patt, L. Liu, and P. P. Friedmann. "Rotorcraft Vibration Reduction and Noise Prediction Using a Unified Aeroelastic Response Simulation". *Journal of the American Helicopter Society*, 50(1):95–106, January 2005.

[88] D. Patt, L. Liu, and P. P. Friedmann. "Simultaneous Vibration and Noise Reduction in Rotorcraft Using Aeroelastic Simulation". *Journal of the American Helicopter Society*, 51(2):127–140, April 2006.

[89] D. Petot. "Differential Equation Modeling of Dynamic Stall". *La Recherche Aérospatiale*, 5:59–71, 1989.

[90] J. Prieur, P. Lafon, M. Caplot, and A. Desopper. "Aerodynamics and Acoustics of Rectangular and Swept Rotor Blade Tips". *Journal of the American Helicopter Society*, 34(1):42–51, Jan 1989.

[91] A. Rabourdin, J. Maurice, O. Dieterich, and P. Konstanzer. "Blue Pulse Active Rotor Control at Airbus Helicopters - New EC145 Demonstrator and Flight Test Results". In *Proceedings of the 70th American Helicopter Society Annual Forum*, Montreal, Quebec, Canada, May 20-22 2014.

[92] G. Rahier and Y. Delrieux. "Blade-Vortex Interaction Noise Prediction Using a Rotor Wake Roll-Up Model". *Journal of Aircraft*, 34(4):522–530, July-August 1997.

[93] G. Reichert. "Helicopter Vibration Control - A Survey". *Vertica*, 5(1):1–20, 1981.

[94] K. L. Rogers, *Airplane Math Modeling Methods for Actively Control Design*. AGARD-CP-228, August 1977.

[95] A. Rosen and P. P. Friedmann, *Nonlinear Equations of Equilibrium for Elastic Helicopter or Wind Turbine Blades Undergoing Moderate Deformation*. NASA CR 159478, December 1978.

[96] D. C. Sargent and F. H. Schmitz. "Fundamental Experimental Studies Supporting On-Blade Tip Air Blowing Control of In-Plane Rotor Harmonic Noise". In *Proceedings of the 18th AIAA/CEAS Aeroacoustics Conference*, 4-6 June 2012.

[97] F. H. Schmitz, *Rotor Noise, Aeroacoustics of Flight Vehicles, Vol.1: Noise Sources*. NASA Technical Report 90-3052, Aug 1991.

[98] F. H. Schmitz, *Rotor Noise, Aeroacoustics of Flight Vehicles, Vol.1*. Acoustical Society of America and American Institute of Physics, New York, 1995. pp. 65-149.

[99] F. H. Schmitz and Y. H. Yu. "Helicopter Impulsive Noise: Theoretical and Experimental Status". *Journal of Sound and Vibration*, 109:361–422, 1986.

[100] O. Schneider and B. van der Wall. "Final Analysis of HART II Blade Deflection Measurement". In *Proceedings of the 29th European Rotorcraft Forum*, Friedrichschafen, Germany, September 2003.

[101] M. P. Scully. *Computation of Helicopter Rotor Wake Geometry and its Influence on Rotor Harmonic Airloads*. PhD Dissertation, Aeroelastic Research Laboratory, Massachusetts Institute of Technology, 1975.

[102] L. F. Shampine and M. K. Gordon. *Computer Solution of Ordinary Differential Equations - The Initial Value Problem*, W. H. Freeman and Co., San Francisco, CA, 1975.

[103] S. J. Shin, C. E. S. Cesnik, and S. R. Hall. "Closed-Loop Control Test of the NASA/Army/MIT Active Twist Rotor for Vibration Reduction". *Journal of the American Helicopter Society*, 50(4):178–194, October 2005.

[104] B. W. Sim. "Suppressing In-Plane, Low Frequency Helicopter Harmonic Noise with Active Controls". In *Proceedings of the American Helicopter Society Aeromechanics Specialist's Meeting*, Jan 2008.

[105] B. W. Sim, R. D. JanakiRam, and B. H. Lau. "Reduced In-Plane, Low-Frequency Noise of an Active Flap Rotor". *Journal of the American Helicopter Society*, 59(2):1–17, April 2014.

[106] B. W. Sim, M. Potsdam, C. Kitaploglu, P LeMasurier, P. Lorber, and J. Andrews. "Localized, Non-Harmonic Active Flap Motions for Low Frequency In-Plane Rotor Noise Reduction". In *Proceedings of the 68th American Helicopter Society Annual Forum*, May 2012.

[107] W. Splettstoesser, R. Kube, W. Wagner, U. Seelhorst, A. Boutier, F. Micheli, E. Mercker, and K. Pengel. "Key Results From a Higher Harmonic Control Aeroacoustic Rotor Test (HART)". *Journal of the American Helicopter Society*, 42(1):58–78, January 1997.

[108] W. Splettstoesser, K. J. Schultz, R. Kube, T. F. Brooks, E. R. Booth, George Niesl, and Olivier Streby. "A Higher Harmonic Control Test in the DNW to Reduce Impulsive BVI Noise". *Journal of the American Helicopter Society*, 39(4):3–13, October 1994.

[109] F. K. Straub, V. R. Anand, T. S. Birchette, and B. H. Lau. "SMART Rotor Development and Wind Tunnel Test". In *Proceedings of the 35th European Rotorcraft Forum*, Hamburg, Germany, Sep 2009.

[110] F. K. Straub, V.R. Anand, T. S. Birchette, and B. H. Lau. "Wind Tunnel Test of the SMART Active Flap Rotor". In *Proceedings of the 65th American Helicopter Society Annual Forum*, May 2009.

[111] A. Thom and K. Duraisamy. "High Resolution Simulations of Parallel Blade-Vortex Interactions". *AIAA Journal*, 48(10), October 2010.

[112] B. G. van der Wall, C. Junker, C. Burley, T. Brooks, Y. Yu, P. Raffel, and W. Wagner. "The HART II test in the LLF of the DNW - a Major Step towards Rotor Wake Understanding". In *Proceedings of the 28th European Rotorcraft Forum*, Bristol, England, September 2002.

[113] S. P. Viswanathan and A. W. Myers. "Reduction of Helicopter Vibration Through Control of Hub Impedance". *Journal of the American Helicopter Society*, 25(4):3–12, October 1980.

[114] K. Washizu. "Some Considerations on a Naturally Curved and Twisted Slender Beam". *Journal of Mathematics and Physics*, 43((2)):111–116, 1964.

[115] G. Wempner. *Mechanics of Solids with Application to Thin Bodies*, Sijthof and Noordoff, 1981.

[116] R.P.Jr. White. "The Status of Rotor Noise Technology". *Journal of the American Helicopter Society*, 25(1):22–29, January 1980.

[117] M. L. Wilbur, P. H. Mirick, Jr. W. T. Yeager, C. W. Langston, S. J. Shin, and C. E. S. Cesnik. "Vibratory Loads Reduction Testing of the NASA/Army/MIT Active Twist Rotor". *Journal of the American Helicopter Society*, 47(4):123–133, October 2002.

[118] G. Wilke. "Applying Multi-Objective Variable-Fidelity Optimization Techniques to Industrial Scale Rotors: Blade Designs for Clean Sky". In *Proceedings of the 41st European Rotorcraft Forum*, Munich, Germany, September 1-4 2015.

[119] J. Wong, J. Andrews, and M. Brigley. "Dynamics of a High Authority Active Flap Rotor". In *Proceedings of the 68th American Helicopter Society Annual Forum*, Fort Worth, TX, May 1-3 2012.

[120] T. Yang and K. S. Brentner. "Loading Schedule Design for Rotor Thickness Noise Reduction". In *Proceedings for the AHS 69th Annual Forum*, May 2013.

[121] Tianxiao Yang and Kennneth S. Brentner. "Understanding In-Plane Noise and Loading for Active Noise Control". In *Proceedings of the 70th American Helicopter Society Annual Forum*, May 2014.

[122] Y. H. Yu. "Rotor Blade-Vortex Interaction Noise". *Progress in Aerospace Sciences*, 36(2):97–115, February 2000.

[123] Y. H. Yu, B. Gmelin, W. Splettstoesser, J. J. Philippe, J. Prieur, and T. F. Brooks. "Reduction of Helicopter Blade-Vortex Interaction Noise by Active Rotor Control Technology". *Progress in Aerospace Sciences*, 33(10):647–687, September 1997.

[124] Y. H. Yu, C. Tung, B. van der Wall, H. J. Pausder, Casey Burley, Thomas Brooks, P. Beaumier, Y. Delrieux, E. Mercker, and K. Pengel. "The HART-II Test: Rotor Wakes and Aeroacoustics with Higher-Harmonic Pitch Control (HHC) Inputs - The Joint German/French/Dutch/US Project -". In *Proceedings of the 58th Annual Forum of the American Helicopter Society*, Montreal, Canada, June 2002.

[125] K. A. Yuan and P. P. Friedmann, *Aeroelastic and Structural Optimization of Composite Helicopter Rotor Blades with Swept Tips*. NASA CR 4665, June 1995.

[126] K. A. Yuan and P.P. Friedmann. "Structural Optimization for Vibratory Loads Reduction of Composite Helicopter Rotor Blades with Advanced Geometry Tips". *Journal of the American Helicopter Society*, 43((3)):246–256, July 1998.